This electronic thesis or dissertation has been downloaded from the King's Research Portal at https://kclpure.kcl.ac.uk/portal/

A stochastic approach to quantum spin systems

De Nicola, Stefano

Awarding institution:
King's College London

The copyright of this thesis rests with the author and no quotation from it or information derived from it may be published without proper acknowledgement.

END USER LICENCE AGREEMENT

Unless another licence is stated on the immediately following page this work is licensed

under a Creative Commons Attribution-NonCommercial-NoDerivatives 4.0 International

licence. https://creativecommons.org/licenses/by-nc-nd/4.0/

You are free to copy, distribute and transmit the work

Under the following conditions:

- Attribution: You must attribute the work in the manner specified by the author (but not in any way that suggests that they endorse you or your use of the work).
- Non Commercial: You may not use this work for commercial purposes.
- No Derivative Works - You may not alter, transform, or build upon this work.

Any of these conditions can be waived if you receive permission from the author. Your fair dealings and other rights are in no way affected by the above.

Take down policy

If you believe that this document breaches copyright please contact librarypure@kcl.ac.uk providing details, and we will remove access to the work immediately and investigate your claim.

Download date: 21. Apr. 2021

A Stochastic Approach to Quantum Spin Systems

Stefano De Nicola

Department of Physics
CANES Centre for Doctoral Training
King's College London

This dissertation is submitted for the degree of
Doctor of Philosophy

December 2018

Acknowledgements

I would like to thank my supervisors M. J. Bhaseen and B. Doyon for their advice and guidance over the course of this PhD, which has been a great experience of personal and intellectual development. I would also like to thank all the other wonderful people I have met at King's College, including Chris, Jean, Peter and all of the academic staff, who gave me so much both on a scientific and a human side, the administrative staff and especially Valeria, and all my CANES fellows and office mates, who made my time at King's as stimulating as it was fun. Finally, I would like to thank my parents and Adriana for their invaluable support over the years of this PhD. I acknowledge funding from the EPSRC Centre for Doctoral Training in Cross-Disciplinary Approaches to Non-Equilibrium Systems (CANES) under grant EP/L015854/1. I am grateful to the UK Materials and Molecular Modelling Hub for computational resources, which is partially funded by EPSRC (EP/P020194/1). I also acknowledge computer time on the Rosalind High Performance Computer Cluster. The work presented in this Thesis is partly based on our recent preprint [1].

Abstract

In this Thesis, we investigate an exact stochastic approach to quantum spins systems [2–4], in which the unitary time evolution of interacting spins is mapped onto the stochastic dynamics of classical variables and the interactions play the role of noise. We study this approach both in real and imaginary time, focussing in particular on the quantum Ising model. In real time, we demonstrate that the stochastic approach is capable of accessing a wide range of systems, including higher dimensional and disordered ones, by numerically computing time-dependent quantum expectation values from stochastic processes. Furthermore, we show that the dynamics of the classical variables contains signatures of dynamical quantum phase transitions [5]. We then consider imaginary time evolution, showing how the stochastic approach can be used to compute grounds state expectation values. In this context, we introduce a measure transformation by means of which we are able to access large systems, as we demonstrate for $N = 150$ spins. We conclude our discussion by outlining directions for further developments.

Contents

Chapter 1

Introduction

Recent advances have made it possible to experimentally investigate the non-equilibrium coherent dynamics of isolated many-body quantum systems; models which were originally introduced to provide a simplified description of real condensed matter systems can now be accurately simulated in laboratories [6–16]. These landmark experiments have motivated great theoretical interest in characterising far-from-equilibrium quantum dynamics, including the emergence of thermalisation (or the lack thereof) and the extension of the concept of universality beyond the equilibrium regime [17–19]. In spite of substantial theoretical developments, a lack of techniques to investigate such systems remains, as analytical approaches are typically only available for integrable models; see Ref. [20] for a review. In addition, the most successful numerical methods are limited both by dimensionality and the growth of entanglement in time [21]. In higher dimensions, this is true even for ground state properties. Motivated by this need for new techniques of broad applicability, we investigate an exact mapping of many-body quantum dynamics to classical stochastic processes [2–4], which does not explicitly rely on integrability or dimensionality.

In this Chapter, we briefly review the broad and ever-expanding field of non-equilibrium many-body quantum dynamics. We begin with an overview of some recent experimental developments, explaining how isolated quantum systems can be accurately simulated in the laboratory and discussing the celebrated *quantum Newton's cradle* experiment [6]. We then introduce a number of central concepts in non-equilibrium quantum dynamics, considering the quantum quench setting to discuss issues such as thermalisation, the role of integrability, the effect of disorder and the phenomenon of dynamical quantum phase transitions [5]. Finally, we briefly outline the main analytical and numerical techniques that are currently available to investigate non-equilibrium quantum systems, highlighting their strengths and limitations. In particular, we discuss pioneering developments based on

an exact quantum-to-classical mapping [2–4], which are at the root of the developments of this Thesis. We conclude this introductory Chapter by outlining the structure of the rest of the Thesis.

1.1 Experimental Realisation of Isolated Quantum Systems

The recent surge of theoretical interest in the non-equilibrium dynamics of many-body quantum systems has been driven by substantial advances in experimental techniques, which have made it possible to engineer systems that can be regarded as isolated from the environment over time scales that are long compared to the relevant coherent quantum dynamics. Furthermore, the parameters of these systems can be accurately tuned, making it possible to experimentally realise specific Hamiltonians of interest. This has opened up the possibility of experimentally investigating a wide range of questions, often giving rise to new research directions, as we will see in the case of the quantum Newton's cradle [6].

The simulation of quantum systems to investigate non-equilibrium quantum dynamics is typically carried out using ultracold neutral atoms [14, 16, 22] and trapped ions [9, 13, 23]. In systems of ultracold atomic gases, the interactions between the constituents can be finely tuned by applying external magnetic fields, exploiting the phenomenon of Feshbach resonances [24]; the position of the atoms can also be precisely controlled by means of *optical lattices*, periodic potentials generated by the interference of laser beams which couple to the atoms via the optical dipole interaction [25, 22]. This makes it possible to realise systems of interest with exquisite control. Quantum field theories can also be studied, using e.g. atom chips [26, 27]. Furthermore, these systems can be probed with extremely powerful imaging techniques, such as fluorescence-based quantum gas microscopes [10, 28], capable of attaining single-atom resolution. Ultracold atoms have been used to investigate a large number of important models [19, 22], including Bose- and Fermi-Hubbard Hamiltonians [29–33] and paradigmatic spin chains such as the quantum Ising [34] and Heisenberg [35] models. Even though ultracold atoms are neutral, it is even possible to use them to study topological phases of matter arising from orbital magnetism. This is done by appropriately emulating the phase shift acquired by a charged particle under the action of a magnetic field [14], the Aharonov-Bohm effect [36]. In trapped ions experiments, each qubit is encoded in an individual ion trapped in e.g. a linear radiofrequency trap [37, 38, 13]. Qubits are manipulated and made to interact with each

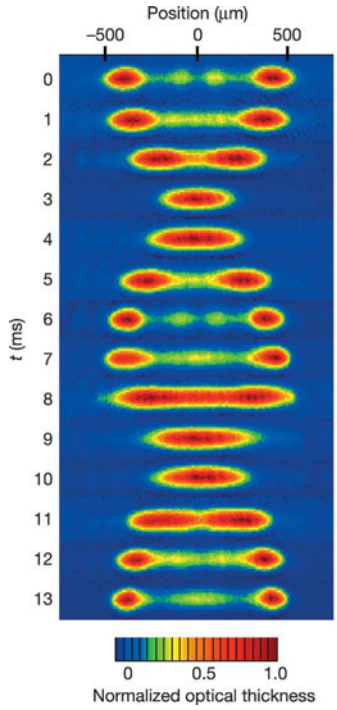

Figure 1.1: Absorption image of the oscillations of ^{87}Rb atoms in the quantum Newton's cradle following an initial momentum kick. In this experiment, even after several oscillations, the atoms are seen not to thermalise. Figure published in Ref. [6].

other by laser pulses or microwave radiation [13], and individual qubit states can be detected by spatially resolved fluorescence measurements with great precision [39]. Thus, systems of trapped ions allow experimentalists to attain great control over the individual constituents of the system [40, 41, 19].

The development of novel experimental techniques has lead to significant breakthroughs, which have paved the way for theoretical investigations. A celebrated example is the so-called *quantum Newton's cradle* [6], a groundbreaking experiment which has motivated a vast body of subsequent research. In this experiment, a system of ^{87}Rb atoms were confined into a two dimensional optical lattice, providing tight transverse confinement, combined with a dipole trap, providing weak axial trapping, so that they were effectively constrained to move in one dimension. By means of optical pulses, the atoms were prepared in a momentum superposition with $p = \pm 2\hbar k$, where k is the wavevector of the lattice light. The atoms were subsequently allowed to oscillate in a confining potential, as shown in Fig. 1.1; even after thousands of oscillations and after dephasing due to the anharmonic potential, the momentum distribution was found not to have thermalised. It was suggested that this could be due to the close resemblance between the atomic gas and

the Lieb-Liniger model, an integrable system [42, 43]; as we will recall in Section 1.2, integrable systems are characterised by an infinite number of conserved quantities and can indefinitely retain memory of their initial conditions, thus failing to thermalise. The observation of non-thermal behaviour in the quantum Netwon's cradle triggered great interest in issues such as the relaxation of isolated many-body quantum systems that are driven out of equilibrium. In the next Section, we will review some important theoretical developments in this area; in the context of quantum quenches, we will discuss the possible fates of an isolated quantum system at late times and novel phenomena that arise in systems that are driven far from equilibrium.

1.2 Non-Equilibrium Quantum Dynamics

As discussed in Section 1.1, experimental breakthroughs have motivated great theoretical interest in the non-equilibrium dynamics of many body quantum systems. The simplest setting to drive an isolated quantum system far from equilibrium is the *quantum quench* [44, 45], in which the system undergoes an abrupt global change in the parameters of the Hamiltonian. This non-equilbrium protocol was originally introduced to investigate the time evolution of enganglement [44], and has since been studied in a wide range of scenarios [45–58, 19, 59]. We begin our review of non-equilibrium quantum dynamics by discussing the quantum quench protocol in relation to the issue of thermalisation in isolated quantum systems and the conditions under which this may or may not occur. In the context of quantum quenches, we then specifically focus on the phenomenon of *dynamical quantum phase transitions* (DQPTs) [5], which have been proposed as non-equilibrium analogues of quantum phase transitions. These will be investigated in Chapter 4 using the stochastic approach which is at the core of this Thesis. While in this Thesis we focus on quantum quenches, we note that these are not the only protocol for driving a system far from equilibrium. Other non-equilibrium scenarios include quantum ramps, where the Hamiltonian is changed continuously in time, and Floquet systems, whose time evolution is determined by a periodic time-dependent Hamiltonian.

1.2.1 Quantum Quenches

Quantum quenches [44, 45, 59] are non-equilibrium protocols in which a system is prepared at $t = 0$ in an initial state $|\psi(0)\rangle$ and then evolved for $t > 0$ with a Hamiltonian $\hat{H}$ which acts non-trivially on $|\psi(0)\rangle$. The initial state $|\psi(0)\rangle$ is often chosen to be the ground state

of a Hamiltonian $\hat{H}_0 \neq \hat{H}$, such that

$$\hat{H}_0|\psi(0)\rangle = E_0|\psi(0)\rangle, \tag{1.1}$$

$$|\psi(t)\rangle = e^{-\frac{i}{\hbar}t\hat{H}}|\psi(0)\rangle. \tag{1.2}$$

One typical quantum quench setting consists in suddenly changing the value of a parameter λ of a given Hamiltonian, so that

$$\hat{H} = \begin{cases} \hat{H}(\lambda_0) & t < 0, \\ \hat{H}(\lambda_f) & t \geq 0. \end{cases} \tag{1.3}$$

The initial state $|\psi(0)\rangle$ can be decomposed in terms of the eigenstates of $\hat{H}$ as

$$\psi(t) = \sum_i c_i e^{-\frac{i}{\hbar}tE_i}, \tag{1.4}$$

where $c_i = \langle\Psi_i|\psi(0)\rangle$ and

$$\hat{H}|\Psi_i\rangle = E_i|\Psi_i\rangle. \tag{1.5}$$

Following a quantum quench, an extensive amount of energy above the ground state is deposited into the system, so that this is driven far from equilibrium.

Quantum quenches were initially introduced to study the spreading of entanglement [44], in the context of the broader question concerning the propagation of information in quantum systems. A fundamental bound to the speed at which information can propagate had been previously derived by Lieb and Robinson [60]; as a consequence, following a quantum quench, correlations are expected to be exponentially suppressed outside a *light cone* in space time. A significant advancement in understanding the spreading of correlations was then the proposal of the *quasi-particle picture* [45]. In this semi-classical picture, entangled pairs of quasi-particles with opposite momenta are created by the quantum quench and propagate across the system without interacting; regions of the systems become correlated when they are reached by two entangled particles. In this context, the authors of Ref. [45] demonstrated that decay constants for different observables are *universal*, providing a ground-breaking example of universality out of equilibrium.

The quantum quench protocol also provides an ideal setting to study issues such as the conditions leading to thermalisation of isolated quantum systems [17] and the circumstances under which this may fail to occur. The definition of thermalisation for isolated quantum systems does not immediately generalise from the classical case. In classical

systems, the notion of thermalisation is closely related to that of *ergodicity*, which can be defined as the equivalence of time and phase-space averages [61]; for every quantity O, one has

$$\langle O \rangle = \lim_{t\to\infty} \frac{1}{t} \int_0^t \mathrm{d}t' O(t'). \tag{1.6}$$

This can be interpreted as the statement that, at late times, the system will have explored all available microstates for equal times. The late time behaviour of a classical system with a thermodynamic number of constituents is then determined by a small set of macroscopic parameters, specifying a statistical ensemble. However, it is clear that under unitary quantum evolution it is not possible for all quantities to relax at late times. A simple example is provided by considering [62]

$$\hat{R} = |a\rangle\langle b| + |b\rangle\langle a|, \tag{1.7}$$

where $|a\rangle$ and $|b\rangle$ are eigenstates of $\hat{H}$. $\hat{R}$ is a Hermitian operator, so that, according to the postulates of quantum mechanics, its expectation value corresponds to an observable. However, it can be easily seen that this evolves according to

$$\langle \hat{R}(t) \rangle \propto \cos[(E_a - E_b)t]. \tag{1.8}$$

Equation (1.8) shows that $\langle \hat{R}(t) \rangle$ oscillates indefinitely and therefore can never thermalise. It is thus impossible to describe the late time behaviour of *all* quantum observables in terms of a statistical ensemble. In order to appropriately define the thermalisation of isolated quantum systems, we need to restrict our attention to *local observables*, defined as observables which can be written as a sum of densities with finite support. Let us partition a system of size N into a subsystem B and its complement $A = \bar{B}$, and only consider local observables $\mathcal{O}_B$ which act trivially outside the subsystem B. A quantum system is said to thermalise if, for all such local observables, the following limit exists:

$$\lim_{t\to\infty} \lim_{N\to\infty} \langle \psi(t) | \hat{\mathcal{O}} | \psi(t) \rangle = \lim_{N\to\infty} \mathrm{Tr}\left(\hat{\rho}_{SS} \hat{\mathcal{O}} \right), \tag{1.9}$$

where the limit defines a steady-state density matrix $\hat{\rho}_{SS}$. For generic (non-integrable) quantum systems, it turns out that $\hat{\rho}_{SS}$ is given by the canonical Gibbs ensemble

$$\rho_{GE}(\beta) = \frac{e^{-\beta\hat{H}}}{\mathrm{Tr}\, e^{-\beta\hat{H}}} \equiv Z e^{-\beta\hat{H}}, \tag{1.10}$$

where the effective inverse temperature $\beta(E_0)$ is fixed by the energy E_0 at $t = 0$. The current understanding of thermalisation in isolated quantum system relies on the notion that this occurs at the level of individual eigenstates. This is encapsulated in the *Eigenstate Thermalisation Hypothesis* (ETH) [63–65], which states that for generic many-body quantum systems expectation values of local observables in individual eigenstates $|\Psi_a\rangle$ with energy E_a above the ground state are the same as those given by the Gibbs distribution Eq. (1.10) with the corresponding $\beta(E_a)$. This can be written as

$$\langle\Psi_a|\hat{\mathcal{O}}|\Psi_a\rangle = \mathrm{Tr}\left(\hat{\rho}_{GE}(\beta(E_a))\hat{\mathcal{O}}\right). \tag{1.11}$$

However, experiments show that not all many-body quantum systems thermalise, as we have seen for the quantum Newton's cradle. It was suggested [6] that the lack of thermalisation in certain systems is related to the presence of additional local[1] conserved quantities which constrain the quantum dynamics, so that memory of the initial conditions is retained at all times and the system cannot be described by an ensemble with a single parameter. For these systems, the late-time behaviour of observables is captured by a statistical ensemble which accounts for the presence of additional local conserved quantities, the Generalised Gibbs Ensemble (GGE) [67, 49, 68]. This is defined as

$$\hat{\rho}_{GGE} = \frac{e^{-\sum_m \hat{I}_m \lambda_m}}{Z_{GGE}}, \tag{1.12}$$

where $\hat{I}_m$ are the local conserved charges satisfying $[\hat{H}, \hat{I}_m] = 0 \;\forall\; m$, $[\hat{I}_m, \hat{I}_n] = 0 \;\forall\; n \neq m$. The Lagrange multipliers λ_m are fixed by the initial conditions, and Z_{GGE} enforces the normalisation $\mathrm{Tr}\,\hat{\rho}_{GGE} = 1$. The presence of additional local conserved quantities is the defining feature of *integrable models*, a class of systems which has received great theoretical attention in recent years, not least because of the availability of analytical solutions. The simplest class of such systems are described by Hamiltonians that can be cast in a diagonal form by appropriate transformations, yielding a formulation in terms of free particles. This class of models includes the transverse-field Ising chain (TFIC), defined by the Hamiltonian

$$\hat{H}_I = -J\sum_i^N \hat{S}_i^z \hat{S}_{i+1}^z - \Gamma \sum_i^N \hat{S}_i^x, \tag{1.13}$$

[1] In some models, one needs to additionally take into account *quasi-local* conserved charges [66].

where $J > 0$ is the strength of ferromagnetic interactions and Γ is an external magnetic field. This Hamiltonian can be diagonalised by a combination of the Jordan-Wigner and Bogoliubov transformations [69], giving the free-fermionic Hamiltonian

$$\hat{H}_I = \sum_k \varepsilon_k \left(\hat{\gamma}_k^\dagger \hat{\gamma}_k - \frac{1}{2} \right), \tag{1.14}$$

where $\hat{\gamma}_k^\dagger$, $\hat{\gamma}_k$ are fermionic creation and annihilation operators, with dispersion given by

$$\varepsilon_k = \frac{1}{2}\sqrt{4\Gamma^2 - 4\Gamma J \cos k + J^2}. \tag{1.15}$$

For quantum quenches in the TFIC, many exact results have been obtained [44, 57, 70, 71] showing that indeed at late times this model is described by the GGE. Integrable systems that cannot be diagonalised in terms of free particles are still part of the broader category of *Yang-Baxter integrable* models. In these systems, multi-particle scattering processes can be factorised in terms of elastic two-particle scatterings. This property is encoded in the Yang-Baxter equation, pictorially represented as the star-triangle relation. This class of systems include the quantum Heisenberg antiferromagnet [72], for which the Bethe ansatz equations were first formulated [73], the Lieb-Liniger model [42, 43] and the one-dimensional Hubbard model [74]. Examples of Yang-Baxter integrable models have been shown to equilibrate to a GGE when all the relevant conserved quantities are included [66, 75]. Integrability is generically very sensitive to the specific details of the Hamiltonian and requires the parameters to be fine-tuned. In certain systems, when integrability is broken by a weak perturbation, expectation values have been shown to initially attain a *pre-thermalization plateau* before eventually decaying to their thermal values at late times [51, 76, 77]. The general conditions leading to the breaking of integrability and the onset of thermalisation are an open topic of research. Another important open question concerns the quantum generalisation of the Kolmogorov-Arnold-Moser (KAM) theorem, which prescribes that the behaviour of classical integrable systems retains a quasi-periodic character for sufficiently weak perturbations [18].

Notably, in recent years, a different mechanism has emerged by which isolated quantum systems may fail to thermalise: many-body localisation (MBL) [78–81]. This phenomenon is the generalisation to interacting systems of the Anderson localisation (AL) of single-particle eigenstates in the presence of disorder [82]. Localisation can survive the presence of sufficiently weak interactions, giving rise to a phenomenology that goes beyond that of AL, e.g. both AL and MBL systems are perfect insulators but in MBL systems the

entanglement grows logarithmically in time while in AL there is no entanglement growth [81]. As the strength of interactions is increased compared to the disorder strength, MBL breaks down. Deep in the MBL phase (strong disorder limit), a theoretical picture has been proposed which captures the key physics. In this picture, the system is described in terms of local[2] integrals of motion (LIOMs). Deep in the MBL phase, the Hamiltonian can be written entirely in terms of the LIOMs and the only dynamics amounts to their dephasing. Due to the presence of LIOMs, MBL systems can indefinitely retain information about their initial conditions and do not thermalise. However, while the behaviour deep into the MBL phase is relatively well understood, a complete understanding of the MBL transition is still missing. This is partly due to the challenge of simulating systems where translation invariance is broken, which is difficult with currently existing techniques and is mostly done for small systems using exact diagonalisation.

As previously anticipated, a very important theoretical question concerns the generalisability of the concept of universality to non-equilibrium settings. Universality is normally associated with low-energy properties, so that naively one would not expect to see it in highly excited systems. However, signatures of universality out of equilibrium have been identified, including ratios of decays constants for different observables [45] or features in the statistics of work [83] and short-time dynamics [84, 85]. These observations motivate the search for other manifestations of universality out of equilibrium as well as a general theoretical framework to understand it. Since in equilibrium universality is often associated with criticality, a promising direction would be identifying non-equilibrium counterparts to equilibrium phase transitions. A recent proposal in this direction [5] is discussed in the next Section.

1.2.2 Dynamical Quantum Phase Transitions

Recent theoretical attention has been given to *dynamical quantum phase transitions* (DQPTs) [5, 86], where physical quantities show non-analytic behaviour as a function of time[3]. Specifically, DQPTs are defined as non-analytic points in the Loschmidt amplitude $A(t)$, which gives the survival amplitude of a given state $|\psi(0)\rangle$ following non-trivial time

[2]The definition of 'locality' for the LIOMs of MBL systems is different from the definition given above for local operators. In the case of LIOMs, locality refers to the fact that the LIOMs τ_i^z are close to the original spins σ_i^z, with contributions from spins σ_j^z at other sites that decay exponentially with the distance $|i-j|$.

[3]A different definition of dynamical phase transitions in quantum systems also exists in the literature, see e.g. Ref. [87–92]. In this definition, the relaxation behaviour of a system following a quantum quench changes sharply as a function of the quench parameters. In this Thesis, we focus on the definition introduced in Ref. [5].

evolution:

$$A(t) \equiv \langle \psi(t) | \psi(0) \rangle. \tag{1.16}$$

Since the Loschmidt amplitude is exponentially suppressed as a function of the system size N, it is convenient to define the Loschmidt rate function $\lambda(t)$ as

$$\lambda(t) \equiv -\frac{1}{N} \log |A(t)|^2, \tag{1.17}$$

which has a finite thermodynamic limit. The quantity $L(t) \equiv |A(t)|^2$ is sometimes termed the Loschmidt echo, although other definitions of this quantity exist in the literature, see e.g. Ref. [93]. The non-analyticities in $A(t)$ are termed DQPTs by analogy with equilibrium phase transitions; this can be understood by noticing that the Loschmidt amplitude $A(t)$ can be written as

$$A(t) \equiv \langle \psi(t) | \psi(0) \rangle = \langle \psi(0) | e^{-\frac{i}{\hbar}\hat{H}t} | \psi(0) \rangle. \tag{1.18}$$

This expression is formally similar to a *boundary partition function* [94], obtained by performing a Wick rotation to imaginary time $t = -i\tau$. In equilibrium phase transitions, the partition function becomes non-analytic as a function of temperature. DQPTs generalise this concept to the real time case, in which the Loschmidt amplitude becomes non-analytic as a function of time. In this sense, DQPTs can be thought of as *phase transitions in time* [95, 86]. DQPTs can be understood more precisely by considering the Lee-Yang analysis of equilibrium phase transitions in the complex plane. Lee and Yang showed that at critical points the zeros of the partition function (Fisher zeros) approach the real axis upon increasing the system size [96]. Analogously, in DQPTs, at particular values of t the zeros of the Loschmidt amplitude approach the time axis. In the thermodynamic limit, these points coalesce into a line and cross the imaginary axis, giving rise to DQPTs [5]. For the transverse field Ising chain, it was shown analytically that for quenches across the quantum critical point the Fisher zeros cross the time axis and DQPTs can be observed at the corresponding times [5]. The occurrence of DQPTs for quenches across quantum critical points has subsequently been observed in a number of other systems, including non-integrable spin chains, such as the quantum Ising chain in a tilted magnetic field and the ANNNI model [97], and higher dimensional systems [98, 99]. However, it is also possible to have DQPTs in quenches that do not cross a quantum critical point and, conversely, quenches across quantum critical points may not be accompanied by DQPTs [100, 101]; thus, a general understanding of the conditions under which DQPTs occur is still missing [86]. For systems with degenerate ground states, in Ref. [95] a relation has

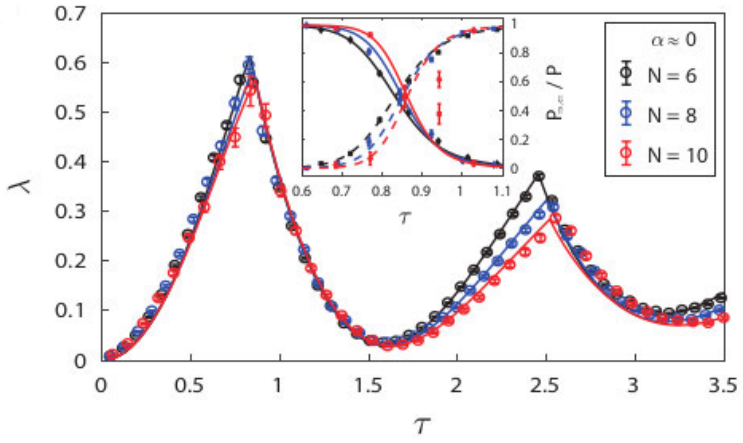

Figure 1.2: Experimental observation of dynamical quantum phase transitions in the long-range quantum Ising chain defined in Eq. (1.22) with $\alpha \approx 0$. The system was initialised in the symmetry-broken ground state $|\Uparrow\rangle$ for $\Gamma = 0$ and quenched to a final value of the transverse field $\Gamma \approx 4.76J$, across the quantum critical point. The dots are experimental data, while the lines are numerical simulations with experimental parameters. The sharp peaks in the rate function $\lambda(t)$ were obtained from small system sizes N by using Eq. (1.21) as a theoretical input. The inset shows that the transition between the normalised ground state probabilities $P_{\Downarrow}$, $P_{\Uparrow}$ becomes sharper for increasing N. Figure published in Ref. [102].

been established between DQPTs in the Loschmidt amplitude and the dynamics of the order parameter. This is based on a generalised Loschmidt echo, defined as the probability to return to the *ground state manifold* following a quantum quench:

$$P(t) = \sum_{\alpha=1}^{n_G} P_\alpha(t), \quad P_\alpha(t) = |\langle \psi_\alpha | \psi(t) \rangle|^2, \tag{1.19}$$

where $|\psi_\alpha\rangle$ are the n_G degenerate ground states of the system. For systems with degenerate ground states, it is generically observed (see e.g. Ref. [57]) that for quenches from a symmetry-broken ground state the relaxation behaviour of the system shows a sharp qualitative change, with the decay of the order parameter shifting from monotonic to oscillatory, as a function of the quench parameter [95]. It can be shown that the onset of oscillatory behaviour and the appearance of DQPTs both occur at the same value of the quench parameter, and DQPTs themselves coincide with the zeros in the oscillations of the order parameter. This is due to the fact that the generalised Loschmidt echo appears in the spectral decomposition of the order parameter, affecting its dynamics [95]. For systems

with degenerate ground states, we can define a set of quantities λ_α as

$$P_\alpha \equiv e^{-N\lambda_\alpha}. \tag{1.20}$$

From Eqs. (1.17) and (1.19), because of the exponential suppression of $P(t)$ with the system size, it can be seen that at any given time the Loschmidt rate function is dominated by the smallest of the λ_α given in Eq. (1.20):

$$\lambda(t) = \min_\alpha \lambda_\alpha(t). \tag{1.21}$$

DQPTs are then associated with the times when a subleading term λ_α becomes dominant, giving rise to a sudden, non-analytic change in $\lambda(t)$. Thanks to this theoretical understanding, it has been possible to observe DQPTs experimentally using trapped ions [102] for quantum quenches in the long-range Ising Hamiltonian

$$\hat{H} = -\sum_{ij} J_{ij}\hat{S}_i^z\hat{S}^z - \Gamma\sum_{i=1}^{N}\hat{S}_i^x, \tag{1.22}$$

where

$$J_{ij} \approx \frac{1}{|i-j|^\alpha} \tag{1.23}$$

and $0 < \alpha < 3$ is a tunable parameter. For $\Gamma = 0$, the Hamiltonian (1.22) has two degenerate ground states $|\Downarrow\rangle$, $|\Uparrow\rangle$ corresponding to all spins pointing up or down respectively. In this case, the generalised Loschmidt echo is given by Eq. (1.19) with $n_G = 2$ and $|\psi_\alpha\rangle \in \{|\Uparrow\rangle, |\Downarrow\rangle\}$. In the experiment [102], the system is prepared in the state $|\psi_0\rangle = |\Uparrow\rangle$ and quenched across the quantum critical point. Assuming the form given in Eq. (1.21), it is possible to infer the occurrence of DQPTs in the thermodynamic limit by studying the individual contributions $\lambda_\Uparrow$, $\lambda_\Downarrow$, defined as in Eq. (1.20), for experimentally accessible system sizes, as shown in Fig. 1.2. Connections between DQPTs and the concepts of scaling and universality have been explicitly made for a two-dimensional (2D) system [99], where a renormalisation group approach was used to show that DQPTs are associated with unstable fixed points of equilibrium models. In spite of these developments, however, a complete theoretical understanding of DPQTs is still missing.

In this Section, we have briefly reviewed the vast field of non-equilibrium quantum dynamics, focussing in particular on quantum quenches and the issue of thermalisation. We have also devoted special attention to dynamical quantum phase transitions, which will play an important role in Chapter 4. In the next Section, we will examine the theoretical

techniques that are currently available to study many-body quantum systems far from equilibrium.

1.3 Theoretical Tools for Quantum Dynamics

Formally, for a time-independent Hamiltonian, the Schröedinger equation is solved by

$$|\psi(t)\rangle = e^{-it\hat{H}}|\psi(0)\rangle. \tag{1.24}$$

However, obtaining the time-evolved state from direct evaluation of Eq. (1.24) requires the diagonalisation of a very large matrix; for instance, in a spin-$1/2$ system with N sites, the number of allowed states of the system is 2^N so that the Hamiltonian is a $2^N \times 2^N$ matrix. With modern computational resources, the exact diagonalisation (ED) of Eq. (1.24) is thus limited to systems of the order of $20-25$ spins.

In the case of integrable systems, it is however sometimes possible to obtain analytical solutions. In free fermionic systems, for instance, steady-state expectation values can be computed by representing correlation functions in the form of determinants and then extracting their asymptotic behaviour [70]. Recently, a significant advancement in this direction has been the development of the *quench action approach* [103, 104], which allows one to obtain the full non-equilibrium dynamics of integrable systems and to characterise their late time properties by considering a single, aptly chosen representative state. For critical systems, analytical progress can be made by exploiting techniques from the realm of conformal field theory (CFT) [105], including the AdS/CFT correspondence and hydrodynamic approaches [106–108]. For integrable systems away from criticality, this was generalised by the introduction of the framework of generalised hydrodynamics [109, 110], which allows one to obtain a full characterisation of the current-carrying non-equilibrium steady states arising from joining two chains with different equilibrium properties.

However, away from integrable systems and critical points, no analytical solutions are typically available and one has to resort to numerical methods. In one dimension, the most powerful numerical tool is provided by tensor network based techniques such as time-dependent density matrix renormalisation group (tDMRG) [111–115], generalising the DMRG algorithm for ground state properties [116], or other algorithms representing the system in terms of matrix product states (MPS) [117–121]. However, tensor networks suffer from intrinsic limitations. Although they can capture the short-time quantum

dynamics of systems initialised in a lowly-entangled state even in the thermodynamic limit, information-theoretic arguments [21] show that their regime of applicability breaks down at late times, when entanglement becomes sizeable. Thus, tensor networks may fail to reach the required time scales to study equilibration of isolated quantum systems. Furthermore, the application of tensor networks, even in equilibrium, is effectively restricted to one-dimensional systems [21], although progress has been made in overcoming this limitation (see Ref. [122] for a review). An extension towards application in higher dimensions has been achieved by combining tDMRG and the truncated spectrum approximation (TSA) for integrable field theories, to describe the real time evolution of a 2D system of coupled continuum chains [123]. Recent developments in the direction of investigating higher dimensional systems, in and out of equilibrium, also include neural network approaches, based on variationally optimising an efficient representation of the wavefunction [124, 125]. These techniques are however still limited to relatively small system sizes.

A promising developing field is that of *phase space methods* [126], based on mappings of the quantum dynamics to classical dynamics in phase space. An important example is the truncated Wigner approximation (TWA) [127–129], a semiclassical approach consisting in expressing observables in terms of a phase-space quasiprobability $\mathcal{W}$ known as the Wigner function (where the 'quasi' indicates that $\mathcal{W}$ is not necessarily positive), and retaining only the leading order in $\hbar$. In this approach, quantum expectation values are approximated as averages over classical deterministic trajectories with random initial conditions. An interesting development for 1D systems is the application of the TWA to clusters (CTWA) [130]. Going beyond approximations, it is possible to perform exact mappings of quantum to classical dynamics. These include the Pos-P representation [131–133], based on a phase space description of the quantum density matrix. Pos-P methods are capable of accessing extremely large system sizes even in 2D (100×100), but appear to be intrinsically limited to short simulation times [132, 133].

1.4 Hubbard-Stratonovich Decoupling of Interactions and Stochastic Fields

A different strand of exact quantum-to-classical maps is based on representing quantum interactions in terms of classical stochastic fields, so as to reduce the many-body problem to a set of stochastic one-body problems [2–4]. Here we summarise the key landmarks

of this approach, which provide the immediate background to the developments of this Thesis.

The decoupling approach has been introduced in Ref. [2] to compute the partition function of a fully frustrated antiferromagnetic quantum spin cluster, described by the Hamiltonian

$$\hat{H} = \frac{J}{2}\left(\sum_{i=1}^{q}\hat{S}_i\right)^2 . \tag{1.25}$$

In Ref. [2], the exchange interactions are decoupled by means of a Hubbard-Stratonovich (HS) transformation [134, 135], following a similar philosophy as in the numerical *auxiliary field Monte Carlo* methods [136–139]. This introduces a functional integral over an auxiliary field, which plays the role of a *stochastic magnetic field* in the resulting single-spin Euclidean time evolution operator. The stochastic differential equations (SDEs) which describe the single-spin dyamics are solved by converting to the Fokker-Planck equation (Appendix A), providing an exact integral representation of the sought partition function. In Ref. [3], the Hubbard-Stratonovich approach is applied to the thermodynamics of quantum lattice systems. Using a generalised HS transformation in combination with the coherent state path integral construction for spins, a formula of broad validity for the partition function is given in terms of non-interacting spins coupled to HS fields. This approach is taken further in Ref. [4], where the Hubbard-Stratonovich transformation is performed in real time to decouple the time evolution operator. This is used to study a cluster of spins coupled to a photonic waveguide, which we revisit in Appendix E. Ref. [4] also suggests the possibility of using this method to study lattice systems, providing preliminary results on the imaginary time evolution of the stochastic variables which describe the transverse field Ising chain. In this Thesis, we investigate the stochastic approach introduced in Refs. [2–4], applying it to the real and imaginary time evolution of lattice quantum spin systems, focussing in particular on the quantum Ising model. The structure of the Thesis is outlined in the next Section.

1.5 Structure of the Thesis

This Thesis begins with a presentation of the stochastic approach in Chapter 2, where we discuss the exact quantum-to-classical map [2–4], involving a set of stochastic *disentangling variables*, and provide explicit formulae of general validity for lattice spin systems. In Chapter 3, we discuss the stochastic representation of the quantum Ising model, investigating the SDEs which encode the quantum dynamics [2, 4] with a number of exact

approaches as well as approximations. To compute quantum observables, in Chapter 4 we numerically solve the real time Ising SDEs, demonstrating the broad applicability of the method and discussing its features and limitations. In this context, we investigate the relation between the disentangling variables and dynamical quantum phase transitions. In Chapter 5, we show how the stochastic approach can be applied in imaginary time to compute ground state expectation values. Considering this problem, we introduce measure transformations capable of improving the numerical performance of the method. We conclude our investigation of the stochastic method in Chapter 6 by outlining current work in progress on a saddle point technique, capable of providing analytical approximate results for ground state properties as well as further improving the sampling efficiency of the stochastic method while retaining its exactness. We demonstrate the potential of this technique to investigate large system sizes. In Chapter 7, we summarise the results we obtained, presenting our overall conclusions and indicating directions for future investigations and further developments.

Chapter 2

Stochastic Representation of Quantum Spin Systems

In this Chapter, we outline a formalism [2–4] that makes it possible to calculate expectation values of quantum spin systems as averages of classical stochastic processes. This approach is based on the combination of two transformations: a Hubbard-Stratonovich (HS) transformation [134, 135], which decouples the interactions between spins, and a subsequent reparameterisation of the time evolution operator. First, the HS transformation encodes the interactions in a set of stochastic auxiliary fields, so that interacting spins are represented as non-interacting spins in stochastic magnetic fields [2, 4]. For a given realisation of the stochastic fields, the time evolution of each spin traces a trajectory in the corresponding single-particle space; this trajectory can be parameterised by means of a set of classical coordinates, the *disentangling variables* [2, 4], which satisfy stochastic differential equations (SDEs). Using this parameterisation, quantum expectation values can be expressed as averages of classical functions of the disentangling variables. We begin this Chapter by reviewing this sequence of transformations, deriving the stochastic formulation of the time evolution operator for quantum spin systems [2, 4]. We then discuss how observables can be represented in the stochastic language, providing formulae of general validity for spin-$1/2$ systems. The stochastic formalism discussed in this Chapter provides the starting point for the rest of the Thesis, where we will further investigate this approach and use it to compute observables for lattice quantum spin systems.

2.1 Time Evolution of Quantum Spin Systems

Consider the quadratic quantum spin Hamiltonian

$$\hat{H} = -\sum_{aij} \mathcal{J}^a_{ij} \hat{S}^a_i \hat{S}^a_j - \sum_{aj} h^a_j \hat{S}^a_j, \tag{2.1}$$

where the indices i, j run over the N sites of a generic lattice and $a \in \{x, y, z\}$ runs over the generators of the Lie algebra of SU(2). The spin operators satisfy the commutation relations $[\hat{S}^a_j, \hat{S}^b_{j'}] = i\delta_{jj'}\varepsilon^{abc}\hat{S}^c_j$. The couplings $\mathcal{J}^a_{ij}$ and fields h^a_i can in general be time-dependent and may take different values at different sites. A system defined by this Hamiltonian evolves according to the the time evolution operator, given by a time-ordered exponential

$$\hat{U}(t_f, t_0) = T\exp\left(-i\int_{t_0}^{t_f} \mathrm{d}t \hat{H}(t)\right), \tag{2.2}$$

where T denotes time ordering and we set $\hbar = 1$. Performing a Wick rotation $\tau = it$, one can also define the Euclidean time evolution operator:

$$\hat{U}(\tau_f, \tau_0) = T\exp\left(-\int_{\tau_0}^{\tau_f} \mathrm{d}\tau \hat{H}(\tau)\right). \tag{2.3}$$

Without loss of generality, we will consider $t_0 = \tau_0 = 0$.

In this Chapter, we will illustrate how the time evolution operator can be re-expressed in a stochastic formulation. For simplicity, we will show this by considering the Euclidean time version given by Eq. (2.3), while the real time equations will be obtained by Wick-rotating the final results. However, the same equations can also be derived by directly working in real time, as shown in Appendix B.1.

2.2 Hubbard-Stratonovich Transformation

The quadratic interaction term can be decoupled by means of a Hubbard-Stratonovich (HS) transformation [134, 135, 2–4]. In order to perform the transformation, the time-ordered exponential appearing in the definition of $\hat{U}$ must first be discretised by performing the

Suzuki-Trotter time slicing:

$$\hat{U}(\tau) = T\exp\Big[-\int_0^\tau \mathrm{d}\tau' \hat{H}(\tau')\Big] \tag{2.4}$$

$$= \lim_{n\to\infty}\prod_{m=1}^{n} T\exp\Big(\Delta\tau\sum_{aij}\mathcal{J}_{ij}^a(m\,\Delta\tau)\hat{S}_i^a\hat{S}_j^a + \Delta\tau\sum_{aj}h_j^a(m\,\Delta\tau)\hat{S}_j^a\Big), \tag{2.5}$$

where $\Delta\tau \equiv \tau/n$. At each time-slice, one can then apply the Hubbard-Stratonovich transformation given by

$$e^{\Delta\tau\sum_{aij}\mathcal{J}_{ij}^a\hat{S}_i^a\hat{S}_j^a} = \mathcal{N}\int\prod_{ai}(\mathrm{d}\varphi_i^a)\, e^{-\frac{1}{4}\Delta\tau\sum_{aij}(\mathcal{J}^{-1})_{ij}^a\varphi_i^a\varphi_j^a + \Delta\tau\sum_{aj}\varphi_j^a\hat{S}_j^a}, \tag{2.6}$$

with a normalisation constant $\mathcal{N}$ (Appendix B.1). For each slice of Eq. (2.5), the argument of the exponential becomes

$$A = \Delta\tau\Big[\sum_{aj}(h_j^a+\varphi_j^a)\hat{S}_j^a - \sum_{aij}\frac{1}{4}(\mathcal{J}^{-1})_{ij}^a\varphi_i^a\varphi_j^a\Big]. \tag{2.7}$$

Notably, while the HS transformation is typically performed after all operators have been replaced by classical fields, e.g. by constructing a path integral over coherent states [140], here the HS transformation is applied at the operator level [2, 4]. Taking the limit $n\to\infty$, we finally get [2, 4]

$$\hat{U}(\tau) = \int\mathcal{D}\varphi \mathrm{e}^{-\sum_{aij}\int\frac{1}{4}(\mathcal{J}^{-1})_{ij}^a\varphi_i^a\varphi_j^a\mathrm{d}\tau'}\mathcal{T}\mathrm{e}^{-\int\sum_{aj}\Phi_j^a(\tau')\hat{S}_j^a\mathrm{d}\tau'}, \tag{2.8}$$

where we have defined the coefficients Φ_i^a multiplying each spin operator as

$$\Phi_j^a(\tau) = \varphi_j^a(\tau) + h_j^a(\tau), \tag{2.9}$$

and we have introduced an integration measure

$$\mathcal{D}\varphi \equiv \mathcal{N}_\varphi\prod_{aj}\mathrm{d}\varphi_j^a, \tag{2.10}$$

with an overall normalisation $\mathcal{N}_\varphi$. We can define the *noise action* $S[\varphi]$ as

$$S[\varphi] \equiv \sum_{aij}\int\frac{1}{4}(\mathcal{J}^{-1})_{ij}^a\varphi_i^a(\tau')\varphi_j^a(\tau')\mathrm{d}\tau'. \tag{2.11}$$

By means of an appropriate change of variables $\varphi_i^a = \sum_j O_{ij}^a \phi_j^a$ (Appendix B.2), the noise action (2.11) can be cast in the diagonal and symmetric form:

$$S[\phi] \equiv \int \frac{1}{2} \sum_{ai} \phi_i^a(\tau') \phi_i^a(\tau') \mathrm{d}\tau'. \tag{2.12}$$

The Gaussian form of this measure suggests that the functional integral Eq. (2.8) affords a probabilistic interpretation as a path integral over realizations of the stochastic processes $\phi_i^a(\tau)$ [2, 4]. In particular, the fields ϕ_i^a satisfy $\langle \phi_i^a(\tau) \rangle = 0$, $\langle \phi_i^a(\tau) \phi_j^b(\tau') \rangle = \delta(\tau - \tau') \delta_{ij} \delta_{ab}$. The time evolution operator can thus be written as

$$\hat{U} = \left\langle T \mathrm{e}^{\int \sum_{aj} \Phi_j^a(\tau') \hat{S}_j^a(\tau') \mathrm{d}\tau'} \right\rangle_\phi \equiv \langle \hat{U}^s \rangle_\phi \tag{2.13}$$

$$\equiv \langle \otimes_i \hat{U}_i^s \rangle_\phi, \tag{2.14}$$

where $\langle \dots \rangle_\phi$ denotes an average with respect to the HS fields, and we defined the *stochastic time evolution operator* $\hat{U}^s$ and its on-site components $\hat{U}_i^s$. Using the HS transformation, the problem is thus reduced to the time evolution of N non-interacting spins coupled to a set of stochastic magnetic fields $\phi_i^a(\tau)$. Each spin evolves according to the effective stochastic Hamiltonian

$$\hat{H}_i^s(\tau) = -\sum_a \hat{S}_i^a \left[h_i^a(\tau) + \sum_j O_{ij}^a \phi_j^a(\tau) \right]. \tag{2.15}$$

The matrix O_{ij}^a is in general complex, implying that $\hat{H}_i^s$ can be non-Hermitian. The correlations between spins arising from the interactions are encoded in the fact that each spin is coupled to all the fields $\phi_j^a(\tau)$, as can be seen from Eq. (2.15).

2.3 Disentanglement Transformation

The action of the time evolution operator in Eq. (2.13) on a given state cannot be computed directly because of the time-ordering operation. However, the argument of the time-ordered exponential is now linear in the spin operators thanks to the HS transformation. Because of this property, the issue of time ordering can be circumvented by application of the Wei-Norman-Kolokolov disentanglement transformation [141, 142, 2–4], which allows one to express the time-ordered exponential as a product of ordinary exponentials. The key idea is that the on-site stochastic time evolution operator $\hat{U}_i^s$ can be written as a product

of exponentials whose arguments are linear combinations of group generators, as can be explicitly seen by considering its Trotter-sliced form. However, unlike the original Hamiltonian, $\hat{H}_i^s$ is not Hermitian and the relevant group is therefore $\mathrm{SL}(2,\mathbb{C})$ [3]. By definition, the exponential of a linear combination of Lie group generators is a member of the corresponding Lie group. Therefore, each term in the Suzuki-Trotter slicing of $\hat{U}_i^s(\tau)$ is a member of $\mathrm{SL}(2,\mathbb{C})$. By group closure, $\hat{U}_i^s(\tau)$ is also a member of the group and it represents a specific trajectory on the complexified single-spin Bloch sphere of the particle at site i. As a group element, a generic trajectory can be parameterised in a number of ways. The focus of this Thesis will be the two-dimensional representation, corresponding to spin-$1/2$. Following Ref. [4], we choose the Gauss parameterisation of $\mathrm{SL}(2,\mathbb{C})$, and impose that a generic group element thus parameterised be equal to the on-site stochastic time evolution operator at a given time τ:

$$\hat{U}_i^s(\tau) \equiv T\mathrm{e}^{\sum_a \int_0^\tau \Phi_i^a(\tau')\hat{S}_i^a(\tau')\mathrm{d}\tau'} \equiv e^{\xi_i^+(\tau)\hat{S}_i^+} e^{\xi_i^z(\tau)\hat{S}_i^z} e^{\xi_i^-(\tau)\hat{S}_i^-}. \tag{2.16}$$

This equation defines a set of *disentangling variables* $\xi_i^a(\tau)$ [4], where the indices $a \in \{+,-,z\}$. To find the equations of motion satisfied by these fields, we differentiate Eq. (2.16) and right-multiply by $(\hat{U}_i^s)^{-1}$ to get the operator equation

$$(\partial_\tau \hat{U}_i^s)(\hat{U}_i^s)^{-1} = \sum_a \Phi_i^a \hat{S}_i^a = \sum_a \left(\partial_\tau \xi_i^a \frac{\partial \hat{U}_i^s}{\partial \xi_i^a}\right)(\hat{U}_i^s)^{-1}. \tag{2.17}$$

By repeated application of Hadamard's lemma and matching the coefficients of each spin operator (Appendix B.3), one can obtain the equations of motion satisfied by the coordinates ξ_i^a [4]:

$$\dot{\xi}_i^+(\tau) = \Phi_i^+ + \Phi_i^z \xi_i^+ - \Phi_i^- {\xi_i^+}^2, \tag{2.18a}$$

$$\dot{\xi}_i^z(\tau) = \Phi_i^z - 2\Phi_i^- \xi_i^+, \tag{2.18b}$$

$$\dot{\xi}_i^-(\tau) = \Phi_i^- \exp \xi_i^z. \tag{2.18c}$$

The identity $\hat{U}(0) = 1$ implies that the disentangling fields satisfy the initial conditions $\xi_i^a(0) = 0 \;\forall\; i,a$. Alternative disentanglement transformations, based on different parameterizations, are also possible and have been used in previous works [2]. The real-time

version of Eq. (2.18) is obtained by performing the Wick rotation $\tau = it$:

$$-i\dot{\xi}_i^+(t) = \Phi_i^+ + \Phi_i^z \xi_i^+ - \Phi_i^- {\xi_i^+}^2, \tag{2.19a}$$

$$-i\dot{\xi}_i^z(t) = \Phi_i^z - 2\Phi_i^- \xi_i^+, \tag{2.19b}$$

$$-i\dot{\xi}_i^-(t) = \Phi_i^- \exp \xi_i^z. \tag{2.19c}$$

When Wick rotating, the noise action picks up a factor i, yielding

$$S[\phi] \equiv \int \frac{i}{2} \sum_{ai} \phi_i^a(t')\phi_i^a(t')\mathrm{d}t'. \tag{2.20}$$

This can be straightforwardly implemented in numerical simulations by generating complex noises (Appendix A.6). Equivalently, the imaginary factor can be removed by rescaling the HS fields as $\phi_i^a \to \phi_i^a/\sqrt{i}$. For notational convenience, i.e. having the right-hand side of Eqs. (2.18-2.19) in the same form for both imaginary and real time evolution, we will choose the first option and retain an imaginary noise action when working in real time.

By parameterising the stochastic time evolution operator, we have thus derived a set of differential equations [2–4] which play the role of equations of motion for the disentangling variables ξ_i^a. These equations depend on the HS fields ϕ_i^a via the overall fields Φ_i^a. In light of the stochastic nature of the ϕ_i^a, Eqs. (2.18-2.19) can be interpreted as stochastic differential equations (SDEs) for the coordinates ξ_i^a [2, 4, 143]. We will now discuss how these SDEs can be handled with a view towards the computation of quantum expectation values using the stochastic approach; a more detailed review of SDEs and stochastic processes can be found in Appendix A.

2.4 Ito and Stratonovich Conventions

In order to consistently define a stochastic differential equation, it is necessary to specify a particular discretisation convention. These are distinguished by the way in which the values of a given function f at the discrete times $\bar{\tau}_j$ are assigned from its value at the times $\tau_j \equiv j\Delta\tau$ with $j = 0, \ldots, n$. Different discretisation schemes are parameterised by a constant α as

$$f(\bar{\tau}_j) = \alpha f(\tau_j) + (1-\alpha) f(\tau_{j-1}), \quad 0 \leq \alpha \leq 1. \tag{2.21}$$

The discretisation of time is required in order to get a consistent definition of the stochastic process; this is because it can be shown that the integral of each Gaussian noise ϕ is a

Wiener process [143]

$$\int_0^\tau \phi(\tau')\mathrm{d}\tau' = W(\tau), \tag{2.22}$$

which is non-differentiable. Therefore, while the corresponding stochastic integral equations or discretised SDEs are well-defined, the continuum limit of SDEs requires $\phi(t)$ to be interpreted as a generalised function. Both stochastic integral equations and discretised SDEs are convention-dependent: the choice $\alpha = 0$ gives the Ito convention $f(\bar{\tau}_j) = f(\tau_i)$, while $\alpha = 1/2$ gives the Stratonovich convention, corresponding to evaluating the function at the mid-point of each time interval by averaging its value at the initial and final times. SDEs in the Stratonovich convention satisfy the rules of ordinary calculus. However, when working with Ito SDEs one needs to use specific rules, known as *Ito calculus* [144, 143].

If we interpret the disentangling equations (2.18) as SDEs, they are to be understood as initially expressed in the Stratonovich convention, since this is the form which is naturally obtained from a well-defined continuous process (noise with finite correlation time, in the limit of the correlation time going to zero), and thus naturally arise in physical applications. However, equations in the Ito convention are often mathematically and computationally simpler to handle and it is therefore convenient to translate our equations into the latter form. In the Stratonovich form, the evolution equation of the stochastic variables ξ_i^a, collectively represented as a vector ξ, can be written as

$$\frac{\mathrm{d}\xi_S}{\mathrm{d}t} = a_S(\,\xi_S, t) + B_S(\xi_S, t)\phi \tag{2.23}$$

in terms of the fields $\phi \equiv \{\phi_i^a\}$, a drift vector a_S and a matrix of diffusion coefficients B_S. The corresponding equation in the Ito convention is given by

$$\frac{\mathrm{d}\xi}{\mathrm{d}t} = a(\xi, t) + B(\xi, t)\phi, \tag{2.24}$$

with

$$a = a_S + \frac{1}{2}(B^T \nabla_\xi) B^T, \tag{2.25a}$$

$$B = B_S. \tag{2.25b}$$

For the SDEs in Eqs. (2.18-2.19), describing a quantum spin system, we find that the extra shift required to convert from the Stratonovich to the Ito SDEs is proportional to $\sum_j O_{ij}^a O_{ij}^a$ in terms of the matrices O_{ij}^a that diagonalise the noise action. For many lattice spin models, the diagonal elements of the interaction matrix $\mathcal{J}_{ij}^a$ are zero as they correspond

to couplings such as $\hat{S}_i^z \hat{S}_i^z$. This implies (Appendix B.2) that the matrix O_{ij}^a multiplying the noises satisfies $\sum_j O_{ij}^a O_{ij}^a = 0$. For such models the Ito and Stratonovich SDEs have the same form[1].

2.5 Stochastic Representation of States and Observables

Having derived the disentanglement transformation, we now discuss how physical quantities can be expressed in the stochastic formalism. We consider real time evolution, but the formulae we will provide are equally valid in imaginary time. The combined action of the HS transformation and the disentangling transformation puts the time evolution operator in the form [4]:

$$\hat{U}(t) = \left\langle \otimes_i e^{\xi_i^+(t)\hat{S}_i^+} e^{\xi_i^z(t)\hat{S}_i^z} e^{\xi_i^-(t)\hat{S}_i^-} \right\rangle_\phi . \tag{2.26}$$

By writing a generic time-dependent observable $\hat{\mathcal{O}}$ in terms of time evolution operators $\hat{U}$ and expressing each $\hat{U}$ in the terms of its stochastic counterpart $\hat{U} = \langle \hat{U}^s \rangle_\phi$, one can formulate any quantum expectation value as a classical average. As an example, consider an observable depending on a single time t:

$$F(t) = \langle \hat{\mathcal{O}}(t) \rangle = \langle \psi_0 | \hat{U}^\dagger(t) \hat{\mathcal{O}} \hat{U}(t) | \psi_0 \rangle. \tag{2.27}$$

Because of the two time evolution operators, one needs to perform two independent Hubbard-Stratonovich and disentanglement transformations. This involves introducing two sets of HS fields $\phi \equiv \{\phi_i^a\}, \tilde{\phi} \equiv \{\tilde{\phi}_i^a\}$ and the corresponding disentangling variables $\xi \equiv \{\xi_i^a[\phi]\}, \tilde{\xi} \equiv \{\tilde{\xi}_i^a[\tilde{\phi}]\}$. The spin operators $\hat{S}_i^a$ in $\hat{U}^s$, $(\hat{U}^s)^\dagger$ and $\hat{\mathcal{O}}$ act on the state $|\psi_0\rangle$ in a simple way and are thus replaced by c-numbers. We are thus left with

$$F(t) = \langle f(\xi, \tilde{\xi}, t) \rangle_{\phi, \tilde{\phi}}, \tag{2.28}$$

where

$$f(\xi, \tilde{\xi}, t) \equiv \langle \psi_0 | \hat{U}_s[\tilde{\phi}] \hat{\mathcal{O}} \hat{U}_s[\phi] | \psi_0 \rangle \tag{2.29}$$

is a particular classical function depending on the specific choice of observable and state. The function $f(\xi, \tilde{\xi}, t)$ depends on the HS fields $\phi, \tilde{\phi}$ via the disentangling variables $\xi, \tilde{\xi}$. Thus, we can compute a quantum expectation value (the matrix element in Eq. (2.27)) by evaluating the classical expectation value of $f(\xi, \tilde{\xi}, t)$ with respect to the HS fields.

[1] In Appendix E we consider a counterexample in the effective description of a matter-light model.

The time dependence of the function $f(\xi,\tilde{\xi},t)$ can be found by applying the rules of Ito calculus. If the disentangling variables ξ evolve according to Eq. (2.24), Ito calculus prescribes that the equation of motion of a function $f(\xi,\tilde{\xi},t)$ is given by:

$$\dot{f} = \sum_{ai} \frac{\partial f}{\partial \xi_i^a} \left(a_i^a + \sum_{jb} B_{ij}^{ab} \phi_j^b \right) + \frac{1}{2} \sum_{abij} \frac{\partial^2 f}{\partial \xi_i^a \partial \xi_j^b} \sum_{ck} B_{ik}^{ac} B_{jk}^{bc}, \tag{2.30}$$

where i, j run over all lattice sites and, for notational convenience, we define the indices a to run over all sets of disentangling variables, i.e. $\{\xi_i^a\} = \{\xi_i^b,\ \tilde{\xi}_i^b\}$ with $b \in \{+,-,z\}$. It is possible to analytically average the SDE (2.30) with respect to the HS fields in order to obtain an ordinary differential equation (ODE) for $\langle f \rangle$:

$$\dot{F} \equiv \langle \dot{f} \rangle_{\phi,\tilde{\phi}} = \sum_{ai} \left\langle \frac{\partial f}{\partial \xi_i^a} a_i^a \right\rangle_{\phi,\tilde{\phi}} + \frac{1}{2} \sum_{abij} \left\langle \frac{\partial^2 f}{\partial \xi_i^a \partial \xi_j^b} \sum_{ck} B_{ik}^{ac} B_{jk}^{bc} \right\rangle_{\phi,\tilde{\phi}}. \tag{2.31}$$

Equation (2.31) features the expectation values of a set of stochastic functions, given by

$$\frac{\partial f}{\partial \xi_i^a} a_i^a,$$

$$\frac{\partial^2 f}{\partial \xi_i^a \partial \xi_j^b} \sum_{ck} B_{ik}^{ac} B_{jk}^{bc},$$

for all i, j, a, b. Applying the Ito chain rule (2.30) to each of these additional functions and analytically averaging the SDEs thus obtained, it is possible to derive a system of ODEs for a particular observable. However, as shown in Appendix B.4, the stochastic functions that arise when computing observables via this procedure are in one-to-one correspondence with matrix elements between different states. Solving such a system of equations is thus equivalent to diagonalising the Hamiltonian[2]. In order to avoid the diagonalisation of matrices whose size grows exponentially with the system size, averages corresponding to observables of interest can computed by numerically simulating the trajectories ξ. The number of trajectories grows linearly with the system size and, unlike some of the more traditional numerical techniques, e.g. exact diagonalisation, the simulation of the SDEs can be straightforwardly parallelised.

[2]This observation clarifies the relation between the SDE formalism and the standard matrix formulation of quantum mechanics; we use this correspondence in Appendix E to directly compute physical observables for a matter-light system, previously solved from the point of view of the stochastic approach in Ref. [4].

By using the stochastic representation of the time evolution operator, we can explicitly write down the stochastic expressions for the operators and observables of the theory. The main focus of this project is spin-$\frac{1}{2}$ systems; in this case, the on-site stochastic time evolution operator $\hat{U}_i^s(t)$ defined in Eq. (2.14) can be explicitly written as a 2×2 matrix:

$$\hat{U}_i^s = \begin{pmatrix} e^{\xi_i^z/2} + e^{-\xi_i^z/2}\xi_i^+\xi_i^- & e^{-\xi_i^z/2}\xi_i^+ \\ e^{-\xi_i^z/2}\xi_i^- & e^{-\xi_i^z/2} \end{pmatrix}. \tag{2.32}$$

We can explicitly see that this matrix has unit determinant but is not necessarily unitary: for instance, anticipating a result of Chapter 3, for the Ising model with $\Gamma = 0$ (the classical limit) the variables $\xi_i^\pm$ vanish and one has

$$\hat{U}_i^s|_{\Gamma=0} = \begin{pmatrix} e^{\xi_i^z/2} & 0 \\ 0 & e^{-\xi_i^z/2} \end{pmatrix}, \quad \hat{U}_i^s|_{\Gamma=0}\hat{U}_i^s|_{\Gamma=0}^\dagger = \begin{pmatrix} e^{\frac{\xi_i^z+(\xi_i^z)^*}{2}} & 0 \\ 0 & e^{-\frac{\xi_i^z+(\xi_i^z)^*}{2}} \end{pmatrix}. \tag{2.33}$$

In this case, $\xi_i^z(t) = \sqrt{i}\sum_j \int_0^t \mathrm{d}t' O_{ij}\phi_j(t')$ where $\phi_j(\tau)$ are real-valued Gaussian white noises. However, O_{ij} is in general complex, so that $\hat{U}_i^s$ is non-unitary. This is ultimately due to fact that in general the stochastic effective Hamiltonian (2.15) is non-Hermitian. Acting on the general initial state of a given site $|\psi_0\rangle_i = \alpha_i|\uparrow\rangle_i + \beta_i|\downarrow\rangle_i$ with the on-site stochastic time evolution operator, we get

$$|\psi(t)\rangle_i = \left\langle \begin{pmatrix} \alpha_i e^{\xi_i^z/2} + \alpha_i e^{-\xi_i^z/2}\xi_i^+\xi_i^- + \beta_i e^{-\xi_i^z/2}\xi_i^+ \\ \alpha_i e^{-\xi_i^z/2}\xi_i^- + \beta_i e^{-\xi_i^z/2} \end{pmatrix} \right\rangle_\phi \tag{2.34}$$

$$= \left\langle |\psi^s(t)\rangle_i \right\rangle_\phi, \tag{2.35}$$

where we have defined a stochastic time-evolved state $|\psi^s(t)\rangle_i$. Using this result, we can construct the full time-evolved state for a generic initial product state:

$$|\psi(t)\rangle = \left\langle \otimes_i |\psi^s(t)\rangle_i \right\rangle_\phi. \tag{2.36}$$

The Loschmidt amplitude $A(t)$, corresponding to the overlap between the time-evolved state and the initial state, is then given by:

$$A(t) = \left\langle \prod_i \left(|\alpha_i|^2 e^{\xi_i^z/2} + |\alpha_i|^2 e^{-\xi_i^z/2}\xi_i^+\xi_i^- + \alpha_i^*\beta_i e^{-\xi_i^z/2}\xi_i^+ + \alpha_i\beta_i^* e^{-\xi_i^z/2}\xi_i^- + |\beta_i|^2 e^{-\xi_i^z/2} \right) \right\rangle_\phi. \tag{2.37}$$

In particular, the Loschmidt amplitude for an initial state $|\psi_0\rangle = \otimes_i |\downarrow\rangle_i \equiv |\Downarrow\rangle$ with all spins pointing down is obtained by setting $\alpha_i = 0$, $\beta_i = 1$ in Eq. (2.37):

$$A(t) = \left\langle \prod_i \exp\left(-\frac{\xi_i^z(t)}{2}\right) \right\rangle_\phi . \tag{2.38}$$

Similarly, we can obtain the explicit stochastic representation for the expectation value of a local observable $\hat{\mathcal{O}}(t)$ by expressing the stochastic time evolution operators as in Eq. (2.32). For illustration, we provide results in the case when the observable $\hat{\mathcal{O}}$ of interest is a product of $\hat{S}_i^z$ operators at different sites. As seen for the Loschmidt amplitude, the argument of the trajectory average factorises over the sites i, and a general observable of this form can be expressed in the stochastic language by multiplying a set of on-site building blocks, given in Appendix B.5. For instance, the expectation value $\langle \hat{S}_i^z(t) \rangle$ for a system initialised in the state $|\psi_0\rangle = |\Downarrow\rangle$ with all spins down is given by

$$\langle \hat{S}_i^z(t) \rangle = -\frac{1}{2} \left\langle e^{-\frac{\xi_i^z + \tilde{\xi}_i^{z*}}{2}} (1 - \xi_i^+ \tilde{\xi}_i^{+*}) \prod_{j \neq i} e^{-\frac{\xi_j^z + \tilde{\xi}_j^{z*}}{2}} (1 + \xi_j^+ \tilde{\xi}_j^{+*}) \right\rangle_{\phi, \tilde{\phi}}. \tag{2.39}$$

This procedure can be used to obtain the stochastic expression for more general observables, involving different $\hat{S}_i^a$ operators and more than one time. We note that the stochastic representation of a given observable is not unique. For example, one could equally well choose to write the time-evolved expectation value of an observable as

$$\langle \hat{\mathcal{O}}(t) \rangle = \langle \psi_0 | \hat{U}(-t) \hat{\mathcal{O}} \hat{U}(t) | \psi_0 \rangle. \tag{2.40}$$

While this expression is equivalent to Eq. (2.27), when translating to the stochastic language the two parameterisations yield different formulae for the observables, which give the same average. Throughout this Thesis, we will use the parameterisation of Eq. (2.27), which allows one to express certain observables in terms of ξ_i^+ and ξ_i^z only, making it unnecessary to compute ξ_i^-.

The stochastic representations of operators and observables which we provided in this Chapter apply to all spin-$1/2$ lattice systems, without restrictions related to integrability, translational invariance, time-dependence of the couplings or dimensionality. We demonstrate this in Chapter 4, where we compute physical observables for a wide range of different settings by numerically solving the SDEs, considering the specific case of the quantum Ising model introduced in the next Chapter.

Chapter 3

Quantum Ising Model

In Chapter 2, we outlined a formalism [2–4] by which quantum expectation values can be expressed as averages of classical functions over stochastic processes. In this approach, the model dependence is encoded in the specific SDEs satisfied by the classical variables ξ_i^a. Throughout this Thesis, the main testing ground for the stochastic approach will be the quantum Ising model and the corresponding *Ising SDEs*, which we provide in this Chapter.

In order to acquire insights about the behaviour of the Ising SDEs, we begin by considering the classical and non-interacting cases, in which the SDEs are exactly solvable. To investigate the SDEs away from these limits, we compute the moment generating function for the variable ξ_i^+, which, as we will argue, plays the most important role. We find that in imaginary time the moments of ξ_i^+ are the same as for the non-interacting problem, showing that all information about the interactions is encoded in the correlations between variables at different sites. In real time, however, the generating function approach fails, due to the presence of poles in the non-interacting trajectory $\xi_{NI}^+(t)$ as a function of time. We also show that an infinite number of monomials involving the real and imaginary parts of ξ_i^+ vanish identically at all times, hinting to a possible redundancy in the Ising SDEs. We then discuss two approximations, namely the linearisation of the SDE for ξ_i^+ and the truncation of the system of ODEs arising from analytically averaging the SDEs, valid at short times and for small transverse fields Γ. We conclude this Chapter by considering the large Γ case. In this limit, we find that in imaginary time both the trajectories ξ_i^+ and the values of $\xi_i^+(\tau)$ at fixed times are Gaussian distributed. However, Gaussianity breaks down in real time. Within a large deviation framework, we argue that this is due to singularities in the real time saddle point trajectory, a manifestation of the same issue encountered for the generating function. In the next Chapter, we will investigate the breakdown of Gaussianity in real time in the context of its relation to dynamical quantum phase transitions.

3.1 Ising SDEs

The $1+1$ dimensional transverse-field Ising chain (TFIC) is defined by the Hamiltonian

$$\hat{H} = -J\sum_{i}^{N}\hat{S}_i^z\hat{S}_{i+1}^z - \Gamma\sum_{i}^{N}\hat{S}_i^x, \tag{3.1}$$

where Γ is an external magnetic field, $J>0$ is the strength of the ferromagnetic nearest-neighbour interactions and we consider periodic boundary conditions. This model exhibits a quantum phase transition between a ferromagnetic (FM) ground state for $\Gamma<\Gamma_c=J/2$ and a paramagnetic (PM) ground state for $\Gamma>\Gamma_c$. As discussed in Chapter 1, this model is exactly solvable in terms of free fermions [69]. While the TFIC will be the main focus of our analysis, we will also consider the non-integrable case with an additional longitudinal magnetic field, as well as the two-dimensional generalisation. In numerical calculations, we will set $J=1$.

In the stochastic approach, a given model is encoded in the SDEs satisfied by ξ_i^a. For the TFIC defind by Eq. (3.1), the real time stochastic equations of motion are given by[1]

$$-i\dot{\xi}_i^+(t) = \frac{\Gamma}{2}(1-\xi_i^{+2}) + \xi_i^+\sum_j O_{ij}\phi_j, \tag{3.2a}$$

$$-i\dot{\xi}_i^z(t) = -\Gamma\xi_i^+ + \sum_j O_{ij}\phi_j, \tag{3.2b}$$

$$-i\dot{\xi}_i^-(t) = \frac{\Gamma}{2}\exp\xi_i^z, \tag{3.2c}$$

where the fields ϕ_j are Gaussian white noises and the matrix O_{ij} is defined as in Chapter 2. These equations are obtained as special cases of Eq. (2.19). One can also consider the imaginary time SDEs, obtained by performing the Wick rotation $t=-i\tau$. As we will discuss in Chapter 5, the imaginary time version of the SDEs can be used to extract the ground state properties of quantum spin systems. By inspecting Eqs. (3.2), one notices that the disentangling variable ξ_i^+ plays a particularly important role for the quantum (real or imaginary time) dynamics. This variable vanishes identically in the classical case (see Section 3.2), and it is the only one that is not coupled to other stochastic variables: ξ_i^z is proportional to the time integral of ξ_i^+ and can be straightforwardly computed once ξ_i^+ is known, and ξ_i^- has a deterministic dependence on ξ_i^z. Furthermore, the non-linearity of Eq. (3.2a) makes it highly non-trivial to solve. In the remainder of this Chapter, we will

[1]For comparison, in Appendix C we provide the stochastic equations of motion describing the XYZ model.

investigate the Ising SDEs using different approaches, focussing in particular on ξ_i^+ for the reasons discussed above. We begin by considering the two limiting cases $\Gamma = 0$ and $J = 0$, in which the SDEs can be solved exactly.

3.2 Classical Limit

Let us first consider the classical case where no transverse field is present, $\Gamma = 0$. The equation of motion for $\xi_i^+(t)$ becomes linear, and because of the initial condition $\xi_i^+(0) = 0$ it admits the trivial solution $\xi_i^+(t) = 0$. Similarly, $\xi_i^-(t) = 0$. $\xi_i^z(t)$ then undergoes Brownian motion and its time evolution can be straightforwardly computed as

$$-i\xi_i^z(t) = \sum_j O_{ij} \int_0^t \mathrm{d}t' \phi_j(t') = \sum_j O_{ij} W_j(t)/\sqrt{i}. \tag{3.3}$$

The quantities $W_j(t)$ are a set of N independent standard Wiener processes, which can be numerically generated as

$$W_j(t) = \sqrt{t}\mathcal{N}(0,1), \tag{3.4}$$

where $\mathcal{N}(0,1)$ is a random number extracted from a zero-mean, unit-variance Gaussian distribution. In the classical case, there is no dynamics; this trivial result is readily recovered by substituting Eq. (3.3) in the stochastic expression for observables. For instance, for the Loschmidt amplitude (Eq. (2.37)) and magnetisation (obtained from Eqs. (B.63-B.64)) from an arbitrary initial state one readily obtains

$$|A(t)| = 1, \tag{3.5}$$

$$\langle \hat{S}_i^z(t) \rangle = \langle \hat{S}_i^z(0) \rangle. \tag{3.6}$$

3.3 Non-Interacting Limit

The non-interacting limit $J = 0$ corresponds to setting $O_{ij} = 0$. In this limit, the equations of motion of the disentangling variables become deterministic and can be solved analytically.

In real time, one obtains

$$\xi_i^+(t) = i\tan(\Gamma t/2) \equiv \xi_{NI}^+(t), \tag{3.7a}$$
$$\xi_i^z(t) = -2\log\cos(\Gamma t/2) \equiv \xi_{NI}^z(t), \tag{3.7b}$$
$$\xi_i^-(t) = i\tan(\Gamma t/2) \equiv \xi_{NI}^-(t). \tag{3.7c}$$

The imaginary-time solution can be analogously found via the Wick rotation $t = -i\tau$. In real time, Eqs. (3.7) parameterise the precession of a single spin under the effect of an external magnetic field in the x direction, as expected. This can be seen by explicitly writing the time-evolved state $|\psi(t)\rangle = \hat{U}(t)|_{J=0}|\psi(0)\rangle$ for generic product-state initial conditions $|\psi(0)\rangle = \otimes_j \left(a_j|\uparrow\rangle_j + b_j|\downarrow\rangle_j\right)$ with $|a_j|^2 + |b_j|^2 = 1$. From the general formula Eq. (2.34), we get

$$|\psi(t)\rangle = \bigotimes_j \begin{pmatrix} a_j\cos(\Gamma t/2) - ib_j\sin(\Gamma t/2) \\ -ia_j\sin(\Gamma t/2) + b_j\cos(\Gamma t/2) \end{pmatrix}. \tag{3.8}$$

3.4 Dynamics of Moments

Away from the non-interacting and classical limits, to the best of our knowledge the SDEs (3.2) cannot be solved exactly. However, it is possible to compute a generating function for the moments of ξ_i^+. It is convenient to first consider the imaginary time SDEs. Let us define a stochastic variable $g_i(\lambda,\tau) \equiv e^{\lambda\xi_i^+(\tau)}$; the Ito SDE for this quantity is obtained by applying the Ito chain rule given in Eq. (2.30):

$$\frac{\mathrm{d}}{\mathrm{d}\tau}g_i(\lambda,\tau) = \lambda\frac{\Gamma}{2}\left(1-\xi_i^{+2}\right)g_i(\lambda,\tau) + \lambda\xi_i^+\sum_j O_{ij}\phi_j g_i(\lambda,\tau) + \frac{1}{2}\lambda^2\xi_i^{+2}\sum_j O_{ij}O_{ij}g_i(\lambda,\tau). \tag{3.9}$$

The matrix OO^T has no diagonal term (Appendix B.2), so the Ito drift term proportional to $\sum_j O_{ij}O_{ij}$ gives no contribution. Furthermore, we can write $\xi_i^+ g_i = \frac{\partial}{\partial\lambda}g_i$. With these simplifications, we obtain

$$\frac{\mathrm{d}}{\mathrm{d}\tau}g_i(\lambda,\tau) = \left[\lambda\frac{\Gamma}{2}\left(1-\frac{\partial^2}{\partial\lambda^2}\right) + \sum_j O_{ij}\phi_j\frac{\partial}{\partial\lambda}\right]g_i(\lambda,\tau). \tag{3.10}$$

Considering the expectation value of Eq. (3.10) and using the property of Ito calculus

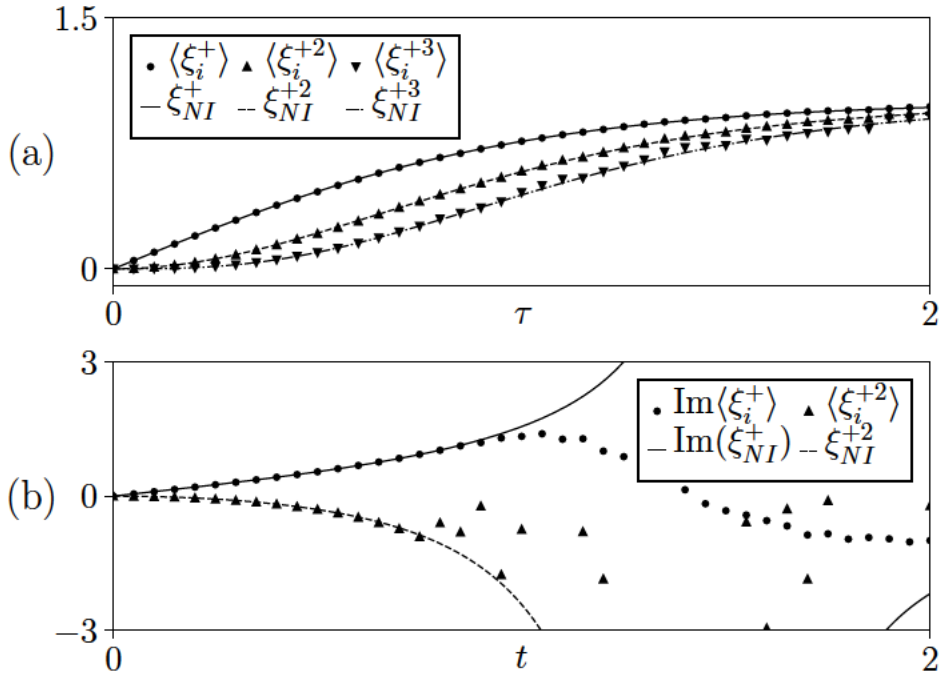

Figure 3.1: Moments of the disentangling variable ξ_i^a evolved according to the Ising SDEs with $J = 1$, $\Gamma = 4\Gamma_c$. (a) In imaginary time, all moments (dots, computed from averaging the SDEs) are equal to powers of the non-interacting trajectory $\xi_{NI}^+(\tau)$ defined in Eq. (3.7a) (full lines), as predicted by the generating function (3.13). (b) In real time, the moments of ξ_i^+ are no longer the same as in the non-interacting case; the analytic continuation of the imaginary time results fails because of the presence of poles in $\xi_{NI}^+(t)$. The results were obtained from $n = 10^4$ numerical simulations, performed using the Euler scheme with a discretisation time step $\Delta t = 10^{-5}$.

$\langle g_i(\tau)\phi_j(\tau)\rangle = 0 \;\forall\; i, j$ we get the ODE

$$\partial_\tau G_i(\lambda,\tau) = \left[\lambda\frac{\Gamma}{2}\left(1 - \frac{\partial^2}{\partial\lambda^2}\right)\right] G_i(\lambda,\tau), \tag{3.11}$$

where we have defined $G_i(\lambda,\tau) \equiv \langle g_i(\lambda,\tau)\rangle$ with initial conditions $G_i(0,\tau) = G_i(\lambda,0) = 1$. The function $G_i(\lambda,\tau)$ is the generating function for the moments[2] of ξ_i^+, satisfying

$$\langle \xi_i^+(t)^n\rangle = \frac{\partial^n}{\partial\lambda^n} G_i(\lambda,\tau)|_{\lambda=0}. \tag{3.12}$$

[2]Since averages of the stochastic variables are always with respect to the fields ϕ, when there is no ambiguity with quantum expectation values we will omit the relative subscript in averages to avoid notational clutter.

Because of translational invariance, we can drop the index i. The equation for $G(\lambda,\tau)$ can be solved by Fourier transforming, yielding

$$G(\lambda,\tau) = e^{\lambda \tanh(\Gamma\tau/2)}. \tag{3.13}$$

This result predicts that all moments of $\xi_i^+(\tau)$ are real-valued and they are simply given by powers of the deterministic trajectory obtained in the non-interacting case with $J = 0$. Thus, the moments of each individual ξ_i^+ contain no information about the interacting quantum system, which is entirely encoded in the correlations between variables at different sites. As shown in Fig. 3.1(a), the predictions of Eq. (3.13) are in good agreement with numerical simulations performed using the Euler scheme, discussed in Appendix D.1. One could then be tempted to analytically continue the imaginary time solution to real time:

$$G(\lambda,t) = e^{i\lambda \tan(\Gamma t/2)}. \tag{3.14}$$

Equation (3.14) would imply that also for real time evolution all moments of $\xi_i^+(t)$ are equal to powers of the non-interacting trajectory. This prediction is however contradicted by numerical simulations (Fig. 3.1(b)), showing that the analytic continuation fails to provide the correct result. This is to be expected, as the function $\tanh(\Gamma\tau/2)$ has poles at $\tau = 2i\pi(n+1/2)/\Gamma$ for all integer n and thus we are not guaranteed that analytic continuation will work. In fact, direct application of the Fourier solution method in real time fails because of the poles in the exponent of Eq. (3.14). In order to compute the generating function in real time, we would need to consider the real and imaginary parts of $\xi_i^+(t)$ separately; however, the resulting system of equations does not appear to be analytically solvable. This hints at a fundamental difference between the behaviour of ξ_i^+ for real and imaginary time evolution, which we will encounter in other guises in the remainder of this Chapter. Generalising this approach, we can introduce the many-site generating function $G(\boldsymbol{\lambda},\tau) \equiv \langle e^{\sum_i \lambda_i \xi_i^+} \rangle$. Following a similar procedure to the one-site case, we find that $G(\boldsymbol{\lambda},\tau)$ satisfies the partial differential equation

$$\partial_\tau G(\lambda,\tau) = \sum_i \left[\lambda_i \frac{\Gamma}{2}\left(1 - \frac{\partial^2}{\partial\lambda_i^2}\right)\right] G(\boldsymbol{\lambda},\tau) + \sum_{ij} \lambda_i\lambda_j \mathcal{J}_{ij} \frac{\partial^2}{\partial\lambda_i\partial\lambda_j} G(\boldsymbol{\lambda},\tau), \tag{3.15}$$

where we used $\sum_k O_{ik}O_{jk} = 2\mathcal{J}_{ij}$ (Appendix B.2). To the best of our knowledge, it is not possible to solve this equation exactly.

Further results can be obtained by considering the equations of motion for the real and imaginary parts of ξ_i^+ separately. In particular, it is possible to show (Appendix B.6) that an infinite number of monomials involving $\mathrm{Re}(\xi_i^+)$ and $\mathrm{Im}(\xi_i^+)$ vanish identically at all times,

$$\left\langle [\mathrm{Re}\,\xi_i^+(\tau)]^n [\mathrm{Im}\,\xi_i^+(\tau)]^m \right\rangle = 0 \quad \forall \quad m \text{ odd}, \tag{3.16a}$$

$$\left\langle [\mathrm{Re}\,\xi_i^+(t)]^n [\mathrm{Im}\,\xi_i^+(t)]^m \right\rangle = 0 \quad \forall \quad n \text{ odd}. \tag{3.16b}$$

In particular, from the above identities we recover as a special case the result $\mathrm{Im}\langle \xi_i^+(\tau)\rangle = 0$ predicted by the generating function (3.13), whereas for real time evolution we get $\mathrm{Re}\langle \xi_i^+(t)\rangle = 0$. The vanishing of an infinite number of expectation values suggests that a degree of redundancy may be present in the Ising SDEs, and that it may be possible to rewrite them in a way that automatically discards all the vanishing expectation values.

Having obtained a number of exact results for the Ising SDEs, we will now discuss a range of approximations in which the equations are simplified, so that it is possible to gain further insight into their behaviour.

3.5 Short-Time Behaviour: Linearised Dynamics

The initial condition $\xi_i^+(0) = 0$ suggests that, for short times, the non-linear term $\sim {\xi_i^+}^2$ is small and it can thus be neglected; in this regime, we can approximate the time evolution of ξ_i^+ by the *linearised SDE*

$$\dot{\xi}_i^+(\tau) = \frac{\Gamma}{2} + \xi_i^+(\tau) \sum_j O_{ij}\phi_j. \tag{3.17}$$

This equation can be solved exactly. For any given standard Wiener process $W_j(\tau)$, one has

$$\xi_i^+(\tau) = \frac{\Gamma}{2} e^{\sum_j O_{ij} W_j(\tau)} \int_0^\tau \mathrm{d}\tau' e^{-\sum_j O_{ij} W_j(\tau')}. \tag{3.18}$$

The mean of ξ_i^+ grows linearly under the linearised dynamics, $\langle \xi_i^+(\tau)\rangle = \tau\Gamma/2$. We can estimate the breakdown time of this approximation from the condition $\langle \xi_i^+(\tau_b)^2\rangle = \tau^2\Gamma^2/4 \sim 1$, yielding $\tau_b \sim 2/\Gamma$. In Fig. 3.2 we compare $\langle \xi_i^+\rangle$ obtained from numerically solving the full SDE (3.7a) with the Euler scheme and from the analytical solution of the real time version of Eq. (3.17), showing that the linearised dynamics reproduces the behaviour of ξ_i^+ at short times. From the linearised solution for ξ_i^+, we can obtain an

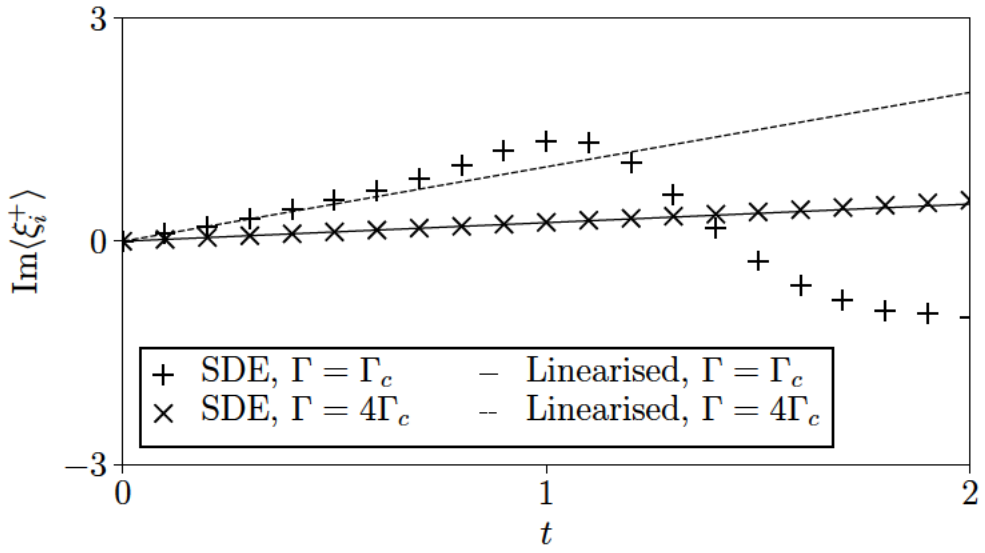

Figure 3.2: Time evolution of $\langle \xi_i^+ \rangle$ for different values of Γ, as obtained by numerically simulating the full SDE (3.7a) (dots) and analytically averaging the real time version of the linearised SDE (3.17) (lines). The range of validity of the linearised equations is inversely proportional to Γ. The expectation value of ξ_i^+ is the same for all i, so we average this quantity over the sites.

exact expression for ξ_i^z:

$$\xi_i^z(\tau) = -\frac{\Gamma^2}{2} \int_0^\tau \mathrm{d}\tau'' e^{\Sigma_j O_{ij} W_j(\tau'')} \int_0^{\tau''} \mathrm{d}\tau' e^{-\Sigma_j O_{ij} W_j(\tau')} + O_{ij} W_j(\tau). \tag{3.19}$$

The real time formula can be obtained analogously. Integrals of exponentials of Wiener processes cannot be written in closed form, so in general one still has to know $\xi_i^+(\tau')$ $\forall\ \tau' < \tau$ in order to compute $\xi_i^z(\tau)$. While a full numerical simulation of the stochastic trajectories is thus necessary also in this regime, it would be interesting to further investigate the exact expressions (3.18-3.19) to see if other analytical insights about the short time regime can be extracted.

3.6 Small Γ: Truncation of the Equations of Motion

As discussed in Chapter 2, solving the full hierarchy of ODEs obtained by analytically averaging the SDEs is equivalent to diagonalising the Hamiltonian. In the small Γ limit, we can approximate the dynamics by truncating the system so that a result can be found by solving finitely many ODEs rather than simulating stochastic trajectories. We will

illustrate this by considering the Loschmidt amplitude for a quantum quench from the ferromagnetic initial state with all spins down $|\psi_0\rangle = |\Downarrow\rangle$. We will carry out intermediate steps in imaginary time to avoid a proliferation of factors of i and Wick-rotate to real time once the final result is obtained, but the calculation can be performed directly in real time giving the same answer. The Loschmidt amplitude for a quantum quench from the FM state with all spins down $|\Downarrow\rangle \equiv \otimes_i |\downarrow\rangle_i$ is given by the particularly simple expression

$$A(\tau) = \langle e^{-\frac{1}{2}\sum_i \xi_i^z(\tau)} \rangle_\phi \equiv \langle f(\tau) \rangle_\phi . \tag{3.20}$$

The time evolution of the corresponding stochastic function $f(\tau)$ is given by the Ito SDE

$$\dot{f}(\tau) = \left(-\frac{\Gamma}{2} \sum_i \xi_i^+(\tau) + \frac{1}{8} \sum_{ijk} O_{ij} O_{kj} - \frac{1}{2} \sum_{ij} O_{ij} \phi_j \right) f(\tau). \tag{3.21}$$

Analytically averaging Eq. (3.21), we find that the Loschmidt amplitude satisfies the ODE

$$\dot{A}(\tau) = -\frac{\Gamma}{2} \sum_i \langle \xi_i^+(\tau) f(\tau) \rangle_\phi + \frac{1}{8} \sum_{ij} O_{ij} O_{ij} A(\tau). \tag{3.22}$$

The equation of motion of $A(\tau)$ features another expectation value, $\langle \xi_i^+(\tau) f(\tau) \rangle_\phi \equiv F_i(\tau)$. Using Ito calculus, we can find the corresponding equation of motion

$$\dot{F}_i(\tau) = \frac{\Gamma}{2}(A - \langle {\xi_i^+}^2 f \rangle_\phi) + \frac{\Gamma}{2} \langle \xi_i^+ \sum_j \xi_j^+ f \rangle_\phi + \frac{1}{8} F_i \sum_{jkl} O_{jk} O_{lk} - \frac{1}{4} F_i \sum_{lj} O_{ij} O_{lj} \tag{3.23}$$

with initial condition $F_i(0) = 0$. It can be seen that this equation contains higher moments $F_{ij} \equiv \langle \xi_i^+ \xi_j^+ f \rangle_\phi$. In fact, as anticipated, by proceeding in this manner we generate an infinite system of coupled ODEs involving higher and higher moments $F_{i_1 \ldots i_n}$. In the limit of small Γ, we can approximate the equation for $F_i(\tau)$ as

$$\dot{F}_i(\tau) \sim \frac{1}{8} F_i \sum_{jkl} O_{jk} O_{lk} - \frac{1}{4} F_i \sum_{jl} O_{ij} O_{lj}. \tag{3.24}$$

This equation is trivially solved by $F_i(\tau) = 0$. To induce a non-trivial time-evolution, we additionally retain the term proportional to $\Gamma A(\tau)$ so that the system of equations still

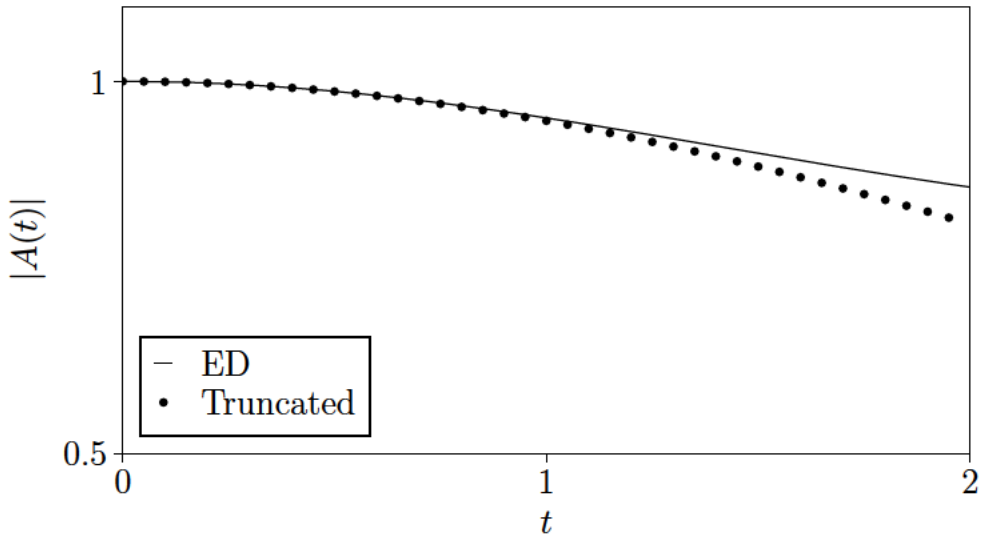

Figure 3.3: Modulus of the Loschmidt amplitude $|A(t)|$ for a TFIC of $N = 7$ spins following a quantum quench from the FM ground state to $\Gamma = \Gamma_c/2$. The result obtained by numerically solving the truncated system of ODEs (3.25) agrees with exact diagonalisation at short times.

closes. This gives the coupled equations

$$\dot{A}(\tau) = \frac{\Gamma}{2}\sum_i F_i + \frac{1}{8}A\sum_{jkl} O_{jk}O_{lk}, \tag{3.25a}$$

$$\dot{F}_i(\tau) = \frac{\Gamma}{2}A + \frac{1}{8}F_i\sum_{jkl} O_{jk}O_{lk} - \frac{1}{4}F_i\sum_{jl} O_{ij}O_{lj}. \tag{3.25b}$$

This system of equations can be interpreted by considering the physical meaning of $F_i = \langle \xi_i^+ f \rangle_\phi$. In the stochastic language, this corresponds to the overlap between an initial all-down state and a state where the spin at site i is flipped. Thus, the system (3.25) describes the Loschmidt echo under the approximate quantum dynamics whereby only a single spin can be flipped at any given time. Comparison to exact diagonalisation shows that this approximation is accurate in predicting the Loschmidt amplitude at short times $t \lesssim t_b$ with $t_b \propto 1/\Gamma$.

3.7 Large Γ: Large Deviation Approach

Having discussed an approximation for small Γ, we will now consider the limit $\Gamma \gg \Gamma_c$. For simplicity, we first focus on the imaginary time case. For large Γ, the system approaches

its deterministic non-interacting behaviour. At infinite Γ/J, in particular, one has

$$\xi_i^+(\tau) = \xi_{NI}^+(\tau) \equiv \tanh(\Gamma\tau/2). \tag{3.26}$$

Since Γ multiplies τ, for increasing Γ the system can be expected to evolve faster. To get a well-defined limiting behaviour, we re-scale time as $\bar{\tau} = \tau\Gamma$. With this rescaling, we get the stochastic equations

$$\dot{\xi}_i^+(\bar{\tau}) = \frac{1}{2}(1-\xi_i^{+2}) + \varepsilon\xi_i^+ \sum_j O_{ij}\phi_j, \tag{3.27a}$$

$$\dot{\xi}_i^z(\bar{\tau}) = -\xi_i^+ + \varepsilon \sum_j O_{ij}\phi_j, \tag{3.27b}$$

$$\dot{\xi}_i^-(\bar{\tau}) = \frac{1}{2}\exp\xi_i^z, \tag{3.27c}$$

where we have defined the noise parameter $\varepsilon = 1/\Gamma$, which in the limit we are considering can be regarded as small. The corresponding real-time version is obtained by letting $\bar{\tau} = i\bar{t}$. In the limit of small noise, stochastic differential equations are described by the Freidlin-Wentzell (FW) large deviation theory [145, 146]. Consider a general stochastic process characterised by the drift and diffusion coefficients a_i and B_{ij}:

$$\dot{x}_i = a_i(x) + \varepsilon \sum_j B_{ij}(x)\phi_j, \tag{3.28}$$

with $x \equiv \{x_i\}$. The effective action for a trajectory x is given by

$$I[x] = \int_o^\tau \mathrm{d}\tau' L(x,\dot{x}), \tag{3.29}$$

$$L(x,\dot{x}) = \frac{1}{2}\sum_{ij}(\dot{x}_i - a_i(x))\mathcal{B}_{ij}^{-1}(x)(\dot{x}_i - a_i(x)), \tag{3.30}$$

$$\mathcal{B}_{ij}(x) \equiv \sum_k B_{ik}(x)B_{jk}(x). \tag{3.31}$$

For the quantum Ising model, $\mathcal{B}_{ij} = J(\delta_{ij+1} + \delta_{ij-1})\xi_i^+\xi_j^+ = 2\mathcal{J}_{ij}\xi_i^+\xi_j^+$ so that $\mathcal{B}_{ij}^{-1} = \frac{1}{2}\mathcal{J}_{ij}^{-1}\xi_i^{+-1}\xi_j^{+-1}$ and

$$L(\xi^+,\dot{\xi}^+) = \frac{1}{4}\sum_{ij}\frac{1}{\xi_i^+\xi_j^+}\left(\dot{\xi}_i^+ - \frac{1}{2}(1-\xi_i^{+2})\right)\mathcal{J}_{ij}^{-1}\left(\dot{\xi}_j^+ - \frac{1}{2}(1-\xi_j^{+2})\right). \tag{3.32}$$

This action can be constructed by expressing the stochastic process as a path integral with respect to the ξ_i^+ variables [147–149, 4]. FW theory predicts that $\xi_i^+(\bar{\tau})$ obeys a large deviation principle (LDP) with rate function I and rate ε^{-2}, so that the probability of a trajectory ξ_i^+ is given by

$$P[\xi_i^+] \sim e^{-\varepsilon^{-2} I[\xi_i^+]}. \tag{3.33}$$

As expected, the solution of the Euler-Lagrange equation for the action (3.32), which yields the saddle point trajectory dominating Eq. (3.33) in the limit $\varepsilon \to 0$, is the non-interacting solution

$$\xi_i^+ = \xi_{NI}^+ \equiv \tanh(\bar{\tau}/2). \tag{3.34}$$

For small ε, the trajectories $\xi_i^+(\bar{\tau})$ are approximately Gaussian distributed around the saddle point trajectory [150]

$$P[\xi_i^+] \sim e^{-\frac{\varepsilon^{-2}}{2} \int_0^{\bar{\tau}} \Sigma_{ij} I_{ij}^{(2)} (\xi_i^+(\bar{\tau}') - \xi_{NI}^+)(\xi_j^+(\bar{\tau}') - \xi_{NI}^+) \mathrm{d}\bar{\tau}'}, \tag{3.35}$$

where we have defined the second variation of the action

$$I_{ij}^{(2)} \equiv \frac{\delta^2 I}{\delta \xi_i^+(\bar{\tau}') \delta \xi_j^+(\bar{\tau}')}\Big|_{\xi_{NI}^+}. \tag{3.36}$$

The approximate Gaussian form of the action for large Γ suggests that the sampling of the SDEs should be efficient in this limit. We will indeed verify this in Chapter 5 when numerically solving the SDEs to obtain ground state expectation values. The FW construction discussed above also applies in real time: however, in this case, the saddle point trajectory, given by the deterministic result (3.7a), has an infinite number of singularities as a function of time. This leads to a breakdown of the expansion about the saddle point, which can be expected to have consequences for the sampling. Indeed, we will see in Chapter 4 that, even for large Γ, regions in time that are close to the singularities in the saddle point trajectory are associated with enhanced fluctuations leading to difficulties in sampling.

3.8 Gaussian Approximation

For large Γ, we found that in imaginary time the distribution of the trajectories ξ_i^+ around the non-interacting result becomes Gaussian. In fact, this is also true for the distribution of

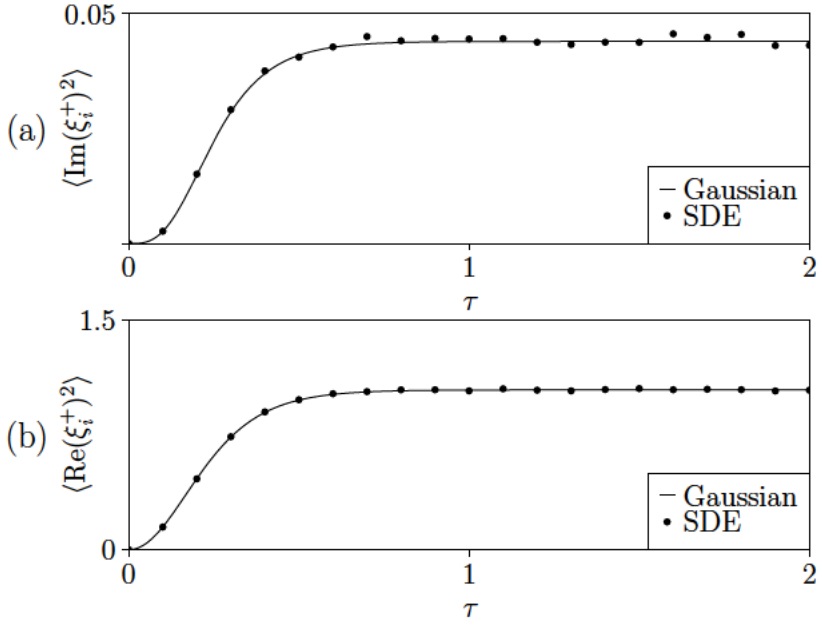

Figure 3.4: Imaginary time evolution of the second moments of the real and imaginary parts of $\xi_i^+(\tau)$ for $\Gamma = 16\Gamma_c$. We find that for large Γ the result obtained from numerical simulations of the SDEs (dots) are accurately predicted by assuming that $\mathrm{Re}(\xi_i^+)$, $\mathrm{Im}(\xi_i^+)$ are Gaussian distributed with time-dependent mean and covariances and solving the resulting closed system of ODEs, given in Appendix B.7.

$\xi_i^+(\tau)$ at a fixed time τ. This can be checked by solving the system of ODEs obtained by assuming that the real and imaginary parts $R_i(\tau)$, $I_i(\tau)$ of $\xi_i^+(\tau)$ are Gaussian distributed and comparing the result obtained using this assumption to numerical simulations. Again, because of translational invariance, we can drop the index i. The assumption of Gaussianity allows us to truncate the system resulting from averaging the SDEs and obtain a solution by solving finitely many ODEs. Let us define time-dependent means m_X and covariances C_{XY} as

$$m_X \equiv \langle X \rangle, \tag{3.37a}$$

$$X = m_X + \delta X, \tag{3.37b}$$

$$C_{XY} \equiv \langle \delta X \, \delta Y \rangle, \tag{3.37c}$$

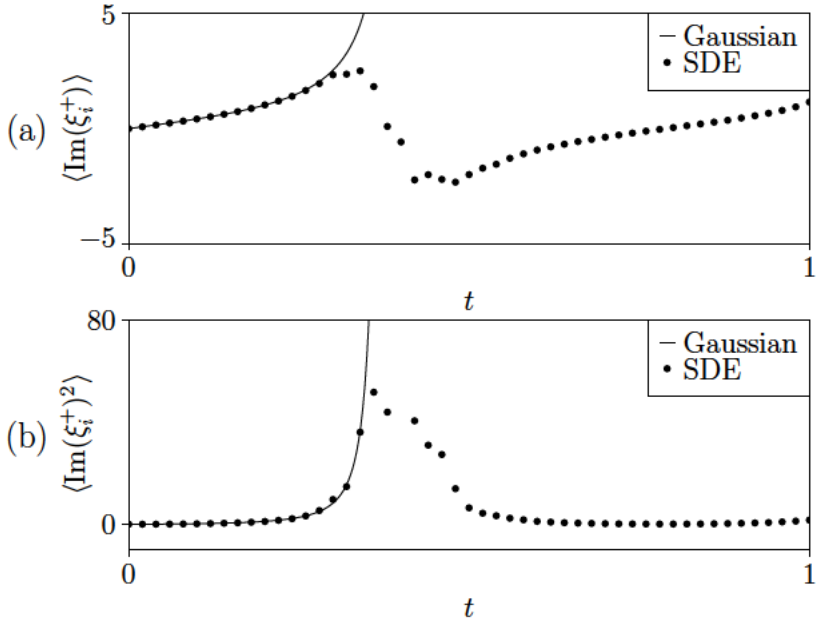

Figure 3.5: Real time evolution of the first and second moments of $\mathrm{Im}(\xi_i^+)$, for $\Gamma = 16\Gamma_c$. In real time, moments involving only $\mathrm{Re}(\xi_i^+)$ vanish identically, so we don't show them here. We find that, unlike the imaginary time case, the Gaussian approximation fails to capture the behaviour of ξ_i^+ beyond a certain time scale.

for $X, Y \in \{R, I\}$. Within the Gaussian approximation all moments can be expressed in terms of these quantities, e.g.

$$\langle R^3 \rangle = \langle (m_R + \delta R)^3 \rangle \tag{3.38}$$

$$= m_R^3 + 3 m_R C_{RR}, \tag{3.39}$$

where we used $\langle \delta R^3 \rangle = \langle \delta R \rangle = 0$. All quantities vanish at $\tau = 0$. Using this approximation, we can derive the imaginary time Gaussian equations of motion for ξ_i^+, given in Appendix B.7. For sufficiently large Γ, we find that the Gaussian approximation accurately captures the behaviour of $\xi_i^+(\tau)$, as shown in Fig. 3.4. The same procedure can be repeated in real time; however, in contrast to imaginary time evolution, we find that in this case the Gaussian approximation breaks down at a particular time scale, where a strongly non-Gaussian behaviour emerges (Fig. (3.5)). In Chapter 4, we will return to this observation in the context of the relation between the behaviour of the disentangling variables and dynamical quantum phase transitions.

In this Chapter, we have investigated the Ising SDEs using a number of different approaches. While for imaginary time evolution the behaviour of ξ_i^+ becomes Gaussian in the large Γ limit, in real time Gaussianity breaks down beyond a certain time scale. This finding will be further investigated in the next Chapter, where we will numerically solve the full Ising SDEs.

Chapter 4

Numerical Solution of the Real Time Ising SDEs

In Chapter 3 we investigated the SDEs which encode the quantum Ising model, obtaining insights about their behaviour for different parameter ranges. In imaginary time, we found that for large transverse fields Γ both the trajectories of the stochastic variables ξ_i^+ and their values at fixed times are approximately Gaussian distributed. However, for real time evolution, we found the even for large Γ there exists a time scale beyond which an approximate Gaussian description fails to capture the behaviour of the stochastic variables.

In this Chapter, we further investigate the behaviour of the classical variables and compute physical observables by numerically solving the real time Ising SDEs (3.2) [1], which, to the best of our knowledge, has not been previously done[1]. We begin by computing the Loschmidt rate function $\lambda(t)$ as the average of the corresponding stochastic function. For quenches across a quantum critical point, $\lambda(t)$ develops sharp peaks at particular values of t. Considering quenches from the ferromagnetic initial state $|\Downarrow\rangle \equiv \otimes_i |\downarrow\rangle_i$, we show that the Loschmidt peaks are accompanied by clear signatures in the stochastic variables, including the presence of enhanced fluctuations. In particular, we find that the occurrence of the Loschmidt peaks is associated with the breakdown of Gaussianity in the distribution of the classical variables, observed in Chapter 3.

We then consider different quantum quenches, showing how the Loschmidt rate function $\lambda(t)$ can be computed by averaging the corresponding functions of the disentangling variables. The same approach can be applied to calculate other observables, as we demonstrate for the time evolution of the magnetisation and correlations following a quantum quench.

[1] In Ref. [4] the Euclidean SDEs were simulated, but not for computing observables.

The realm of applicability of the stochastic method is however not limited to integrable systems; we show this by considering the quantum Ising chain with an integrability-breaking longitudinal field and the two-dimensional transverse field quantum Ising model, discussing how these can be treated within the stochastic framework. Finally, we show that the method can be applied in disordered settings by considering a TFIC in the presence of random site-dependent transverse fields.

Throughout this Chapter, we compute physical observables for small system sizes in order to demonstrate the applicability in principle of the stochastic approach to a range of physical problems. We conclude our discussion by assessing the numerical performance of our current implementation of the SDE method, quantifying the extent to which averages corresponding to observables are affected by fluctuations. We estimate that these fluctuations grow exponentially in time and with the system size, posing a limitation to the application of this approach in its current form for the simulation of large systems. However, in Chapters 5 and 6, considering Euclidean time evolution we will discuss how this limitation can be overcome by means of measure transformations, with a view to generalising this approach to real time.

The Ising SDEs given by Eqs. (3.2) were solved numerically using the Euler discretisation scheme [143]; the corresponding update rules are given in Eqs. (D.3). In general, the numerical solution of non-linear SDEs using the Euler scheme may give rise to divergent trajectories where the stochastic variables $\xi_i^+(t)$ grow without bound. Throughout this Thesis, we present results obtained by retaining the nondivergent trajectories at any given time t. Thus, for a given observable, the number of trajectories that the average is performed over is a function of time. To give an estimate of this, when presenting the results we specify the fraction of surviving trajectories at the stopping time. The divergence of trajectories was mitigated by employing an appropriately small discretisation time step $\Delta t = 10^{-5}$. A more detailed discussion of the issue of diverging trajectories, including the specific definition of divergence used when selecting trajectories and the dependence on Δt, can be found in Appendix D.2. Other simulation schemes may be beneficial in this respect, as discussed in Appendix D.1. For observables computed from the stochastic approach, we estimate error bars as the standard error s of the averages obtained by splitting the data set into n_b batches of independent trajectories: for an observable x, $s = n_b^{-1}\sqrt{\sum_{i=1}^{n_b}(\bar{x}-\bar{x}_i)^2} = \sigma/\sqrt{n_b}$, where $\bar{x}_i$ are the batch means, $\bar{x} = \sum_{i=1}^{n_b}\bar{x}_i/n_b$ and σ is the standard deviation. The bars are not shown when they are smaller or comparable to the size of the plot markers. We compare our results to exact diagonalisation (ED) performed using the QuSpin package [151]. In simulations, we set $J = 1$ and measure time in units of $1/J$.

4.1 Loschmidt Echo and Dynamics of the Disentangling Variables

Consider a generic quantum system initialised in a state $|\psi(0)\rangle$. The survival amplitude for the state after unitary evolution for time t is given by

$$A(t) = \langle \psi(0)|\hat{U}(t,0)|\psi(0)\rangle. \tag{4.1}$$

The Loschmidt echo is defined as the probability for the system to return to its initial state after evolving unitarily for time t, $L(t) \equiv |A(t)|^2$. Since this quantity decays exponentially with the system size N, it is convenient to define the Loschmidt rate function $\lambda(t)$

$$\lambda(t) \equiv -\frac{1}{N}\log L(t). \tag{4.2}$$

The rate function has recently been studied in the context of *dynamical quantum phase transitions* (DQPTs) [5], defined as non-analyticities in $\lambda(t)$ that typically occur in systems quenched across a quantum critical point, as discussed in Chapter 1. While DQPTs only arise in the thermodynamic limit, signatures of the transitions are visible for finite system size N.

In this Section, we look at DQPTs in the framework of the stochastic approach. The Loschmidt amplitude $A(t)$ following a quantum quench from a general initial condition is given by the stochastic expression in Eq. (2.37). If the initial state is the ferromagnetic ground state with all spins down $|\psi_0\rangle = |\Downarrow\rangle$, the general expression simplifies to

$$A(t) = \left\langle \prod_i^N \exp\left(-\frac{\xi_i^z(t)}{2}\right) \right\rangle_\phi. \tag{4.3}$$

Following a quantum quench, the disentangling variables ξ_i^a evolve according to the Ising SDEs (3.2), where Γ is given by the transverse field of the final Hamiltonian. The Loschmidt amplitude can thus be obtained by numerically solving the Ising SDEs for different realisations of the noises $\phi_i(t)$ and performing the average in Eq. (4.3). Figure 4.1 shows $\lambda(t)$ obtained from the SDEs for a quantum quench from the initial state $|\Downarrow\rangle$ with $\Gamma = 0$ to $\Gamma = 16\ \Gamma_c$, deep in the paramagnetic phase. The results obtained from the stochastic method are in good agreement with exact diagonalisation (ED). $\lambda(t)$ shows sharp peaks, corresponding to DQPTs in the thermodynamic limit.

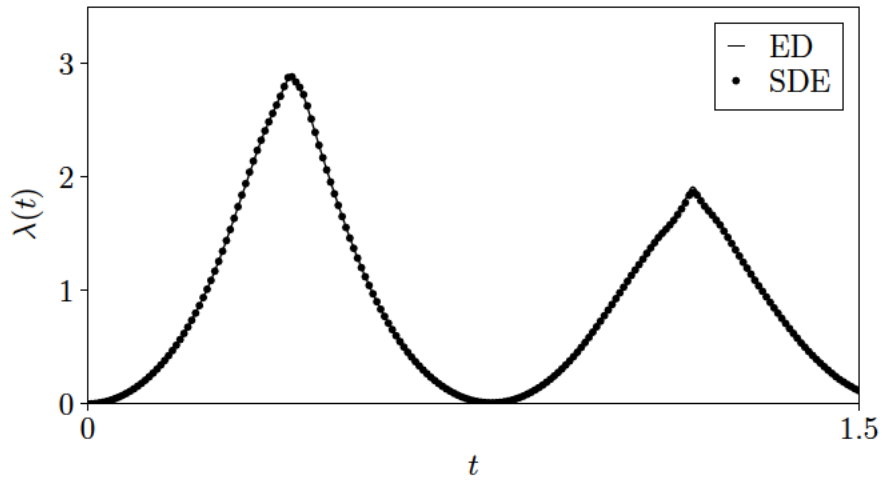

Figure 4.1: Loschmidt rate function for the 1D transverse-field Ising chain (TFIC), following a quantum quench from the FM ground state with $\Gamma = 0$ to $\Gamma = 16\Gamma_c$. The results obtained from the SDEs are in good agreement with exact diagonalisation (ED) for a system of size $N = 9$. The results shown were computed by averaging 10^5 simulations. The fraction of surviving trajectories at the stopping time is $\sim 1\%$.

For this choice of initial conditions, the particularly simple stochastic expression (4.3) for $A(t)$ reveals that the statistics of the quantity $\sum_i \xi_i^z(t)$ fully determine the Loschmidt amplitude for this quantum quench. In particular, heuristically, one may expect that the turning points of $\sum_i \xi_i^z(t)$ are related to the maxima and minima of $A(t)$. This begs the question as to whether signatures of the Loschmidt dynamics are visible at the level of the stochastic variables themselves. Motivated by these observations, we now turn to considering different quantities in order to characterise the behaviour of the disentangling variables in relation to the Loschmidt peaks. We define site-averaged intensive quantities which can be compared for different system sizes:

$$\chi^a(t) \equiv \frac{1}{N}\sum_{i=1}^{N} \xi_i^a(t), \tag{4.4}$$

so that the Loschmidt rate function for quenches initiating in the state $|\Downarrow\rangle$ can be written as

$$\lambda(t) = -\frac{1}{N}\log\left|\langle e^{-\frac{N}{2}\chi^z(t)}\rangle_\phi\right|^2. \tag{4.5}$$

Focussing on quantum quenches from $\Gamma = 0$ to $\Gamma \gg \Gamma_c$, we see that signatures of the DQPTs are present in the full distribution of χ^z and χ^+. The distribution of $\mathrm{Re}(\chi^z)$ attains its maximal mean and variance in the vicinity of the DQPTs (Figs. 4.2(a) and 4.4(a)),

and the imaginary part also shows pronounced features in the same region (Fig. 4.2(b)). Similarly, the real and imaginary parts of χ^+ attain their broadest distributions in the vicinity of DQPTs, as illustrated in Fig. 4.3.

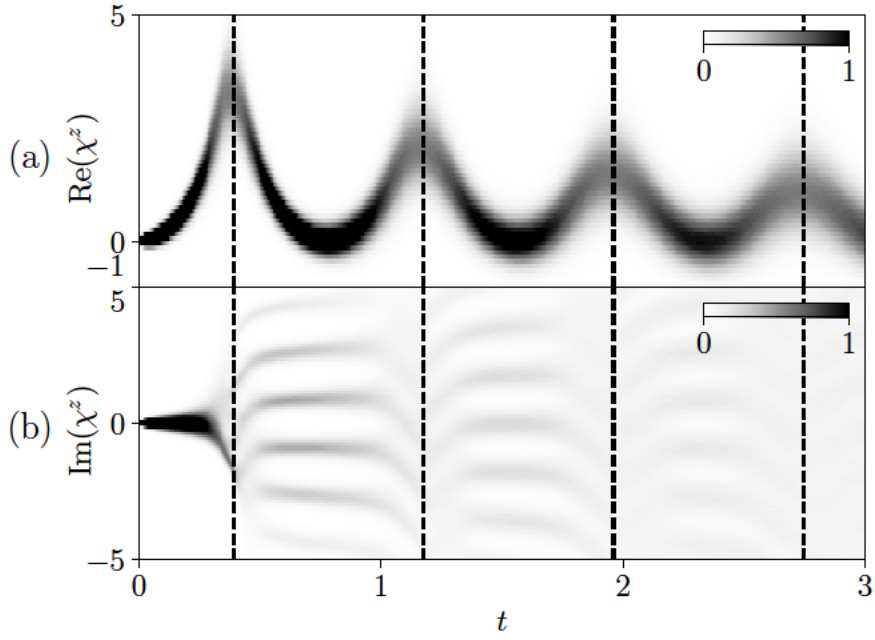

Figure 4.2: Distribution of the real and imaginary parts of the site-averaged classical variable χ^z time-evolved with $\Gamma = 16\Gamma_c$ for a TFIC of size $N = 7$. (a) The distribution $\mathrm{Re}(\chi^z)$ attains its maximum mean and variance in the vicinity of the Loschmidt peaks (dashed lines, obtained from ED). (b) Pronounced features are also visible in $\mathrm{Im}(\chi^z)$.

This behaviour is observed for all system sizes N, with the distributions becoming narrower as N is increased. This is illustrated in Fig. 4.4(b) considering the distribution of $\mathrm{Re}(\chi^z)$. Notably, the distribution of $\mathrm{Re}(\chi^z)$ is well approximated by a Gaussian except in the vicinity of the Loschmidt peaks, where Gaussianity breaks down, as shown in Fig. 4.4(a). By applying a Kolmogorov-Smirnov test, we find that the null hypothesis that $\mathrm{Re}(\chi^z)$ is sampled from a Gaussian distribution is rejected at the 5% confidence level in the region $0.38 < t < 0.45$, i.e. around the first Loschmidt peak at $t_1 = 0.39$. It is instructive to contrast this with the non-interacting case $\Gamma = \infty$, where χ^z is purely deterministic, and the classical case $\Gamma = 0$, where χ^z is a linear combination of Gaussian distributed variables and is therefore Gaussian distributed. Hence, the non-Gaussianity in the distribution of χ^z can be regarded as a signature of non-trivial quantum dynamics in the classical variables. The observed behaviour is consistent with the findings of Section 3.8, where we showed that even for large Γ the Gaussian approximation for the time evolution of ξ_i^+ fails to predict its

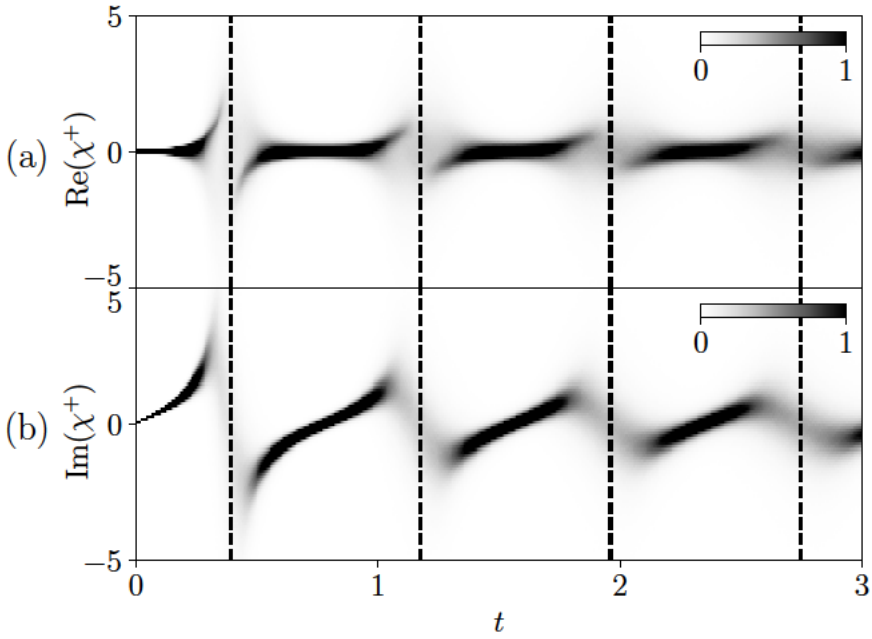

Figure 4.3: Distribution of the (a) real and (b) imaginary parts of the site-averaged classical variable χ^+ for a TFIC of size $N = 7$ time-evolved with $\Gamma = 16\,\Gamma_c$. It can be seen that both distributions are broadest and show characteristic features in the vicinity of the Loschmidt peaks (dashed lines, obtained from ED).

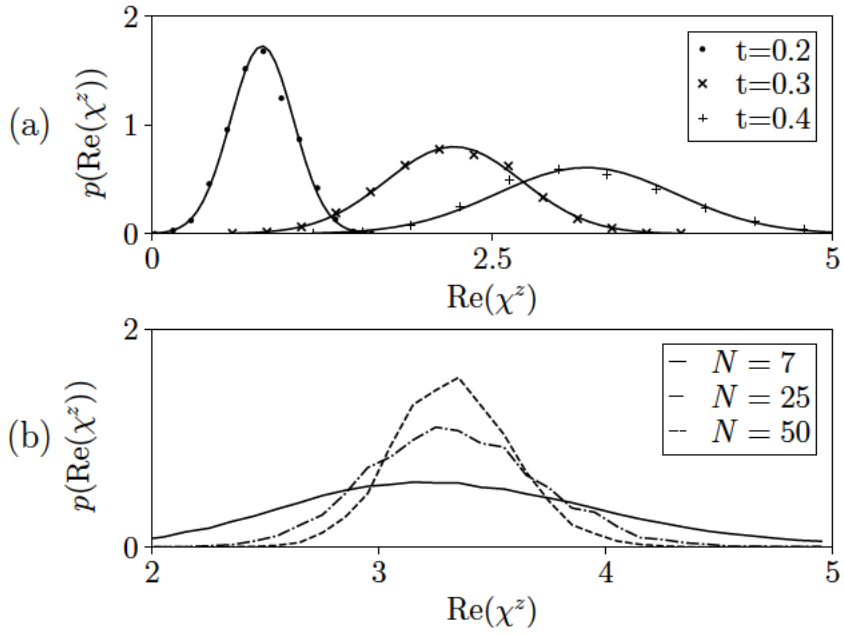

Figure 4.4: Distribution of $\mathrm{Re}(\chi^z)$ for χ^z satisfying the Ising SDEs with $N = 7$ and $\Gamma = 16\,\Gamma_c$. (a) Profile of the distribution at different times. The distribution broadens as the first Loschmidt peak is approached at $t_1 = 0.39$. The observed data are compatible with a Gaussian distribution (the full lines represent the best Gaussian fit at a given t), except in the vicinity of the Loschmidt peak. (b) Profile of the distribution for the same parameters at $t = t_1$, for increasing system sizes N. The distribution can be seen to become more sharply peaked as N increases.

behaviour beyond a particular time scale; we identify this time scale as associated with the presence of the Loschmidt peaks. The observed enhanced fluctuations and non-Gaussian character of the disentangling variables χ^z as the Loschmidt peaks are approached implies that sampling these regions is particularly difficult; indeed, as shown in Fig. 4.5(a), we find that accurately resolving the Loschmidt peaks requires a greater number of simulations compared to the regions in $\lambda(t)$ immediately away from the peak. It is notable that the results obtained from the SDEs accurately reproduce ED even after the peak, where the distribution of the stochastic variable χ^z is less broad and a smaller number of simulation is sufficient to attain convergence. This sampling difficulty is aggravated for larger system sizes, as it can be seen in Fig. 4.5(b): for $N = 21$, 5×10^6 simulations are not sufficient to resolve the Loschmidt peak, while away from the peak the ED result is accurately reproduced.

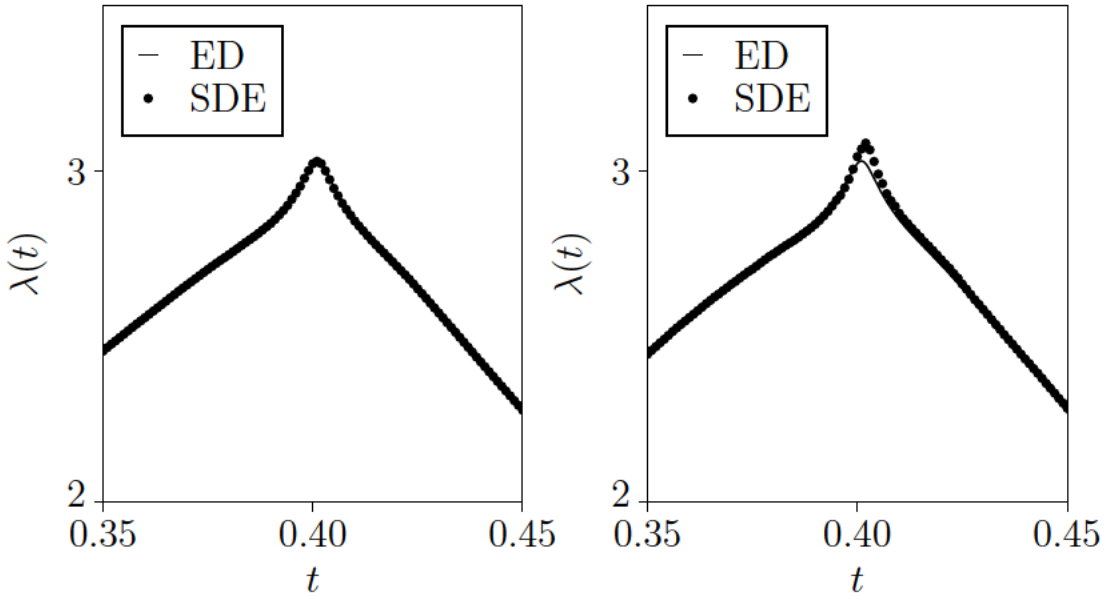

(a)

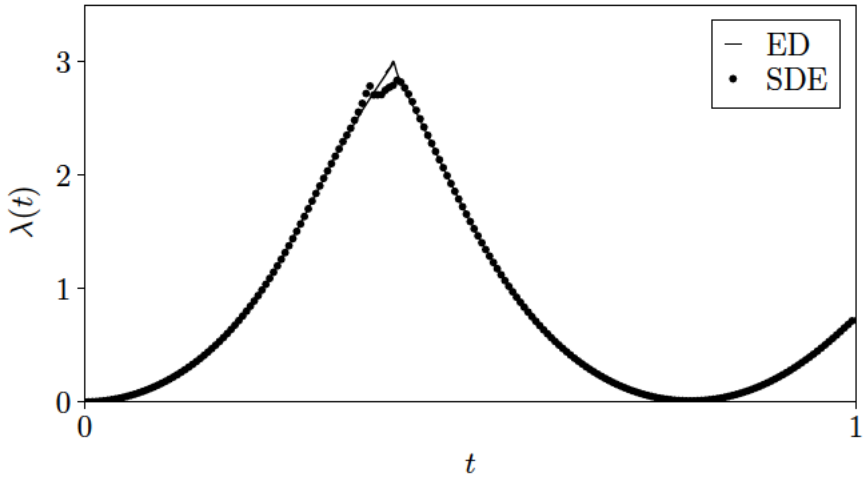

(b)

Figure 4.5: (a) Left panel: close-up of the first Loschmidt peak for a TFIC of size $N = 14$ following a quantum quench from $\Gamma = 0$ to $\Gamma = 16\Gamma_c$. (a) Left panel: Using $n = 3 \times 10^6$ independent trajectories, we are able to accurately reproduce the ED result for $\lambda(t)$. Right panel: results for the same quench, but considering $n = 3 \times 10^5$ trajectories. For this smaller number of simulations, $\lambda(t)$ has converged to the ED result everywhere except in the immediate vicinity of the peak. (b) Loschmidt rate function for the quench considered in Fig. 4.5(a), but for system size $N = 21$. It can be seen that, for $n = 5 \times 10^6$ simulations, the Loschmidt rate function $\lambda(t)$ at the peak has not yet converged to the ED value. This is due to the enhanced fluctuations in the disentangling variables ξ_i^z in the vicinity of the Loschmidt peaks, which grow with the system size. Near the peak, the sampling is insufficient to accurately reproduce the ED result. However, in all other regions of the plot, including times beyond the peak, the result obtained from the SDEs is in good agreement with ED.

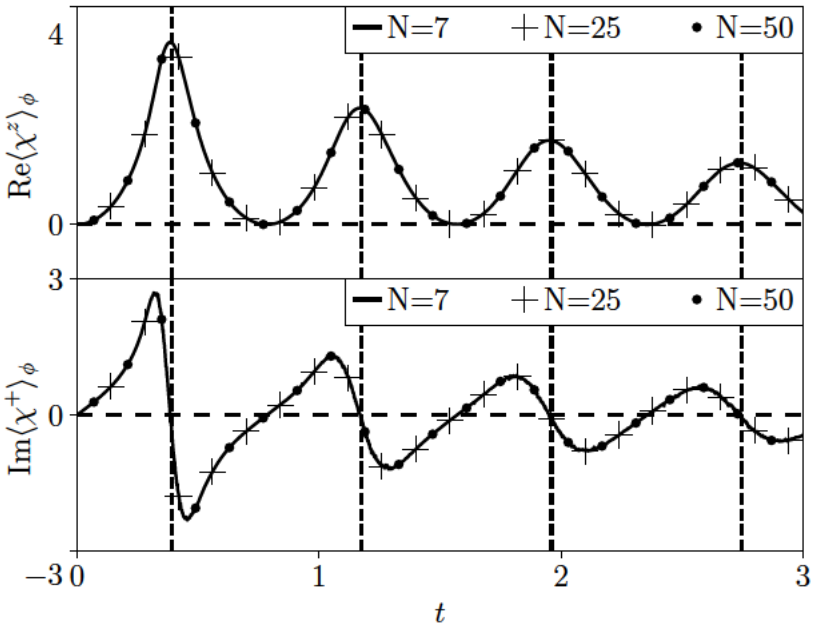

Figure 4.6: Mean of χ^+, χ^z obtained from the distributions shown in Figs. 4.2-4.3. The time when $\mathrm{Re}\langle\chi^z\rangle$ is maximal and $\mathrm{Im}\langle\chi^+\rangle$ goes through zero is strikingly close to the location of the Loschmidt peaks (vertical dashed lines, obtained from ED).

In Fig. 4.6 we plot the means obtained by averaging the distributions in Figs. 4.2-4.3, showing that the zeros of $\mathrm{Im}\langle\chi^+\rangle$ and, as a consequence of Eq. (3.2b), the maxima of $\mathrm{Re}\langle\chi^z\rangle$ occur in proximity to the Loschmidt peaks. $\mathrm{Im}\langle\chi^z\rangle$ and $\mathrm{Re}\langle\chi^+\rangle$ (not shown) are found to be zero at all times, consistently with the identities given in Chapter 3. Notably, the means of the site-averaged stochastic variables χ^+, χ^z are independent of system size, as illustrated in Fig. 4.6 and in Fig. 4.7 by considering the position of the zeros of $\mathrm{Im}\langle\chi^z\rangle$.

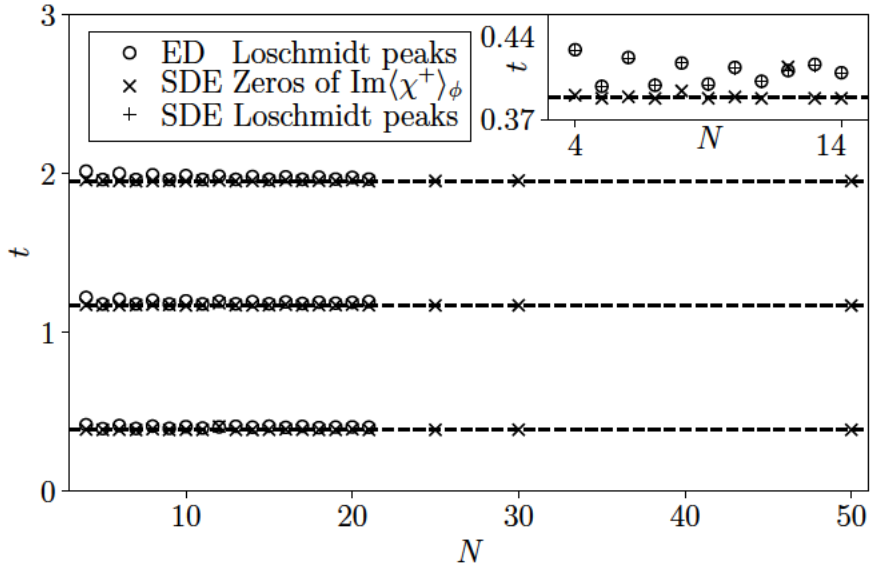

Figure 4.7: Positions of the first 3 zeros in $\mathrm{Im}\langle\chi^+\rangle$ for TFICs of different lengths N, following quantum quenches from $\Gamma = 0$ to $\Gamma = 16\,\Gamma_c$. It can be seen that these positions are independent of system size. The inset shows a close-up of the locations of the first zero, compared to the position of the first Loschmidt peak computed from ED and the SDEs.

It is possible to obtain a lower bound $\lambda_b(t)$ to both the Loschmidt rate function $\lambda(t)$ and $\mathrm{Re}\langle\chi^z(t)\rangle$. By swapping the expectation value and the absolute value in Eq. (4.3), we get

$$\lambda(t) \geq -\frac{2}{N}\log\langle|e^{-\frac{N}{2}\chi^z}|\rangle_\phi \equiv \lambda_b(t), \tag{4.6}$$

while Jensen's inequality implies that

$$\mathrm{Re}\langle\chi^z\rangle = -\frac{2}{N}\log|e^{-\frac{N}{2}\langle\chi^z\rangle}| \geq \lambda_b. \tag{4.7}$$

This is seen in numerical simulations (Fig. 4.8). As $\Gamma \to \infty$, these three quantities all converge to the deterministic result, so the bound $\lambda_b(t)$ can be expected to get increasingly close to $\lambda(t)$ in this limit.

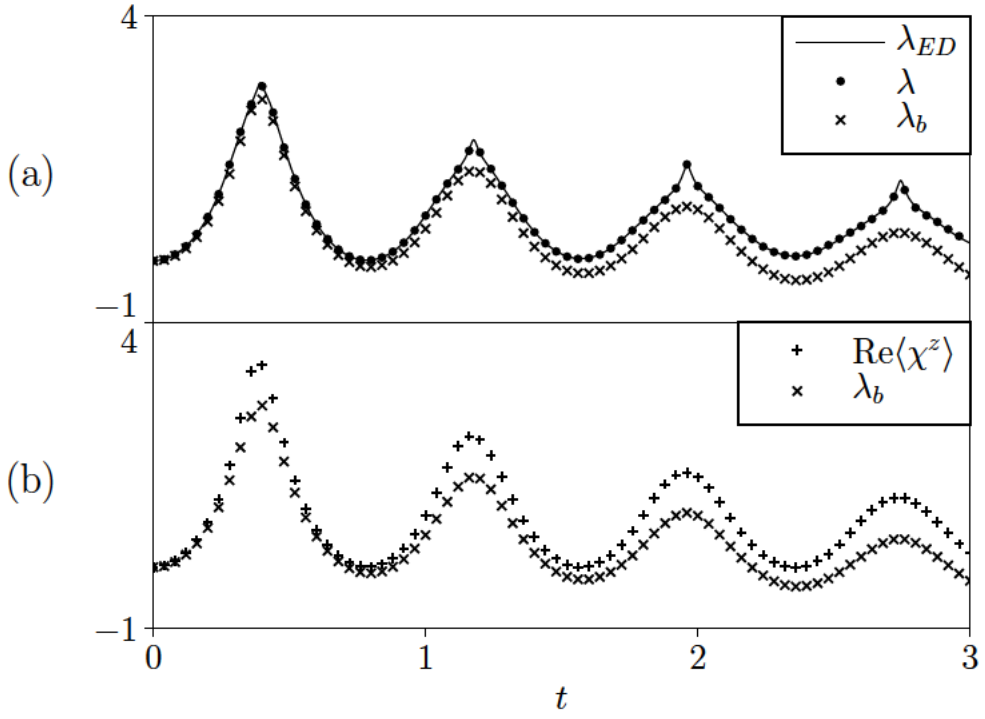

Figure 4.8: Approximations and bounds to the Loschmidt rate function λ for a TFIC of size $N = 7$ following a quantum quench from $\Gamma = 0$ to $\Gamma = 16\,\Gamma_c$. (a) Comparison between the exact Loschmidt rate function $\lambda(t)$, obtained from the SDEs (dots) and from ED (full line), and the bound function $\lambda_b(t)$ defined in Eq. (4.6) obtained from the same numerical simulations. (b) Comparison between the approximation to the Loschmidt rate function given by $\mathrm{Re}(\chi^z)$ and $\lambda_b(t)$. In both cases (a) and (b) it can be seen that the function $\lambda_b(t)$ provides a lower bound.

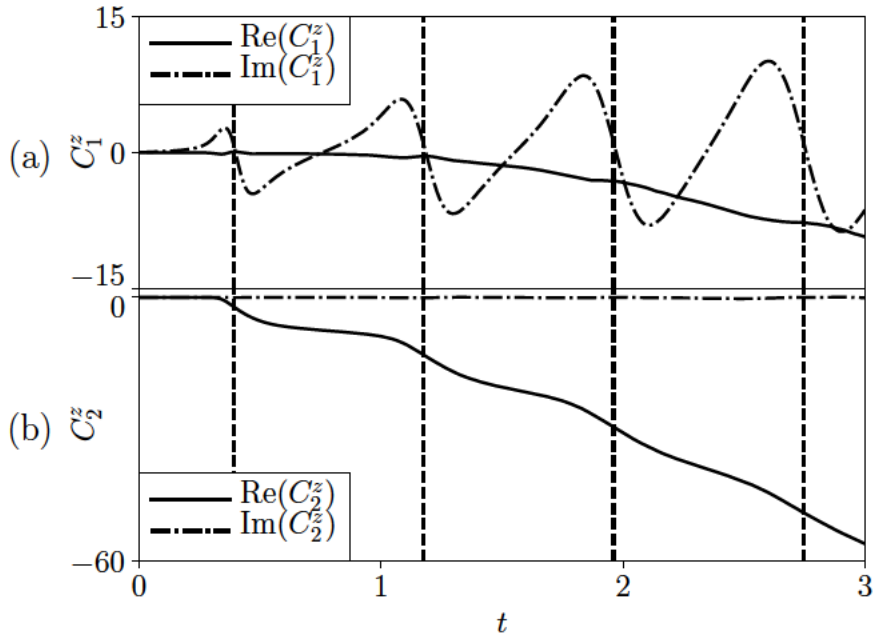

Figure 4.9: Connected correlations of the disentangling variables ξ_i^z, defined in Eq. (4.8), for $N = 10$ and $\Gamma = 16\Gamma_c$. (a) The nearest-neighbour (NN) correlation C_1^z has a monotonically decreasing real part and an oscillating imaginary part, with zeros occurring in the vicinity of the Loschmidt peaks (dashed lines, obtained from ED). (b) The next-to-nearest-neighbour (NNN) correlation C_2^z has a vanishing imaginary part. The real part of C_2^z decreases monotonically, and shows more pronounced growth in proximity of the Loschmidt peaks.

The presence of DQPTs is also reflected in the correlations between classical variables at different sites. Let us consider the site-averaged connected correlations between the classical variables, given by

$$C_l^a \equiv \sum_{i=1}^{N} \left(\langle \xi_i^a \xi_{i+l}^a \rangle - \langle \xi_i^a \rangle \langle \xi_{i+l}^a \rangle \right). \tag{4.8}$$

From numerical simulations, we find that the real part of the nearest-neighbour (NN) connected correlation C_1^z decreases smoothly over time, but its imaginary part shows oscillating behaviour within an increasing envelope, and in particular has zeros in the vicinity of the Loschmidt positions, as shown in Fig. 4.9(a). Next-to-nearest neighbour (NNN) correlations C_2^z have vanishing imaginary part, whilst the real part decreases most pronouncedly in the vicinity of the Loschmidt times; this can be seen in Fig. 4.9(b). Figure 4.10 shows an analogous analysis for C_l^+. It can be seen that NN correlations

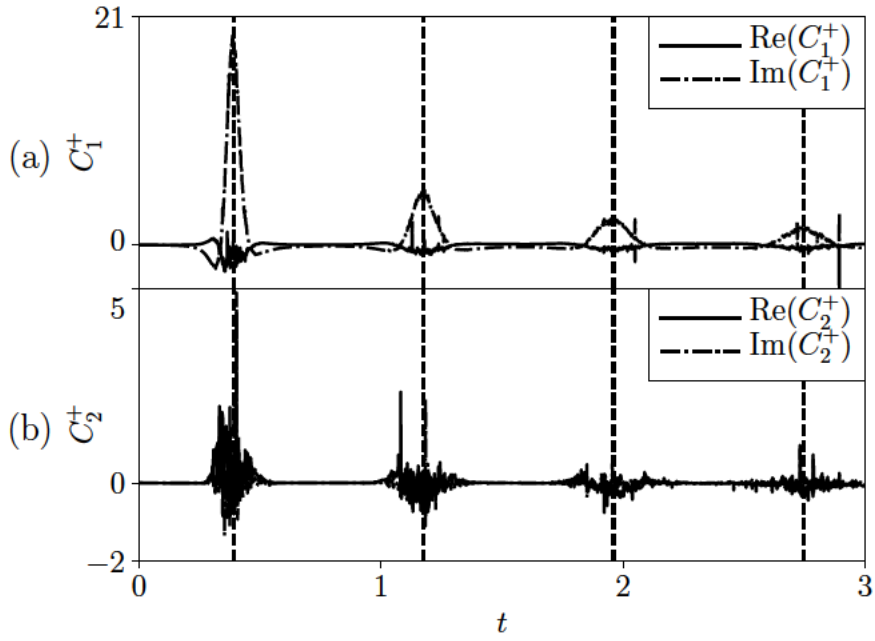

Figure 4.10: Connected correlations of the disentangling variables ξ_i^+ for $N = 10$, time evolved with $\Gamma = 16\Gamma_c$. (a) NN correlations are small except in the vicinity of the Loschmidt peaks, when their imaginary part exhibits a sharp peak. (b) NNN correlations vanish everywhere, but show enhanced fluctuations as the Loschmidt peaks are approached.

take small values everywhere except in the vicinity of the Loschmidt peaks, where the imaginary part peaks. NNN correlations appear to vanish at all times, but display large fluctuations in the vicinity of the Loschmidt peaks. The behaviour of C_l^z, C_l^+ with $l > 2$ (not shown) follows the same pattern as the NNN correlations ($l = 2$) but in a less pronounced fashion. This is due to the form of the nearest-neighbour interaction matrix $\mathcal{J}_{ij}$. When computing the stochastic equations of motion for the correlations C_l^a according to the Ito chain rule, the form of $\mathcal{J}_{ij}$ implies that the Ito drift, given by the last term in Eq. (2.30), is only non-zero for C_1^z, C_1^+, so that this equation is qualitatively different from all others. The behaviour of the stochastic variables that we investigated for the TFIC persists for the 2D quantum Ising model, described by the Hamiltonian

$$\hat{H}_{\mathrm{I}}^{\mathrm{2D}} = -J \sum_{\langle \mathbf{ij} \rangle} \hat{S}_{\mathbf{i}}^z \hat{S}_{\mathbf{j}}^z - \Gamma \sum_{\mathbf{i}} \hat{S}_{\mathbf{i}}^x. \tag{4.9}$$

This is illustrated in Fig. 4.11 by considering (a) $\lambda(t)$ and (b) the distribution of $\mathrm{Re}(\chi^z)$ following a quench across the quantum critical point at $\Gamma_c^{\mathrm{2D}} = 1.523J$ [152, 153]. The

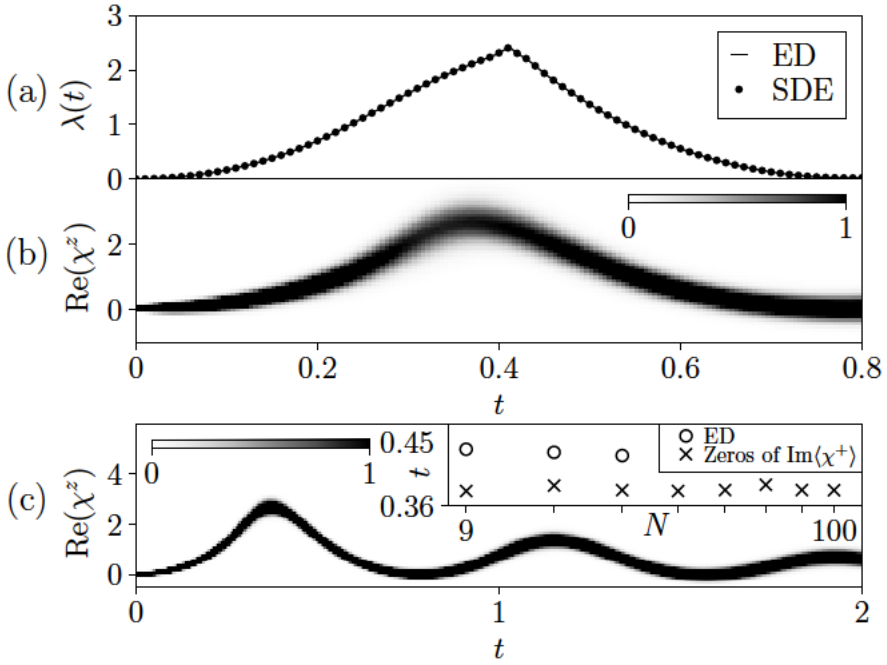

Figure 4.11: (a) Loschmidt rate function $\lambda(t)$ for the 2D quantum Ising model following a quantum quench from the initial state $|\Downarrow\rangle$ with $\Gamma = 0$ to $\Gamma = 8J$, across the quantum critical point at $\Gamma_c^{2D} = 1.523J$. We compare the result obtained from ED and from the numerical solution of the SDEs, using 2.5×10^7 trajectories. The presence of the Loschmidt peak affects the behaviour of the stochastic variables even in 2D. (b) The corresponding distribution of $\mathrm{Re}\,\chi^z(t)$ for a 3×5 system shows smooth maxima and increased fluctuations in the vicinity of the Loschmidt peaks. (c) Time-evolution of $\mathrm{Re}\,\chi^z(t)$ for a 10×10 spin system showing additional turning points. Inset: comparison of the exact times of the first Loschmidt peak (circles) and zeros of $\mathrm{Im}\langle\chi^+\rangle$ (crosses) for square lattices of size up to $N = 100$ spins.

stochastic expressions for the Loschmidt amplitude in the 2D case generalises from Eq. (4.3) by extending the product to all lattice sites. The stochastic variables can be tracked to large system sizes, as shown in panel (c) for a 10×10 system. Finally, we consider how the observed phenomenology in the stochastic variables varies with Γ, corresponding to the transverse field of the final Hamiltonian in a quantum quench. We find that the features described in this Section are robust for deep quenches. As the post-quench transverse field Γ is decreased towards the quantum critical value Γ_c, an increasing lag develops between the location of the DQPTs in $\lambda(t)$ and the features observed in the classical variables. We illustrate this in Fig. 4.12 by considering the location of the zeros of $\mathrm{Im}\langle\chi^+\rangle$. For $\Gamma < \Gamma_c$, the features in the classical variables get pushed to late times and no longer correspond to DQPTs. However, while the direct correspondence

between the Loschmidt dynamics and signatures in the stochastic variables is lost for small Γ, the stochastic method remains valid also in this parameter range, as we demonstrate in Section 4.2 where we consider other quantum quench settings.

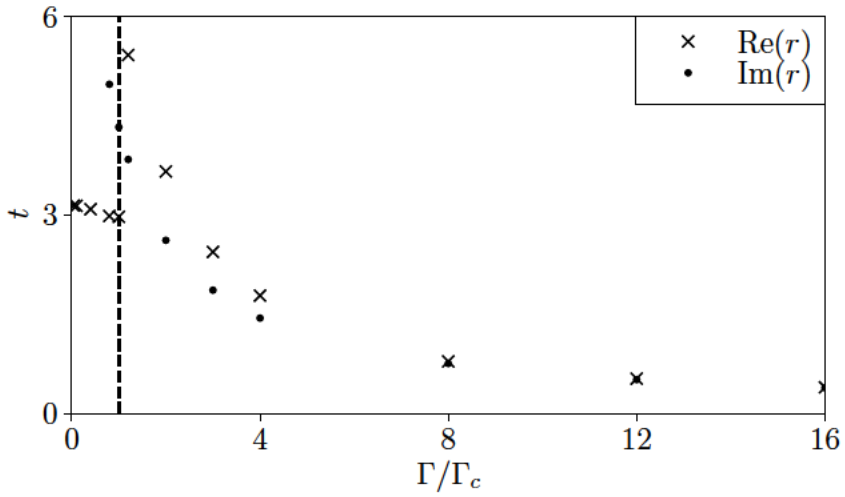

Figure 4.12: Times t_λ of the first maximum in the Loschmidt rate function, obtained from ED, and times t_{χ^+} of the first zero of $\mathrm{Im}\langle\chi^+\rangle$, for a TFIC of size $N = 7$. We consider quantum quenches from $\Gamma = 0$ to different values of Γ. For $\Gamma \gg \Gamma_c$, the two times are nearly coincident. As Γ is reduced and approaches Γ_c (dashed line), an increasing lag between t_λ and t_{χ^+} develops. For $\Gamma \leq \Gamma_c$, a secondary maximum in the Loschmidt rate function develops at a smaller value of t, which is however known to remain smooth in the thermodynamic limit. In this parameter range, the zeros of $\mathrm{Im}\langle\chi^+\rangle$ persist but get pushed to late times. While the direct correspondence between the Loschmidt peaks and features in the disentangling values breaks down for small $\Gamma \lesssim \Gamma_c$, the Loschmidt rate function $\lambda(t)$ is still correctly reproduced when averaging the appropriate stochastic function, as shown in Fig. 4.13.

In this Section, we have considered the Loschmidt amplitude $A(t)$ following a quantum quench from the ferromagnetic initial state $|\Downarrow\rangle$ to large values of Γ, across the quantum critical point at $\Gamma_c = J/2$. We found that the peaks of $\lambda(t)$ are accompanied by signatures in the classical variables, including enhanced fluctuations and the breakdown of Gaussianity. The stochastic approach can also be used to calculate the Loschmidt rate function for different quantum quenches; this will be discussed in the next Section.

4.2 Other Quantum Quenches

In the previous Sections, we have focussed on quantum quenches initiated from the FM ground state $|\Downarrow\rangle$ and across the quantum critical point $\Gamma = J/2$. However, the stochastic method is not restricted to this parameter range. We demonstrate this in Fig. 4.13 by considering a quench within the FM phase. For $\Gamma < \Gamma_c$, the system undergoes non-trivial quantum dynamics, mirrored in the time evolution of the stochastic variables, but the Loschmidt rate function gives a very small signal; this result is accurately reproduced using the stochastic approach.

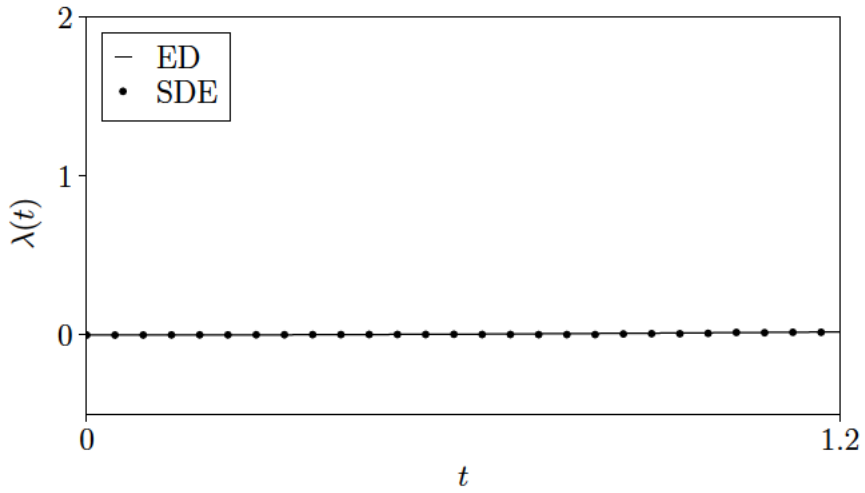

Figure 4.13: Loschmidt rate function $\lambda(t)$ for a TFIC with $N = 10$ spins following a quantum quench from the ferromagnetic ground state with $\Gamma = 0$ to $\Gamma = \Gamma_c/2$, within the ferromagnetic phase. For quenches within the critical point, the Loschmidt rate function takes small values and no DQPTs occur. However, both the system and the SDEs (3.2) undergo non-trivial time evolution. As found for quenches across the critical point, the stochastic method is in good agreement with ED also in this parameter range. The SDE result was obtained from 10^5 trajectories. The error bars, obtained from 5 batches of 2×10^4 simulations each, are not visible on the scale of the plot. No trajectories were found to diverge in these simulations.

We can also compute the Loschmidt rate function $\lambda(t)$ for quantum quenches initialised in other initial states $|\psi_0\rangle \neq |\Downarrow\rangle$. For each $|\psi_0\rangle$, $\lambda(t)$ can be obtained by numerically solving the Ising SDEs and averaging the appropriate function, corresponding to a special case of Eq. (2.37). We begin by considering a system initialised in the paramagnetic ground state $|\psi_0\rangle = \otimes_i |\rightarrow\rangle_i$ with $\Gamma = \infty$, where all the spins are aligned in the x direction.

For this initial state, the Loschmidt amplitude $A(t)$ is given by

$$A(t) = \left\langle \prod_i^N \frac{1}{2} e^{-\frac{\xi_i^z}{2}} \left(\xi_i^- \xi_i^+ + \xi_i^- + \xi_i^+ + e^{\xi_i^z} + 1 \right) \right\rangle_\phi . \tag{4.10}$$

Again, the SDE approach is in good agreement with the ED result, as illustrated in Fig. 4.14. For this quantum quench, we find enhanced fluctuations in the vicinity of the maximum of $\lambda(t)$, corresponding to a DQPT in the thermodynamic limit.

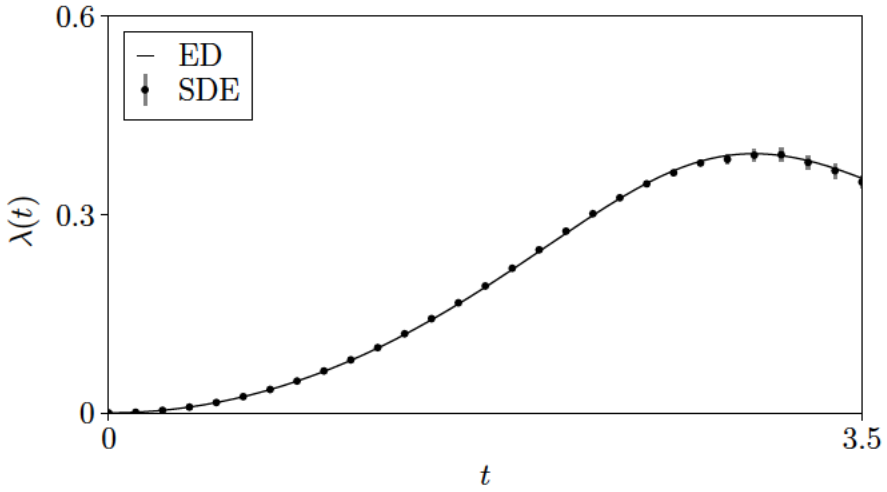

Figure 4.14: Loschmidt rate function $\lambda(t)$ for a TFIC with $N = 5$ spins following a quantum quench from the paramagnetic ground state with $\Gamma = \infty$ to $\Gamma = \Gamma_c/4$, deep into the ferromagnetic phase. The SDE result, computed from 10^5 trajectories, is in good agreement with ED. The bars show the standard error over the means of 5 batches of 2×10^4 simulations. At the stopping time, no trajectories were found to have diverged.

The stochastic approach can also handle non-uniform initial conditions. To illustrate this, we consider the initial state with a single spin pointing up and all others pointing down,

$$|\psi_0\rangle = |\uparrow\rangle_1 \otimes |\downarrow\rangle_2 \cdots \otimes |\downarrow\rangle_N,$$

and a domain-wall initial state,

$$|\psi_0\rangle = |\uparrow\rangle_1 \otimes \ldots |\uparrow\rangle_{N/2} \otimes |\downarrow\rangle_{N/2+1} \cdots \otimes |\downarrow\rangle_N.$$

For these initial conditions, the Loschmidt amplitude is given by

$$A(t) = \left\langle \prod_{j=1}^{M} \left(e^{\xi_j^z} + \xi_j^- \xi_j^+ \right) \prod_{i=1}^{N} e^{-\frac{\xi_i^z(t)}{2}} \right\rangle_{\phi}, \tag{4.11}$$

with $M = 1$ for a single spin flip and $M = N/2$ for domain wall initial conditions. Figures. 4.15 and 4.16 show the Loschmidt rate function for these two cases, calculated by numerically averaging the appropriate form of Eq. (4.11).

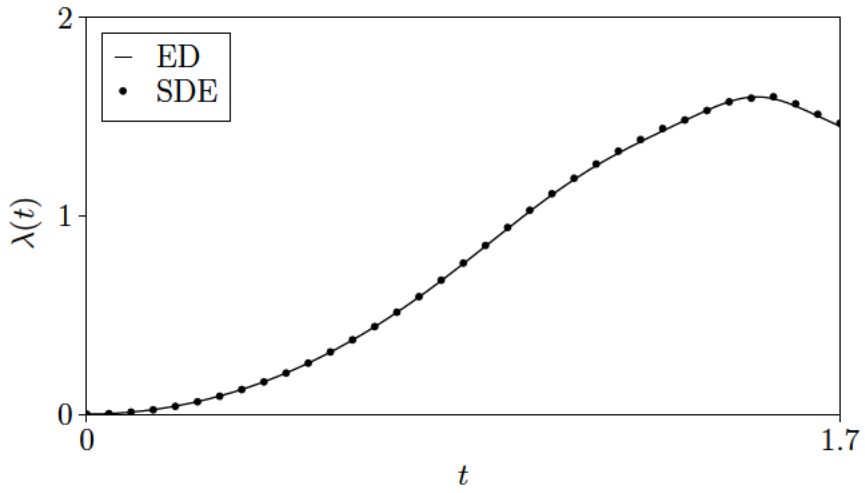

Figure 4.15: Loschmidt rate function $\lambda(t)$ for a 5-site TFIC following a quantum quench from an initial state with a single spin up and all others down, where at $t = 0$ we apply a transverse field $\Gamma = 4\Gamma_c$. The SDE result, computed from 10^5 trajectories, shows good agreement with ED. Less than 0.1% of trajectories were found to be divergent at the stopping time.

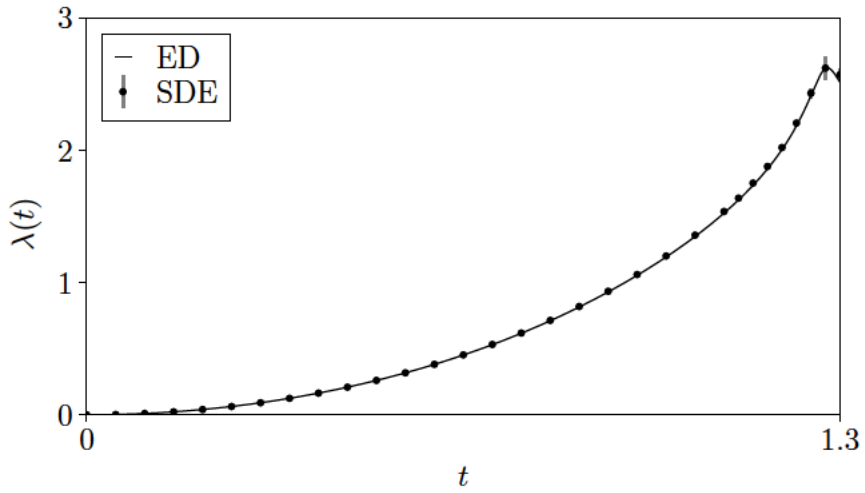

Figure 4.16: Loschmidt rate function $\lambda(t)$ for a TFIC with $N = 5$ spins where 3 consecutive spins are initially pointing up and the remaining ones down, following the application of a transverse field $\Gamma = 4\Gamma_c$ at $t = 0$. The SDE result, obtained from 10^5 trajectories, is again in agreement with ED. Enhanced error bars are visible in the vicinity of the peak, signalling the presence of stronger fluctuations. The bars were computed by considering the standard error of $\lambda(t)$ obtained from 5 batches of 2×10^4 simulations each. Less than 0.1% of trajectories were divergent at the stopping time.

4.3 Local Observables

Going beyond the Loschmidt amplitude, the stochastic approach can also be applied to compute other physical observables. We begin by considering the magnetisation

$$m(t) = \sum_i m_i(t) = \sum_i \langle \hat{S}_i^z(t) \rangle. \tag{4.12}$$

We will consider quantum quenches from the symmetry-broken ferromagnetic ground state $|\psi_0\rangle = |\Downarrow\rangle$. In this case, the time evolution of the magnetisation has two qualitatively different regimes depending on the value of the final transverse field Γ. While for $\Gamma \leq \Gamma_c$ the magnetisation relaxes to 0 without changing sign, for $\Gamma > \Gamma_c$ the magnetisation oscillates within an exponentially decaying envelope and crosses the line $m = 0$ multiple times [57]. For quenches initialised in a paramagnetic ground state there is no ensuing magnetisation dynamics because of the $\mathbb{Z}_2$ symmetry of the model, so this case was not considered here. For our choice of initial conditions, the magnetisation $m_i(t) = \langle \hat{S}_i^z(t) \rangle$ at site i is given by

the expression

$$m_i(t) = -\frac{1}{2}\left\langle e^{-\frac{\xi_i^z+(\tilde{\xi}_i^z)^*}{2}}(1-\xi_i^+(\tilde{\xi}^+)_i^*)\prod_{j\neq i} e^{-\frac{\xi_j^z+(\tilde{\xi}_j^z)^*}{2}}(1+\xi_j^+(\tilde{\xi}_j^+)^*)\right\rangle_{\phi,\tilde{\phi}}, \tag{4.13}$$

where the subscripts $\phi, \tilde{\phi}$ denote averaging with respect to two sets of Hubbard-Stratonovich fields, introduced to decouple the forwards and backwards time-evolution operators as discussed in Chapter 3. Because of the presence of two sets of noises, the magnetisation is affected by stronger fluctuations. However, by numerically averaging Eq. (4.13) where the disentangling variables evolve according to the Ising SDEs (3.2), we are able to correctly reproduce the results of ED for small system sizes, as shown in Fig. 4.17.

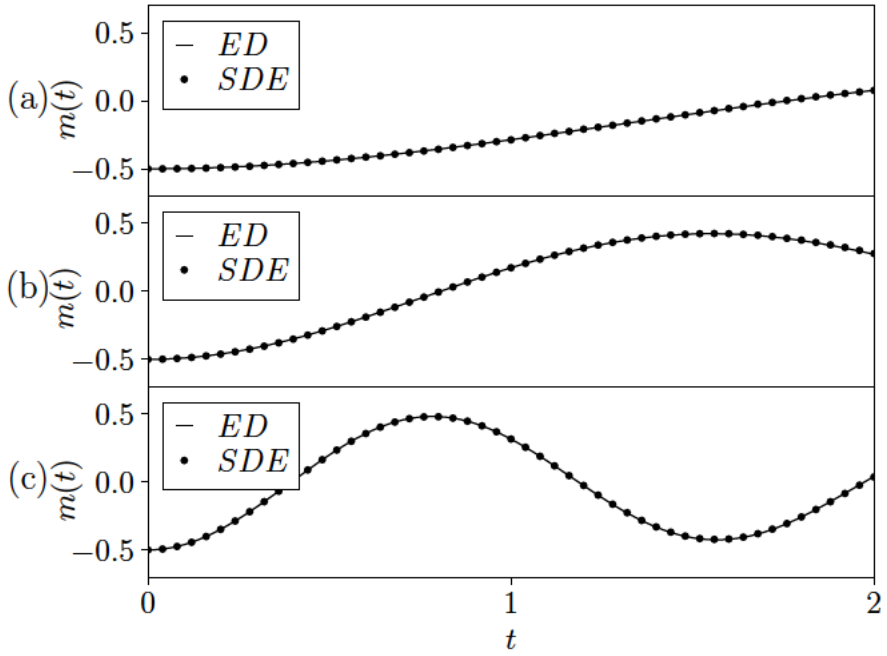

Figure 4.17: Magnetisation $m(t)$ for a TFIC with $N = 3$ following a quantum quench from an initial FM ground state with all spins down to (a) $\Gamma = 2\Gamma_c$, (b) $\Gamma = 4\Gamma_c$, (c) $\Gamma = 8\Gamma_c$. The SDE results were obtained from $n = 4 \times 10^5$ independent trajectories. In all cases we find good agreement with ED. The error bars, obtained from batches of 10^5 simulations each, are not visible on the scale of the plot. The divergent trajectories were $\sim 0.1\%$ of the total number at the stopping time.

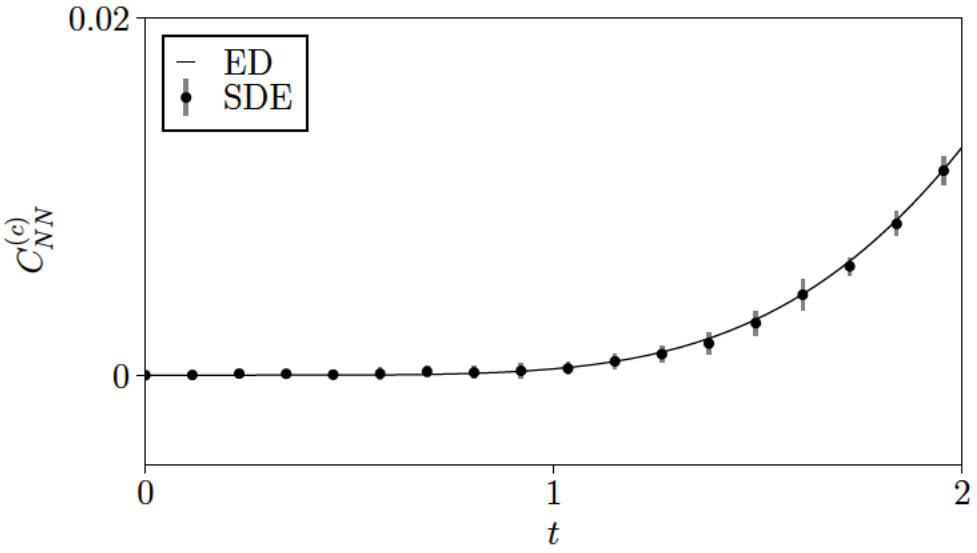

Figure 4.18: Nearest-neighbours connected longitudinal correlations for a TFIC with $N = 3$ spins following a quantum quench from the FM ground state with all spins down to $\Gamma = \Gamma_c$. The SDE result was obtained from 4×10^6 independent simulations. The bars show the standard error over the averages obtained by dividing the data set into 5 independent batches of 8×10^5 simulations each. The average obtained from all trajectories (dots) is in good agreement with the ED result. No trajectories were divergent at the stopping time.

The stochastic method can also be used to computed 2-point functions. We illustrate this by considering the equal-time nearest-neighbour connected correlations defined by

$$C^{(c)}_{NN} = \sum_i \left(\langle \hat{S}^z_i \hat{S}^z_{i+1} \rangle - \langle \hat{S}^z_i \rangle \langle \hat{S}^z_{i+1} \rangle \right). \tag{4.14}$$

In the stochastic language, the correlator of the z-component of the spin at sites i and j, $C_{ij}(t) = \langle \hat{S}^z_i(t) \hat{S}^z_j(t) \rangle$, can be obtained from the building blocks in Eqs. (B.63-B.64). For the initial state $|\Downarrow\rangle$, one has

$$C_{ij}(t) = \frac{1}{4} \left\langle e^{-\frac{\xi^z_i + (\tilde{\xi}^z_i)^*}{2}} (1 - \xi^+_i (\tilde{\xi}^+)^*_i) e^{-\frac{\xi^z_j + (\tilde{\xi}^z_j)^*}{2}} (1 - \xi^+_j (\tilde{\xi}^+)^*_j) \prod_{k \neq i,j} e^{-\frac{\xi^z_k + (\tilde{\xi}^z_k)^*}{2}} (1 + \xi^+_k (\tilde{\xi}^+_k)^*) \right\rangle_{\phi, \tilde{\phi}}. \tag{4.15}$$

Using this formula, we can compute $C^{(c)}_{NN}(t)$ from the stochastic approach; we find good agreement with exact diagonalisation, as shown in Fig. 4.18 considering a quench to the quantum critical point. We notice that, relative to $C^{(c)}_{NN}$, the fluctuations obtained by considering the standard deviation over independent batches of simulations are stronger

compared to other observables for batches of the same size; see Figs. 4.14-4.16. In spite of this, the average over all trajectories is in good agreement with exact diagonalisation.

4.4 Other Models

By considering the integrable case of the transverse field Ising chain, we have shown how the time evolution of different observables for different initial conditions can be computed by numerically averaging the appropriate function over realisations of the Ising SDEs.

The stochastic approach can similarly be applied to other systems. As an example, we consider the quantum Ising model in the presence of an integrability-breaking longitudinal field h. This model is described by the Hamiltonian

$$\hat{H}_{NI} = -J\sum_{i}^{N}\hat{S}_i^z\hat{S}_{i+1}^z - \Gamma\sum_{i}^{N}\hat{S}_i^x + h\sum_{i}^{N}\hat{S}_i^z. \tag{4.16}$$

In the stochastic formalism, Eq. (4.16) corresponds to the SDEs

$$-i\dot{\xi}_i^+ = \frac{\Gamma}{2}(1-{\xi_i^+}^2) - h\xi_i^+ + \xi_i^+\sum_j O_{ij}\phi_j, \tag{4.17a}$$

$$-i\dot{\xi}_i^z = -h - \Gamma\xi_i^+ + \sum_j O_{ij}\phi_j, \tag{4.17b}$$

$$-i\dot{\xi}_i^- = \frac{\Gamma}{2}\exp\xi_i^z. \tag{4.17c}$$

As discussed in Chapter 2, the Loschmidt amplitude for given initial conditions has the same model-independent stochastic formulation for all spin-$1/2$ systems. For the initial state $|\Downarrow\rangle$, this is given by Eq. (4.3). The specific model (4.16) is encoded in the time evolution of the stochastic variables, determined by the SDEs (4.17). Again, we find good agreement between the result obtained from direct simulation of the SDEs and exact diagonalisation, as shown in Fig. 4.19. Similarly, the magnetisation is given by the same stochastic expression as in the integrable case. The results obtained by solving the SDEs (4.17) accurately reproduce ED for this non-integrable model, as illustrated in Fig. 4.20.

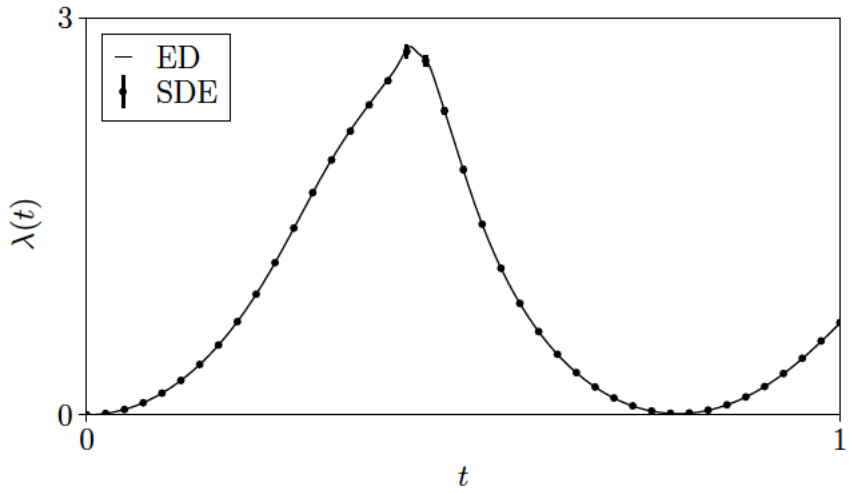

Figure 4.19: Loschmidt rate function for a 1D Ising chain with $N = 10$ spins in the presence of a longitudinal field $h = J$, following a quantum quench from the FM ground state $|\Downarrow\rangle$ to $\Gamma = 8J$. The result obtained by averaging 10^5 trajectories is in good agreement with ED. The error bars, estimated from 5 batches of 2×10^4 trajectories, are only visible in the vicinity of the peak. Less than 1% of trajectories were divergent at the stopping time.

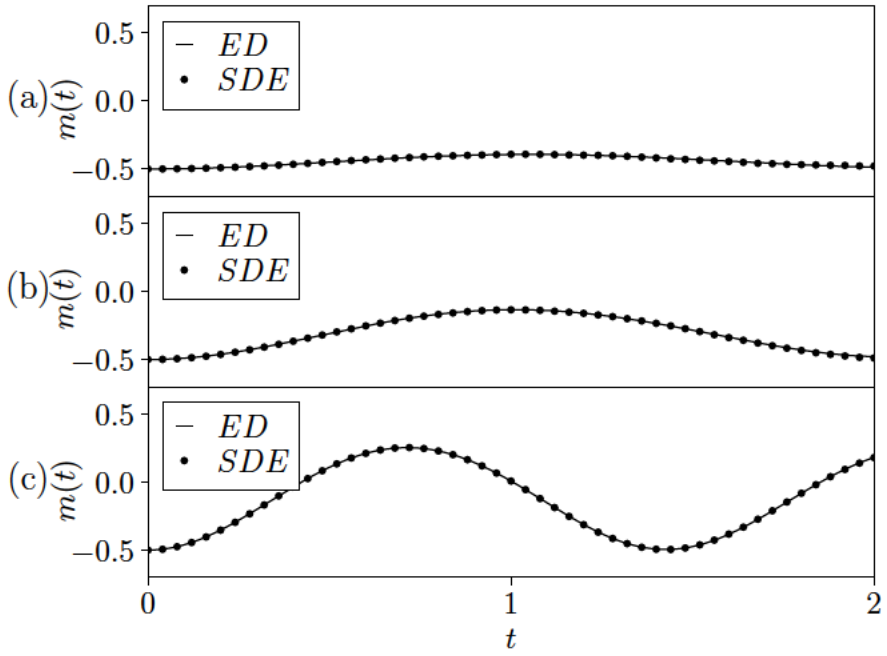

Figure 4.20: Magnetisation $m(t)$ for a 1D quantum Ising chain with $N = 3$ and a constant longitudinal field $h = 2J$. We consider quantum quenches from the FM ground state with all spins down to (a) $\Gamma = J$, (b) $\Gamma = 2J$, (c) $\Gamma = 4J$. The SDE results were obtained from $n = 6 \times 10^5$ simulations, with $< 0.1\%$ of diverging trajectories at the stopping time. The error bars, obtained from batches of 10^5 simulations each, are not visible on the scale of the plot. We find good agreement with ED for all the parameters considered.

The stochastic approach can be also be applied to compute observables in higher dimensions, such as the Loschmidt amplitude for the 2D quantum Ising model which we discussed in Section 4.1 in relation to DQPTs. The stochastic expressions for observables in $D > 1$ straightforwardly generalise from the 1D case, as explained in Chapter 2. For instance, the magnetisation is given by Eq. (4.13) where the product runs over all sites of the two dimensional lattice. Again, as shown in Fig. 4.21, we find excellent agreement between the SDE result and ED for small system sizes.

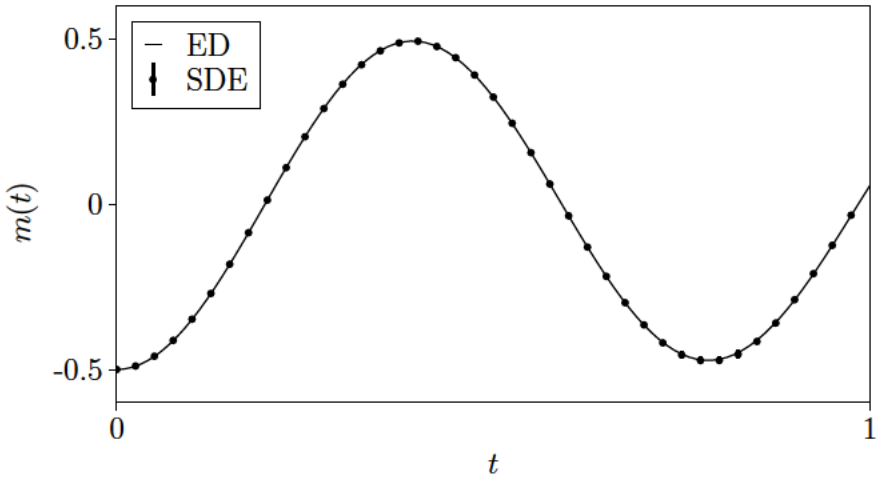

Figure 4.21: Magnetisation $m(t)$ for a 2×3 quantum Ising model following a quantum quench from the FM ground state with all spins down to $\Gamma = 8J$. The SDE results, computed by averaging 5×10^5 trajectories, are in excellent agreement with ED. Less than 1% of the trajectories were divergent at the stopping time.

A key feature of the stochastic approach is that it does not require the underlying system to be translationally invariant. To demonstrate this, we consider a transverse-field Ising chain where the transverse fields Γ_i are now different at the various sites. In particular, we choose the fields Γ_i to be uniformly distributed random variables in the interval $[-\bar{\Gamma}, \bar{\Gamma}]$ with an overall disorder strength $\bar{\Gamma}$. This model has been recently considered in the context of many-body localisation [154], introduced in Chapter 1. For site-dependent transverse

fields, the Ising SDEs straightforwardly generalise to

$$-i\dot{\xi}_i^+ = \frac{\Gamma_i}{2}(1-\xi_i^{+2}) + \xi_i^+ \sum_j O_{ij}\phi_j, \tag{4.18a}$$

$$-i\dot{\xi}_i^z = -\Gamma_i \xi_i^+ + \sum_j O_{ij}\phi_j, \tag{4.18b}$$

$$-i\dot{\xi}_i^- = \frac{\Gamma_i}{2}\exp\xi_i^z. \tag{4.18c}$$

In Fig. 4.22, we show a comparison between the results obtained from averaging the SDEs and from ED for a specific realization of $\{\Gamma_i\}$, finding good agreement.

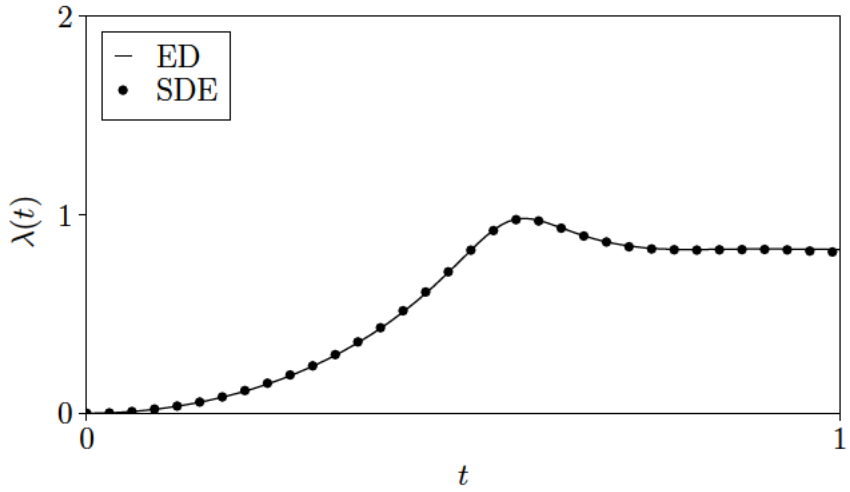

Figure 4.22: Loschmidt rate function $\lambda(t)$ for a particular realization of the TFIC with $N = 5$ and site-dependent transverse fields Γ_i. The system is initialised in the FM ground state with all spins down. The fields Γ_i are randomly drawn from a uniform distribution in the range $[-12J, 12J]$. The SDE result, obtained from 10^5 runs with $< 1\%$ divergent trajectories at the stopping time, is in good agreement with exact diagonalisation.

In this Chapter, for the purposes of benchmarking the stochastic method and showing its general applicability, we have computed the Loschmidt echo in a wide range of quantum quench settings. For the TFIC, we have considered various initial conditions and values of the final transverse field. We have also broken integrability by including a longitudinal field or considering higher dimensions, and broken the translational invariance of the Ising Hamiltonian by considering random site-dependent magnetic fields. In all cases, we found good agreement between the SDE result and exact diagonalisation for small system sizes. However, if we run the same simulations to later times, we eventually reach a time scale were fluctuations in the stochastic variables become dominant. This is illustrated in

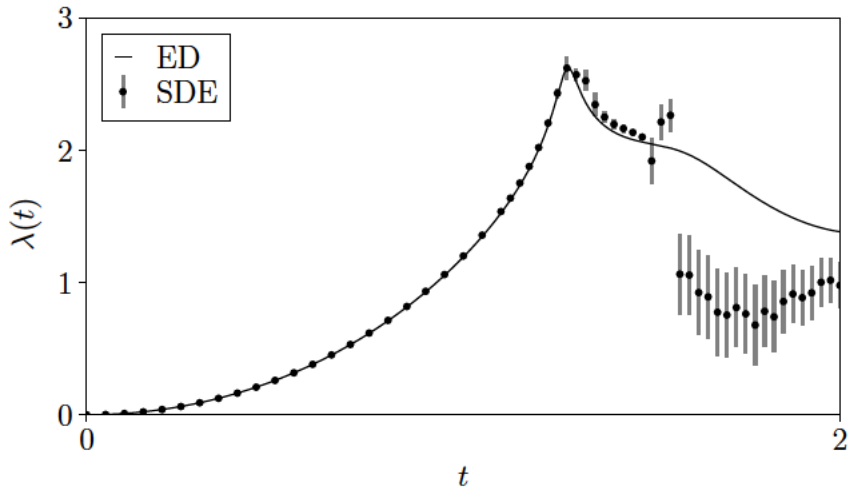

Figure 4.23: Loschmidt rate function $\lambda(t)$ for the same quantum quench considered in Fig. 4.16 but extending the simulation to a longer stopping time. The bars show the standard deviation $\sigma = \sqrt{n_b^{-1}\sum_{i=1}^{n_b}(\lambda - \lambda_i)^2}$ over the means $\lambda_i(t)$ obtained by splitting the data set into $n_b = 5$ independent batches of simulations, where $\lambda = n_b^{-1}\sum_{i=1}^{n_b}\lambda_i$; it can be seen that for $t \gtrsim 1.3$ enhanced fluctuations hamper the convergence of the average of the SDEs to the ED result.

Fig. 4.23 by considering the same quench as in Fig. 4.16 but extending the simulation time. The onset of strong fluctuations is the main numerical difficulty associated with the direct numerical solution of the SDEs. In Section 4.5 we will examine this issue, investigating the behaviour of fluctuations and the numerical performance of this approach.

4.5 Numerical Performance

In the previous Sections, we have shown that the stochastic approach is in principle applicable to a wide range of problems, as confirmed by comparison to exact diagonalisation. Our results were obtained by direct solution of the real time SDEs by means of the Euler scheme discussed in Appendix D.1, discarding divergent trajectories whose number increases with the transverse field Γ. For the purposes of benchmarking this method, we focussed on short times and small systems. We now turn to examining the limitations of the approach followed in this Chapter, studying the extent of fluctuations as a function of time and system size for the TFIC.

We begin our analysis by defining the *breakdown time* for a given set of numerical simulations in terms of an error threshold. Considering the Loschmidt rate function $\lambda(t)$, we observe that breakdown times defined in terms of absolute errors are approximately independent of the transverse field Γ. However, the magnitude of $\lambda(t)$ itself is strongly dependent on Γ, so that breakdown times obtained by considering the error relative to $\lambda(t)$ increase for large Γ. We then consider how fluctuations grow in time and with the system size N. We find that the growth of the error in $\lambda(t)$ can be approximated by a power law in t and N. Because of the definition $\lambda(t) = -\log|A(t)|^2/N$, this implies that fluctuations in the quantity $A(t)$ computed from the SDEs show approximately exponential growth with t and N. We obtain qualitatively similar results for the magnetisation. However, in this case, fluctuations are enhanced by the presence of two sets of Hubbard-Stratonovich fields in order to disentangle two time evolution operators; this makes it more difficult to obtain quantitative estimates. Finally, we comment on the computational cost of our approach. For a given number of simulations, the computation time grows only linearly with the time t of the physical problem and with the system size N, so that neither of these parameters provides an intrinsic computational bottleneck.

A given set of simulations is characterised by two computational parameters, namely the number of runs n and the discretisation time step Δt, and by the physical parameters of the problem. For the transverse field Ising chain, the latter are given by the number of spins N and the magnitude of the transverse field Γ, as we set the interaction strength $J = 1$ and measure time in units of $1/J$. When performing numerical simulations, the discretisation time step Δt is typically chosen empirically; a standard procedure is progressively reducing Δt until the result of the numerical calculation does not change up to a desired precision [143]. For the non-linear SDEs we consider here, when using the Euler scheme Δt must

also be sufficiently small that on average only a small fraction of trajectories diverge at the stopping time, as discussed in Appendix D.2.

4.5.1 Breakdown Time

We first consider the performance of our approach in computing the Loschmidt rate function. Here we focus on quantum quenches from the ferromagnetic ground state with all spins down $|\psi_0\rangle = |\Downarrow\rangle$; the qualitative behaviour we find is however rather general. We begin our analysis by directly inspecting $\lambda(t)$ obtained from the SDEs (3.2). We consider a range of quantum quenches from the FM ground state to different transverse field values Γ, considering a TFIC of size $N = 10$. Figure 4.24 shows results for quenches within and up to the quantum critical point, whilst Fig. 4.25 considers quenches across the QCP. We see that in all cases the result obtained from the SDEs is in good agreement with ED for short times, while the effect of fluctuations becomes pronounced at late times. Since peaks get pushed to earlier times for large Γ, for this parameter range it is possible to resolve one or more peaks before the eventual breakdown, as can be seen in Figs. 4.25(b-d).

In order to assess the performance of the current implementation of the stochastic method in a more quantitative way for a given set of physical and computational parameters, one needs to consider appropriate measures of performance.
A first possibility is to investigate the *breakdown time* t_b of a given simulation, defined as the earliest time-step when the error becomes greater than a given error threshold $\mathcal{E}$:

$$t_b = \min_i \{t_i\},\ t_i : \Delta O(t_i) \geq \mathcal{E}. \tag{4.19}$$

We begin by considering the absolute error $\Delta O(t) = |O_{SDE}(t) - O_{ED}(t)|$, where $O_{SDE}(t)$ and $O_{ED}(t)$ are the results obtained from the SDEs and ED respectively. The threshold $\mathcal{E}$ has no natural or obvious definition and can be chosen freely; in Fig. 4.26 we consider different values of $\mathcal{E}$. Our results show that the breakdown time is broadly independent of the transverse field Γ.

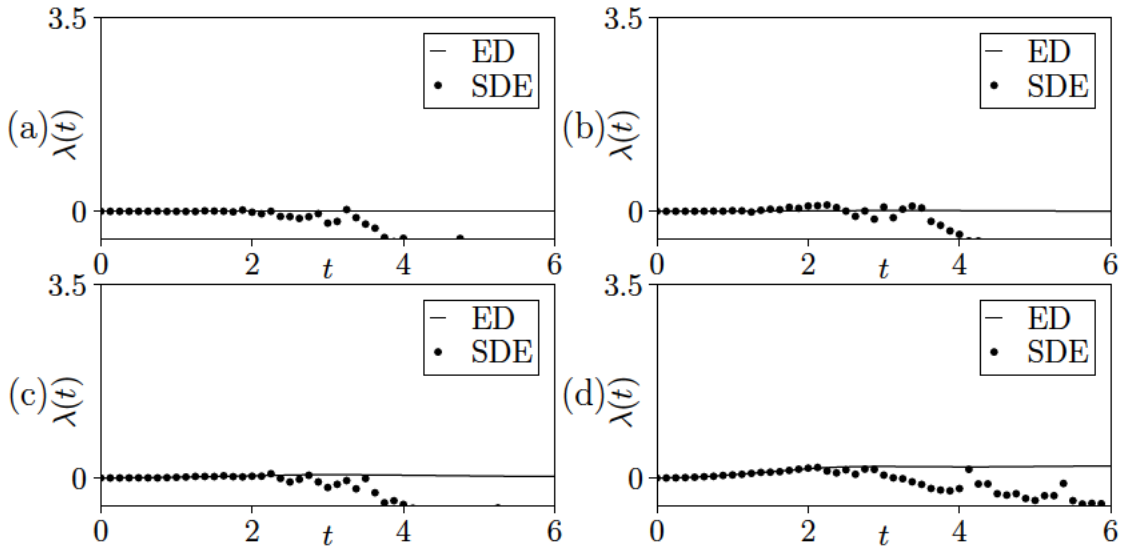

Figure 4.24: Loschmidt rate function $\lambda(t)$ for a TFIC of size $N = 10$ initialised in the ferromagnetic ground state, for final transverse field (a) $\Gamma = 0$, (b) $\Gamma = \Gamma_c/4$, (c) $\Gamma = \Gamma_c/2$, (d) $\Gamma = \Gamma_c$. The SDEs results were obtained from 10^5 simulations. In all cases, we find good agreement with ED at short times, whilst at late times the result obtained from the SDEs is affected by enhanced fluctuations.

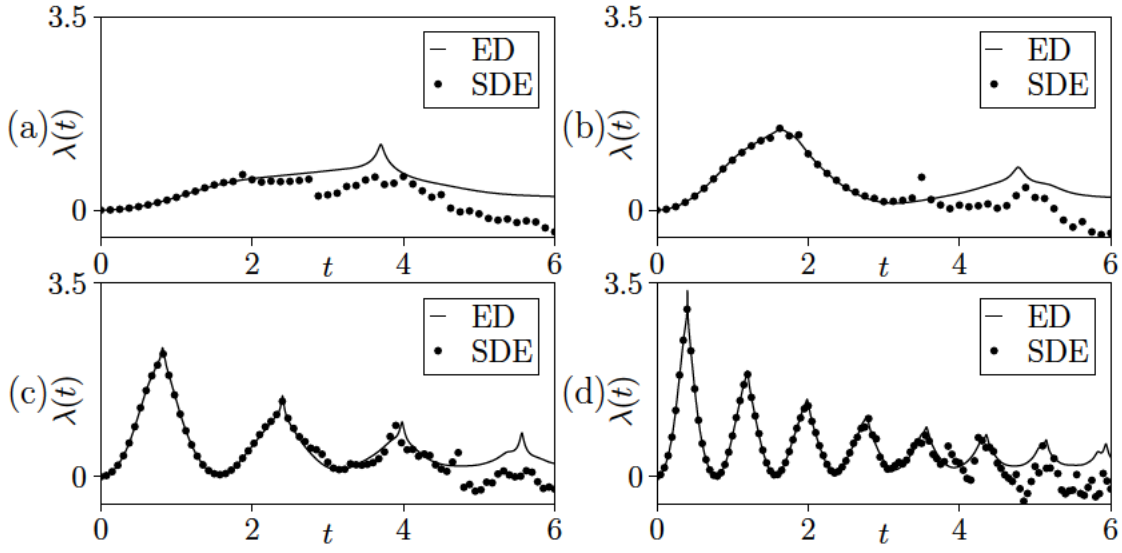

Figure 4.25: Loschmidt rate function $\lambda(t)$ for a TFIC of size $N = 10$ initialised in the ferromagnetic ground state, for final transverse field (a) $\Gamma = 2\Gamma_c$, (b) $\Gamma = 4\Gamma_c$, (c) $\Gamma = 8\Gamma_c$, (d) $\Gamma = 16\Gamma_c$. The SDEs results were obtained from 10^5 simulations. Similarly to the case of quenches within the FM phase, we find that the stochastic approach agrees well with ED at short times while it is affected by enhanced fluctuations at late times.

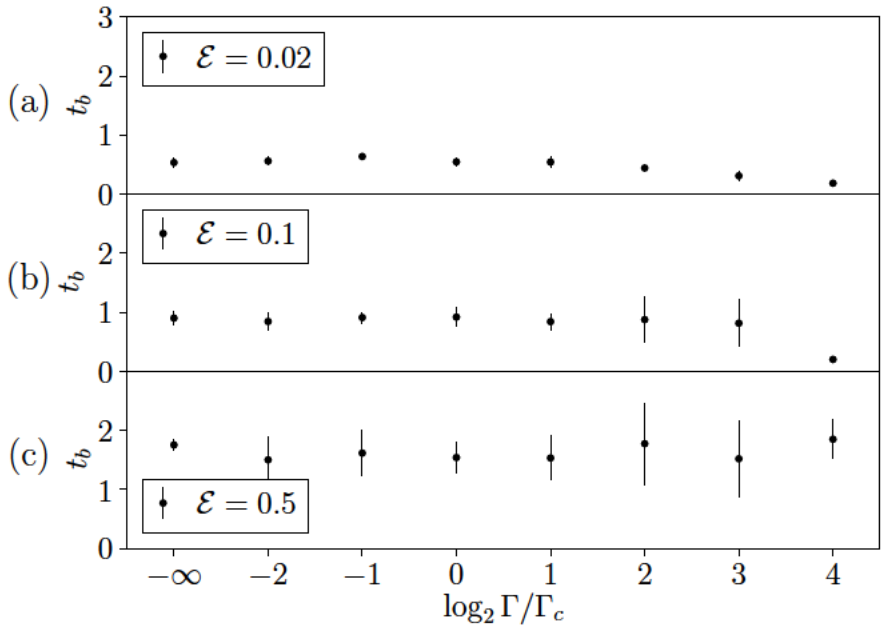

Figure 4.26: Breakdown time for the Loschmidt rate function following a quantum quench from the FM state $|\Downarrow\rangle$ to different values of Γ. We consider a TFIC of size $N = 10$ and use the same data set as in Figs. 4.24-4.25. The breakdown times, as defined in Eq. (4.19), were obtained by imposing different thresholds $\mathcal{E}$ on the absolute error $\Delta O(t)$. The behaviour of t_b appears to be rather independent of Γ for a given choice of ε. The bars show the standard deviation over the breakdown times obtained by splitting the data set into 5 batches of independent simulations.

As the magnitude of the Loschmidt rate function $\lambda(t)$ varies significantly as a function of Γ, is it also useful to consider the relative error, defined as

$$\Delta O_N \equiv \frac{|O_{SDE}(t) - O_{ED}(t)|}{\max_t O_{ED}}. \tag{4.20}$$

We normalise the error by $\max_t O(t)$, which sets the overall scale, since naively normalising by $\Delta O(t)$ by $O(t)$ for each t would give excessive weight to small errors at times when $O(t)$ is also small. In Fig. 4.27 we show the breakdown times as obtained by considering the normalised error. For small Γ, the Loschmidt rate function also takes small values, so that the relative fluctuations are large. The extreme case is for a "quench" to $\Gamma = 0$, i.e. the purely classical case; in this case, one has $\lambda(t) = 0$ at all times even though from the point of view of the stochastic equations there is still a time evolution, and fluctuations do become manifest at late times, as can be seen in Fig. 4.24(a). In this case, the normalised

definition gives $t_b = 0$. The breakdown time is seen to increase as a function of Γ, as fluctuations remain of comparable size while $\max_t \lambda(t)$ grows. Our findings appears to be relatively insensitive to the specific choice of the threshold $\mathcal{E}$ if this is sufficiently large.

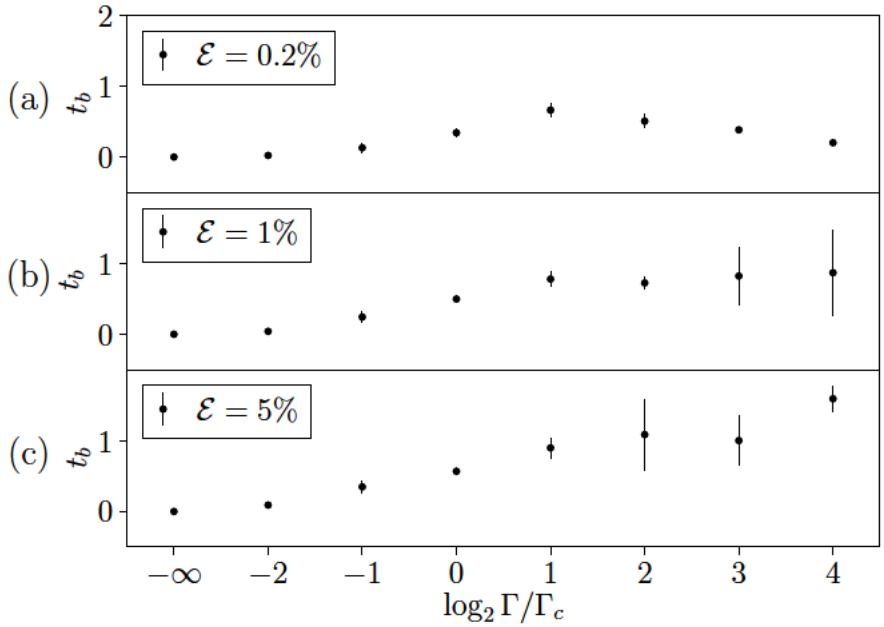

Figure 4.27: Breakdown times for the Loschmidt rate function following a quantum quench from the FM state to different values of Γ. We consider a TFIC of size $N = 10$, using the same data set as in Figs. 4.24-4.25. The breakdown time was obtained by imposing different thresholds $\mathcal{E}$ on the normalised error defined by Eq. (4.20), with bars showing the standard deviation over the breakdown times for 5 batches of independent simulations. For small Γ, we get very small values of t_b because of the choice of normalisation. The breakdown time is seen to increase with Γ. This trend appears to be independent of the precise choice of threshold, provided that this is large enough.

4.5.2 Growth of Fluctuations

To further develop a quantitative understanding of the performance of our numerical implementation, we investigate how the error grows as a function of time and of the system size. By considering different possibilities, it was found that the best fits to simple functions are obtained when considering the *integrated absolute error*, defined as

$$\Delta\lambda_{int}(t) = \int_0^t |\lambda_{SDE}(t) - \lambda_{ED}(t)|. \tag{4.21}$$

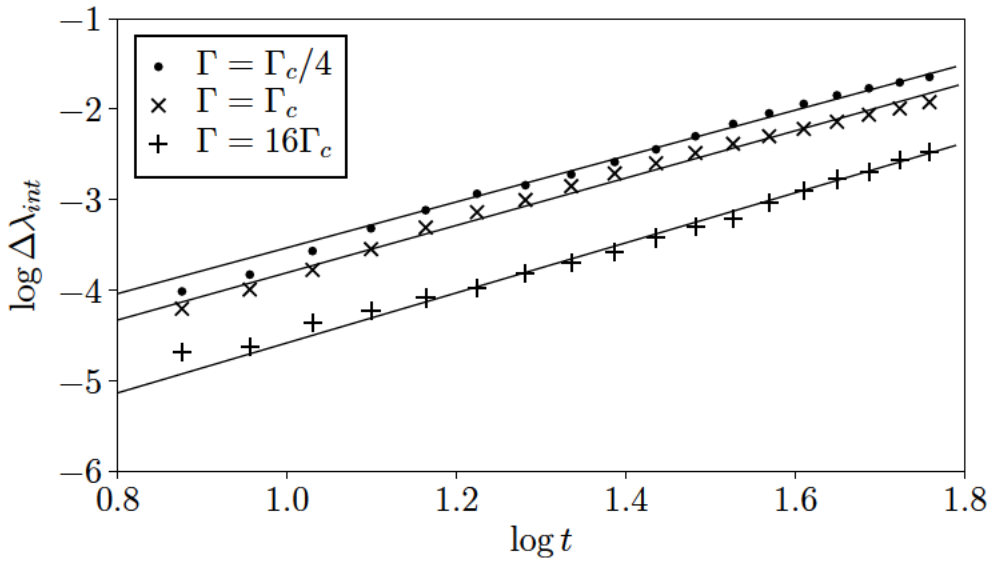

Figure 4.28: Growth of the integrated time error defined in Eq. (4.21) for different values of the transverse field Γ. As visible on the log-log plot, this is well described across a wide parameter range by the power law in Eq. (4.22) with $b \approx 2.5 \pm 0.5$. This is further discussed in Fig. 4.30.

In particular, as shown in Fig. 4.28, the time growth of $\Delta\lambda_{int}(t)$ for fixed parameters was found to be best described by the power law

$$\Delta\lambda_{int}(t) = at^b, \tag{4.22}$$

were a and b are parameters obtained from fitting the data. Notably, unlike breakdown times, this measure of performance is free from the issues of normalisation and defining thresholds. Having chosen a suitable way to assess the performance of the method, we now discuss the results of the analysis of the data set of Figs. 4.24-4.25. As a testing ground, we focus on quantum quenches initiating in the ferromagnetic ground state, but similar behaviour is found when considering other initial conditions.

Figure 4.30 shows the parameters a, b defined in Eq. (4.22). For each quench and system size, the left column (panels (i), (iii), (v)) shows results obtained by fitting a power law to $\Delta\lambda_{int}$ obtained from the full data set, consisting of 10^5 trajectories. In the right column, (panels (ii), (iv), (vi)), we show results obtained by splitting the data set in $n_b = 5$ batches of $n = 20000$ simulations each and fitting each individually to a power law, in order to obtain error bars. This also allows us to assess how the estimate for a, b varies when increasing the number of runs. We find that the time dependence of the integrated absolute error (4.21) is well approximated by a power law, as demonstrated by the large value of

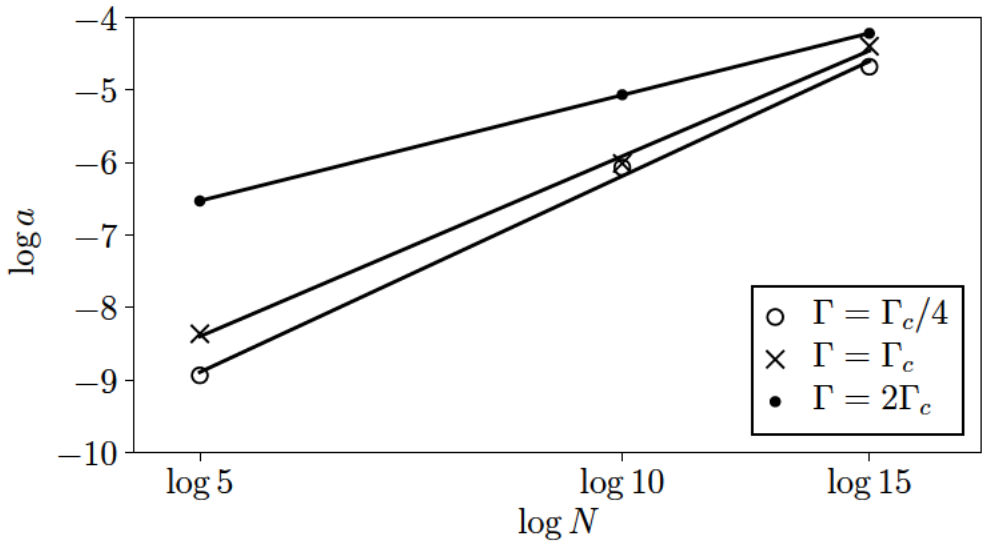

Figure 4.29: Dependence of the parameter a on the system size N for different values of the transverse field Γ. By plotting $a(N)$ on a logarithmic scale, we find that this dependence can be approximated by a power law with $\zeta \approx 3$ across the parameter range $0 \lesssim \Gamma \lesssim 2\Gamma_c$.

the coefficient of determination R^2, where $R^2 = 1$ indicates a perfect match between the observed data and the fitted curve. The power b consistently takes values in the range $2 \lesssim b \lesssim 3$ for all quenches considered and for all system sizes. From this data, it is not possible to conclusively determine a trend for the effect on Γ on a and b, but this effect appears to be small. The exponents obtained by averaging over the full data set (left column) are not significantly different from the average of the parameters obtained from batches each containing $1/5$ of the simulations (right column); this shows that a five-fold increase in the number of runs has a small effect on the overall behaviour of the error, and is likely to be reflected at the level of the prefactor a.

The increasing system size N is also reflected in the growth of the proportionality constant a. In order to estimate this dependence, for fixed Γ we parameterise $a(N)$ as

$$a(N) = \gamma(\Gamma) \times N^{\zeta(\Gamma)}. \tag{4.23}$$

Figure 4.29 shows the result of this fit for different quantum quenches. We find that for $0 \lesssim \Gamma \lesssim 2\Gamma_c$, the growth of a with N is approximately given by the power law in Eq. (4.23) with $\langle \zeta(\Gamma) \rangle \sim 3 \pm 1$.

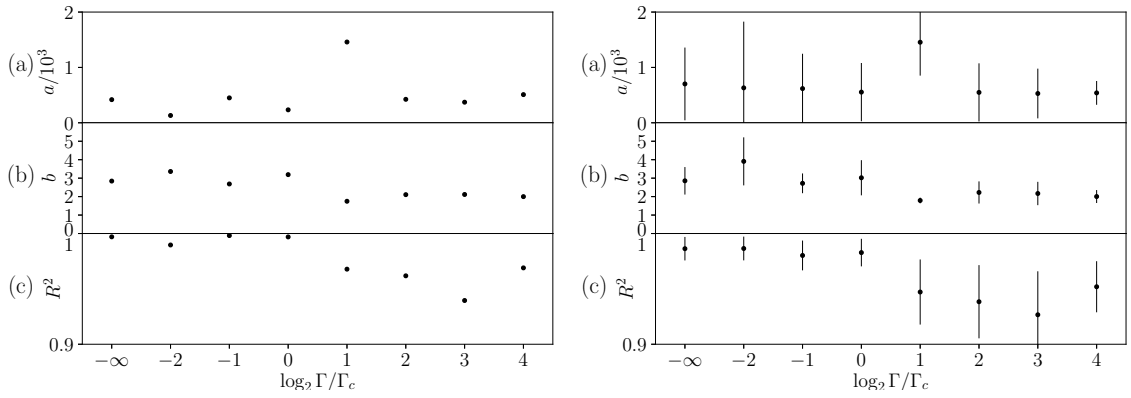

(i) $N = 5$, $n = 10^5$.

(ii) $N = 5$, $n_b = 5$, $n = 2 \times 10^4$.

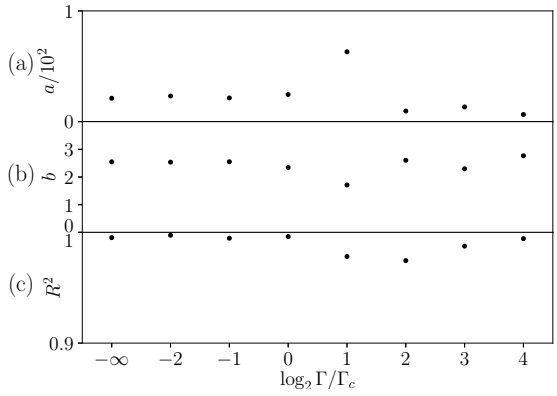

(iii) $N = 10$, $n = 10^5$.

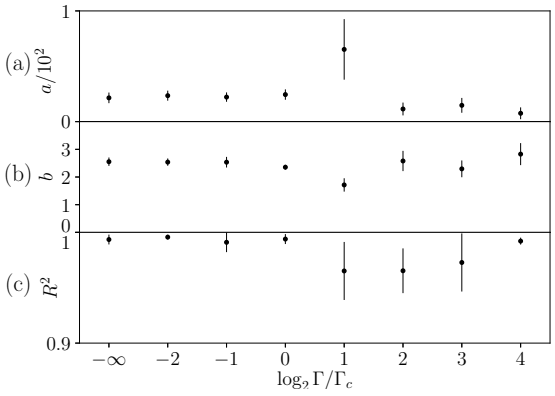

(iv) $N = 10$, $n_b = 5$, $n = 2 \times 10^4$.

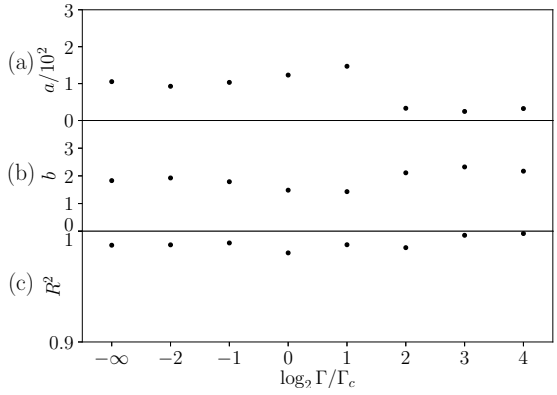

(v) $N = 15$, $n = 10^5$.

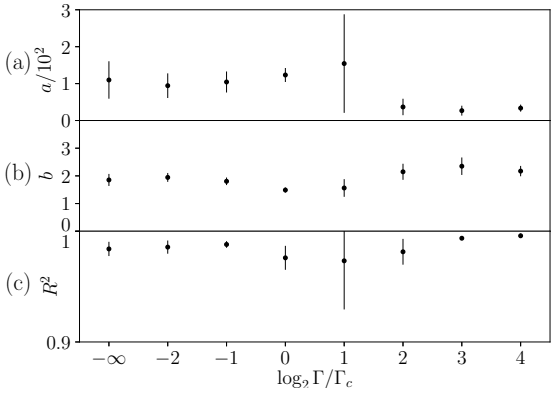

(vi) $N = 15$, $n_b = 5$, $n = 2 \times 10^4$.

Figure 4.30: Parameters describing the growth of the integrated error in the Loschmidt rate function for quantum quenches from the FM initial state. We consider system sizes (i,ii) $N = 5$, (iii,iv) $N = 10$, (v,vi) $N = 15$ and different final transverse fields Γ. For each figure, we show the parameters (a) a (b) b and (c) the value of the coefficient of determination R^2 obtained from fitting $\Delta\lambda_{int} = at^b$, where the integrated absolute error $\Delta\lambda_{int}$ is defined in Eq. (4.21). Left-hand side panels: fit parameters obtained from $n = 10^5$ independent trajectories for each value of Γ. Right-hand side panels: average parameters obtained from individually fitting $n_b = 5$ batches of 2×10^4 independent simulations each; to illustrate the fluctuations in these quantities, the bars show the corresponding standard deviations, computed as in Fig. 4.23. The integrated error in the Loschmidt rate function is found to consistently grow in time with a power $b \approx 2.5 \pm 0.5$, while the system size mostly affects the proportionality constant a. The power b is broadly independent of Γ, whereas a appears to mildly decrease with Γ, as seen for the larger systems where a shows smaller fluctuations.

Summarising our findings, we estimate that the integrated error in the Loschmidt rate function $\lambda(t)$ grows approximately as a power law with respect to time and the system size,

$$\Delta\lambda_{int}(t) \sim N^{\zeta} t^{b}, \tag{4.24}$$

with $b \approx 2.5$, $\zeta \approx 3$. For the initial state we considered, the rate function is computed as

$$\lambda(t) \equiv -\frac{1}{N}\log L(t) = -\frac{1}{N}\log\left|\langle\prod_{i}^{N}\exp\left(-\frac{\xi_i^z(t)}{2}\right)\rangle_{\phi}\right|^2. \tag{4.25}$$

Hence, we can estimate that fluctuations in the stochastic average $\left\langle \prod_i^N \exp\left(-\frac{\xi_i^z(t)}{2}\right)\right\rangle_{\phi}$ grow as $\sim e^{\bar{a}N^{\zeta+1}t^b}$, with a parameter $\bar{a}$ which depends on the specific quench parameters. This implies that it rapidly becomes prohibitive with this approach to access late times or large system sizes. Our analysis suggests that an increase in the number of runs or the choice of a favourable parameter range is mostly reflected at the level of the parameter $\bar{a}$ and does not significantly affect the overall behaviour. The exponents we obtained in this analysis of our numerical implementation are to be regarded as estimates, but the evidence we found, obtained from a large number of independent simulations and over a wide parameter space, is broadly consistent with exponential or faster growth of the fluctuations with time and with the system size. Because of the extent of the fluctuations, a more detailed quantitative study would require a large amount of additional data, so it was not pursued further here.

A similar analysis can be repeated to assess the performance of our numerical approach in computing the magnetisation. As shown in Appendix D.3, fluctuations for this observable are significantly stronger than for the Loschmidt rate function, due to the presence of two sets of Hubbard-Stratonovich fields (Chapter 2). This makes it difficult to provide quantitative estimates; our observations are however compatible with exponential growth in time parameterised as

$$\Delta m(t) \propto e^{ut}, \tag{4.26}$$

where $u \approx 1$ across all the range of Γ. Comparable results were obtained across system sizes; however, because of the large fluctuations, we were not able to identify a clear pattern concerning the effect of N. The effect of fluctuations is seen to be even stronger for correlation functions, as anticipated in Section 4.3. We did not attempt to estimate the time dependence of the error in this case, but we expect a qualitatively similar behaviour to the magnetisation because of the similarity of the corresponding stochastic expressions.

The growth of fluctuations in time can be expected, due to the form of the noise action (2.20): rescaling $t' = st_f$, we can express it as

$$S[\phi] = i \int_0^1 \frac{1}{2t_f} \sum_{i=1}^{N} \phi_i(s)\phi_i(s)\mathrm{d}s, \tag{4.27}$$

so that the final time t_f plays the role of a variance for the noises. Further intuition can be obtained by considering the fully classical case with $\Gamma = 0$. In this case, the Loschmidt amplitude is given by $A(t) = \langle f(t) \rangle_\phi$ with

$$f(t) = \exp\left(\frac{(i+1)}{2} \sqrt{NJ} W_1(t) \right), \tag{4.28}$$

where $W_1(t)$ is a standard Wiener process, as obtained from the Ising SDEs (3.2) and from the properties of the O_{ij} matrix reported in Appendix B.2. We can compute the variance of f using the Ito chain rule (2.30). Since f is complex, its variance is given by $\langle |f|^2 \rangle_\phi - |\langle f \rangle_\phi|^2 = e^{NJt/2} - 1$. This grows exponentially with time and the system size, consistently with our observations. Away from the classical limit, a non-zero transverse field Γ introduces an interplay between the stochastic process ϕ and the deterministic dynamics driven by Γ. The competition between these effects may lead to a more complex behaviour of the fluctuations.

4.5.3 Computational Cost

To conclude this discussion of the numerical performance of our implementation, we consider another key factor: the computational cost that is necessary to produce a given data set. Let us take as as an example the data used to calculate the Loschmidt rate function in Fig. 4.24. For each plot, the generation of the $n = 10^5$ independent trajectories with $\Delta t = 10^{-5}$ up to time $t = 6$ takes ~ 2 days on 96 cores. Because of the need to include two separate time evolution operators, each batch of simulations used to compute local observables takes approximately twice as long as for the Loschmidt amplitude. As it can be expected, the simulation time scales linearly with t and n, and inversely with Δt. The simulation time also scales approximately linearly with the system size N, so that this does not provide an intrinsic computational bottleneck for this approach.

In this Chapter, we have used the Euler scheme in order to solve the real time SDEs for the quantum Ising model. Using the stochastic approach, we have studied dynamical quantum phase transitions, finding that the presence of the Loschmidt peaks is reflected in signatures

in the classical disentangling variables. Solving the SDEs to compute observables, we have shown that the stochastic method can be applied in principle to a wide range of integrable and non-integrable problems, including higher dimensional and disordered settings. Investigating the performance of the approach used in this Chapter, we have estimated that fluctuations in the stochastic quantities grow exponentially with time and the system size across a broad parameter range. This scaling poses a limitation for the practical use of this approach in its current form. However, if the problem of diverging trajectories (which obliges one to use small Δt, as explained in Appendix D.2) and the issue of strong fluctuations can be overcome, the generality of the stochastic framework and the linear dependence of the computational cost of generating a trajectory $\{\xi_i^a(t)\}$ on the time t and on the system size could make this technique a powerful tool to investigate large systems. Progress in resolving these issues could be made by using alternative simulation schemes, which we discuss in Appendix D.1. Moreover, a promising direction towards improving the sampling efficiency of the method is based on measure transformations. This approach will be discussed in Chapters 5 and 6 in the context of Euclidean time evolution, on which we focus in the remainder of this Thesis.

Chapter 5

Ground State Properties From Imaginary Time Evolution

So far, after a general discussion of the Ising SDEs in Chapter 3, we have focussed on quantum dynamics, encoded in the real time equations. Remarkably, the stochastic formalism can also be used in imaginary time to compute the ground state expectation value of physical observables. In the remainder of this Thesis, we will focus on imaginary time evolution, showing the applicability of the stochastic approach to compute ground state expectation values and highlighting analogies and differences with the real time case. We will also use the Euclidean problem as a useful testing ground to develop the stochastic method beyond the approach of Chapter 4, consisting in directly solving the SDEs.

In this Chapter, we first discuss how ground state expectation values can be computed from the stochastic approach by evolving to late imaginary times. We demonstrate this in practice by numerically solving the imaginary time SDEs for the ground state energy and magnetisation, considering both integrable and non-integrable cases. Consistently with the discussion of Chapter 3, we find that, away from the large Γ limit where trajectories are Gaussian distributed, the large deviation nature of the problem makes it computationally expensive to accurately reproduce the ED result. In order to improve the sampling efficiency, we apply a variance-reducing measure transformation [143], based on extrapolating an exactly solvable case. We demonstrate that this technique substantially improves the numerical performance, making it possible to obtain results for which the direct sampling of the SDEs would require a prohibitively large computation time. This approach will be developed from a different perspective in the next Chapter, leading to a further enhancement of the numerical efficiency.

5.1 Imaginary Time Evolution

The ground state expectation value of a given observable $\hat{\mathcal{O}}$ is given by

$$\mathcal{O}_G = \langle \psi_G | \hat{\mathcal{O}} | \psi_G \rangle, \tag{5.1}$$

where $|\psi_G\rangle$ is the ground state. If $|\psi_G\rangle$ is unique, it can be obtained up to a proportionality constant from a generic state $|\psi(0)\rangle$ by performing imaginary time evolution. Setting $\hbar = 1$, one has

$$|\psi_G\rangle \sim \lim_{\tau\to\infty} e^{-\hat{H}\tau} |\psi(0)\rangle, \tag{5.2}$$

since all excited states are exponentially suppressed compared to the ground state at late imaginary times. It is then natural to consider the Euclidean time evolution operator

$$\hat{U}(\tau) = e^{-\hat{H}\tau}. \tag{5.3}$$

The time evolution operator (5.3) can be expressed in the stochastic formalism, analogously to the real time case discussed in the previous Chapters:

$$\hat{U}(\tau) = \Big\langle \otimes_j e^{\xi_j^+(\tau)\hat{S}_j^+} e^{\xi_j^z(\tau)\hat{S}_j^z} e^{\xi_j^-(\tau)\hat{S}_j^-} \Big\rangle_\phi, \tag{5.4}$$

where the average $\langle \dots \rangle_\phi$ is taken with respect to the action

$$S[\phi] \equiv \frac{1}{4}\int_0^\tau \mathrm{d}\tau \sum_{aij} (J^{-1})^a_{ij} \phi_i^a(\tau)\phi_j^a(\tau) \tag{5.5}$$

and the disentangling variables $\xi_j^a(\tau)$ satisfy the imaginary-time SDEs

$$\dot{\xi}_j^+ = \Phi_j^+ + \Phi_j^z \xi_j^+ - \Phi_j^- \xi_j^{+2}, \tag{5.6a}$$

$$\dot{\xi}_j^z = \Phi_j^z - 2\Phi_j^- \xi_j^+ , \tag{5.6b}$$

$$\dot{\xi}_j^- = \Phi_j^- \exp \xi_j^z , \tag{5.6c}$$

again with $\Phi_j^a = h_j^a + \phi_j^a$ and $\xi_i^a(0) = 0$. In analogy with the real time case, a matrix element involving one or more time evolution operators expressed as in Eq. (5.4) yields the average of a scalar function over stochastic processes; thus, ground state expectation values can be computed as averages of classical quantities at late imaginary times. This will be

illustrated by considering different physical observables, providing their formulation in the stochastic formalism and showing how they can be computed within this approach.

5.1.1 Ground State Energy

At late imaginary times, the time-evolved wavefunction takes the form

$$|\psi(\tau)\rangle = e^{-\hat{H}\tau}|\psi(0)\rangle \sim e^{-E_G\tau}|\psi_G\rangle. \tag{5.7}$$

Thus, the ground state energy density $\varepsilon_G = E_G/N$ can be computed as

$$\varepsilon_G = \lim_{\tau\to\infty} -\frac{1}{N\tau}\log\left(\langle\psi(0)|e^{-\hat{H}\tau}|\psi(0)\rangle\right). \tag{5.8}$$

This quantity can be expressed in terms of the imaginary time Loschmidt rate function $\lambda(\tau) \equiv -1/N\log|A(\tau)|^2$, where $A(\tau) \equiv \langle\psi(0)|\psi(\tau)\rangle$ is the Loschmidt amplitude. In terms of $\lambda(\tau)$, one has

$$\varepsilon_G = \frac{1}{2}\lim_{\tau\to\infty}\frac{\lambda(\tau)}{\tau}. \tag{5.9}$$

The imaginary time Loschmidt rate function takes the same functional form as the real time one given in Eq. (2.37). Since generic initial states will have a non-vanishing overlap with the ground state, we restrict our analysis to the all-down ferromagnetic initial state $|\psi(0)\rangle = \otimes_j|\downarrow\rangle_j \equiv |\Downarrow\rangle$, which yields the simplest expression for the Loschmidt rate function, in analogy with the real-time case:

$$\lambda(\tau) = -\frac{2}{N}\log\left|\left\langle\prod_{j=1}^{N}\exp\left(-\frac{\xi_j^z(\tau)}{2}\right)\right\rangle_\phi\right|. \tag{5.10}$$

The equations of motion of $\xi_j^z(\tau)$ are given by the imaginary-time SDEs (5.6). In particular, we consider the quantum Ising model discussed in Chapter 3 and the corresponding imaginary time SDEs

$$\dot{\xi}_i^+(\tau) = \frac{\Gamma}{2}(1-\xi_i^{+2}) + \xi_i^+\sum_j O_{ij}\phi_j, \tag{5.11a}$$

$$\dot{\xi}_i^z(\tau) = -\Gamma\xi_i^+ + \sum_j O_{ij}\phi_j, \tag{5.11b}$$

$$\dot{\xi}_i^-(\tau) = \frac{\Gamma}{2}\exp\xi_i^z. \tag{5.11c}$$

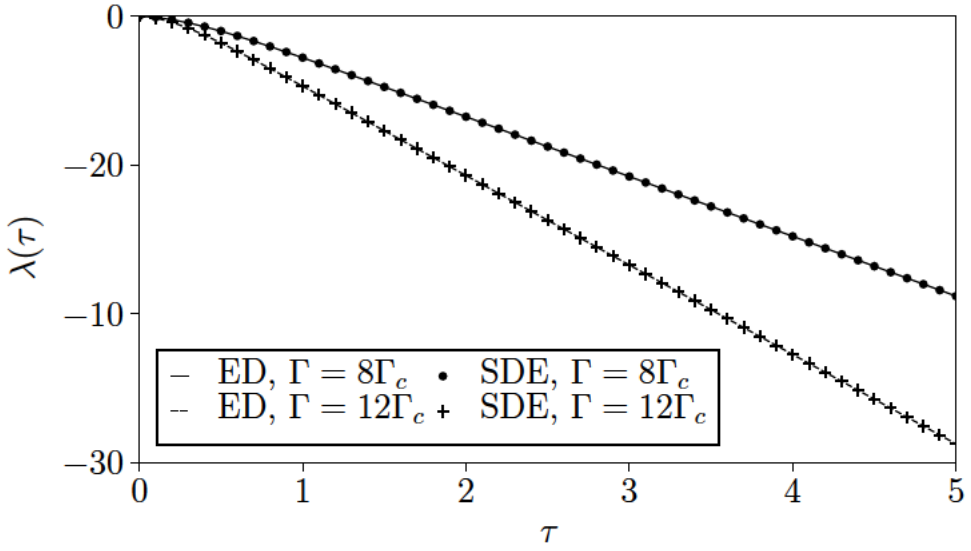

Figure 5.1: Imaginary time Loschmidt rate function $\lambda(\tau)$ for at TFIC of $N = 21$ spins initialised in the ferromagnetic initial state, following imaginary time evolution with different Γ. The SDE results were obtained from $n = 10^6$ simulations with $\Delta t = 10^{-1}$. In the large τ limit, this quantity can be used to extract the ground state energy. With $\tau = 5$, we get an estimate of the ground state energy within $\sim 5\%$ for these values of Γ. The accuracy of this estimate can be systematically improved by increasing τ.

As for the real time case, the average in Eq. (5.10) is performed by numerically solving the SDEs with the Euler method and averaging over the resulting ensemble of trajectories. For large values of the transverse field, $\Gamma \gg \Gamma_c$, we find very good agreement between the result obtained from the SDEs and ED, as shown in Fig. 5.1. For the values of Γ, N, τ considered in Fig. 5.1, the ground state of energy has converged to the thermodynamic result obtained from free fermions to $\sim 5\%$.

However, when considering transverse fields $\Gamma \lesssim \Gamma_c$, we find that the SDE result differs significantly from ED. This is illustrated in Fig. 5.2 for a TFIC of size $N = 21$. This observation is a manifestation of the very different behaviour of the imaginary time equations. Unlike the real time case, the divergence of trajectories is found to be extremely rare and the typical fluctuations tend to be of finite extent; however, the non-interacting result appears to act as an attractor for the sampling. This can be understood in the light of the findings of Chapter 3. In the large Γ limit, the saddle point trajectory given by the non-interacting result dominates and the fluctuations around it are approximately Gaussian, so the sampling of the SDEs is efficient. As Γ decreases, the weight of the saddle point trajectory is reduced and the tails of the distribution become very broad, so that the required number of simulations to achieve convergence becomes extremely large

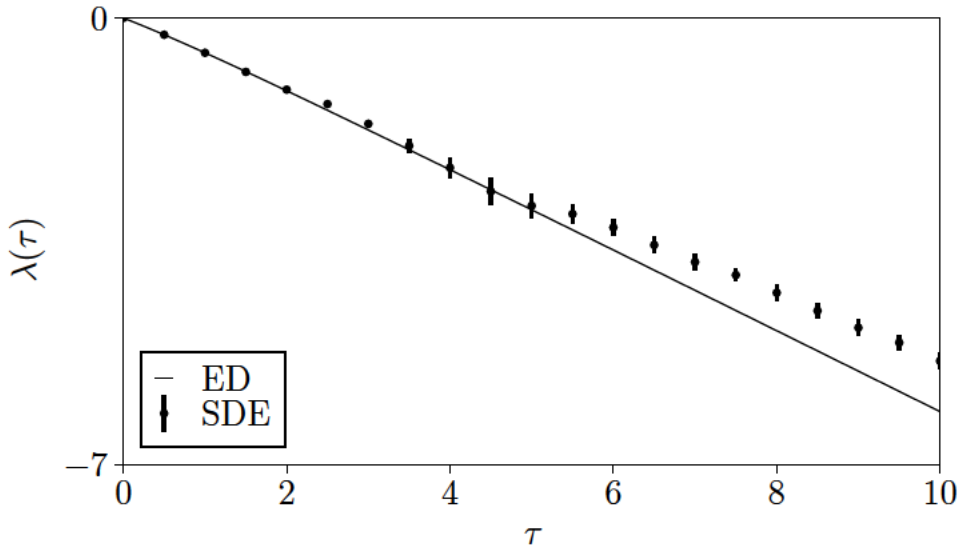

Figure 5.2: Imaginary time Loschmidt rate function $\lambda(\tau)$ for the same system as Fig. 5.1, evolved with $\Gamma = \Gamma_c$. The SDE result was obtained from $n = 10^6$ independent simulations with $\Delta t = 5 \times 10^{-4}$. The generation of these trajectories required ~ 24 hours on 48 cores. For this value of n, the SDE result is seen to still be far from convergence to the ED result. The bars show the standard deviation over the results obtained for $n_b = 10$ batches of 10^5 independent simulations each; the small extent of fluctuations suggest that the observed behaviour is systematic. This result can be contrasted with Fig. 5.6, where we calculate the same quantity using an improved sampling scheme, leading to much faster convergence. A further substantial advancement is shown in the next Chapter (Fig. 6.3), where a 20 second calculation on a single core is sufficient to obtain very precise results.

even for small system sizes. This is demonstrated in Fig. 5.3 by considering time evolution with $\Gamma = \Gamma_c/2$: as more trajectories are added, the average obtained from the SDEs shifts from the non-interacting value towards the correct result. The number of simulations that are needed to attain convergence increases with the stopping time τ and the system size N. These observations suggest that the direct sampling of the imaginary time SDEs is generically inefficient, and we should seek a more effective way of performing the required numerical averages; how this can be achieved will be the subject of Section 5.2.

5.1.2 Ground State Magnetisation

The stochastic approach can also be applied to the ground state expectation value of local observables. The stochastic expressions for local observables are similar to the real time case, but with the inclusion of an appropriate normalisation in order to account for the overlap of a generic state with the ground state. We will illustrate this by considering the

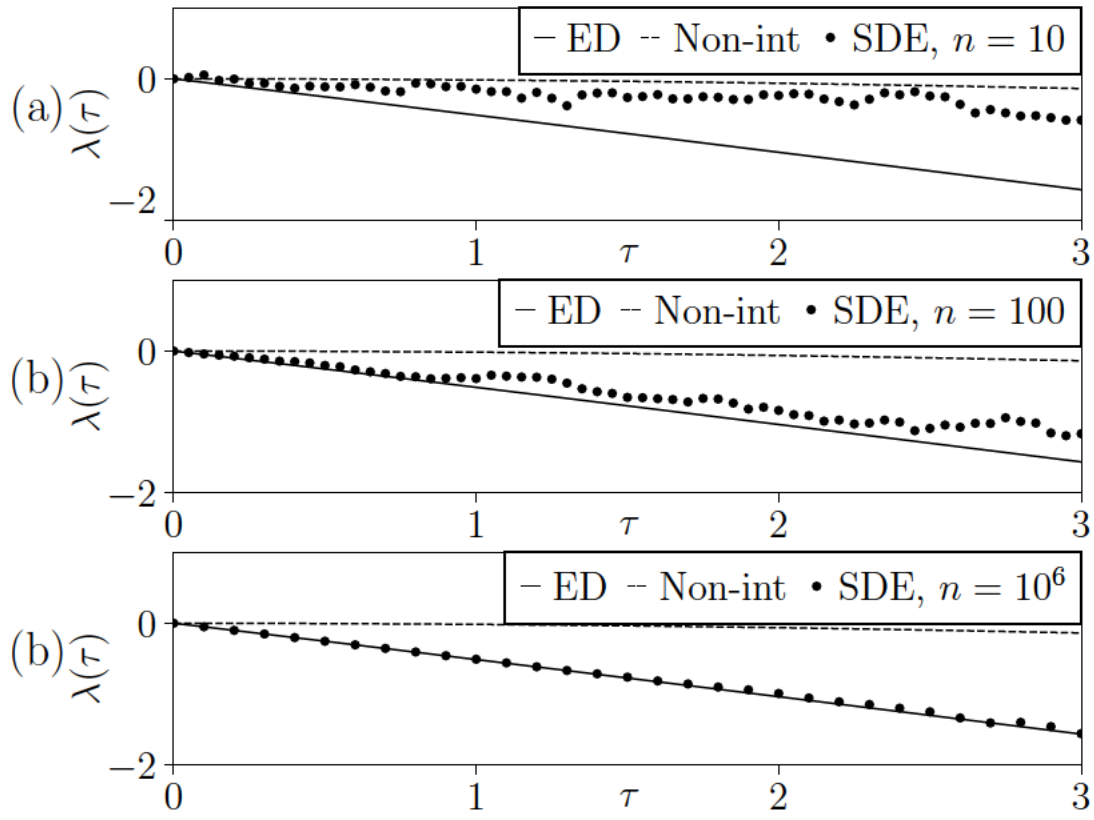

Figure 5.3: Imaginary time Loschmidt rate function $\lambda(\tau)$ for a TFIC of size $N = 15$ evolved from the FM ground state with $\Gamma = \Gamma_c/2$. (a) When computing an average over $n = 10$ trajectories, the rate function one obtains is significantly displaced in the direction of the non-interacting result obtained for $J = 0$ (dashed line). By increasing the number of samples to (b) $n = 100$, (c) $n = 10^6$, the resulting average progressively shifts towards the correct result given by ED (full line). This shows how the non-interacting result acts as an attractor for the trajectories.

ground state magnetization, given by $m_G = N^{-1}\sum_i^N \langle \hat{S}_i^z \rangle_G$. Expressing the ground state in terms as in Eq. (5.2) for a generic initial state $|\psi(0)\rangle$, we get

$$\langle \hat{S}_i^z \rangle_G = \lim_{\tau\to\infty} \frac{1}{\mathcal{N}(\tau)} \langle \psi(0)|\hat{U}(\tau)\hat{S}_i^z\hat{U}(\tau)|\psi(0)\rangle, \tag{5.12}$$

where we defined a normalisation factor

$$\mathcal{N}(\tau) \equiv \langle \psi(0)|\hat{U}(2\tau)|\psi(0)\rangle. \tag{5.13}$$

We see that the normalisation factor for an observable computed at imaginary time τ is the Loschmidt amplitude for imaginary time evolution up to 2τ. The functional form is then the same as Eq. (2.37). However, in practice, it is convenient to write $\hat{U}(2\tau) = \hat{U}(\tau)\hat{U}(\tau)$ so that one can use the same trajectories (all of which running up to imaginary time τ) to compute both the numerator and the denominator of Eq. (5.12). Furthermore, we can use the identity $\hat{U}(\tau) = \hat{U}^{\dagger}(\tau)$ to express $\mathcal{N}(\tau) = \hat{U}^{\dagger}(\tau)\hat{U}(\tau)$. This, together with the choice of the all-down initial state, allows one to express observables in terms of ξ_i^+ and ξ_i^z only, which is advantageous in terms of computational speed and numerical error. The two time evolution operators can be decoupled by introducing independent Hubbard–Stratonovich fields, ϕ and $\tilde{\phi}$, and disentangling variables, $\xi(\phi)$ and $\tilde{\xi}(\tilde{\phi})$. The expression for the numerator of Eq. (5.12) is given by the same functional form as for the corresponding observable in real time, given in Chapter 2, while the denominator can be constructed from the building blocks in Eq. (B.63). For example, choosing the ferromagnetic initial state $|\psi(0)\rangle = |\Downarrow\rangle$, the expectation value of $\hat{S}_i^z$ can be expressed in the stochastic formalism as

$$\langle \hat{S}_i^z \rangle_G = \lim_{\tau\to\infty} \frac{\langle f_i \rangle_{\phi,\tilde{\phi}}}{\langle \prod_j n_j^{dd} \rangle_{\phi,\tilde{\phi}}}, \tag{5.14}$$

for n_j^{dd} defined in Eq. (B.63) and

$$f_i = -\frac{1}{2} e^{-\Sigma_j \frac{\xi_j^z + \tilde{\xi}_j^z}{2}} (1 - \xi_i^+ \tilde{\xi}_i^+) \prod_{j\neq i} (1 + \xi_j^+ \tilde{\xi}_j^+), \tag{5.15}$$

in analogy with the real time case. We numerically compute the corresponding average for the non-integrable case of a 1D quantum Ising chain in the presence of a constant longitudinal field $h = 2J$. Figure 5.4 shows the ground state magnetization m_G at fixed h and for various values of the transverse field Γ. We find that the presence of a longitudinal field improves the convergence of the method and the stochastic approach is seen to accurately reproduce the results of ED for a wide range of parameters. However, for small values of Γ and h (not shown), more simulations are required to achieve convergence to the ED result, as seen for the ground state energy. In order to address this issue, we return to considering the ground state energy, showing how the performance of the method can be improved by means of measure transformations.

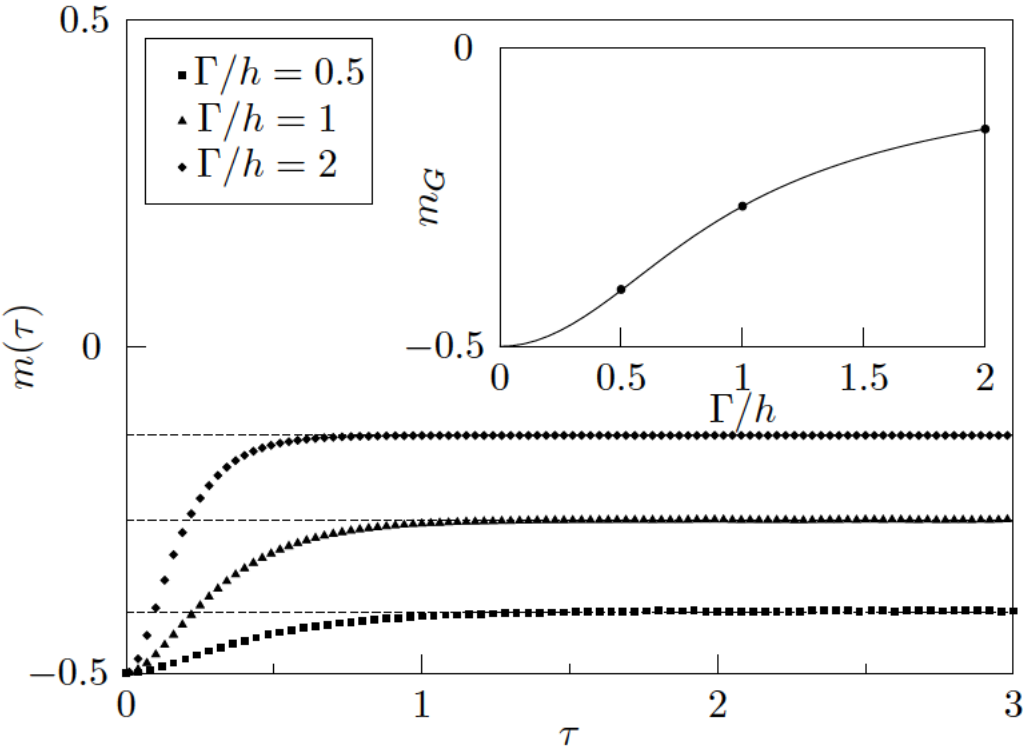

Figure 5.4: Imaginary time evolution of the magnetisation for a quantum Ising chain of size $N = 7$ in the presence of a constant longitudinal field $h = 2J$, considering different values of the transverse field Γ. The system is initialised in the all-down state $|\Downarrow\rangle$. For these parameters, the result computed using the stochastic approach rapidly converges to the ground state value obtained from ED (dashed line). The inset shows the evolution of the ground state magnetisation for fixed $h = 2J$ and as a function of Γ/h, where the full line is computed using ED. The SDE results were obtained from 3×10^6 simulations with $\Delta t = 10^{-3}$.

5.2 Measure Transformations

In the previous Section, we have shown that ground state expectation values can be computed by averaging over imaginary time trajectories of the stochastic variables. However, considering the case of the quantum Ising model, we have demonstrated how in practice the heavy-tailed distribution of the stochastic trajectories makes it difficult to appropriately sample the SDEs, except for large values of the transverse field Γ. This observation suggests that, in order to improve the performance of the stochastic method, we need to sample the underlying probability distribution in a way that is targeted to the observable we want to compute. In the language of stochastic processes, this amounts to performing an appropriate *change of measure*. In this Section, we will provide a practical introduction

to changes of measures in the context of SDEs. We will subsequently discuss a particular choice of measure transformation, which we will refer to as the *variance-reducing transformation* (VRT) following Ref. [143]. We will derive the exact form of this transformation for a system of $N = 2$ spins, and propose how this can be generalised to larger systems by a suitable ansatz. We will show that the VRT constructed by generalising the $N = 2$ result is capable of substantially improving the performance of the stochastic method in computing ground state energies.

5.2.1 Girsanov's Theorem

In its essence, the VRT is an application of Girsanov's theorem [155, 143]. As we illustrate in this Section, this theorem enables one to perform a change of measure so that a given stochastic function, corresponding to an observable, is replaced by a different one having the same mean. In particular, given a generic multicomponent stochastic process[1] ξ_i, Girsanov's theorem allows one to relate it to a stochastic process $\tilde{\xi}_i$ with a different drift coefficient. Let us consider the stochastic process defined by

$$\dot{\xi}_i = a_i(\xi) + \sum_j B_{ij}(\xi)\phi_j, \tag{5.16}$$

with drift coefficients a_i and diffusion coefficients B_{ij}, and where we collectively denote all the components by the shorthand $\xi \equiv \{\xi_i\}$. This process is defined with respect to a measure $\mathcal{P}$ such that the multicomponent process $\phi(t) = \{\phi_j(t)\}$ is a Wiener process (Appendix A). Consider the modified process

$$\dot{\tilde{\xi}}_i = \tilde{a}_i + \sum_j B_{ij}\phi_j \tag{5.17}$$

with the same initial conditions and a modified drift given by $\tilde{a}_i = a_i - \sum_j B_{ij}d_j$, where $d_j(\tilde{\xi})$ is an arbitrary vector. This process can be regarded as the Ito process in Eq. (5.16) where ϕ_j is replaced by a modified stochastic process

$$\tilde{\phi}_j(t) = \phi_j(t) - d_j\left(\xi(t)\right) \tag{5.18}$$

[1] To prevent notational clutter, here we use a single subscript i which can be thought of as a multi-index labelling each component of the stochastic process, e.g. for the disentangling variables $\xi_j^+ \equiv \xi_i$ with $i = \{j, +\}$.

with the same measure $\mathcal{P}$. We can then define the modified equivalent[2] measure $\tilde{\mathcal{P}}$ such that (5.18) is a standard Wiener process with respect to $\tilde{\mathcal{P}}$ and the process $\tilde{\xi}$ satisfies an Ito process with *the same* a_i and B_{ij} as ξ but with respect to the modified measure $\tilde{\mathcal{P}}$. Girsanov's theorem tells us how to relate $\tilde{\mathcal{P}}$ and the original measure $\mathcal{P}$, namely

$$\int \mathrm{d}\mathcal{P} f(\xi) = \int \mathrm{d}\tilde{\mathcal{P}} f(\tilde{\xi}) \tag{5.19}$$

$$= \int \mathrm{d}\mathcal{P} \frac{\Omega(t)}{\Omega(0)} f(\tilde{\xi}), \tag{5.20}$$

where $\Omega(t)/\Omega(0) \equiv \frac{\mathrm{d}\tilde{\mathcal{P}}}{\mathrm{d}\mathcal{P}}$ is the *Radon-Nikodym derivative* of the new measure with respect to the old and is itself a random variable, satisfying

$$\dot{\Omega} = \Omega \sum_j d_j \phi_j. \tag{5.21}$$

Equation (5.21) is geometric Brownian motion, solved by

$$\Omega(t) = \Omega(0) \exp \int_0^t \mathrm{d}t' \left(\sum_j d_j \phi_j - \frac{1}{2} \sum_j d_j^2 \right). \tag{5.22}$$

From Eq. (5.20), it is clear that if the distribution of $\Omega f(\tilde{\xi})$ with respect to the measure $\mathcal{P}$ has lighter tails than that of $f(\xi)$, sampling the former provides a more efficient way of computing $\int \mathrm{d}\mathcal{P} f(\xi)$. This application of Girsanov's theorem can thus be seen as the generalisation of importance sampling for continuous variables, where the Radon-Nikodym derivative $\Omega(t)$ plays the role of the *likelihood ratio*.

We have thus shown how, by means of Girsanov's theorem, we can express a given expectation value in terms of a stochastic process whose drift is shifted by d_j compared to the original one, at the expense of introducing a correction term given by $\Omega(t)$. Any such transformation is formally exact, so that in the limit of an infinite number of samples all the corresponding stochastic processes average to the same expected value. However, the speed of convergence varies greatly depending on the specific choice of d_j. In particular, for the Ising SDEs, we find that generic measure transformations, e.g. choosing d_j so as to eliminate the non-linear term in the equation for ξ_i^+, lead to comparable or worse convergence rate compared to the direct sampling of the SDEs. In the next Section, we will

[2]The equivalence of two measures $\mathcal{P}$, $\mathcal{Q}$ corresponds to the property $\mathcal{P}[A] = 0$ iff $\mathcal{Q}[A] = 0 \; \forall \, A$, where A is any element of the relevant space.

see how in practice it is possible to choose a shift d_j such that the corresponding measure transformation enhances the convergence speed of the numerical averaging.

5.2.2 The Variance-Reducing Transformation

The variance-reducing transformation (VRT) [143] is based on the following idea: suppose that the expectation value $u = \langle f \rangle$ of a particular stochastic function f was known at all times; we would then be able to perform a measure transformation such that at a particular time t_f the variance of the modified function Ωf defined in Eq. (5.20) is zero or indeed, more strongly, $\Omega(t_f) f(t_f)$ is deterministic.

Let us now formulate this statement mathematically. Consider a multi-component Ito process with drift a_i and diffusion B_{ij}

$$\dot{\xi}_i = a_i(\xi) + \sum_j B_{ij}(\xi)\phi_j \tag{5.23}$$

where again we collectively denote all the components with the shorthand $\xi \equiv \{\xi_i\}$. The stochastic process ξ has non-random initial conditions at $t = s$ given by $\xi(s) = \xi_0 \equiv \{\xi_{0i}\}$. We consider $s \leq t \leq t_f$, such that $\xi_i(t) \equiv \xi_i(t|\xi_0, s)$. Let us define a functional $u(t_f|\xi_0, s) = \langle f\left(\xi(t_f|\xi_0, s)\right)\rangle$ that depends on the stochastic process Eq. (5.23) and thus has a non-random initial condition $u(s|\xi_0, s) = f(\xi_0)$. Assume the expectation value $u(t_f|\xi(t), t)$ is known for all initial times t. Then, consider the particular measure transformation defined by

$$d_j(t) = -\frac{1}{u(t_f|\xi_0, t)} \sum_{k=1}^{d} B_{kj}\left(\xi(t)\right) \frac{\partial u(t_f|\xi_0, t)}{\partial \xi_{0k}}. \tag{5.24}$$

For this choice of d_j, one can show that

$$u\Big(t_f\Big|\tilde{\xi}(t|\xi_0, 0), t\Big)\Omega(t) = u\Big(t_f\Big|\xi_0, 0\Big)\Omega(0), \tag{5.25}$$

where $\Omega(t)$ is defined by Eq. (5.21). Considering the special case $t = t_f$ and using $u(t_f|\xi, t_f) = f(\xi)$, we get

$$f\Big(\tilde{\xi}(t_f|\xi_0, 0)\Big)\Omega(t_f)/\Omega(0) = u\Big(t_f\Big|\xi_0, 0\Big). \tag{5.26}$$

Since the right-hand side of Eq. (5.26) is deterministic, its left-hand side must also be so. We recognise the left-hand side of Eq. (5.26) as the integrand of Eq. (5.20); thus, by

appropriately choosing d_i we were able to make the modified process Ωf deterministic at time t_f.

At this stage, this construction relies on the knowledge of the exact solution $u(t|\xi(0),0)$ that we are interested in, so it does not have any practical utility per se. However, if we are able to guess a function $\bar{u}(t|\xi(0),0)$ that is similar enough (in a sense that we will clarify) to $u(t|\xi_i(0),0)$, we can expect that the variance of $f\Big(\xi(t_f|\xi_0,0)\Big)\Omega(t_f)/\Omega(0)$ will still be reduced. This construction provides a practical way of choosing which Girsanov transformation to perform in order to improve the convergence of averages corresponding to physical observables. However, the main difficulty one is faced with is the choice of an appropriate ansatz $\bar{u}$. This will be illustrated with a few practical examples.

5.3 Variance-Reducing Ansätze

As discussed in the previous Section, the VRT relies on the choice of an ansatz $\bar{u}$ which can be expected to 'resemble' the observable we are interested in. More precisely, the ansatz should have a similar dependence on the initial conditions of the SDEs (which do not simply correspond to different physical initial conditions) as the solution we are after. For a given observable, the simplest choice of drift shift d_i can be obtained by choosing the solution to the classical problem with $\Gamma = 0$ as our ansatz:

$$\bar{u} = \bar{u}_c. \tag{5.27}$$

In the classical case, the dependence of observables on $\xi_i^a(0)$ can be found straightforwardly, and in that limit the ansatz Eq. (5.27) is exact. In spite of its simplicity, this measure transformation was found to produce better convergence compared to naive sampling away from $\Gamma = 0$. An improvement on Eq. (5.27) is obtained by choosing $\bar{u}$ as a combination of the classical solution ($\Gamma = 0$) $\bar{u}_c$ and the non-interacting solution ($J = 0$) $\bar{u}_n$, both of which are easy to compute for general initial conditions $\xi_i^a(0)$:

$$\bar{u} = (J\bar{u}_c + 2\Gamma\bar{u}_{ni})/(J + 2\Gamma) \tag{5.28}$$

so that $\bar{u}_c$ and $\bar{u}_{ni}$ are recovered in the limit $\Gamma/J \to 0$ and $J/\Gamma \to 0$ respectively and at criticality, $\Gamma = \Gamma_c = J/2$, the two terms contribute in equal amounts. This choice of $\bar{u}$ was found to lead to a further improvement in performance compared to the purely classical ansatz.

However, the most successful choice over all parameter ranges is based on obtaining the exact solution for a given observable and for generic Γ in the analytically solvable case of a small number of spins N, and, after a suitable extrapolation, using it as the ansatz $\bar{u}$ for larger systems. This ansatz includes both the classical and the deterministic result as limiting cases. We will illustrate this considering the Loschmidt rate function $\lambda(\tau)$.

The difficulty in applying the proposed ansatz lies in the need to find solutions for $\lambda(\tau)$ when the SDEs have general initial conditions $\xi_i^a(0) \neq 0$ and both Γ and J are non-zero. For non-zero $\xi_i^a(0)$, functionals of the stochastic variables no longer represent physical observables and hence cannot be directly obtained from the mapping

$$\hat{U}(t) = \left\langle \otimes_i e^{\xi_i^+(t)\hat{S}_i^+} e^{\xi_i^z(t)\hat{S}_i^z} e^{\xi_i^-(t)\hat{S}_i^-} \right\rangle_\phi . \tag{5.29}$$

However, we will show that the SDEs with non-zero initial conditions can be mapped to a more general effective quantum problem. Let us write the initial conditions as $\xi_i^a(0) \equiv \xi_{0i}^a$. We can perform a change of variables $\xi_i^a(t) \to \bar{\xi}_i^a(t) + \xi_{0i}^a$ such that the new variables $\bar{\xi}_i^a(t)$ have initial condition $\bar{\xi}_i^a(0) = 0$. $\bar{\xi}_i^a(t)$ satisfy the SDEs

$$-\frac{d\bar{\xi}_i^+}{d\tau} = h_i^+ + \phi_i^+ + [\hat{\bar{\xi}}_i^+ + \xi_{0i}^+](h_i^z + \phi_i^z) - [\bar{\xi}_i^+ + \xi_{0i}^+]^2(h_i^- + \phi_i^-), \tag{5.30}$$

$$\frac{d\bar{\xi}_i^z}{d\tau} = h_i^z + \phi_i^z - 2(h_i^- + \phi_i^-)[\bar{\xi}_i^+ + \xi_{0i}^+], \tag{5.31}$$

$$\frac{d\bar{\xi}_i^-}{d\tau} = (h_i^- + \phi_i^-)\exp[\bar{\xi}_i^z + \xi_{0i}^z]. \tag{5.32}$$

These equations can be brought to the form of the Ising SDEs (5.11) if we define a set of effective fields

$$\bar{h}_i^+ \equiv h_i^+ + \xi_{0i}^+ h_i^z - (\xi_{0i}^+)^2 h_i^-, \tag{5.33}$$

$$\bar{h}_i^z \equiv h_i^z - 2\xi_{0i}^+ h_i^-, \tag{5.34}$$

$$\bar{h}_i^- \equiv h_i^-, \tag{5.35}$$

$$\bar{\Phi}_i^+ \equiv \bar{h}_i^+ + \phi_i^+ + \xi_{0i}^+ \phi_i^z - (\xi_{0i}^+)^2 \phi_i^-, \tag{5.36}$$

$$\bar{\Phi}_i^z \equiv \bar{h}_i^z + \phi_i^z - 2\xi_{0i}^+ \phi_i^-, \tag{5.37}$$

$$\bar{\Phi}_i^- \equiv \bar{h}_i^- + \phi_i^-. \tag{5.38}$$

Additionally, we need to perform the rescaling $\bar{\xi}_i^- \to e^{-\xi_{0i}^z}\bar{\xi}_i^-$. Applying the following, for non-zero ξ_{0i}^a we can write:

$$e^{\xi_i^+(\tau)\hat{S}_i^+}e^{\xi_i^z(\tau)\hat{S}_i^z}e^{\xi_i^-(\tau)\hat{S}_i^-} = e^{\xi_{0i}^+\hat{S}_i^+}e^{\bar{\xi}_i^+(\tau)\hat{S}_i^+}e^{\bar{\xi}_i^z(\tau)\hat{S}_i^z}e^{\xi_0^z\hat{S}_i^z}e^{e^{\xi_{0i}^z}\bar{\xi}_i^-(\tau)\hat{S}_i^-}e^{\xi_0^-\hat{S}_i^-}, \tag{5.39}$$

where the $\bar{\xi}_i^a$ fields satisfy the equations of motion (5.11) in terms of the fields $\bar{\Phi}_i^a$. Using

$$e^{\xi_{0i}^z\hat{S}_i^z}e^{e^{\xi_{0i}^z}\bar{\xi}_i^-(\tau)\hat{S}_i^-} = e^{\bar{\xi}_i^-(\tau)\hat{S}_i^-}e^{\xi_{0i}^z\hat{S}_i^z} \tag{5.40}$$

we finally obtain the relation

$$\langle\otimes_i e^{\xi_i^+(\tau)\hat{S}_i^+}e^{\xi_i^z(\tau)\hat{S}_i^z}e^{\xi_i^-(\tau)\hat{S}_i^-}\rangle_\phi = e^{\Sigma_i\xi_{0i}^+\hat{S}_i^+}\bar{U}[\bar{\xi}](\tau)e^{\Sigma_i\xi_{0i}^z\hat{S}_i^z}e^{\Sigma_i\xi_{0i}^-\hat{S}_i^-}, \tag{5.41}$$

where $\bar{U}[\bar{\xi}](\tau)$ is an effective time-evolution operator which depends deterministically on the initial conditions ξ_{0i}^a. $\bar{U}[\bar{\xi}](\tau)$ is defined as

$$\bar{U} \equiv \exp(-\tau\bar{H}), \tag{5.42}$$

$$\bar{H} \equiv -\sum_{aij}\mathcal{J}_{ij}^a\bar{S}_i^a\bar{S}_j^a + \sum_{ia}\bar{h}_i^a\bar{S}_i^a, \tag{5.43}$$

where the modified spin operators $\bar{S}_i^a$ are given by

$$\bar{S}_i^+ \equiv \hat{S}_i^+, \tag{5.44}$$

$$\bar{S}_i^z \equiv \hat{S}_i^z + \xi_{0i}^+\hat{S}_i^+, \tag{5.45}$$

$$\bar{S}_i^- \equiv \hat{S}_i^- - 2\xi_{0i}^+\hat{S}_i^z - [\xi_{0i}^+]^2\hat{S}_i^+, \tag{5.46}$$

as found by considering which operator multiplies each $\bar{\Phi}_j^a$ when inverting the Hubbard-Stratonovich transformation. Thus, the SDEs with non-zero initial conditions can be mapped to a quantum problem involving a modified time evolution operator multiplied by some constant matrices. Considering the Loschmidt rate function $\lambda(\tau)$ for our specific choice of observable, it is possible to obtain the analytical solution $\lambda(\tau|\xi_0)$ with general initial conditions for a system of size $N = 2$ spins. The transformation performed by choosing $\bar{u} = \lambda(\tau|\xi_0)_{N=2}$ is then expected to reduce the variance to zero at time τ independently of the number of trajectories. This is indeed observed in numerical simulations (Fig. 5.5) confirming the exactness of this approach. $N = 2$ is the largest system for which $\lambda(\tau|\xi_0)$ can be obtained analytically, which is necessary in order to implement the VRT. However,

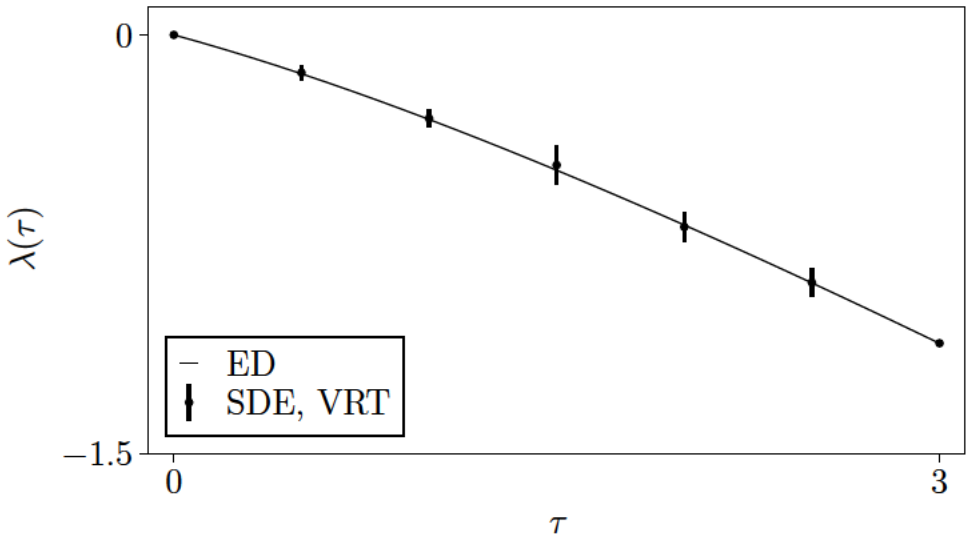

Figure 5.5: Imaginary time Loschmidt rate function $\lambda(\tau)$ for a TFIC of $N = 2$ spins, initialised in the FM initial state with all spins down and evolved with $\Gamma = \Gamma_c$. The SDE result was computed from $n = 10$ simulations with $\Delta t = 10^{-4}$, using the variance-reducing transformation (VRT). For such small system size, the VRT can be performed exactly and the variance of the SDE result (shown as error bars) computed from the 10 simulations is seen to vanish at the stopping time up to numerical precision.

we can extrapolate $\bar{u}$ obtained for $N = 2$ to larger system sizes. In particular, in order to calculate d_i, we need to compute the derivative $\partial\bar{u}/\partial\xi_i^+$, which singles out a particular spin i. A natural extrapolation is then given by

$$\xi_{01}^+\xi_{02}^+ \to \prod_{j=1}^{N} \xi_{0j}^+, \tag{5.47a}$$

$$\xi_{02}^+ \to \sum_{\substack{j=1 \\ j\neq i}}^{N} \xi_{0j}^+, \tag{5.47b}$$

where the second replacement (5.47b) is performed after all of the substitutions (5.47a), and only on terms that have not yet been replaced. The ξ_0^z dependence can be extracted in a simple fashion and is accounted for exactly in the choice of $\bar{u}$.

Constructing a VRT with this choice of $\bar{u}$, we find that the performance of the method improves dramatically. This is demonstrated in Fig. 5.6 for the same parameters that we considered in Fig. 5.2. The application of the VRT leads to a much better agreement with ED, for a much smaller computational cost, compared to the direct sampling of the SDEs performed in Section 5.1.1.

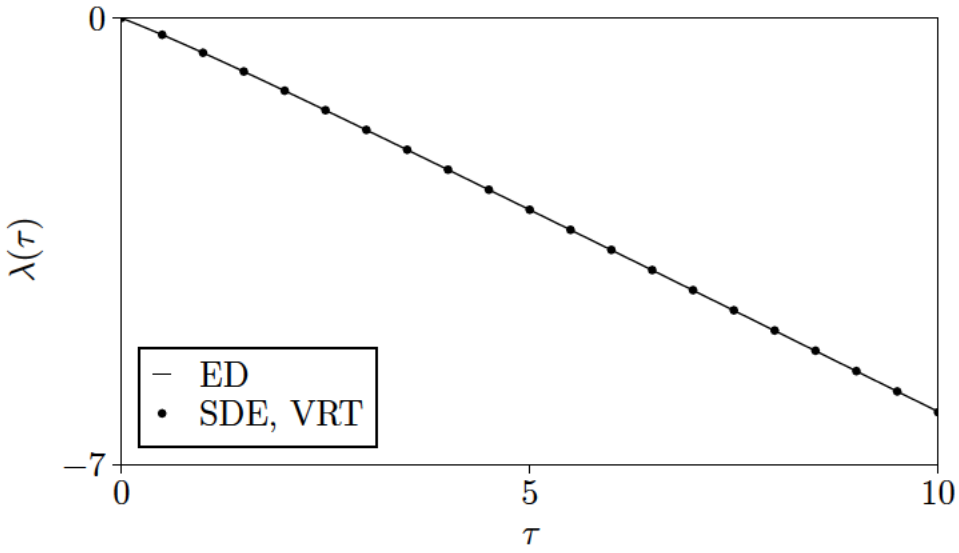

Figure 5.6: Imaginary time Loschmidt rate function $\lambda(\tau)$ for a TFIC of $N = 21$ spins, initialised in the FM initial state with all spins down and evolved with $\Gamma = \Gamma_c$. The result obtained from the SDEs using the variance-reducing transformation (VRT) is in excellent agreement with ED (full line). $\lambda(\tau)$ was computed from 10^4 independent trajectories with $\Delta t = 5 \times 10^{-4}$, which took ~ 12 hours to produce using 2 cores. By comparing the data shown here with Fig. 5.2, we find that the VRT can obtain results that are not accessible to a 100 times longer computation performed via the direct sampling of the SDEs.

This technique comes however with its own drawbacks. The key issue lies in choice of the ansatz $\bar{u}$. This needs to be a known function of the initial conditions, so that it is possible to analytically differentiate it to construct the drift shift d_i. While extrapolating the result obtained for a small system size N has proved a fruitful choice for $\bar{u}$, this is only possible for $N = 2$, which is of course very far from the thermodynamic limit. Furthermore, in the case of more complicated observables such as the ground state magnetisation, obtaining an analytical result for general initial conditions is challenging even for $N = 2$.

In spite of its limitations, the VRT is a substantial improvement over the direct sampling of the SDEs. Moreover, the effectiveness of the VRT suggests that the key to improving the performance of the stochastic approach is to perform the sampling in an *observable-specific* way. This idea is at the core of the approach that we will explore in the next Chapter, based on constructing the effective action corresponding to a specific observables and finding the corresponding saddle point trajectory.

Chapter 6

Saddle Point Equation for Observables

In Chapter 5, we have seen how it is possible to improve the sampling of the Euclidean SDEs by an appropriate observable-specific measure transformation. In this Chapter, we will push this idea further, developing a scheme to find the transformation which can be expected to yield the most efficient sampling for a given quantity of interest. This is based on defining an effective action $S[\phi]$ corresponding to a specific observable $\hat{\mathcal{O}}$, so that

$$\langle \hat{\mathcal{O}} \rangle = \int \mathcal{D}\phi e^{-S[\phi]}. \tag{6.1}$$

Instead of directly evaluating this functional integral by performing numerical simulations, we will show how it is possible to find the saddle point trajectory ϕ_S yielding the largest contribution to the integral. The action can then be expanded to second order around ϕ^S, yielding a Gaussian functional integral which can be computed analytically. Alternatively, however, one can perform a measure transformation using ϕ^S and then numerically sample the resulting integral. We will show that this approach, while retaining the exactness of the stochastic method, leads to a dramatic improvement in sampling efficiency. This makes it possible to compute ground state energies for large systems, as we illustrate for $N = 150$ spins. We conclude this Chapter by discussing a number of directions for the further development of this method.

As done in Chapter 5, we will develop the saddle point approach in imaginary time. The starting point is once again the Euclidean time evolution operator

$$\hat{U}(\tau_f) = \int \mathcal{D}\phi \; e^{-S[\phi]} \otimes_j e^{\xi_j^+(\tau_f)\hat{S}_j^+} e^{\xi_j^z(\tau_f)\hat{S}_j^z} e^{\xi_j^-(\tau_f)\hat{S}_j^-}, \tag{6.2}$$

where the diagonal noise action $S[\phi]$ is defined as

$$S[\phi] \equiv \frac{1}{2}\int_0^{\tau_f} \mathrm{d}\tau \sum_i \phi_i^2. \tag{6.3}$$

The Euclidean time evolution operator in Eq. (6.2) is not in the form of a conventional path integral, as it involves spin operators. However, as we have seen, by acting on specific observables and states we can replace the operators by c-numbers: the resulting integral is then a bona fide functional integral, and can be treated by using the toolbox of the calculus of variations. In the next Section, we will provide a preliminary discussion of how such integrals can be handled, which will be the basis for the subsequent developments, focussing in particular on path integrals with a Gaussian action such as (6.3).

6.1 Functional Integrals

Suppose one is interested in evaluating a functional integral in the form

$$\mathcal{I} = \int \mathcal{D}\phi e^{-S[\phi]}. \tag{6.4}$$

The largest contribution to the integral is given by the saddle point (SP) trajectory (or trajectories) $\phi_i^S(t)$, defined by the stationarity condition

$$\frac{\delta S}{\delta \phi_i(t)}\Big|_{\phi_i^S(t)} = 0. \tag{6.5}$$

If the action can be expressed as the time-integral of a Lagrangian $L(\phi, \dot{\phi}, t)$ which depends explicitly on $\phi \equiv \{\phi_i\}$, $\dot{\phi} \equiv \{\dot{\phi}_i\}$,

$$S[\phi] = \int_0^{t_f} L(t)\mathrm{d}t,$$

by explicitly varying the action S one can show that the stationarity condition Eq. (6.5) is equivalent to the Euler-Lagrange equations

$$\frac{\partial L}{\partial \phi_i} - \frac{\partial}{\partial t}\frac{\partial L}{\partial \dot{\phi}_i} = 0 \quad \forall \quad i \tag{6.6}$$

up to a boundary contribution which in many physical applications vanishes due to the constraints $\delta\phi(0) = \delta\phi(t_f) = 0$. Here, however, we will consider a case where the Lag-

rangian $L(t)$ is itself a functional of ϕ; in this case, as we will see, it is not possible to formulate the stationarity condition Eq. (6.5) as a differential equation.

The action $S[\phi]$ can be expanded around its saddle point value $S^S = S[\phi^S]$ as

$$S[\phi] = S^S + \frac{1}{2}\sum_{ij}\int_0^{t_f} \mathrm{d}t \int_0^{t_f} \mathrm{d}t' S_{ij}^{(2)}(t,t')[\phi_i(t) - \phi_i^S(t)][\phi_j(t') - \phi_j^S(t')] + \dots \tag{6.7}$$

in terms of the *second variation*

$$S_{ij}^{(2)}(t_1,t_2) \equiv \frac{\delta^2 S[\phi]}{\delta\phi_i(t_1)\delta\phi_j(t_2)}\Big|_{\phi=\phi^S}. \tag{6.8}$$

Performing the change of variables $\phi_i'(t) = \phi_i(t) - \phi_i^S(t)$, the functional integral Eq. (6.4) can be expressed as

$$I = \int \mathcal{D}\phi e^{-S[\phi]} = e^{-S^S}\int \mathcal{D}\phi' e^{-\frac{1}{2}\int\int \sum_{ij} S_{ij}^{(2)}(t,t')\phi_i'(t)\phi_j'(t')\mathrm{d}t\mathrm{d}t' + \dots}. \tag{6.9}$$

We can truncate the expansion of the action around the saddle point field to second order and evaluate the corresponding Gaussian integral. Assuming that the matrix $S^{(2)} \equiv \{S_{ij}^{(2)}(t,t')\}$ is positive definite, the path integral I can thus be approximated as

$$\int \mathcal{D}\phi e^{-S[\phi]} \simeq e^{-S[\phi^{(S)}]} \det\left(S^{(2)}\right)^{-\frac{1}{2}}, \tag{6.10}$$

or, if Eq. (6.5) admits more than one solution,

$$\int \mathcal{D}\phi e^{-S[\phi]} \simeq \sum_p e^{-S[\phi^{(S,p)}]} \det\left(S^{(2,p)}\right)^{-\frac{1}{2}}, \tag{6.11}$$

where the superscript p runs over all the saddle point trajectories. Estimating an integral by considering only the largest contribution ϕ^S and Gaussian fluctuations around it is known as the *saddle point approximation*, which is is expected to work well for integrals in the form

$$I = \int \mathcal{D}\phi e^{-zS[\phi]} \tag{6.12}$$

where $z \gg 1$. This is commonly the case for path integrals in quantum mechanics [140], where $z = 1/\hbar$; the saddle point equation is typically solved by the classical trajectory, which becomes the only contribution in the classical limit $\hbar \to 0$. Here, we will consider

functional integrals where there is no explicit large parameter z; we will return to discussing this point towards the end of this Chapter.

In general, we may be interested in the average of a function f,

$$\langle f \rangle = \int \mathcal{D}\phi e^{-S[\phi]} f[\phi]. \tag{6.13}$$

Here, the action $S[\phi]$ acts as a weight and f can have a general functional dependence on ϕ. To approximate this integral, we can find the saddle point *of the whole integrand*, and not just the original action. This amounts to finding the saddle point of a modified action $S' \equiv S[\phi] - \log f[\phi]$ such that the integral in Eq. (6.13) can be written as

$$F = \langle f[\phi] \rangle_\phi = \int \mathcal{D}\phi e^{-S'[\phi]}. \tag{6.14}$$

The stationarity condition for S' is given by

$$\frac{\delta}{\delta \phi} \left(S[\phi] - \log f[\phi] \right) \Big|_{\phi=\phi^S} = 0. \tag{6.15}$$

We can then approximate the integral in Eq. (6.13) by finding the saddle point field, expanding the action around it to second order and evaluating the corresponding Gaussian integral:

$$F \sim e^{-S'^S} \int \mathcal{D}\phi e^{-\frac{1}{2}\int \mathrm{d}t \mathrm{d}t' \phi_i(t) \phi_j(t') S'^{(2)}_{ij}} = e^{-S'^S} \det \left(S'^{(2)} \right)^{-\frac{1}{2}}. \tag{6.16}$$

However, we can circumvent the need to truncate the expansion by combining the saddle point approach with the stochastic interpretation of a quadratic Gaussian action. Consider a path integral of the form of Eq. (6.14), where $S'[\phi]$ is the effective action for a given observable. Let us further assume that $S[\phi] = \int \mathrm{d}t \phi^2(t)/2$. Using the saddle point field ϕ^S satisfying Eq. (6.15), we can perform the change of variables $\phi = \phi^S + \phi'$:

$$F = \int \mathcal{D}\phi e^{-S'[\phi]} = \int \mathcal{D}\phi' e^{-S'[\phi^S + \phi']}. \tag{6.17}$$

We can write $S'[\phi^S+\phi'] = S[\phi^S] + S[\phi'] + \int \mathrm{d}t\,\phi'(t)\phi^S(t) - \log f[\phi^S+\phi']$. The functional integral then becomes

$$F = e^{-S[\phi^S]} \int \mathcal{D}\phi e^{-S[\phi']} e^{-\int \mathrm{d}t\,\phi'(t)\phi^S(t) + \log f[\phi^S+\phi']} \tag{6.18}$$

$$= e^{-S[\phi^S]} \langle e^{-\int \mathrm{d}t\,\phi'(t)\phi^S(t)} f[\phi^S+\phi'] \rangle_{\phi'}, \tag{6.19}$$

where in the final step we expressed the functional integral as an average over trajectories ϕ' thanks to the Gaussian action $S[\phi']$. By performing this transformation, the functional integral is computed as the average of a 'biased' observable and the equations of motion for the disentangling variables are also biased. This is nothing but a measure transformation in the spirit of Section 5.2, whereby the sampling is now centered around the trajectory that yields the largest contribution. This transformation can thus be expected to yield the most efficient sampling for a given observable. In this approach, no truncation was performed at any stage, and the final expression is still exact.

6.2 Saddle Point for the Loschmidt Amplitude

We will illustrate the procedure outlined in the previous Section by computing the ground state energy of the transverse-field Ising chain, defined by the Hamiltonian

$$\hat{H} = -J\sum_i \hat{S}_i^z \hat{S}_i^z - \Gamma \sum_i \hat{S}_i^x \tag{6.20}$$

and corresponding to the Euclidean Ising SDEs

$$\dot{\xi}_i^+(\tau) = \frac{\Gamma}{2}(1-\xi_i^{+2}) + \xi_i^+ \sum_j O_{ij}\phi_j, \tag{6.21a}$$

$$\dot{\xi}_i^z(\tau) = -\Gamma\xi_i^+ + \sum_j O_{ij}\phi_j, \tag{6.21b}$$

$$\dot{\xi}_i^-(\tau) = \frac{\Gamma}{2}\exp\xi_i^z, \tag{6.21c}$$

subject to the initial conditions $\xi_i^a(0) = 0$. The ground state energy is encoded in the Loschmidt amplitude $A(\tau)$, defined by

$$A(\tau) = \langle\psi(0)|\hat{U}(\tau)|\psi(0)\rangle. \tag{6.22}$$

For late imaginary times τ_f, the Loschmidt amplitude takes the form $A(\tau_f) \sim \exp(-N\varepsilon_G\tau_f)$ so that the ground state energy density ε_G can be obtained as

$$\varepsilon_G = -\lim_{\tau_f\to\infty}\frac{1}{N\tau_f}\log A(\tau_f) = \lim_{\tau_f\to\infty}\frac{\lambda(\tau_f)}{2\tau_f}, \tag{6.23}$$

where $\lambda(\tau)$ is the Loschmidt rate function. Choosing the all-down initial state $|\Downarrow\rangle$, the Loschmidt amplitude can be written in functional integral form as

$$A(\tau) = \langle e^{-\frac{1}{2}\sum_i \xi_i^z(\tau)}\rangle_\phi \tag{6.24}$$

$$= \int \mathcal{D}\phi e^{-S[\phi]} e^{-\frac{1}{2}\sum_i \xi_i^z(\tau)}. \tag{6.25}$$

This is in the form of Eq. (6.13) with $f = e^{-\frac{1}{2}\sum_i \xi_i^z(\tau)}$. Since, due to Eq. (6.21b), the variable $\xi_i^z(\tau)$ is given by

$$\xi_i^z(\tau) = \int_0^\tau \mathrm{d}\tau' \left(\sum_j O_{ij}\phi_j(\tau') - \Gamma\xi_i^+(\tau')\right), \tag{6.26}$$

the Loschmidt amplitude (6.24) can be written as

$$A(\tau) = \int \mathcal{D}\phi e^{-S_{\text{losch}}} \tag{6.27}$$

in terms of an effective Euclidean Loschmidt action

$$S_{\text{losch}} = \frac{1}{2}\sum_i \int_0^\tau \mathrm{d}\tau' \left(\phi_i^2(\tau') - \Gamma\xi_i^+(\tau') + \sum_j O_{ij}\phi_j(\tau')\right). \tag{6.28}$$

This integral is in the form of Eq. (6.4) and can then be treated with the techniques discussed in Section 6.1. The first necessary step is identifying the saddle point trajectory.

6.2.1 Loschmidt Saddle Point Equation

The saddle point equation is obtained by minimising the effective Loschmidt action with respect to field configurations ϕ. Since ξ^+ is itself a functional of ϕ, it is not possible to use the Euler-Lagrange equations (6.6). Rather, we must directly consider the full variation of the action

$$\frac{\delta}{\delta\phi_j(\tau')}\frac{1}{2}\sum_i \int_0^{\tau_f} \mathrm{d}\tau \left(\phi_i^2(\tau) - \Gamma\xi_i^+(\tau) + \sum_k O_{ik}\phi_k(\tau)\right)\Big|_{\phi_j^S} = 0. \tag{6.29}$$

This condition yields the Euclidean *Loschmidt saddle point equation*

$$\phi_j^S(\tau', \tau_f) = \frac{\Gamma}{2}\sum_i \int_0^{\tau_f} \mathrm{d}\tau \frac{\delta \xi_i^+(\tau)}{\delta \phi_j(\tau')}\Big|_{\phi^S} - \frac{1}{2}\sum_i O_{ij}, \tag{6.30}$$

which is an implicit equation for the saddle point trajectory ϕ^S. For notational compactness, let us define the matrix

$$\Xi_{ij}(\tau, \tau') \equiv \frac{\delta \xi_i^+(\tau)}{\delta \phi_j(\tau')}. \tag{6.31}$$

The equation of motion for $\Xi_{ij}(\tau, \tau')$ is obtained by functionally differentiating Eq. (6.21a):

$$\frac{d}{d\tau}\Xi_{ij}(\tau, \tau') = -\Gamma \xi_i^+(\tau)\Xi_{ij}(\tau, \tau') + \Xi_{ij}(\tau, \tau')\sum_k O_{ik}\phi_k, \tag{6.32}$$

where $\Xi_{ij}(\tau, \tau') = 0$ for $\tau < \tau'$ and the initial condition is given by $\Xi_{ij}(\tau, \tau) = \xi_i^+(\tau)O_{ij}$. Equation (6.32) describes a geometric Brownian motion (GBM), an exactly solvable stochastic process: if ξ_i^+ and ϕ_i are known, Ξ_{ij} can be obtained exactly as

$$\Xi_{ij}(\tau, \tau') = \xi_i(\tau')O_{ij}\theta(\tau - \tau')\exp\int_{\tau'}^{\tau}[-\Gamma\xi_i^+(s) + \sum_k O_{ik}\phi_k(s)]\mathrm{d}s. \tag{6.33}$$

The saddle point equation (6.30) features the quantity[1]

$$\Xi_{ij}^S(\tau, \tau') \equiv \Xi_{ij}(\tau, \tau')|_{\phi^S} = \xi_i^{+S}(\tau')O_{ij}\theta(\tau - \tau')\exp\int_{\tau'}^{\tau}[-\Gamma\xi_i^{+S}(s) + \sum_k O_{ik}\phi_k^S(s)]\mathrm{d}s, \tag{6.34}$$

where we have also defined $\xi_i^{+S} \equiv \xi_i^+|_{\phi^S}$ satisfying the equation of motion

$$\frac{d}{d\tau}\xi_i^S(\tau, \tau') = \frac{\Gamma}{2}(1 - \xi_j^{+S2}) + \xi_i^{+S}\sum_j O_{ij}\phi_j^S. \tag{6.35}$$

The saddle point equation (6.30) can be solved exactly in the classical and non-interacting limits. In the classical case with $\Gamma = 0$, we have $\xi_i^+ = 0$ and the Loschmidt action for the Ising model is quadratic:

$$S_c[\phi] = \int_0^{\tau_f} \mathrm{d}\tau_f \left[\sum_i \frac{1}{2}\phi_i^2(\tau_f) + \frac{1}{2}\sum_{ij} O_{ij}\phi_j(\tau_f)\right]. \tag{6.36}$$

[1] As the saddle point field ϕ_i^S, Ξ_{ij}^S also depends on the end time τ_f. We leave this dependence implicit to avoid excessive notational clutter.

In this case, truncating the expansion about the saddle point to second order gives the exact solution, as

$$\frac{\delta^n S_c}{\delta\phi_{i_1}\dots\delta\phi_{i_n}} = 0 \;\forall\; n > 2.$$

We get $\phi_j^S = \phi_j^C \equiv -\frac{1}{2}\sum_i O_{ij}$ and $(S_c)^{(2)}_{ij}(\tau,\tau') = 1$. Thus,

$$A_c(\tau_f) = e^{-S_c[\phi^{(S)}]}\det\left(S_c^{(2)}\right)^{-\frac{1}{2}} = e^{-S_c[\phi^{(S)}]}. \tag{6.37}$$

The saddle point action can be computed exactly:

$$S_c = \int_0^{\tau_f} \mathrm{d}\tau \sum_j \left[-(\sum_i O_{ij})^2/8\right] = -NJ\tau_f/4, \tag{6.38}$$

where we used the property $\sum_j(\sum_i\sum O_{ij})^2 = 2NJ$ (Appendix B). As prescribed by Eq. (6.23), dividing by τ_f yields the ground state energy, which simply amounts to a contribution $-J/4$ for each pairwise interaction.

In the non-interacting limit $J = 0$, one has $O_{ij} = 0$, $\Xi^S_{ij} = 0$ and the saddle point equation is simply solved by $\phi^S \equiv \phi^{NI} = 0$ corresponding to the deterministic limit of the SDEs. Hence, the saddle point approach is exact in both the limits $\Gamma/J \to 0$, $\Gamma/J \to \infty$.

For generic Γ, both ϕ^S and ξ^S are non-zero. For a given stopping time τ_f of interest, the value of the saddle point field $\phi^S(\tau',\tau_f)$ at τ' is coupled to $\phi^S(\tau'',\tau_f)$ for all $0 < \tau'' < \tau_f$ via the integral of Ξ^S. In general, to determine the saddle point field $\phi(\tau',\tau_f)$, together with ξ^{+S}, one would then have to discretise the interval τ_f in n time steps and solve a set of $2\times n$ coupled difference equations, an arduous task. However, an arbitrarily precise approximation to the solution of Eq. (6.30) can be found by means of a recursive procedure, which we illustrate in the next Section.

6.2.2 Recursive Solution of the Saddle Point Equation

The saddle point equation for the Loschmidt amplitude can be solved recursively, exploiting the intuition that the saddle point field configuration[2] $\phi_j^S(\tau',\tau_f)$ should change little if we increase τ_f by a small amount Δt. In practice, one assumes

$$\phi_j^S(\tau',\tau_f+\Delta t) \sim \phi_j^S(\tau',\tau_f) \tag{6.39}$$

[2] $\phi_j^S(\tau',\tau_f)$ should be seen as a field with respect to the coordinate τ', while the stopping time τ_f acts as a fixed parameter.

for all $\tau' < \tau_f + \Delta t$. The field $\phi_j^S(\tau', \tau_f)$ is then used to compute ξ_i^{+S} and Ξ_{ij}^S. With these quantities, one can in turn produce a better approximation of $\phi_j^S(\tau', \tau_f + \Delta t)$ according to the saddle point equation (6.30). This procedure can be iterated until the field configuration has converged to a desired level of accuracy. The convergence of the recursion is determined by defining a quantity ε which measures how much the approximate saddle point field varies after an iteration of the algorithm. For example, a suitable definition is

$$\varepsilon \equiv \frac{1}{k} \sum_{m=1}^{k} |\bar{\phi}^S(\tau_m) - \phi^S(\tau_m)| \tag{6.40}$$

where ϕ^S and $\bar{\phi}^S$ are the old and updated estimates of the SP field respectively, evaluated at the discrete times τ_m. Convergence is then defined as $\varepsilon < \varepsilon^*$ where ε^* is a threshold of choice. The runtime of this recursive algorithm scales quadratically with the number of time steps n; this is because for each $1 < k < n$ one needs to perform k calculations in order to compute ξ_i^{+S}, so that summing over all k the total number of calculations to perform is of order $n(n+1)/2$. In principle, the computational cost is further increased by having to repeat each step multiple times to attain convergence. However, for reasonable values of the threshold ε^*, numerical simulations show that the recursive algorithm has rapid convergence, typically requiring only $1-2$ iterations.

A significant speed-up to the naive implementation of the algorithm described above can be obtained by inspecting the behaviour of $\phi^S(\tau', \tau_f)$. As a first observation, the direct recursive solution of the SP equation shows that, up to numerical precision, the saddle point field ϕ_i^S has a single non-zero component and the trajectory ξ_i^{+S} is symmetric with respect to the site indices i. It can be shown that these findings are due to the translational invariance of the TFIC, which makes it possible to derive a simpler form of the saddle point equation; this will be discussed in Section 6.2.3. From recursively solving the SP equation, we also find that for sufficiently large τ_f the value $\phi^S(\tau', \tau_f)$ with $\tau' \ll \tau_f$ no longer changes with τ_f and it settles to a value $\phi^S(\tau', \infty) \equiv \phi^S(\tau')$, as illustrated in Fig. 6.1(a). This means that, when recursively solving the SP equation, we don't have to update the entire SP field configuration but only its value at the times τ' such that $\phi^S(\tau', \tau_f) \neq \phi^S(\tau')$ to a desired level of precision. This leads to a substantial reduction in the computational cost of the recursive solution.

The SP equation (6.30) prescribes that the value of the saddle point field $\phi^S(\tau_f, \tau_f)$ at the end time is always the classical one ϕ^C defined above. Thus, the saddle point field $\phi^S(\tau', \tau_f)$ can never attain a steady state, i.e. for finite τ_f there exists no time scale τ_{SS} such that $\partial_{\tau'} \phi(\tau', \tau_f) \approx 0 \; \forall \; \tau' > \tau_{SS}$. However, numerical calculations show that for sufficiently

large τ_f the SP field $\phi^S(\tau', \tau_f)$ has a *plateau* at times $0 \ll \tau' \ll \tau_f$. This is shown in Fig. 6.1(b). The extent of this plateau grows as τ_f is increased; since the action is extensive in time, the plateau value provides the dominant contribution to observables in the large τ_f limit. Crucially, the plateau value of ϕ_S can be found analytically, as it will be illustrated in Section 6.2.4.

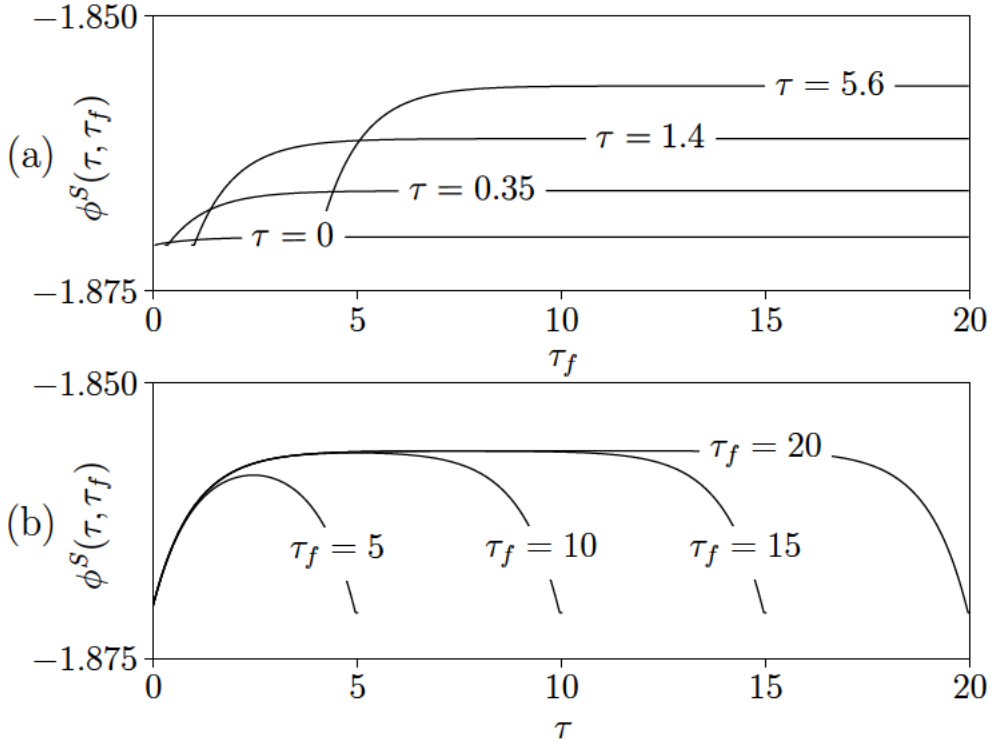

Figure 6.1: Behaviour of the saddle point field $\phi^S(\tau, \tau_f)$ obtained from the recursive solution of the saddle point equation for $\Gamma = \Gamma_c/2$ and $N = 7$. We plot the only component of $\phi^S(\tau, \tau_f)$ which is non-vanishing (see the relevant discussion in Section 6.2.3). (a) For sufficiently large stopping time τ_f, the saddle point field $\phi^S(\tau, \tau_f)$ at times $\tau \ll \tau_f$ attains a τ_f-independent value and can be considered to have converged. (b) At short times $0 \lesssim \tau$, we see a transient behaviour in the SP field which depends on the initial conditions and corresponds to the imaginary time evolution of the initial state towards the ground state. At late times $\tau \lesssim \tau_f$, the SP field is affected by the constraint $\phi^S(\tau_f, \tau_f) = \phi^C$. For intermediate times $0 \ll \tau \ll \tau_f$ the saddle point field attains a plateau value, which gives the main contribution to observables as $\tau_f \to \infty$.

6.2.3 Translationally Invariant Saddle Point Equations

The SP equation for the Loschmidt amplitude,

$$\phi_j^S(\tau', \tau_f) = \frac{\Gamma}{2}\sum_i \int_0^{\tau_f} \mathrm{d}\tau \Xi_{ij}(\tau, \tau')\Big|_{\phi^S} - \frac{1}{2}\sum_i O_{ij}, \tag{6.30}$$

can be significantly simplified by exploiting the translational invariance of the quantum Ising model. Because of this property, we can expect that the value of the disentangling variables at the saddle point will be symmetric, $\xi_i^{+S} \equiv \xi_S^+$ for all sites i. Furthermore, due to the symmetry of the interaction matrix $\mathcal{J}_{ij}$, in general one has $\sum_i O_{ij} = \delta_{j1}\sqrt{2NJ}$ where $j = 1$ is the unique component for which $O_{i1} = \sqrt{\frac{2J}{N}}$ (this always exists and can be chosen to be the first component - see Appendix B.2). Thus, at $\tau_f = 0$, only the first component of ϕ_j^S has a non-zero value. Since ϕ_j^S determines Ξ_{ij}, it follows that $\Xi_{ij} \propto \delta_{j1}$. This, combined with the symmetry of ξ_S^+, implies that also Ξ_{ij}^S takes a single value Ξ_S. Equation (6.30) entails that the properties we found for $\tau_f = 0$ propagate to later times, such that e.g. $\phi_j^S(\tau) = \delta_{j1}\phi_1^S(\tau) \equiv \delta_{j1}\phi_S(\tau)$. This argument immediately generalises to D dimensions: due to symmetry, the saddle pont equation for a system of $N = N_1 \times \cdots \times N_D$ spins, parameterised by the coordinates ξ_i^a and where the interactions are represented by $N \times D$ fields, can be reduced to a problem involving a single set of coordinates ξ_S^a interacting with D fields.

To summarise, the simplified translationally invariant saddle point (TISP) equations are obtained from the general case by means of the replacements

$$\phi_j^S = \phi_S \delta_{j1}, \tag{6.41}$$

$$\xi_j^{aS} = \xi_S^a, \tag{6.42}$$

$$\sum_j O_{ij}\phi_j^S = \sqrt{\frac{2J}{N}}\phi_S, \tag{6.43}$$

$$\sum_i O_{ij} = \delta_{j1}\sqrt{2NJ}, \tag{6.44}$$

$$\Xi_{ij}^S = \delta_{j1}\Xi_S. \tag{6.45}$$

Performing these substitutions, the system of Euclidean TISP equations for the Loschmidt amplitude is given by

$$\phi_S(\tau') = -\sqrt{\frac{NJ}{2}} + \frac{N\Gamma}{2}\int_0^{\tau_f} \mathrm{d}\tau \Xi_S(\tau,\tau'), \tag{6.46}$$

$$\frac{d}{dt}\xi_S^+ = \frac{\Gamma}{2}(1-\xi_S^{+2}) + \sqrt{\frac{2J}{N}}\xi_S^+\phi_S, \tag{6.47}$$

$$\Xi_S(\tau,\tau') = \sqrt{\frac{2J}{N}}\xi_S^+(\tau')\theta(\tau-\tau')\exp\int_{\tau'}^{\tau}[-\Gamma\xi_S^+(s)+\sqrt{2J/N}\phi^S(s)]\mathrm{d}s. \tag{6.48}$$

6.2.4 Plateau of the Saddle Point Trajectory

As discussed in Section 6.2.2, numerical simulations show that the solution $\phi_S(\tau,\tau_f)$ of the saddle point equation has a plateau for $0 \ll \tau \ll \tau_f$, while at short times it shows transient behaviour and at late times is constrained by the boundary conditions.

We can exploit this observation to reduce the saddle point equation, an integro-differential equation as it features the time integral of the functional derivative $\Xi_S \equiv \frac{\delta\xi_S^+}{\delta\phi_S}$, to an algebraic equation for the plateau value $\phi_P \equiv \lim_{\tau\to\infty}\lim_{\tau_f\to\infty}\phi_S(\tau,\tau_f)$ (this ordering of the limits is essential to remove the effect of the boundary condition).

The TISP equation for the imaginary-time Loschmidt echo is given by

$$\phi_S(\tau') = -\sqrt{\frac{NJ}{2}} + \frac{N\Gamma}{2}\int_0^{\tau_f} \mathrm{d}\tau \Xi_S(\tau,\tau'), \tag{6.46}$$

where

$$\Xi_S(\tau,\tau') = \sqrt{\frac{2J}{N}}\xi_S(\tau')\theta(\tau-\tau')\exp\int_{\tau'}^{\tau}\gamma_S(s)\mathrm{d}s \tag{6.49}$$

and we have defined $\gamma_S \equiv -\Gamma\xi_S^+ + \sqrt{2J/N}\phi_S$ for notational convenience. Consider $\tau_f \gg \tau' \gg 0$. All quantities at τ' can be assumed to have reached their constant plateau value, indexed by the subscript P. We can thus approximate

$$\Xi_P(\tau,\tau') \sim \sqrt{\frac{2J}{N}}\xi_P\theta(\tau-\tau')e^{(\tau-\tau')\gamma_P}. \tag{6.50}$$

Inserting this in the saddle point equation and assuming $\gamma_P < 0$, we get

$$\phi_P \sim N\frac{\Gamma}{2}\sqrt{\frac{2J}{N}}\xi_P^+ \int_{\tau'}^{\infty} \mathrm{d}\tau e^{(\tau-\tau')\gamma_P} - \frac{1}{2}\sum_i O_{i1} \tag{6.51}$$

$$= -\sqrt{\frac{JN}{2}}\left(\Gamma\frac{\xi_P^+}{\gamma_P}+1\right). \tag{6.52}$$

We can find an independent condition on the plateau values of ϕ_S, ξ_S^+ by imposing $\dot{\xi}_P^+ = 0$ in the equation of motion (6.47):

$$\frac{\Gamma}{2}[1-(\xi_P^+)^2] + \xi_P^+\sqrt{\frac{2J}{N}}\phi_P = 0. \tag{6.53}$$

Defining $\bar{\phi}_P \equiv \sqrt{\frac{2}{JN}}\phi_P$, we obtain the system of equations

$$\bar{\phi}_P = -\frac{\Gamma}{2J}\frac{1-(\xi_P^+)^2}{\xi_P^+}, \tag{6.54a}$$

$$\bar{\phi}_P = \left(\frac{J\bar{\phi}_P}{\Gamma\xi_P^+ - J\bar{\phi}_P}\right). \tag{6.54b}$$

This can be solved analytically, yielding

$$\xi_P^+ = \begin{cases} -1 \\ 1 \\ \frac{1-\sqrt{1-\bar{\Gamma}^2}}{\bar{\Gamma}} \\ \frac{1+\sqrt{1-\bar{\Gamma}^2}}{\bar{\Gamma}} \end{cases} \quad \bar{\phi}_P = \begin{cases} 0 \\ 0 \\ -\sqrt{1-\bar{\Gamma}^2} \\ \sqrt{1-\bar{\Gamma}^2} \end{cases} \quad \gamma_P = \begin{cases} \Gamma \\ -\Gamma \\ -J \\ -J \end{cases} \tag{6.55}$$

with $\bar{\Gamma} = \Gamma/J$. We see that the plateau solutions exhibit a transition at $\bar{\Gamma} = 1$, different from the quantum phase transition of the Ising model at $\bar{\Gamma} = 1/2$; for $\bar{\Gamma} < 1$ there are four real-valued solutions while for $\bar{\Gamma} > 1$ there are only the two solutions $\xi_P^+ = \pm 1$, $\phi_P = 0$, corresponding to the non-interacting result. The solution $\xi_P^+ = -1$ cannot be accepted as it gives a positive γ_P, which goes against the assumptions of the above derivation.

The Loschmidt action estimated from the plateau values $S_P \sim \tau_f(\phi_P^2 + N\gamma_P)/2$ can be obtained using the results in Eq. (6.55), yielding the two solutions

$$S_P \sim \begin{cases} -N\tau_f\Gamma/2 \quad \text{for all} \quad \Gamma \\ -N\tau_f\frac{J^2+\Gamma^2}{4J} \quad \text{for} \quad \Gamma \leq J, \end{cases} \tag{6.56}$$

since the actions obtained from the third and fourth cases of Eq. (6.55) take the same value. We see that the first action is greater for $\Gamma > J$ while the second is greater for $\Gamma < J$. The saddle point trajectories corresponding to these two cases turn out to be the same ones that are obtained numerically from the recursive solution scheme of Section 6.2.2. As a check, we repeated the above calculation without assuming translational invariance, finding that additional non-symmetric plateau solutions exist. These were however found to either yield a complex action, which is not acceptable as it would give a complex ground state energy, or to correspond to maxima of the action.

6.3 Beyond the Saddle Point

We have discussed how to solve the saddle point equation for the effective Loschmidt action (6.28) to obtain the saddle point trajectory. Once this is known, we can proceed following the approaches outlined in Section 6.1. In order to obtain an analytical approximation to the ground state energy, we can evaluate the functional determinant accounting for the Gaussian fluctuations around the SP trajectory. Alternatively, we can use the SP trajectory to perform an exact measure transformation leading to enhanced sampling efficiency. In this Section, we will discuss both these approaches in turn.

6.3.1 Evaluation of the Fluctuation Determinant

The approximation obtained by expanding the action to second order around the SP trajectory is given by

$$A(\tau) \sim e^{-S_S} \det \Big[\frac{\delta^2 S}{\delta\phi_k(\tau_2)\delta\phi_j(\tau_1)}\Big|_{SP} \Big]^{-\frac{1}{2}}, \tag{6.57}$$

so that, for large τ_f, ε_G can be expressed as

$$N\tau_f\varepsilon_G = S_S + \frac{1}{2}\log\det \frac{\delta^2 S}{\delta\phi_k(\tau_2)\delta\phi_j(\tau_1)}\Big|_{SP} \tag{6.58}$$

$$= S_S + \frac{1}{2}\mathrm{Tr}\log \frac{\delta^2 S}{\delta\phi_k(\tau_2)\delta\phi_j(\tau_1)}\Big|_{SP}. \tag{6.59}$$

The second variation of the imaginary time Loschmidt effective action is given by

$$\frac{\delta^2 S}{\delta\phi_k(\tau_2)\delta\phi_j(\tau_1)} = \delta_{jk}\delta(\tau_2-\tau_1) - \frac{\Gamma}{2}\sum_i \int_0^{\tau_f} \mathrm{d}\tau \frac{\delta}{\delta\phi_k(\tau_2)}\frac{\delta}{\delta\phi_j(\tau_1)}\xi_i^+(\tau). \tag{6.60}$$

In turn, this involves the second variation of ξ_i^+, given by

$$\begin{aligned}\frac{\delta^2\xi_i^+(\tau)}{\delta\phi_k(\tau_2)\delta\phi_j(\tau_1)} &= \frac{\delta}{\delta\phi_k(\tau_2)}\Xi_{ij}(\tau,\tau_1) &(6.61)\\ &= \theta(\tau-\tau_1)O_{ij}e^{\int_{\tau_1}^{\tau}\gamma_i(s)\mathrm{d}s}\Big[O_{ik}\theta(\tau_1-\tau_2)\xi_i^+(\tau_2)e^{\int_{\tau_2}^{\tau_1}\gamma_i(s)\mathrm{d}s} \\ &\quad -\Gamma\xi_i^+(\tau_1)O_{ik}\theta(\tau-\tau_2)\int_{\tau_1}^{\tau}\theta(s-\tau_2)\xi_i^+(\tau_2)e^{\int_{\tau_2}^{s}\gamma_i(s')\mathrm{d}s'}\mathrm{d}s &(6.62)\\ &\quad +\xi_i^+(\tau_1)O_{ik}\theta(\tau_2-\tau_1)\theta(\tau-\tau_2)\Big],\end{aligned}$$

where we used the exact form of Ξ_{ij} given by Eq. (6.33). At the saddle point, we have

$$\left.\frac{\delta^2 S}{\delta\phi_k(\tau_2)\delta\phi_j(\tau_1)}\right|_{SP} = \delta_{jk}\delta(\tau_2-\tau_1) - \Gamma\delta_{jk}\lambda_j\int_0^{\tau_f}\mathrm{d}\tau\theta(\tau-\tau_1)e^{\int_{\tau_1}^{\tau}\gamma_S(s)\mathrm{d}s}I_S(\tau,\tau_1,\tau_2), \tag{6.63}$$

with

$$\begin{aligned}I_S(\tau,\tau_1,\tau_2) \equiv&\theta(\tau_1-\tau_2)\xi_S^+(\tau_2)e^{\int_{\tau_2}^{\tau_1}\gamma_S(s)\mathrm{d}s} \\ &-\Gamma\theta(\tau-\tau_2)\xi_S^+(\tau_1)\xi_S^+(\tau_2)\int_{\tau_1}^{\tau}\theta(s-\tau_2)e^{\int_{\tau_2}^{s}\gamma_S(s')\mathrm{d}s'}\mathrm{d}s &(6.64)\\ &+\theta(\tau-\tau_2)\theta(\tau_2-\tau_1)\xi_S^+(\tau_1).\end{aligned}$$

In the above, we used $\sum_i O_{ij}O_{ik} = 2\lambda_j\delta_{jk}$, where λ_j are the eigenvalues of the interaction matrix $\mathcal{J}_{ij}$ (Appendix B). We can define

$$\left.\frac{\delta^2 S}{\delta\phi_k(\tau_2)\delta\phi_j(\tau_1)}\right|_{SP} \equiv \delta_{jk}\delta(\tau_2-\tau_1) - \delta_{jk}\Delta_j^S(\tau_1,\tau_2). \tag{6.65}$$

Letting $\tau_f\to\infty$ and assuming that the plateau value of all variables gives the dominant contribution in this limit, we get

$$\Delta_j^S(\tau_1,\tau_2)\Big|_P = -\Gamma\lambda_j\xi_P^+\left[\theta(\tau_1-\tau_2)\frac{e^{(\tau_1-\tau_2)\gamma_P}}{\gamma_P} + \Big(\tau_1\leftrightarrow\tau_2\Big) + \frac{\Gamma\xi_P^+}{2\gamma_P^2}e^{[2\max(\tau_1,\tau_2)-\tau_1-\tau_2]\gamma_P}\right]. \tag{6.66}$$

We can expand Eq. (6.59) as [156]

$$N\tau_f\varepsilon_G = S_S + \frac{1}{2}\mathrm{Tr}\log\Big[\frac{\delta^2 S}{\delta\phi_k(\tau_2)\delta\phi_j(\tau_1)}\Big|_{SP}\Big] \tag{6.67}$$

$$= S_S + \frac{1}{2}\mathrm{Tr}\log\big(\delta_{jk}\delta(\tau_2-\tau_1) - \delta_{jk}\Delta_j(\tau_1,\tau_2)\big) \tag{6.68}$$

$$= S_S - \frac{1}{2}\sum_j \mathrm{Tr}\left(\Delta_j + \frac{1}{2}\Delta_j\cdot\Delta_j + \dots\right) \tag{6.69}$$

$$\equiv S_S - (T_1 + T_2 + \dots), \tag{6.70}$$

where we used the definition of the logarithm as a Taylor series, and we defined the shorthand $a\cdot b = \int_0^{\tau_f} a(\tau_1,s)b(s,\tau_2)\,\mathrm{d}s$ and the quantities T_i. We can readily see that $T_1 = 0$ because of the identity[3] $\sum_j \lambda_j = \mathrm{Tr}(\mathcal{J})$. The lowest-order correction to the ground state energy density is then given by T_2. Using $\sum_j \lambda_j^2 = \mathrm{Tr}(\mathcal{J}^2) = NJ^2/2$, we obtain

$$T_2 = -\frac{\Gamma^2\xi_P^{+2}(\gamma_P + \xi_P^+\Gamma/2)^2}{4\gamma_P^5}\tau_f + O(\tau_f^0), \tag{6.71}$$

where the terms $O(\tau_f^0)$ do not contribute to the ground state energy. Evaluating the above using the plateau values from Eq. (6.55), we get

$$\varepsilon_G \sim \varepsilon_G^{(2)}(\Gamma,J) = \max\left(-\frac{\Gamma}{2} - \frac{J^2}{32\Gamma}, -\frac{\Gamma^4}{32J^3} - \frac{\Gamma^2+J^2}{4J}\right), \tag{6.72}$$

where for any Γ, J we select the greater of the two saddle point values due to the exponential suppression of any subleading contribution when considering the logarithm of Eq. (6.11). This expression matches the result of second order perturbation theory [69] for $\Gamma \to 0$ and $\Gamma \to \infty$. The fluctuation determinant appears to contain a simultaneous expansion in large Γ and small Γ. However, the terms T_i in Eq. (6.70) are not in one-to-one correspondence with the terms of a perturbative expansion. This can be readily seen by considering e.g. the tree level result including only S_S; this coincides with the result of second order perturbation theory for small Γ but is merely the non-interacting value for large Γ. Figure 6.2 shows the comparison between the approximate result $\varepsilon_G^{(2)}$ and the exact ground state energy obtained

[3] For sums of higher powers of the eigenvalues, this generalises to $\sum_j \lambda_j^a = \mathrm{Tr}(\mathcal{J}^a)$. To compute $\mathrm{Tr}(\mathcal{J}^a) = 0$, we note that for the quantum Ising model $\mathcal{J}^2 \sim \delta_{ij-2} + 2\delta_{ij} + \delta_{ij+2}$, $\mathcal{J}^3 \sim \delta_{ij-3} + 3\delta_{ij-1} + 3\delta_{ij+1} + \delta_{ij+3}$, i.e. $\mathcal{J}^b$ is non-zero only in the diagonals above and below the non-zero diagonals of $\mathcal{J}^{b-1}$. Iterating, we find that all odd powers $\mathcal{J}^a$ have vanishing trace up to $a = N$, where N is the dimension of the matrix $\mathcal{J}$, due to the effect of the periodic boundary conditions. For finite N, odd terms give a finite size correction.

from free fermions. The discrepancy is $\sim 1.2\%$ for $\Gamma = \Gamma_c \equiv J/2$. Interestingly, for intermediate values of Γ the subleading terms are found to give a better approximation to the exact result than the leading terms. This is likely to be an artifact due to the truncation of Eq. (6.70); whether this can be improved by including additional terms T_i will be investigated in future work.

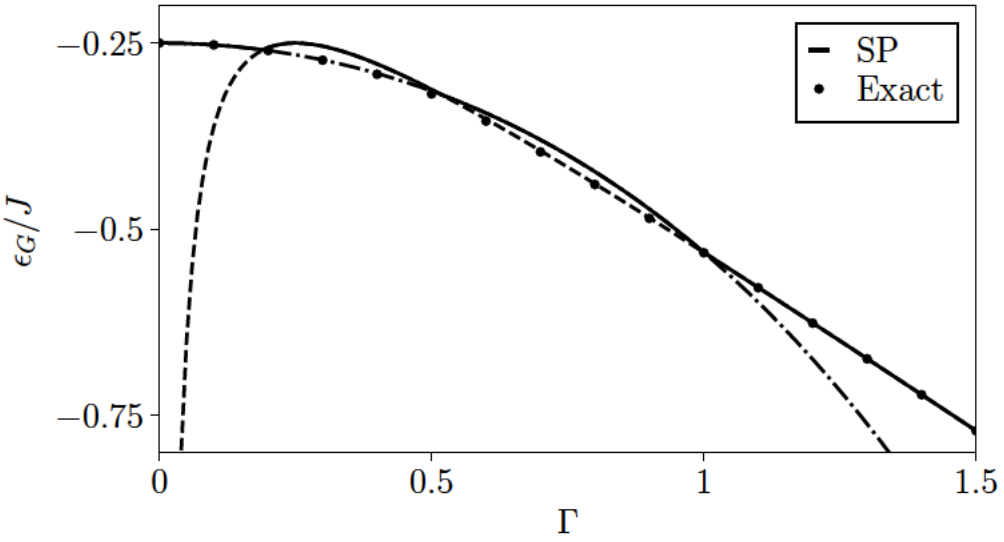

Figure 6.2: Ground state energy of the TFIC. We compare the exact result obtained from free fermions to the approximate one obtained from performing the Gaussian integral around the saddle point trajectories, truncating the corresponding expansion to the second term. The dashed and dashed-dotted lines indicate the subleading contribution for each value of Γ, which is exponentially suppressed. The saddle point result is exact for both small and large Γ. For intermediate Γ, the subleading terms give a better approximation to the exact result than the leading terms.

We conclude this Section by discussing the validity of the saddle point approximation we applied. Indeed, we did not explicitly identify an expansion parameter to justify this procedure, and a priori we might expect terms beyond Gaussian fluctuations to be important. Consider once again the Loschmidt action

$$S_{\text{losch}} = \frac{1}{2}\int_0^\tau \mathrm{d}\tau' \left(\sum_i \phi_i^2(\tau') - \Gamma \sum_i \xi_i^+(\tau') + \sqrt{2JN}\phi_1(\tau') \right), \tag{6.28}$$

where we exploited the property $\sum_i O_{ij} = \delta_{j1}\sqrt{2JN}$ to simplify the expression. Except for the term proportional to ϕ_1, this is a sum of N terms that are typically of order 1. Hence, we may speculate that the large parameter justifying the saddle point approxim-

ation is the system size N. Indeed, we found that both the saddle point action and the first contribution to the quadratic correction are $O(N)$. The quadratic correction, which normally is subleading with respect to the saddle point trajectory in the limit in which the approximation becomes exact, here is of the same order because the N fields ϕ_i give rise to a product of N functional determinants. If the saddle point approximation we performed were indeed a large N expansion, Eq. (6.70) would give the exact ground state energy in the thermodynamic limit when all terms T_i are included. In this case, it may be possible to establish an interpretation of quantum phase transitions in terms of the crossing between two saddle point trajectories: upon approaching a particular value of Γ, the trajectory that is dominant in a regime becomes subleading and the resulting ground state energy changes in a non-analytic fashion. It should be possible to clarify this point analytically; this will be pursued in future work. If this were found to be the case, a similar argument could apply in real time to explain dynamical quantum phase transitions (see Chapter 1), providing a unified framework valid both in and out of equilibrium.

6.3.2 Stochastic Sampling Around the Saddle Point Trajectory

Instead of truncating the expansion of the action, we can use the saddle point field ϕ_j^S to perform a measure transformation. In this case, there is no need to justify the saddle point approximation; the SP trajectory is just a convenient choice around which to perform the sampling. For the Euclidean Loschmidt amplitude and the quantum Ising model, we have

$$A(\tau_f) = \langle e^{-\sum_i \xi_i^z(\tau_f)/2} \rangle_\phi \tag{6.73}$$

$$= \int \mathcal{D}\phi' e^{-\frac{1}{2}\int \mathrm{d}\tau \sum_i (\phi_i'(\tau)+\phi_i^S(\tau))^2} e^{-\frac{1}{2}\sum_i \xi_i^z[\phi'+\phi^S]} \tag{6.74}$$

$$= e^{-\frac{1}{2}\int \mathrm{d}\tau \phi_S(\tau)^2} \langle e^{-\int \mathrm{d}\tau \sum_i \phi_i^S(\tau)\phi_i'(\tau)} e^{-\frac{1}{2}\sum_i \xi_i^z[\phi'+\phi^S]} \rangle_{\phi'}. \tag{6.75}$$

The Loschmidt rate function $\lambda(\tau)$ sampled according to Eq. (6.75) is shown in Fig. 6.3. The estimate of the ground state energy obtained from the saddle point trajectory alone, corresponding to truncating Eq. (6.70) at tree level, is already rather close to the ED result. After using this to perform a measure transformation, a small number of simulations taking about 20 seconds is sufficient to reduce the error to $< 0.1\%$. This is substantially more efficient than the the direct solution of the SDEs as shown in Fig. 5.2, where 10^6 simulations are not sufficient to accurately reproduce ED for the same problem considered here. The transformation based on the saddle point trajectory also leads to a significant improvement in sampling efficiency over the variance-reducing transformation (Fig. 5.6).

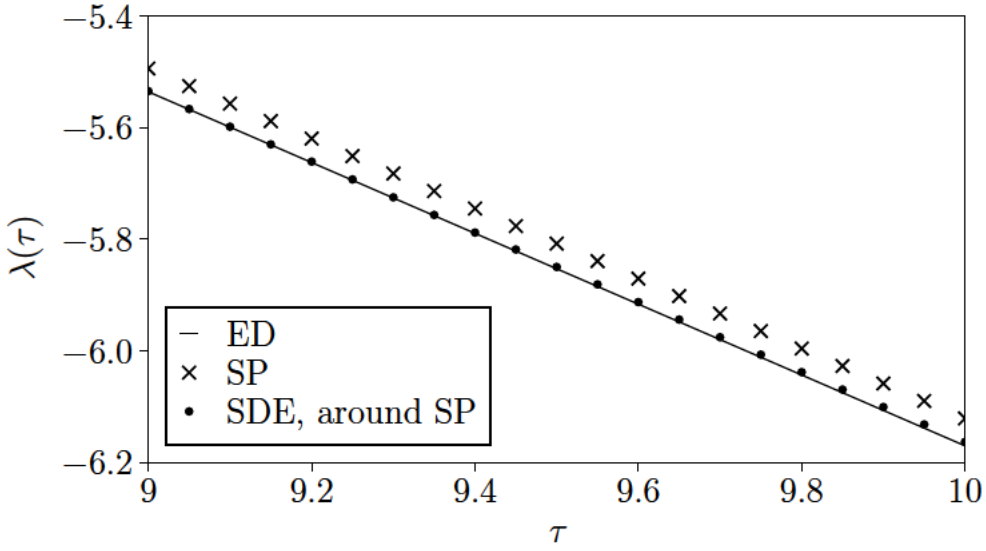

Figure 6.3: Imaginary time Loschmidt rate function for a TFIC with $N = 21$ spins, initialised in the all-down state $|\Downarrow\rangle$ and evolved with $\Gamma = \Gamma_c$. We compare the purely saddle point result, corresponding to truncating Eq. (6.70) at tree level, and the value obtained from sampling the SDEs around the saddle point. In this figure, we only show late times to make the difference between the SP and SDE results visible on the scale of the plot. The saddle point field was computed using the recursive algorithm presented in the main text and used to perform the measure transformation in Eq. (6.75). The SDE result was obtained from averaging 200 trajectories with $\Delta t = 0.1$. The recursive calculation of the saddle point trajectory took ~ 2 minutes and the subsequent simulations took < 20 seconds using a single core. This is a substantial improvement over the direct sampling of the SDEs shown in Fig. 5.2 for the same problem, where a substantially longer computation, lasting several hours on a supercomputer, is not sufficient to reproduce the ED result.

Using this technique, the stochastic approach can be efficiently applied to compute ground state energies for large systems. We demonstrate this in Fig. 6.4 by considering a TFIC with $N = 150$ spins. We show the approach of the ratio $\lambda(\tau)/2\tau$ to the ground state energy density at late imaginary times, as per Eq. (6.23), comparing our calculation to the exact free fermionic result. We find that, for $\tau = 15$, the SDE result has converged to the infinite time limit up to 0.1% for $\Gamma = \Gamma_c/4$ and 0.4% for $\Gamma = \Gamma_c/2$. This precision can be systematically improved by extending the simulation to later imaginary times τ, which only costs a linear increase in computation time.

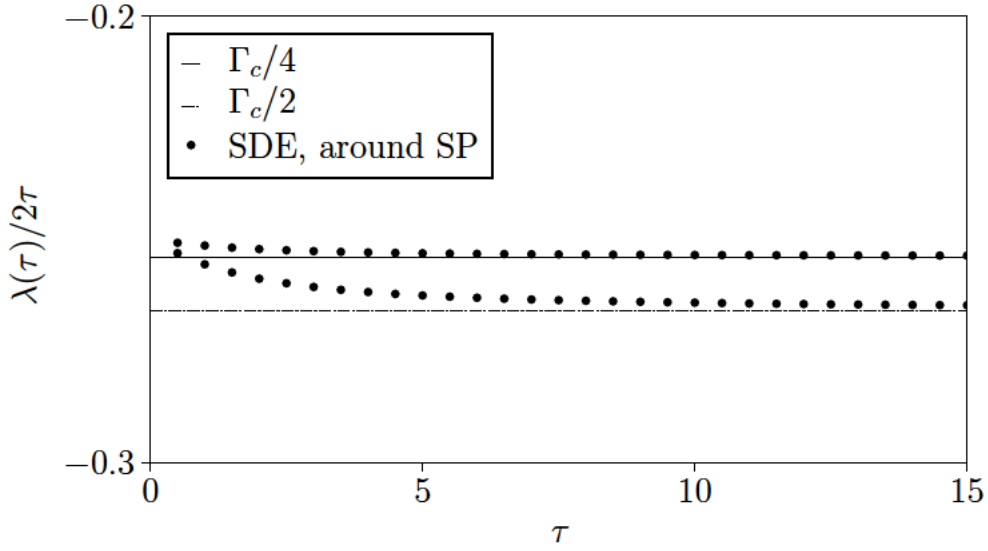

Figure 6.4: Computation of the ground state energy for a TFIC with $N = 150$ spins by sampling around the saddle point trajectory. The system was initialised in the all-down state $|\Downarrow\rangle$ and evolved with different values of $\Gamma = \Gamma_c$. At late times, the ratio $\lambda(\tau)/2\tau$ approaches the ground state energy density. We compare the result of our simulations (dots) at $\tau = 15$ to the exact ground state energy obtained from free fermions (horizontal lines); for $\Gamma = \Gamma_c/4$ and $\Gamma = \Gamma_c/2$, the discrepancy between the SDE and the free fermionic result is 0.1% and 0.4% respectively. As Γ approaches the critical point, longer imaginary times τ are required to attain comparable precision; this however only amounts to a linear increase in computation time. Our simulations were performed on the basis of the measure transformation in Eq. (6.75). For each value of Γ, the SDE result was obtained by averaging 1000 trajectories with $\Delta t = 0.05$, whose generation took $\sim$15 minutes using a single core.

6.4 Further Developments

In this Chapter, we have introduced a technique based on finding the saddle point trajectory of an effective action corresponding to a particular observable. We have discussed how the saddle point field can be computed, showing that simplifications arise for translationally invariant systems and at late times. Using the saddle point trajectory to perform an exact measure transformation, the sampling efficiency of the stochastic approach can be substantially improved, as we demonstrated by computing ground state energies for a system of $N = 150$ spins.

We conclude our discussion by outlining further directions for the application of the saddle point method combined to the stochastic approach. An immediate first generalisation is the calculation of observables beyond the ground state energy; the procedure we discussed can be carried out in complete analogy to the case of the Loschmidt amplitude

by defining the appropriate effective action as in Eq. (6.14). The saddle point method could also be applied to other models, including those in higher dimensions. For translationally invariant systems, the argument of Section 6.2.3 generalises and TISP equations can be obtained, leading to a substantial simplification of the problem. Another interesting direction is investigating the possibility of sampling directly around the plateau value, combining the advantages of the analytical approach, which does not require the recursive calculation of a transient, with the exactness of the stochastic formulation. With this modification, the stochastic technique would be able to circumvent the issue of critical slowing down in approaching the infinite τ limit, which affects other numerical methods in the vicinity of critical points. Finally, a key development will be the generalisation of this approach to real time evolution, in order to study non-equilibrium quantum systems.

Chapter 7

Conclusions

In this Thesis, we have investigated an exact mapping of quantum spin systems to stochastic processes [2–4], whereby quantum expectation values are expressed as averages over classical stochastic trajectories, parameterised by a set of *disentangling variables*.

In Chapter 2 we discussed the general framework of the method, providing formulae of broad applicability for different operators and observables. In order to investigate the stochastic approach, in Chapter 3 we considered a specific model, the transverse field Ising chain. For this system, we studied the behaviour of the stochastic differential equations which describe the quantum evolution, deriving insights from both exact and approximate approaches. We found that, while in imaginary time the behaviour of the disentangling variables becomes approximately Gaussian for large transverse fields Γ, in real time Gaussianity breaks down at some particular times.

In Chapter 4 we investigated this by numerically solving the real time Ising SDEs, finding that for large Γ the breakdown of Gaussianity, together with a number of other distinctive signatures in the disentangling variables, is associated with the presence of dynamical quantum phase transitions [5]. By numerically solving the real time SDEs, we computed quantum observables such as the Loschmidt amplitude and the magnetisation, demonstrating that the stochastic approach can in principle be applied to a wide range of problems in both integrable and non-integrable settings, including higher dimensional and disordered systems. We investigated the computational efficiency of this numerical implementation of the stochastic approach, finding evidence of the exponential growth of fluctuations with time and the system size.

In order to develop intuition about how fluctuations can be controlled, in Chapter 5 we then turned to considering imaginary time evolution, demonstrating that the Euclidean SDEs can be used to compute ground state properties of quantum spin systems, including

the energy and magnetisation. In this context, we showed that measure transformations can be used to significantly improve the numerical performance of the stochastic method.

Building on these developments, in Chapter 6 we introduced a saddle point technique based on identifying the trajectory which gives the largest contribution to a given average. We showed that this method can dramatically improve the sampling efficiency of the stochastic approach while retaining its exactness, making it possible to access late imaginary times and large systems. We demonstrated this by computing ground state energies for a transverse field Ising chain with $N = 150$ spins.

Thanks to the very general applicability of the stochastic approach, there are many directions for future developments. As we showed, the main bottleneck of the method is the large number of simulations required to compute observables, due to the effect of fluctuations. However, we have demonstrated that for imaginary time evolution the sampling efficiency can be improved significantly by means of appropriate transformations. An important development would then be generalising this technique to real time evolution; if a better sampling efficiency can be achieved, it will be possible to apply the stochastic formalism to a plethora of problems, including higher dimensional and disordered systems, to investigate issues such as the relaxation dynamics and the breakdown of ergodicity in non-equilibrium quantum systems.

Bibliography

[1] S. De Nicola, B. Doyon, and M. J. Bhaseen, arXiv:1805.05350v1 .

[2] P. M. Hogan and J. T. Chalker, J. Phys. A: Math. Gen. **37**, 11751 (2004).

[3] V. Galitski, Phys. Rev. A **84**, 012118 (2011).

[4] M. Ringel and V. Gritsev, Phys. Rev. A **88**, 062105 (2013).

[5] M. Heyl, A. Polkovnikov, and S. Kehrein, Phys. Rev. Lett. **110**, 135704 (2013).

[6] T. Kinoshita, T. Wenger, and D. S. Weiss, Nature **440**, 900 (2006).

[7] S. Hofferberth, I. Lesanovsky, B. Fischer, T. Schumm, and J. Schmiedmayer, Nature **449**, 324 (2007).

[8] C. N. Weiler, T. W. Neely, D. R. Scherer, A. S. Bradley, M. J. Davis, and B. P. Anderson, Nature **455**, 948 (2008).

[9] M. Johanning, A. F. Varón, and C. Wunderlich, J. Phys. B: At. Mol. Opt. Phys. **42**, 154009 (2009).

[10] W. S. Bakr, J. I. Gillen, A. Peng, S. Fölling, and M. Greiner, Nature **462**, 74 (2009).

[11] W. S. Bakr, A. Peng, M. E. Tai, R. Ma, J. Simon, J. I. Gillen, S. Fölling, L. Pollet, and M. Greiner, Science **329**, 547 (2010).

[12] C. Weitenberg, M. Endres, J. F. Sherson, M. Cheneau, P. Schausz, T. Fukuhara, I. Bloch, and S. Kuhr, Nature **471**, 319 (2011).

[13] R. Blatt and C. F. Roos, Nat. Phys. **8**, 277 (2012).

[14] I. Bloch, J. Dalibard, and S. Nascimbène, Nat. Phys. **8**, 267 (2012).

[15] G. Lamporesi, S. Donadello, S. Serafini, F. Dalfovo, and G. Ferrari, Nature Phys. **9**, 656 (2013).

[16] T. Langen, R. Geiger, and J. Schmiedmayer, Annu. Rev. Condens. Matter Phys. **6**, 201 (2015).

[17] M. Rigol, V. Dunjko, and M. Olshanii, Nature **452**, 854 (2008).

[18] A. Polkovnikov, K. Sengupta, A. Silva, and M. Vengalattore, Rev. Mod. Phys. **83**, 863 (2011).

[19] J. Eisert, M. Friesdorf, and C. Gogolin, Nature Phys. **11**, 124 (2015).

[20] P. Calabrese, F. H. L. Essler, and G. Mussardo, J. Stat. Mech. Theor. Exp. **2016**, 064001 (2016).

[21] U. Schollwöck, Ann. Phys. **326**, 96 (2011), January 2011 Special Issue.

[22] C. Gross and I. Bloch, Science **357**, 995 (2017).

[23] S. C., D. Porras, and T. Schaetz, Rep. Prog. Phys. **75**, 024401 (2012).

[24] C. Chin, R. Grimm, P. Julienne, and E. Tiesinga, Rev. Mod. Phys. **82**, 1225 (2010).

[25] I. Bloch, Nat. Phys. **1**, 23 EP (2005).

[26] M. Keil, O. Amit, S. Zhou, D. Groswasser, Y. Japha, and R. Folman, J. Mod. Opt. **63**, 1840 (2016).

[27] T. Schweigler, V. Kasper, S. Erne, I. Mazets, B. Rauer, F. Cataldini, T. Langen, T. Gasenzer, J. Berges, and J. Schmiedmayer, Nature **545**, 323 EP (2017).

[28] J. F. Sherson, C. Weitenberg, M. Endres, M. Cheneau, I. Bloch, and S. Kuhr, Nature **467**, 68 (2010).

[29] M. Greiner, O. Mandel, T. W. Hänsch, and I. Bloch, Nature **419**, 51 (2002).

[30] T. Esslinger, Annu. Rev. Condens. Matter Phys **1**, 129 (2010).

[31] M. Cheneau, P. Barmettler, D. Poletti, M. Endres, P. Schauß, T. Fukuhara, C. Gross, I. Bloch, C. Kollath, and S. Kuhr, Nature **481**, 484 (2012).

[32] U. Schneider, L. Hackermüller, J. P. Ronzheimer, S. Will, S. Braun, T. Best, I. Bloch, E. Demler, S. Mandt, D. Rasch, and A. Rosch, Nat. Phys. **8**, 213 (2012).

[33] J. P. Ronzheimer, M. Schreiber, S. Braun, S. S. Hodgman, S. Langer, I. P. McCulloch, F. Heidrich-Meisner, I. Bloch, and U. Schneider, Phys. Rev. Lett. **110**, 205301 (2013).

[34] F. Meinert, M. J. Mark, E. Kirilov, K. Lauber, P. Weinmann, A. J. Daley, and H.-C. Nägerl, Phys. Rev. Lett. **111**, 053003 (2013).

[35] T. Fukuhara, A. Kantian, M. Endres, M. Cheneau, P. Schauß, S. Hild, D. Bellem, U. Schollwöck, T. Giamarchi, C. Gross, I. Bloch, and S. Kuhr, Nat. Phys. **9**, 235 EP (2013).

[36] Y. Aharonov and D. Bohm, Phys. Rev. **115**, 485 (1959).

[37] J. I. Cirac and P. Zoller, Phys. Rev. Lett. **74**, 4091 (1995).

[38] H. Häffner, C. Roos, and R. Blatt, Phys. Rep. **469**, 155 (2008).

[39] A. H. Myerson, D. J. Szwer, S. C. Webster, D. T. C. Allcock, M. J. Curtis, G. Imreh, J. A. Sherman, D. N. Stacey, A. M. Steane, and D. M. Lucas, Phys. Rev. Lett. **100**, 200502 (2008).

[40] R. Islam, E. Edwards, K. Kim, S. Korenblit, C. Noh, G.-D. Carmichael, H.and Lin, L.-M. Duan, C.-C. Joseph Wang, J. Freericks, and C. Monroe, Nat. Commun. **2**, 377 (2011).

[41] S. Ulm, G. Rossnagel, J.and Jacob, C. Degünther, S. T. Dawkins, U. G. Poschinger, R. Nigmatullin, A. Retzker, M. B. Plenio, F. Schmidt-Kaler, and K. Singer, Nat. Commun. **4**, 2290 (2013).

[42] E. H. Lieb and W. Liniger, Phys. Rev. **130**, 1605 (1963).

[43] E. H. Lieb, Phys. Rev. **130**, 1616 (1963).

[44] P. Calabrese and J. Cardy, J. Stat. Mech. Theor. Exp. **2005**, P04010 (2005).

[45] P. Calabrese and J. Cardy, Phys. Rev. Lett. **96**, 136801 (2006).

[46] G. De Chiara, S. Montangero, P. Calabrese, and R. Fazio, J. Stat. Mech. Theor. Exp. **2006**, P03001 (2006).

[47] M. A. Cazalilla, Phys. Rev. Lett. **97**, 156403 (2006).

[48] C. Kollath, A. M. Läuchli, and E. Altman, Phys. Rev. Lett. **98**, 180601 (2007).

[49] M. Rigol, V. Dunjko, V. Yurovsky, and M. Olshanii, Phys. Rev. Lett. **98**, 050405 (2007).

[50] M. Cramer, C. M. Dawson, J. Eisert, and T. J. Osborne, Phys. Rev. Lett. **100**, 030602 (2008).

[51] M. Moeckel and S. Kehrein, Phys. Rev. Lett. **100**, 175702 (2008).

[52] S. R. Manmana, S. Wessel, R. M. Noack, and A. Muramatsu, Phys. Rev. B **79**, 155104 (2009).

[53] P. Barmettler, M. Punk, V. Gritsev, E. Demler, and E. Altman, Phys. Rev. Lett. **102**, 130603 (2009).

[54] S. Sotiriadis, P. Calabrese, and J. Cardy, EPL **87**, 20002 (2009).

[55] L. F. Santos, A. Polkovnikov, and M. Rigol, Phys. Rev. Lett. **107**, 040601 (2011).

[56] A. Polkovnikov, K. Sengupta, A. Silva, and M. Vengalattore, Rev. Mod. Phys. **83**, 863 (2011).

[57] P. Calabrese, F. H. L. Essler, and M. Fagotti, Phys. Rev. Lett. **106**, 227203 (2011).

[58] J.-S. Caux and F. H. L. Essler, Phys. Rev. Lett. **110**, 257203 (2013).

[59] A. Mitra, Annu. Rev. Condens. Matter Phys **9**, 245 (2018).

[60] E. H. Lieb and D. W. Robinson, Commun. Math. Phys **28**, 251 (1972).

[61] D. Chandler, *Introduction to Modern Statistical Mechanics* (Oxford University Press, 1987).

[62] F. Essler, Lecture notes given at the Les Houches School "Integrability in Atomic and Condensed Matter Physics", to be published by Oxford University Press (2018).

[63] J. M. Deutsch, Phys. Rev. A **43**, 2046 (1991).

[64] M. Srednicki, Phys. Rev. E **50**, 888 (1994).

[65] M. Rigol, V. Dunjko, and M. Olshanii, Nature **452**, 854 (2008).

[66] E. Ilievski, J. De Nardis, B. Wouters, J.-S. Caux, F. H. L. Essler, and T. Prosen, Phys. Rev. Lett. **115**, 157201 (2015).

[67] M. Rigol, A. Muramatsu, and M. Olshanii, Phys. Rev. A **74**, 053616 (2006).

[68] L. Vidmar and M. Rigol, J. Stat. Mech. Theor. Exp. **2016**, 064007 (2016).

[69] S. Sachdev, *Quantum Phase Transitions*, 2nd ed. (Cambridge University Press, 2011).

[70] P. Calabrese, F. H. L. Essler, and M. Fagotti, J. Stat. Mech. Theor. Exp. **2012**, P07016 (2012).

[71] P. Calabrese, F. H. L. Essler, and M. Fagotti, J. Stat. Mech. Theor. Exp. **2012**, P07022 (2012).

[72] W. Heisenberg, Zeitschrift für Physik **49**, 619 (1928).

[73] H. Bethe, Zeitschrift für Physik **71**, 205 (1931).

[74] F. H. L. Essler and M. Fagotti, J. Stat. Mech. Theor. Exp. **2016**, 064002 (2016).

[75] E. Ilievski, M. Medenjak, T. Prosen, and L. Zadnik, J. Stat. Mech. Theor. Exp. **2016**, 064008 (2016).

[76] M. Moeckel and S. Kehrein, Ann. Phys. **324**, 2146 (2009).

[77] T. Langen, T. Gasenzer, and J. Schmiedmayer, J. Stat. Mech. Theor. Exp. **2016**, 064009 (2016).

[78] B. L. Altshuler, Y. Gefen, A. Kamenev, and L. S. Levitov, Phys. Rev. Lett. **78**, 2803 (1997).

[79] I. V. Gornyi, A. D. Mirlin, and D. G. Polyakov, Phys. Rev. Lett. **95**, 206603 (2005).

[80] D. Basko, I. Aleiner, and B. Altshuler, Ann. Phys. **321**, 1126 (2006).

[81] R. Nandkishore and D. A. Huse, Annu. Rev. Condens. Matter Phys **6**, 15 (2015).

[82] P. W. Anderson, Phys. Rev. **109**, 1492 (1958).

[83] A. Gambassi and A. Silva, Phys. Rev. Lett. **109**, 250602 (2012).

[84] E. G. Dalla Torre, E. Demler, and A. Polkovnikov, Phys. Rev. Lett. **110**, 090404 (2013).

[85] A. Chiocchetta, M. Tavora, A. Gambassi, and A. Mitra, Phys. Rev. B **91**, 220302 (2015).

[86] M. Heyl, Rep. Prog. Phys. **81**, 054001 (2018).

[87] M. Eckstein, M. Kollar, and P. Werner, Phys. Rev. Lett. **103**, 056403 (2009).

[88] J. P. Garrahan and I. Lesanovsky, Phys. Rev. Lett. **104**, 160601 (2010).

[89] S. Diehl, A. Tomadin, A. Micheli, R. Fazio, and P. Zoller, Phys. Rev. Lett. **105**, 015702 (2010).

[90] M. Schiró and M. Fabrizio, Phys. Rev. Lett. **105**, 076401 (2010).

[91] B. Sciolla and G. Biroli, Phys. Rev. Lett. **105**, 220401 (2010).

[92] A. Gambassi and P. Calabrese, EPL **95**, 66007 (2011).

[93] T. Prosen, T. H. Seligman, and M. Žnidarič, Prog. of Theor. Phys. Supp. **150**, 200 (2003).

[94] A. LeClair, G. Mussardo, H. Saleur, and S. Skorik, Nucl. Phys. B **453**, 581 (1995).

[95] M. Heyl, Phys. Rev. Lett. **113**, 205701 (2014).

[96] C. N. Yang and T. D. Lee, Phys. Rev. **87**, 404 (1952).

[97] C. Karrasch and D. Schuricht, Phys. Rev. B **87**, 195104 (2013).

[98] A. J. A. James and R. M. Konik, Phys. Rev. B **92**, 161111 (2015).

[99] M. Heyl, Phys. Rev. Lett. **115**, 140602 (2015).

[100] F. Andraschko and J. Sirker, Phys. Rev. B **89**, 125120 (2014).

[101] S. Vajna and B. Dóra, Phys. Rev. B **89**, 161105 (2014).

[102] P. Jurcevic, H. Shen, P. Hauke, C. Maier, T. Brydges, C. Hempel, B. P. Lanyon, M. Heyl, R. Blatt, and C. F. Roos, Phys. Rev. Lett. **119**, 080501 (2017).

[103] J.-S. Caux and F. H. L. Essler, Phys. Rev. Lett. **110**, 257203 (2013).

[104] J.-S. Caux, J. Stat. Mech. Theor. Exp. **2016**, 064006 (2016).

[105] D. Bernard and B. Doyon, J. Stat. Mech. Theor. Exp. **2016**, 064005 (2016).

[106] S. A. Hartnoll, Class. Quant. Grav. **26**, 224002 (2009).

[107] J. McGreevy, Adv. High Energy Phys. , 224002 (2010).

[108] M. J. Bhaseen, B. Doyon, A. Lucas, and K. Schalm, Nat. Phys. **11**, 509 EP (2015).

[109] O. A. Castro-Alvaredo, B. Doyon, and T. Yoshimura, Phys. Rev. X **6**, 041065 (2016).

[110] B. Bertini, M. Collura, J. De Nardis, and M. Fagotti, Phys. Rev. Lett. **117**, 207201 (2016).

[111] M. A. Cazalilla and J. B. Marston, Phys. Rev. Lett. **88**, 256403 (2002).

[112] G. Vidal, Phys. Rev. Lett. **93**, 040502 (2004).

[113] S. R. White and A. E. Feiguin, Phys. Rev. Lett. **93**, 076401 (2004).

[114] A. J. Daley, C. Kollath, U. Schollwöck, and G. Vidal, J. Stat. Mech. Theor. Exp. **2004**, P04005 (2004).

[115] P. Schmitteckert, Phys. Rev. B **70**, 121302 (2004).

[116] S. R. White, Phys. Rev. Lett. **69**, 2863 (1992).

[117] J. J. García-Ripoll, New J. Phys. **8**, 305 (2006).

[118] F. Verstraete, V. Murg, and J. Cirac, Adv. Phys. **57**, 143 (2008).

[119] M. C. Bañuls, M. B. Hastings, F. Verstraete, and J. I. Cirac, Phys. Rev. Lett. **102**, 240603 (2009).

[120] A. Holzner, A. Weichselbaum, I. P. McCulloch, U. Schollwöck, and J. von Delft, Phys. Rev. B **83**, 195115 (2011).

[121] J. Haegeman, J. I. Cirac, T. J. Osborne, I. Pizorn, H. Verschelde, and F. Verstraete, Phys. Rev. Lett. **107**, 070601 (2011).

[122] E. Stoudenmire and S. R. White, Annu. Rev. Condens. Matter Phys. **3**, 111 (2012).

[123] A. J. A. James and R. M. Konik, Phys. Rev. B **92**, 161111 (2015).

[124] G. Carleo and M. Troyer, Science **355**, 602 (2017).

[125] M. Schmitt and M. Heyl, SciPost Phys. **4**, 013 (2018).

[126] P. Blakie, A. Bradley, M. Davis, R. Ballagh, and C. Gardiner, Adv. Phys. **57**, 363 (2008).

[127] M. Hillery, R. O'Connell, M. Scully, and E. Wigner, Phys. Rep. **106**, 121 (1984).

[128] A. Polkovnikov, Ann. Phys. **325**, 1790 (2010).

[129] J. Schachenmayer, A. Pikovski, and A. M. Rey, Phys. Rev. X **5**, 011022 (2015).

[130] J. Wurtz, A. Polkovnikov, and D. Sels, arXiv:1804.10217 (2018).

[131] P. D. Drummond and C. W. Gardiner, J. Phys. A: Math. Gen **13**, 2353 (1980).

[132] R. Ng and E. S. Sørensen, J. Phys. A: Math. Theor. **44**, 065305 (2011).

[133] R. Ng, E. S. Sørensen, and P. Deuar, Phys. Rev. B **88**, 144304 (2013).

[134] R. L. Stratonovich, Sov. Phys. Dokl. **2**, 416 (1957).

[135] J. Hubbard, Phys. Rev. Lett. **3**, 77 (1959).

[136] R. Blankenbecler, D. J. Scalapino, and R. L. Sugar, Phys. Rev. D **24**, 2278 (1981).

[137] G. Sugiyama and S. Koonin, Ann. Phys. **168**, 1 (1986).

[138] S. Fahy and D. R. Hamann, Phys. Rev. B **43**, 765 (1991).

[139] J. H. Samson, Int. J. Mod. Phys. C **6**, 765 (1991).

[140] A. Altland and B. D. Simons, *Condensed Matter Field Theory*, 2nd ed. (Cambridge University Press, 2010).

[141] J. Wei and E. Norman, J. Math. Phys. **4**, 575 (1963).

[142] I. Kolokolov, Phys. Lett. A **114**, 99 (1986).

[143] P. E. Kloeden and E. Platen, *Numerical Solution of Stochastic Differential Equations* (Springer, 1992).

[144] K. Itô, Proc. Imp. Acad. **20**, 519 (1944).

[145] M. I. Freidlin and A. D. Wentzell, *Random Perturbations of Dynamical Systems* (Springer, 1998).

[146] A. Dembo and O. Zeitouni, *Large Deviations Techniques and Applications* (Springer, 1998).

[147] F. Langouche, D. Roekaerts, and E. Tirapegui, *Functional Integration and Semiclassical Expansions* (Springer Netherlands, 1982).

[148] P. Arnold, Phys. Rev. E **61**, 6091 (2000).

[149] P. Arnold, Phys. Rev. E **61**, 6099 (2000).

[150] H. Touchette, Phys. Rep. **478**, 1 (2009).

[151] P. Weinberg and M. Bukov, SciPost Phys. **2**, 003 (2017).

[152] P. Pfeuty and R. J. Elliott, J. Phys. C: Solid State Phys. **4**, 2370 (1971).

[153] M. S. L. du Croo de Jongh and J. M. J. van Leeuwen, Phys. Rev. B **57**, 8494 (1998).

[154] R. Vosk and E. Altman, Phys. Rev. Lett. **112**, 217204 (2014).

[155] I. Girsanov, Theory Probab. Its Appl. **5**, 285 (1960).

[156] J. Zinn-Justin, *Quantum Field Theory and Critical Phenomena* (Oxford University Press, 1996).

[157] C. Gardiner, *Stochastic Methods*, 4th ed. (Springer, 2009).

[158] G. van Kampen, *Stochastic Processes in Physics and Chemistry* (North Holland, 1981).

[159] P. Langevin, C. R. Acad. Sci. Paris. **146**, 530–533 (1908).

[160] I. Karatzas and S. E. Shreve, *Brownian Motion and Stochastic Calculus* (Springer-Verlag, 1988).

[161] R. Farnoosh, H. Rezazadeh, A. Sobhani, and M. Behboudi, Math. Sci. **9**, 87 (2015).

[162] V. I. Rupasov and V. I. Yudson, Sov. Phys. JETP **60**, 927 (1984).

[163] M. E. Peskin and D. V. Schroeder, *An Introduction to Quantum Field Theory* (Addison-Wesley, Reading, USA, 1995).

[164] J. W. Negele and H. Orland, *Quantum Many-Particle Systems* (Westview Press, 1998).

Appendix A

Stochastic Processes

In this Appendix, we introduce some key concepts in the field of stochastic processes, which play a central role in this Thesis. Our discussion is mostly based on Refs. [143, 157, 158], and will predominantly focus on topics that are relevant to this Thesis but are not specifically covered in the main text.

A.1 Stochastic Processes

A *stochastic process* is an indexed[1] sequence of random variables X_i with $i = 1, \ldots, n$, which can be thought of as describing the time-evolution of a process over time instants $t_1 < \cdots < t_n$ [143]. For simplicity, we consider real valued stochastic processes; the relevant definitions can be generalised to complex processes by separately considering the real and imaginary parts. The set of all the joint probability distributions of a stochastic process, $F_{X_{i_1} X_{i_2} \ldots}$, is known as its *probability law*. The simplest example of a probability law is for the case of i.i.d. (independent identically distributed) random variables, where $F_{X_{i_1} \ldots X_{i_j}} = F_{X_{i_1}} \ldots F_{X_{i_j}}$. If the joint distributions are all Gaussian, one has the special case of a *Gaussian process*. Stochastic processes may be defined at all times within a (potentially infinite) time set, in which case they are referred to as *continuous*.

For a given time set T and probability space $(\Omega, \mathcal{A}, \mathbb{P})$, where Ω is the set of all possible outcomes, $\mathcal{A}$ is the set of all events and $\mathbb{P}(A)$ gives the probability of an event $A \in \mathcal{A}$ [143], a stochastic process $X = \{X(t), t \in T\}$ is as a function $X : T \times \Omega \to \mathbb{R}$ such that $X(t, \cdot) = X(t)$ is a random variable for each t. For any specific outcome $\omega \in \Omega$, corresponding for example to a set of numbers generated by an pseudo-random generator, the map $X(\cdot, \omega) : T \to \mathbb{R}$

[1] In this Section, we will sometimes denote the time dependence of a quantity by a subscript, following the established convention for stochastic processes.

is referred to as a *realisation*, a *sample path* or a *trajectory* of the stochastic process. Of particular relevance is the class of stochastic processes with *independent increments*, i.e. such that the random variables $X(t_{j+1}) - X(t_j)$ are independent for any t_{j+1}, $t_j \in T$. A stochastic process is said to be *stationary* if it is time-translation invariant in some particular sense; specifically, it is said to be *strictly stationary* if its joint probability distributions are invariant under a time translation $t_i \to t_i + \Delta t$, whereas it is said to be *weakly stationary* if its mean and variance $\mu(t) = \langle X(t) \rangle$ and $\sigma(t) = \langle (X(t) - m(t))^2 \rangle$ are time-independent whereas the covariances $C(t,s) = \langle X(t)X(s) \rangle - m(t)m(s)$ satisfy $C(s,t) = C(t-s)$.

Many stochastic processes that are relevant to physical situations are characterised by the property that in discrete time the probability distribution of the process $X_{t_{i+1}}$ at a given time t_{i+1} only depends on its value at t_i, $P(X_{t+1} = x_j) = P(X_{t+1} = x_j | X_t = x_k)$. Processes with this property are known as *markovian*. This property can be generalised to continuous time, and indeed the central class of stochastic processes considered in this Thesis is that of continuous-time Markov chains taking continuous values. An important family of such processes are *diffusion processes*.

A.2 Diffusion Processes

For a given continuous-time process with continuous state space, the Markov property is expressed in terms of conditional probabilities as

$$P(X(t_{n+1}) \in B | X(t_1) = x_1, \ldots, X(t_n) = x_n) = P(X(t_{n+1}) \in B | X(t_n) = x_n) \tag{A.1}$$

for all subset B of the state space and time instants $0 < t_1 < \cdots < t_n$. The process $X(t)$ is then termed a Markov process and its transition probabilities are given by

$$P(t, B | s, x) \equiv P(X(t) \in B | X(s) = x) \tag{A.2}$$

for $s < t$, and we can define the corresponding transition densities $p(t, y | s, x)$ by

$$P(t, B | s, x) = \int_B p(t, y | s, x) \mathrm{d}y. \tag{A.3}$$

If the time dependence of all transition densities $p(t, y | s, x)$ is only via the difference $t - s$, the process is *homogeneous*. The Markov property implies that the transition densities

$p(t,y|s,x)$ satisfy the *Chapman-Kolmogorov equation*

$$p(t,y|s,x) = \int_{-\infty}^{\infty} p(t,y|\tau,z)p(\tau,z|s,x)\mathrm{d}z \tag{A.4}$$

for all $s \leq \tau \leq t$. A Markov process with transition densities $p(t,y|s,x)$ is termed a *diffusion process* if the limits

$$\lim_{t\to s^+} \frac{1}{t-s} \int_{|y-x|>\varepsilon} p(t,y|s,x)\mathrm{d}y = 0, \tag{A.5a}$$

$$\lim_{t\to s^+} \frac{1}{t-s} \int_{|y-x|<\varepsilon} (y-x)p(t,y|s,x)\mathrm{d}y = a(s,x), \tag{A.5b}$$

$$\lim_{t\to s^+} \frac{1}{t-s} \int_{|y-x|<\varepsilon} (y-x)^2 p(t,y|s,x)\mathrm{d}y = b^2(s,x) \tag{A.5c}$$

exist for all $\varepsilon > 0, s \geq 0$. If this is the case, $a(s,x)$ and $b(s,x)$ are respectively known as the *drift* and *diffusion coefficient* of the stochastic process. The quantities $a(s,x)$ and $b(s,x)^2$ can be interpreted, respectively, as the instantaneous rate of change of the mean of the process and of its squared fluctuations given $X(s) = x$. The condition expressed by Eq. (A.5a) can be interpreted as forbidding instantaneous jumps. For sufficiently smooth drift and diffusion coefficients, the transition densities $p(t,y|s,x)$ satisfy the partial differential equations

$$\frac{\partial p}{\partial t} + \frac{\partial}{\partial y}\left[a(t,y)p\right] - \frac{1}{2}\frac{\partial^2}{\partial y^2}\left[b^2(t,y)p\right] = 0 \text{ for fixed } (s,x), \tag{A.6}$$

$$\frac{\partial p}{\partial s} + a(s,x)\frac{\partial p}{\partial x} + \frac{1}{2}b^2(s,x)\frac{\partial^2 p}{\partial y^2} = 0 \text{ for fixed } (t,y), \tag{A.7}$$

known as the *Kolmogorov forward* and *backward equation* respectively. The Kolmogorov forward equation is more famously known as the *Fokker-Planck equation*. Diffusion processes are *sample-path continuous*, meaning that the union of all non-continuous paths has probability zero. However, they may not be differentiable. For a d-dimensional stochastic process, the drift and diffusion coefficients are replaced by a drift vector a_i and a diffusion matrix D_{ij} respectively. The off-diagonal entries of the diffusion matrix give the instantaneous rate of change of the covariances between pairs of components of the multidimensional vector process. In terms of these coefficients, the Fokker-Planck equation (or Kolmogorov forward equation) and the Kolmogorov backward equation can

be expressed compactly as

$$\frac{\partial p}{\partial t} - \mathcal{L}^* p = 0, \tag{A.8}$$

$$\frac{\partial u}{\partial s} + \mathcal{L} u = 0 \tag{A.9}$$

respectively, where $u(s,x) \equiv p(t,y|s,x)$ for fixed t and y, the operator $\mathcal{L}$ is defined as

$$\mathcal{L}u(x,s) \equiv \sum_{i=1}^{d} a_i(s,x)\frac{\partial u}{\partial x_i}(s,x) + \frac{1}{2}\sum_{i,j=1}^{d} D_{ij}(s,x)\frac{\partial^2}{\partial x_i \partial x_j}(s,x) \tag{A.10}$$

and $\mathcal{L}^*$ denotes its formal adjoint.

A.3 Wiener Processes and Gaussian White Noise

An important stochastic process is the *standard Wiener process* $W = \{W(t), t \geq 0\}$, which plays a fundamental role in this project. Standard Wiener processes, sometimes referred to as Brownian motions in physical applications, are Gaussian processes with independent increments satisfying

$$W(0) = 0, \tag{A.11a}$$

$$E(W(t)) = 0, \tag{A.11b}$$

$$\mathrm{Var}(W(t) - W(s)) = |t - s|, \tag{A.11c}$$

from which it follows that

$$\mathrm{Cov}(W(s), W(t)) = \langle W(s)W(t)\rangle = \min(t,s). \tag{A.12}$$

Hence, Wiener processes are not stationary. It can be shown [143] that the paths of a Wiener process are almost surely non-differentiable anywhere. However, let us consider the stochastic process

$$\phi^h(t) = \frac{W(t+h) - W(h)}{h}. \tag{A.13}$$

One can readily show that ϕ^h has zero mean and covariance given by

$$C_h(t-s) = \langle \phi^h(t)\phi^h(s)\rangle = \frac{1}{h}\max\left(0, 1 - \frac{1}{h}|t-s|\right). \tag{A.14}$$

Since the process ϕ^h is a sum of Gaussian variables, it is also Gaussian; it is then fully specified by its mean and covariance. In the limit $h \to 0$, Eq. (A.13) shows that the stochastic process $\phi^h(t)$ formally becomes the derivative of $W(t)$; we see that in this limit

$$\lim_{h\to 0} C_h(t-s) = C(t-s) = \delta(t-s). \tag{A.15}$$

Thus, $\phi(t)$ can be interpreted as the derivative of $W(t)$ in the sense of generalised functions. This object is termed a *Gaussian white noise*, because it is a Gaussian process and its Fourier transform is a constant.

A.4 Stochastic Differential Equations and Ito Calculus

Stochastic differential equations (SDEs) were first introduced in physics to model the Brownian motion of a particle in a noisy environment, and were initially written in the Langevin form [159]

$$\frac{dX_t}{dt} = a(t,X_t) + b(t,X_t)\phi_t, \tag{A.16}$$

where ϕ_t are independent Gaussian variables drawn at each t, or, in integral form,

$$X_t(\omega) = X_{t_0}(\omega) + \int_{t_0}^{t} a(s,X_s(\omega))\mathrm{d}s + \int_{t_0}^{t} b(s,X_s(\omega))\phi_s(\omega)\mathrm{d}s. \tag{A.17}$$

for a given sample path ω (see Section A.1). The random orientation and rapid variation of the driving term ϕ_t were modelled as $\langle\phi_t\rangle = 0$, $\langle\phi_t\phi_s\rangle = \delta(t-s)$ [158]. Further assuming that ϕ_t is Gaussian-distributed leads to identifying this object with the Gaussian white noise we defined in the previous Section. We formally defined ϕ_t as the derivative of a Wiener process, suggesting that we can write

$$X_t(\omega) = X_{t_0}(\omega) + \int_{t_0}^{t} a(s,X_s(\omega))\mathrm{d}s + \int_{t_0}^{t} b(s,X_s(\omega))\mathrm{d}W_s \tag{A.18}$$

However, a Wiener process is nowhere differentiable, implying that ϕ_t cannot be a conventional function of t and the final integral in Eq. (A.18) cannot be interpreted as any sort of conventional integral (Riemann-Stjeltes or Lebesgue) [143]. The precise meaning of integrals of this form was put on a firm mathematical footing by Kiyosi Ito [144], who

defined the *Ito stochastic integral* of a function f as

$$I(f) = \int f(s,\omega)\mathrm{d}W_s(\omega) \tag{A.19}$$

$$\equiv \lim_{n\to\infty} \sum_{j=1}^{n} f^{(n)}\left(t_j^{(n)},\omega\right)\left[W_{t_{j+1}^{(n)}}(\omega) - W_{t_j^{(n)}}(\omega)\right], \tag{A.20}$$

where $f^{(n)}$ are a sequence of random stepwise functions $f^{(n)}(t,\omega) = f(t_j^{(n)},\omega)$ for $t_j^{(n)} < t < t_{j+1}^{(n)}$ converging to the function $f(t,\omega)$ of interest as the number of time-steps n tends to infinity. Here convergence is intended in the mean-squared sense; for a more detailed discussion of this definition see Ref. [143]. With this definition, the stochastic integral equation Eq. (A.18) is now well-defined. From the definition Eq. (A.20), it follows that Ito stochastic integrals have the property

$$\int_0^t W_s(\omega)\mathrm{d}W_s(\omega) = \frac{1}{2}W_t^2(\omega) - \frac{1}{2}t. \tag{A.21}$$

This can be re-written in differential form, yielding the famous *Ito identity*

$$E((\mathrm{d}W_t)^2) = \mathrm{d}t. \tag{A.22}$$

This formula has important repercussions, most notably the fact if a stochastic process X_t satisfies

$$\mathrm{d}X_t(\omega) = a(t,\omega)\mathrm{d}t + b(t,\omega)\mathrm{d}W_t, \tag{A.23}$$

the Ito chain rule for a stochastic process $Y_t(\omega) = U(t,X_t(\omega))$ features an extra term proportional to $\frac{\partial^2}{\partial x^2}U(x,t)$ compared to ordinary calculus:

$$\mathrm{d}Y_t = \left(\frac{\partial U(t,x)}{\partial t}\Big|_{x=X_t} + a\frac{\partial U(t,x)}{\partial x}\Big|_{x=X_t} + \frac{1}{2}b^2\frac{\partial^2 U(t,x)}{\partial x^2}\Big|_{x=X_t}\right)\mathrm{d}t + b\frac{\partial U(t,x)}{\partial x}\Big|_{x=X_t}\mathrm{d}W_t. \tag{A.24}$$

Stochastic differentials such as Eq. (A.23) and SDEs written in the Langevin form (A.16) must be interpreted as a symbolic representation of the corresponding stochastic integral equations

$$X_t = X_{t_0} + \int_{t_0}^{t} a(X_s)\mathrm{d}s + \int_{t_0}^{t} b(X_s)\mathrm{d}W_s, \tag{A.25}$$

where the last term is an Ito stochastic integral defined as in Eq. (A.20). The solution of a given SDE can only be written in closed form in terms of its driving Wiener process in few specific cases, including in particular *linear SDEs* where both the drift and the diffusion

coefficients are linear in the stochastic variables. SDEs that can be transformed to linear SDEs by means of a change of variables and hence solved exactly are known as *reducible*. A sufficient existence and uniqueness condition for the solutions of SDEs is given by the combined requirements that the relevant drift and diffusions coefficients $a(x)$, $b(x)$ satisfy the Lipshitz condition

$$\exists\, K > 0 : |a(x) - a(y)| \leq K|x - y| \;\forall\, x, y \in \mathbb{R} \tag{A.26}$$

and the growth bound

$$\exists\, L > 0 : |a(x)|^2 \leq L(1 + |x|^2) \;\forall\, x \in \mathbb{R}, \tag{A.27}$$

and similarly for $b(x)$. For multicomponent SDEs, the Lipshitz condition and the growth bound generalise from the scalar case by replacing absolute values by Euclidean norms. Although the growth bound (A.27) is not a necessary condition for existence and uniqueness of the solution of a given SDE, its absence may lead to the existence of a finite *explosion time* $t_e(W_t)$ whereby for a given Weiner process W_t the solution of the SDE of interest only exists for $t < t_e$. For one-dimensional diffusion processes, a criterion exists to determine whether at infinite time trajectories explode with probability 0, 1 or finite, the *Feller explosion test* [160].

Consider a given multicomponent stochastic differential equation for a set of variables $x = \{x_i\}$, written in Langevin form:

$$\dot{x}_i = a_i(x,t) + B_{ij}(x,t) \sum_j \phi_j(t), \tag{A.28}$$

with a drift vector a_i, a diffusion matrix B_{ij} and initial conditions $x_0 = \{x_i(t_0)\}$. Instead of seeking a solution for the trajectories $x_i(t)$, we may be interested in the probability density $p(x,t|x_0,t_0)$. This can be obtained by solving the corresponding Fokker-Planck equation (see Section A.2); by considering the time dependence of the expectation value of a general function f, we can show that this is given by [157]

$$\partial_t p(x,t|x_0,t_0) = -\sum_i \partial_i \left[a_i(x,t) p(x,t|x_0,t_0)\right] + \frac{1}{2} \sum_{ijk} \partial_i \partial_k \left[B_{ik}(x,t) B_{jk}(x,t) p(x,t|x_0,t_0)\right]. \tag{A.29}$$

A.5 Strong and Weak Convergence of Numerical Solutions

Consider an Ito stochastic differential equation given by

$$\mathrm{d}X_t = a(X_t)\mathrm{d}t + b(X_t)\mathrm{d}W_t. \tag{A.30}$$

Let us denote the exact trajectory of the Ito process by X_t and a particular discretised approximation of this trajectory by Y_n, where $t = n\Delta t$. An approximating process Y_n is said to *converge strogly* with order $\gamma \in (0,\infty]$ if there exists a finite constant K and a constant $\delta_0 > 0$ such that, for a given final time t,

$$\mathbf{E}(|X_t - Y_n|) \leq K\Delta t^{\gamma} \tag{A.31}$$

for any time-discretisation with maximum time step $\Delta t \in (0, \delta_0)$. Since it concerns the difference between exact and approximated trajectories, strong convergence is also known as *path-wise* convergence. However, for practical applications one is often interested in expectation values of functions of an Ito process X_t. In this case, a numerical scheme should closely approximate the probability distribution of X_t, rather than individual paths. To quantify the convergence of a given time-discrete approximation Y in this probabilistic sense, one defines Y to *converge weakly* with order $\beta \in (0,\infty]$ if, for any polynomial g, there exists a finite constant K and a constant $\delta_0 > 0$ such that, for a given final time t,

$$|\mathbf{E}(g(X_t)) - \mathbf{E}(g(Y_n))| \leq K\Delta t^{\beta} \tag{A.32}$$

for any time-discretisation with maximum time-step $\Delta t \in (0, \delta_0)$. For example, the Euler discretisation scheme (see Appendix D) converges with $\gamma = 0.5$, $\beta = 1$ when the coefficients of the SDE satisfy appropriate conditions [143].

A.6 Stochastic Differential Equations and Gaussian Functional Integrals

Stochastic differential equations are closely related to Gaussian functional integrals. Consider a Langevin equation

$$\dot{\xi}(t) = a(\xi) + B(\xi)\phi(t), \tag{A.33}$$

where $\phi(t)$ is Gaussian white noise satisfying

$$\langle \phi(t) \rangle = 0, \tag{A.34}$$

$$\langle \phi(t)\phi(t') \rangle = \delta(t-t'). \tag{A.35}$$

Due to Eq. (A.33), stochastic functions $A(\xi)$ are functionals $A[\phi]$ of the fields $\phi(t)$; their averages are then computed as

$$\langle A[\phi] \rangle = \frac{\int D\phi A[\phi] P[\phi]}{\int D\phi P[\phi]}, \tag{A.36}$$

where the denominator ensures normalisation of the continuum limit, and can be explicitly included or absorbed in a redefinition of the integration measure. The probability distribution of Gaussian white noise is given by

$$P[\phi] = e^{-\frac{1}{2}\int \mathrm{d}t \phi^2(t)}. \tag{A.37}$$

In practise, when numerically solving a SDE, one has to discretise time and generate the fields from a Gaussian distribution. The variables $\tilde{\phi}_i$ appearing in the discretised form of an SDE are sampled from a zero-mean, unit-variance Gaussian distribution, and thus satisfy $\langle \tilde{\phi}_i \tilde{\phi}_j \rangle = \delta_{ij}$. Comparison with $\langle \phi_i \phi_j \rangle = \Delta^{-1}\delta_{ij}$ obtained by discretising Eq. (A.35) then implies

$$\tilde{\phi}_j = \sqrt{\Delta}\phi_j. \tag{A.38}$$

For a path integral with imaginary action

$$P[\phi] \propto e^{-\frac{i}{2}\int \mathrm{d}\tau \phi^2}, \tag{A.39}$$

corresponding to a discretised condition

$$\langle \phi_i \phi_j \rangle = (i\Delta)^{-1}\delta_{ij}, \tag{A.40}$$

the discretised variables ϕ_j are related to the unit-variance Gaussian fields $\tilde{\phi}_j$ as

$$\tilde{\phi}_j = \sqrt{i\Delta}\phi_j. \tag{A.41}$$

Appendix B

Derivations

B.1 Operator Hubbard-Stratonovich Transformation

In order to decouple the quadratic term in Eq. (2.5), we apply the Hubbard-Stratonovich (HS) transformation in the form:

$$e^{\Delta\tau\sum_{aij}\mathcal{J}^a_{ij}\hat{S}^a_i\hat{S}^a_j} = \mathcal{N}\int\prod_{ai}\mathrm{d}\varphi^a_i e^{-\frac{1}{4}\Delta\tau\sum_{aij}(\mathcal{J}^{-1})^a_{ij}\varphi^a_i\varphi^a_j+\Delta\tau\sum_{aj}\varphi^a_j\hat{S}^a_j}, \tag{B.1}$$

where $\varphi^a_i(t)$ are scalar fields and $\hat{S}^a_i$ are spin operators at different lattice sites[1]. For infinitesimal time slices, it is possible to split the exponentials and separately consider the different components $a \in \{x,y,z\}$:

$$e^{\Delta\tau\sum_{aij}\mathcal{J}^a_{ij}\hat{S}^a_i\hat{S}^a_j} \sim \prod_a e^{\Delta\tau\sum_{ij}\mathcal{J}^a_{ij}\hat{S}^a_i\hat{S}^a_j}, \tag{B.2}$$

applying the HS transformation to each separately. Let us consider the exponential involving the z-component first; we want to show that

$$e^{\Delta\tau\sum_{ij}\mathcal{J}^z_{ij}\hat{S}^z_i\hat{S}^z_j} = \mathcal{N}\int\prod_i\mathrm{d}\varphi^z_i e^{-\frac{1}{4}\Delta\tau\sum_{ij}(\mathcal{J}^{-1})^z_{ij}\varphi^z_i\varphi^z_j+\Delta\tau\sum_j\varphi^z_j\hat{S}^z_j}. \tag{B.3}$$

Since operators $\hat{S}^z_i$ at different sites commute, a general eigenstate of the above exponentials can be written in terms of the eigenstates of the individual $\hat{S}^z_i$ as

$$|\lambda_1,\ldots,\lambda_N\rangle \equiv |\lambda_1\rangle\otimes\cdots\otimes|\lambda_N\rangle \tag{B.4}$$

[1] At this stage, we do not specify whether the fields φ^a_i are real or complex valued; we will impose such restriction retrospectively to make the integral in Eq. (B.1) convergent

and any state of the theory can be written as a linear combination of such (orthonormal) eigenstates. Thus, to verify Eq. (B.3) as an operator identity valid in the relevant space, one just needs to show it holds for a general eigenstate of the form Eq. (B.4). Applying the right-hand side of Eq. (B.3) to a general eigenstate $|\lambda\rangle$, where $\lambda \equiv \{\lambda_1, \ldots, \lambda_N\}$, gives

$$\mathcal{N}\int \prod_i \mathrm{d}\varphi_i e^{-\frac{1}{4}\Delta\tau\sum_{ij}(\mathcal{J}^{-1})^z_{ij}\varphi^z_i\varphi^z_j+\Delta\tau\varphi^z_j\hat{S}^z_j}|\lambda\rangle = |\lambda\rangle\mathcal{N}\int\prod_i \mathrm{d}\varphi^z_i e^{-\frac{1}{4}\Delta\tau\sum_{ij}(\mathcal{J}^{-1})^z_{ij}\varphi^z_i\varphi^z_j+\Delta\tau\sum_j\varphi^z_j\lambda_j}. \tag{B.5}$$

The Gaussian integral over scalar fields can then be carried out by diagonalising $\mathcal{J}^{-1}$:

$$\int\prod_i \mathrm{d}\varphi^z_i e^{-\frac{1}{4}\Delta\tau\sum_{ij}(\mathcal{J}^{-1})^z_{ij}\varphi^z_i\varphi^z_j+\Delta\tau\sum_j\varphi^z_j\lambda_j} = e^{\Delta\tau\sum_{ij}\mathcal{J}^z_{ij}\lambda^z_i\lambda^z_j}\int\prod_i \mathrm{d}\varphi^z_i e^{-\frac{1}{4}\Delta\tau\sum_{ij}(\mathcal{J}^{-1})^z_{ij}\varphi^z_i\varphi^z_j} \tag{B.6}$$

$$= e^{\Delta\tau\sum_{ij}\mathcal{J}^z_{ij}\lambda^z_i\lambda^z_j}\int\prod_i \mathrm{d}\theta_i e^{-\frac{1}{4}\Delta\tau\sum_i\Lambda_{ii}\theta^2_i}. \tag{B.7}$$

In the fist step, we have shifted each φ^z_i as $\varphi^z_i \to \varphi^z_i + 2\sum_j J^z_{ij}\lambda_j$ to remove the linear term, and in the second step we have defined $\varphi^z_i \equiv \sum_j Q_{ij}\theta_j$, where the matrix Q satisfies $Q^TQ = 1$, $\det Q = 1$, $Q^T\mathcal{J}^{-1}Q = \Lambda$. Λ is a diagonal matrix whose elements are the eigenvalues of $(\mathcal{J}^{-1})^z$. In order for the integral in Eq. (B.7) to converge, we see that for each positive eigenvalue Λ_{ii} the corresponding θ_i must be real valued and the integral must run over the range $(-\infty, +\infty)$, while for negative Λ_{ii} the variable θ_i must be imaginary and the integral must run over $(-\infty i, +\infty i)$. With these caveats, the Gaussian integral is equal to a constant $\mathcal{N}^{-1}$ where

$$\mathcal{N} = i^{N_-}\sqrt{\left(\frac{\Delta\tau}{4\pi}\right)^N\frac{1}{\det\mathcal{J}^z}} \tag{B.8}$$

where N_- is the number of negative eigenvalues of $\mathcal{J}^z$ and N is the number of lattice sites. Using this result, we find

$$\mathcal{N}\int\prod_i \mathrm{d}\varphi_i e^{-\frac{1}{4}\Delta\tau\sum_{ij}(\mathcal{J}^{-1})^z_{ij}\varphi^z_i\phi^z_j+\Delta\tau\varphi^z_j\hat{S}^z_j}|\lambda\rangle = |\lambda\rangle e^{\Delta\tau\sum_{ij}\mathcal{J}^z_{ij}\lambda_i\lambda_j} = e^{\Delta\tau\sum_{ij}\mathcal{J}^z_{ij}\hat{S}^z_i\hat{S}^z_j}|\lambda\rangle. \tag{B.9}$$

This holds for all states, so Eq. (B.3) is verified. The same proof can be repeated for the x and y components, showing that Eq. (B.1) holds in general.

The Hubbard-Stratonovich transformation can be applied directly in real time. Let us begin by Trotter-slicing the time-ordered exponential:

$$U(t) = T\exp\Big[-i\int_0^t \mathrm{d}t'\hat{H}(t')\Big] \tag{B.10}$$

$$= T\lim_{n\to\infty}\prod_{m=1}^{n}\exp\Big(-i\Delta t\hat{H}(m\Delta t)\Big) \tag{B.11}$$

$$= T\lim_{n\to\infty}\prod_{m=1}^{n}\exp\Big(i\Delta t\sum_{ija}J_{ij}^{a}(m\Delta t)\hat{S}_i^a\hat{S}_j^a + i\Delta t\sum_{aj}h_j^a(m\Delta t)\hat{S}_j^a\Big), \tag{B.12}$$

where $\Delta t \equiv t/n$. The Hubbard-Stratonovich transformation can then be performed at each time slice. In real time, the appropriate transformation is

$$e^{i\Delta t\sum_{ija}\mathcal{J}_{ij}^a\hat{S}_i^a\hat{S}_j^a} = \mathcal{N}\int\prod_i \mathrm{d}\varphi_i e^{-\frac{1}{4}\Delta t\sum_{ija}(\mathcal{J}^{-1})_{ij}^a\varphi_i^a\varphi_j^a + \sqrt{i}\Delta t\sum_{aj}\varphi_j^a\hat{S}_j^a} \tag{B.13}$$

with a normalisation constant $\mathcal{N}$ defined as for the imaginary time case. The argument of the exponential at each time slice is then

$$A = \Delta t\Big[i\sum_j(h_j^a + \varphi_i^a/\sqrt{i})\hat{S}_j^a - \sum_{ij}\frac{1}{4}(\mathcal{J}^{-1})_{ij}^a\varphi_i^a\varphi_j^a\Big]. \tag{B.14}$$

Taking the limit for $n\to\infty$ as before, we get

$$\hat{U}(t_f,t_0) = T\int\mathcal{D}\varphi e^{-S[\varphi]}\prod_j \mathrm{e}^{i\int\sum_j\Phi_j^a(t')\hat{S}_j^a(t')\mathrm{d}t'} \tag{B.15}$$

with

$$\Phi_j^a(t) = \frac{\varphi_j^a(t)}{\sqrt{i}} + h_j^a(t). \tag{B.16}$$

and a noise action $S[\varphi]$ which has the same form as for imaginary time evolution and can be analogously diagonalised by introducing new fields ϕ, as shown in the next Section. The factor of $(\sqrt{i})^{-1}$ multiplying the HS fields φ can be absorbed in a redefinition of the ϕ fields, so that the diagonalised noise action is in the form

$$S[\phi] \equiv \frac{i}{2}\int\sum_{ai}\phi_i^a(t')\phi_i^a(t')\mathrm{d}t'. \tag{B.17}$$

B.2 Diagonalisation of the Noise Action

Following the application of the Hubbard-Stratonovich transformation, we defined the *noise action* $S[\varphi]$ as

$$S[\varphi] \equiv \sum_{ij} \int_0^\tau \frac{1}{4} (\mathcal{J}^{-1})^a_{ij} \varphi^a_i(\tau') \varphi^a_j(\tau') \mathrm{d}\tau'. \tag{B.18}$$

We want to perform a change of variables $\varphi^a_i = \sum_{jb} O^{ab}_{ij} \phi^b_j$ so that Eq. (B.18) can be cast in the form

$$S[\phi] \equiv \int_0^\tau \frac{1}{2} \sum_{ai} \phi^a_i(\tau') \phi^a_i(\tau') \mathrm{d}\tau'. \tag{B.19}$$

If the interaction matrix $\mathcal{J}^a_{ij}$ is symmetric, one can always construct a matrix O^a_{ij} that diagonalise the noise action. We will illustrate this for a specific component a, suppressing the respective index to streamline our notation. Define the matrix Q whose columns are the orthonormal eigenvectors $e^{(i)}$ of $\mathcal{J}^{-1}$, $Q_{ij} = e^{(j)}_i$. This is an orthogonal matrix, satisfying $QQ^T = Q^T Q = \mathbb{1}$. Also define the diagonal matrix D whose elements are the (real-valued) eigenvalues of $\mathcal{J}^{-1}$, i.e. the inverses of the eigenvalues λ_i of $\mathcal{J}$, arranged in the same order as the columns of Q:

$$Q \equiv \begin{bmatrix} e^{(1)} & \cdots & e^{(N)} \\ \downarrow & \cdots & \downarrow \end{bmatrix}, \quad D \equiv \mathrm{diag}(\lambda_1^{-1}, \ldots, \lambda_N^{-1}), \tag{B.20}$$

such that $Q^T \mathcal{J}^{-1} Q = D$. Then, the matrix $O \equiv \sqrt{2} Q D^{-1/2}$ satisfies

$$O^T \mathcal{J}^{-1} O = 2\mathbb{1} \tag{B.21}$$

and can be used to perform the change of variables $\varphi^a_i = \sum_{jb} O^{ab}_{ij} \phi^b_j$ to put the noise action in the desired form. The definition of the matrix O is non-unique and depends on the specific ordering of the eigenvalues in Eq. (B.20). Since Q has real valued entries, we see that the columns of O are either purely real or purely imaginary, depending on whether the corresponding eigenvalue is positive or negative. This implies that $O_I \equiv \mathrm{Im}(O)$, $O_R \equiv \mathrm{Re}(O)$ satisfy $O_I O_R^T = O_R O_I^T = 0$. From the symmetric definition of $\mathcal{J}^a_{ij}$, we can

derive other properties which are used in this Thesis, namely

$$\mathcal{J}^{-1} = QDQ^T \tag{B.22}$$

$$QD^{-1}Q^T = \mathcal{J} \tag{B.23}$$

$$OO^T = 2\mathcal{J}. \tag{B.24}$$

This property allows us to simplify several equations. The orthogonality of Q further implies that

$$O^T O = 2D^{-1} = 2\,\mathrm{diag}(\lambda_1, \ldots, \lambda_N), \tag{B.25}$$

where λ_i are the eigenvalues of $\mathcal{J}$. By writing O in terms of its real and imaginary part, we also get $O_R O_R^T - O_I O_I^T = \mathcal{J}$. If $\mathcal{J}$ has no diagonal elements, this implies $(O_I O_I^T)_{ii} = (O_R O_R^T)_{ii}$. Notably, if $\mathcal{J}$ has translational symmetry, the vector

$$e^{(1)} \equiv \frac{1}{\sqrt{N}}(1, \ldots, 1) \tag{B.26}$$

is always an eigenvector of $\mathcal{J}$. If $\mathcal{J}_{ij} = \frac{J}{2}(\delta_{ij+1} + \delta_{ij-1})$, as for the quantum Ising model, $e^{(1)}$ has eigenvalue

$$\lambda_1 = J. \tag{B.27}$$

We chose $e^{(1)}$ to be the first eigenvector in Eq. (B.20), so that

$$O_{j1} = \sqrt{2J/N}. \tag{B.28}$$

The orthonormality of the eigenvectors,

$$e^{(1)} \cdot e^{(i)} = \delta_{i1}, \tag{B.29}$$

implies that all other eigenvectors have components which add up to zero:

$$\sum_j e_j^{(1)} = \sqrt{N} \quad \text{for} \quad i = 1, \tag{B.30a}$$

$$\sum_j 1 \cdot e_j^{(i)} = 0 \quad \text{for} \quad i \neq 1. \tag{B.30b}$$

It is then easy to show that Eq. (B.30) in turn implies

$$\sum_i O_{ij} = \delta_{1j}\sqrt{2NJ}. \tag{B.31}$$

B.2.1 System Sizes Multiple of 4

For the quantum Ising model, where the interaction matrix is given by

$$\mathcal{J}^a_{ij} = \frac{J}{2}\delta_{az}(\delta_{ij+1} + \delta_{ij-1}), \tag{B.32}$$

the case where the system size N is a multiple of 4 requires a separate discussion. In this case, it is not possible to simply follow the recipe explained previously because one of the eigenvalues of the matrix $\mathcal{J}$ turns out to be zero so that $\mathcal{J}$ cannot be inverted. A way to resolve the problem is by including a shift proportional to the identity in the time evolution operator, exploiting the fact that $\sum_i S^z_i S^z_i = \frac{N}{4}\mathbb{1}$:

$$\hat{U}(t) = e^{-iHt - iN\frac{J_s}{4}t\mathbb{1}}, \tag{B.33}$$

or

$$\hat{U}(\tau) = e^{-H\tau - N\frac{J_s}{4}\tau\mathbb{1}} \tag{B.34}$$

in imaginary time. This is equivalent to adding a term $J_s\delta_{ij}\delta_{az}$ to the interaction matrix. For $J_s \neq 1$, $\mathcal{J}$ becomes invertible. The additional diagonal shift amounts to a phase in real time, and can be removed by dividing by $e^{-\frac{J_s}{4}N\tau}$ in imaginary time.

With this definition, however, the matrix O_{ij} no longer satisfies $(OO^T)_{ii} = 0$; hence, the Ito and Stratonovich equations for observables become different. The conversion formula, for a standard SDE of the form

$$\frac{d}{dt}\xi^a_i = a^a_i(\xi) + \sum_{jb} B^{ab}_{ij}(\xi)\tilde{\phi}^b_j, \tag{B.35}$$

is given by

$$B^I = B^S, \quad (a^I)^a_i = (a^S)^a_i + \frac{1}{2}\sum_{bcjk} B^{bc}_{kj}\frac{\partial}{\partial\xi^b_k}B^{ac}_{ij}. \tag{B.36}$$

For the transverse field Ising model, this only affects the Ito SDE for ξ_i^+, which becomes

$$\dot{\xi}_i^+ = \frac{1}{2}\Gamma_i - \frac{1}{2}\Gamma_i \xi_i^{+2} + \frac{1}{2}\xi_i^+ \sum_k O_{ik}O_{ik} + \xi_i^+ \sum_j O_{ij}\phi_j, \tag{B.37}$$

where the linear term $\xi_i^+ \sum_k O_{ik}O_{ik}/2$ is non-vanishing due to the shift in $\mathcal{J}$.

B.3 Derivation of the Disentangling Equations

By parameterising the on-site stochastic time evolution operator and differentiating, we have obtained the operator equation

$$(\partial_\tau \hat{U}_i^s)(\hat{U}_i^s)^{-1} = \sum_a \Phi_i^a \hat{S}_i^a = \sum_a \left(\partial_\tau \xi_i^a \frac{\partial \hat{U}_i^s}{\partial \xi_i^a}\right)(\hat{U}_i^s)^{-1}. \tag{B.38}$$

Let us compute the three contributions to the right-hand side corresponding to $a \in \{+, z, -\}$ separately, and then match the coefficients multiplying each $\hat{S}_i^a$. This yields three independent equations that need to be simultaneously satisfied for Eq. (2.16) to hold. We will need Hadamard's lemma:

$$e^A B e^{-A} \equiv e^{\mathrm{adj}A} B = B + [A,B] + \frac{1}{2!}[A,[A,B]] + \ldots \tag{B.39}$$

and the commutation relations of $SU(2)$: $[\hat{S}^z, \hat{S}^+] = \hat{S}^+$, $[\hat{S}^z, \hat{S}^-] = -\hat{S}^-$, $[\hat{S}^+, \hat{S}^-] = 2\hat{S}^z$. Since Eq. (B.38) refers to a single lattice site i, we can temporarily drop the corresponding index and define $\xi_a \equiv \xi_i^a$. We get

1. $a = +$:

$$\left(\frac{\partial \hat{U}^s}{\partial \xi_+}\right)(\hat{U}^s)^{-1} = \hat{S}^+, \tag{B.40}$$

2. $a = z$:

$$\left(\frac{\partial \hat{U}^s}{\partial \xi_z}\right)(\hat{U}^s)^{-1} = e^{(+)} e^{(z)} \hat{S}^z e^{(-)} e^{-(-)} e^{-(z)} e^{-(+)} \tag{B.41}$$

$$= e^{(+)} \hat{S}^z e^{-(+)}, \tag{B.42}$$

where the shorthand notation $e^{(a)}$ denotes $e^{\hat{S}^a \xi_a}$. Invoking Hadamard's lemma, the above becomes

$$\left(\frac{\partial \hat{U}^s}{\partial \xi_z}\right)(\hat{U}^s)^{-1} = \hat{S}^z + \xi_+[\hat{S}^+, \hat{S}^z] = \hat{S}^z - \xi_+ \hat{S}^+ \tag{B.43}$$

since all other terms in the expansion (B.39) vanish.

3. $a = -$:

$$\left(\frac{\partial \hat{U}^s}{\partial \xi_-}\right)(\hat{U}^s)^{-1} = e^{(+)} e^{(z)} \hat{S}^- e^{-(z)} e^{-(+)} \tag{B.44}$$

$$= e^{(+)} \left(\hat{S}^- + \xi_z[\hat{S}^z, \hat{S}^-] + \frac{\xi_z^2}{2}[\hat{S}^z, [\hat{S}^z, \hat{S}^-]] + \dots\right) e^{-(+)} \tag{B.45}$$

$$= e^{-\xi_z} e^{(+)} \hat{S}^- e^{-(+)} \tag{B.46}$$

$$= e^{-\xi_z} \left(\hat{S}^- + \xi_+[\hat{S}^+, \hat{S}^-] + \frac{\xi_+^2}{2} 2[\hat{S}^+, \hat{S}^z]\right) \tag{B.47}$$

$$= e^{-\xi_z} \left(\hat{S}^- + 2\xi_+ \hat{S}^z - \xi_+^2 \hat{S}^+\right). \tag{B.48}$$

We can now collect the overall coefficient multiplying each $\hat{S}^a$ and equate it to Φ^a to find the conditions that must be satisfied by the ξ_a fields at each site:

$$\begin{aligned} \Phi^+ &= \dot{\xi}_+ - e^{-\xi_z} \xi_+^2 \dot{\xi}_- - \xi_+ \dot{\xi}_z, \\ \Phi^z &= \dot{\xi}_z + 2\xi_+ e^{-\xi_z} \dot{\xi}_-, \\ \Phi^- &= e^{-\xi_z} \dot{\xi}_-. \end{aligned} \tag{B.49}$$

Expressing the conditions in Eq. (B.49) in terms of $\dot{\xi}_i$ yields the imaginary time equations of motion of the disentangling variables:

$$\dot{\xi}_i^+ = \Phi_i^+ + \Phi_i^z \xi_i^+ - \Phi_i^- {\xi_i^+}^2, \tag{B.50}$$

$$\dot{\xi}_i^z = \Phi_i^z - 2\Phi_i^- \xi_i^+, \tag{B.51}$$

$$\dot{\xi}_i^- = \Phi_i^- \exp \xi_i^z. \tag{B.52}$$

The real-time equations are obtained by Wick-rotating: $\tau = it \Rightarrow \partial_\tau = -i\partial_t$.

B.4 Analytical Averaging of the SDEs

Consider an observable $\hat{\mathcal{O}}(t)$. In the stochastic approach, its expectation value following time evolution from an initial state $|\psi_0\rangle$ can be expressed as as

$$\langle\hat{\mathcal{O}}\rangle = \langle f\rangle_{\phi,\tilde{\phi}}, \tag{B.53}$$

where $f(\xi,\tilde{\xi},t)$ is a function of the disentangling variables ξ, $\tilde{\xi}$ depending on the chosen observable and state. By analytically averaging Eq. (B.53), one can obtain a system of coupled ordinary differential equations which encode the dynamics of $\langle\hat{\mathcal{O}}\rangle$. However, solving this system of equations is equivalent to diagonalising the Hamiltonian. This can be seen by applying the Ito chain rule Eq. (2.30) to the definition of $f(\xi,\tilde{\xi},t)$ given by Eq. (2.29). From the definition of $\hat{U}^s$ in Eq. (2.16), we have

$$\left\langle\left[\sum_{ai}\left(a_i^a+\sum_{jb}B_{ij}^{ab}\phi_j^b\right)\frac{\partial}{\partial\xi_i^a}+\frac{1}{2}\sum_{abij}\sum_{ck}B_{ik}^{ac}B_{jk}^{bc}\frac{\partial^2}{\partial\xi_i^a\partial\xi_j^b}\right]\hat{U}^s(t)\right\rangle_{\phi,\tilde{\phi}} = \left\langle\frac{d}{dt}\hat{U}^s(t)\right\rangle_{\phi} \tag{B.54}$$

$$= -i\hat{H}\hat{U}(t), \tag{B.55}$$

where for notational economy we define the indices a,b to run both over $\{+,-,z\}$ and over the $\xi,\tilde{\xi}$ variables. Eq. (B.55) can also be proved by directly differentiating the left-hand side of Eq. (B.54) and using the commutation relations of SU(2). The equation of motion of $\langle\hat{\mathcal{O}}(t)\rangle$ can thus be written as

$$\left\langle\frac{d\hat{\mathcal{O}}}{dt}\right\rangle = \langle\dot{f}\rangle_{\phi,\tilde{\phi}} = i\langle\psi_0|\left(\hat{H}\langle\hat{U}^{s\dagger}\rangle_{\tilde{\phi}}\hat{\mathcal{O}}\langle\hat{U}^s\rangle_{\phi}-\langle\hat{U}^{s\dagger}\rangle_{\tilde{\phi}}\hat{\mathcal{O}}\langle\hat{U}^s\rangle_{\phi}\hat{H}\right)|\psi_0\rangle, \tag{B.56}$$

where the two terms on the right-hand side arise from the ξ and the $\tilde{\xi}$ derivatives respectively. We recognise Eq. (B.56) as a matrix element of the Heisenberg equation of motion

$$\hat{\mathcal{O}}(t) = i[\hat{H},\hat{\mathcal{O}}(t)]. \tag{B.57}$$

The action of the Hamiltonian on the initial state $|\psi_0\rangle$ generates other states $|\psi_{\pm 1,j}\rangle$ in the computational basis that are related to $|\psi_0\rangle$ by no more than one spin flip:

$$\hat{H}|\psi_0\rangle = \sum_j C_j |\psi_{\pm 1,j}\rangle, \tag{B.58}$$

where the index j labels different states and, by definition, $|\psi_0\rangle \in \{\psi_{\pm 1,j}\}$. Inserting this in Eq. (B.56), we obtain

$$\langle \dot{f} \rangle_{\phi,\tilde{\phi}} = -2\mathrm{Im} \sum_j \langle f_{\pm 1,j} \rangle_{\phi,\tilde{\phi}}, \tag{B.59}$$

with

$$f_{\pm,j} \equiv C_j \langle \psi_0 | \hat{U}_s^\dagger \mathcal{O} \hat{U}_s | \psi_{\pm 1,j} \rangle. \tag{B.60}$$

We have thus shown that the equation of motion for $\langle f \rangle_{\phi,\tilde{\phi}}$ involves a linear combination of other amplitudes $\{\langle f_{\pm 1,j} \rangle_{\phi,\tilde{\phi}}\}$. In turn, by following the same line of reasoning, we see that the equations of motion of $\{\langle f_{\pm 1,j} \rangle_{\phi,\tilde{\phi}}\}$ involve all the amplitudes $\{\langle f_{\pm 2,j} \rangle_{\phi,\tilde{\phi}}\}$ which differ from the initial state $|\psi_0\rangle$ by no more than two spin flips. Iterating this procedure, since the Hamiltonian couples all states in the computational basis, we get a system of 2^N coupled linear ODEs for the amplitudes

$$F_j = \langle \psi_0 | \hat{\mathcal{O}}(t) | \psi_j \rangle, \tag{B.61}$$

where $|\psi_j\rangle$ is any state written in the computational basis. This system of equations can be written as

$$\frac{d}{dt}\boldsymbol{F} = \boldsymbol{M}\boldsymbol{F}, \tag{B.62}$$

where $F = \{F_j\}$ and M is a $2^N \times 2^N$ matrix. The solution of this system is equivalent to the diagonalisation of the Hamiltonian, as it can be seen by expanding the computational states $|\psi_j\rangle$ in terms of the eigenstates $|j\rangle$ of the Hamiltonian.

B.5 Building Blocks for Local Observables

Since the stochastic time evolution operator defined in Eq. (2.16) factorises over states, it is possible to obtain the stochastic expression corresponding to a particular observable by multiplying a set of on-site building blocks. We illustrate this by considering the example of an observable $\hat{\mathcal{O}}$ which is a product of $\hat{S}_i^z$ operators at different sites i. For a generic matrix element between product states, the stochastic expression corresponding to $\langle\hat{\mathcal{O}}\rangle$ is obtained as follows. For each site i, if $\hat{S}_i^z$ is not present in $\hat{\mathcal{O}}$ one includes one of the terms

$$\begin{aligned} n_i^{uu} &\equiv \langle\uparrow|_i \hat{U}_i^s[\tilde{\xi}]^\dagger \hat{U}_i^s[\xi]|\uparrow\rangle_i \\ &= e^{-\frac{\xi_i^z+\tilde{\xi}_i^{z*}}{2}}\left(e^{\xi_i^z+\tilde{\xi}_i^{z*}} + e^{\tilde{\xi}_i^{z*}}\xi_i^-\xi_i^+ + e^{\xi_i^z}\tilde{\xi}_i^{-*}\tilde{\xi}_i^+ + \xi_i^-\tilde{\xi}_i^{-*}(1+\xi_i^+\tilde{\xi}_i^{+*})\right), \end{aligned} \tag{B.63a}$$

$$n_i^{ud} \equiv \langle\uparrow|_i \hat{U}_i^s[\tilde{\xi}]^\dagger \hat{U}_i^s[\xi]|\downarrow\rangle_i = e^{-\frac{\xi_i^z+\tilde{\xi}_i^{z*}}{2}}\left(\tilde{\xi}_i^{-*} + e^{\tilde{\xi}_i^{z*}}\xi_i^+ + \tilde{\xi}_i^{-*}\xi_i^+\tilde{\xi}_i^{+*}\right), \tag{B.63b}$$

$$n_i^{du} \equiv \langle\downarrow|_i \hat{U}_i^s[\tilde{\xi}]^\dagger \hat{U}_i^s[\xi]|\uparrow\rangle_i = e^{-\frac{\xi_i^z+\tilde{\xi}_i^{z*}}{2}}\left(\xi_i^- + e^{\xi_i^z}\tilde{\xi}_i^{+*} + \xi_i^-\xi_i^+\tilde{\xi}_i^{+*}\right), \tag{B.63c}$$

$$n_i^{dd} \equiv \langle\downarrow|_i \hat{U}_i^s[\tilde{\xi}]^\dagger \hat{U}_i^s[\xi]|\downarrow\rangle_i = e^{-\frac{\xi_i^z+\tilde{\xi}_i^{z*}}{2}}(1+\xi_i^+\tilde{\xi}_i^{+*}), \tag{B.63d}$$

depending on the overlap of interest, whereas if $\hat{S}_i^z$ is present in $\hat{\mathcal{O}}$ one includes one of the terms

$$\begin{aligned} s_i^{z,uu} &\equiv \langle\uparrow|_i \hat{U}_i^s[\tilde{\xi}]^\dagger \hat{S}_i^z \hat{U}_i^s[\xi]|\uparrow\rangle_i \\ &= \frac{1}{2}e^{-\frac{\xi_i^z+\tilde{\xi}_i^{z*}}{2}}\left(e^{\xi_i^z+\tilde{\xi}_i^{z*}} + e^{\tilde{\xi}_i^{z*}}\xi_i^-\xi_i^+ + e^{\xi_i^z}\tilde{\xi}_i^{-*}\tilde{\xi}_i^{+*} + \xi_i^-\tilde{\xi}_i^{-*}(-1+\xi_i^+\tilde{\xi}_i^{+*})\right), \end{aligned} \tag{B.64a}$$

$$s_i^{z,ud} \equiv \langle\uparrow|_i \hat{U}_i^s[\tilde{\xi}]^\dagger \hat{S}_i^z \hat{U}_i^s[\xi]|\downarrow\rangle_i = \frac{1}{2}e^{-\frac{\xi_i^z+\tilde{\xi}_i^{z*}}{2}}\left(-\tilde{\xi}_i^{-*} + e^{\tilde{\xi}_i^{z*}}\xi_i^+ + \tilde{\xi}_i^{-*}\xi_i^+\tilde{\xi}_i^{+*}\right), \tag{B.64b}$$

$$s_i^{z,du} \equiv \langle\downarrow|_i \hat{U}_i^s[\tilde{\xi}]^\dagger \hat{S}_i^z \hat{U}_i^s[\xi]|\uparrow\rangle_i = \frac{1}{2}e^{-\frac{\xi_i^z+\tilde{\xi}_i^{z*}}{2}}\left(-\xi_i^- + e^{\xi_i^z}\tilde{\xi}_i^{+*} + \xi_i^-\xi_i^+\tilde{\xi}_i^{+*}\right), \tag{B.64c}$$

$$s_i^{z,dd} \equiv \langle\downarrow|_i \hat{U}_i^s[\tilde{\xi}]^\dagger \hat{S}_i^z \hat{U}_i^s[\xi]|\downarrow\rangle_i = \frac{1}{2}e^{-\frac{\xi_i^z+\tilde{\xi}_i^{z*}}{2}}(-1+\xi_i^+\tilde{\xi}_i^{+*}). \tag{B.64d}$$

This construction straightforwardly generalises to operators $\hat{\mathcal{O}}$ involving also $\hat{S}_i^x$, $\hat{S}_i^y$.

B.6 Vanishing Expectation Values in the Ising SDEs

For the Ising SDEs given in Eq. (3.2), it is possible to derive an infinite number of exact identities whereby expectation values of monomials in $R_i \equiv \mathrm{Re}(\xi_i^+)$, $I_i \equiv \mathrm{Im}(\xi_i^+)$ vanish identically at all times. In order to derive these identities, we will introduce a notation that will allow us to efficiently analyse the system of ODEs which arise from averaging the SDEs. Let us begin by considering the imaginary time case. The coupled SDEs for R_i, I_i can be readily obtained by appropriately combining Eq. (3.2a) with its complex conjugate:

$$\dot{R}_i(\tau) = \frac{\Gamma}{2}(1 - R_i^2 + I_i^2) + R_i O_R \phi - I_i O_I \phi \tag{B.65a}$$

$$\equiv A_R(\tau) + B_R(\tau)\phi, \tag{B.65b}$$

$$\dot{I}_i(\tau) = -\Gamma R_i I_i + R_i O_I \phi + I_i O_R \phi \tag{B.65c}$$

$$\equiv A_I(\tau) + B_I(\tau)\phi. \tag{B.65d}$$

For real time evolution, we similarly get

$$\dot{R}_i(t) = \Gamma R_i I_i + \frac{\sqrt{2}}{2}[R_i(O_R - O_I) - I_i(O_R + O_I)]\phi \tag{B.66a}$$

$$\equiv C_R(t) + D_R(t)\phi, \tag{B.66b}$$

$$\dot{I}_i(t) = \frac{\Gamma}{2}(1 - R_i^2 + I_i^2) + \frac{\sqrt{2}}{2}[R_i(O_R + O_I) + I_i(O_R - O_I)]\phi \tag{B.66c}$$

$$\equiv C_I(t) + D_I(t)\phi. \tag{B.66d}$$

In the above, we have introduced $(O_R)_{ij} \equiv \mathrm{Re}(O_{ij})$ and the shorthand notation $O_R\phi \equiv \sum_j (O_R)_{ij}\phi_j$, and similarly for O_I. The identities we wish to find are most easily proved by introducing a convenient formal notation. In particular, let us represent the expectation value of a given monomial $\langle R_i^n I_i^m \rangle$ as a *state* $|n,m\rangle$. Each derivative with respect to R_i (I_i) decreases n (m) by 1, and annihilates a state where n (m) is equal to zero. This suggests that we can formally define *annihilation operators* $a_R \equiv \frac{\partial}{\partial R}$, $a_I \equiv \frac{\partial}{\partial I}$ satisfying

$$a_R|n,m\rangle = n|n-1,m\rangle, \tag{B.67a}$$

$$a_I|n,m\rangle = m|n,m-1\rangle. \tag{B.67b}$$

Following the same line of reasoning, we can represent R_i and I_i themselves as creation operators satisfying

$$a_R^\dagger |n,m\rangle = |n+1,m\rangle, \tag{B.68a}$$
$$a_I^\dagger |n,m\rangle = |n,m+1\rangle. \tag{B.68b}$$

It can be readily seen that the operators satisfy bosonic commutation relations $[a_X, a_{X'}^\dagger] = \delta_{XX'}$ where $X, X' \in \{R, I\}$. The time evolution of a general state $|n,m\rangle = \langle R_i^n I_j^m \rangle$ is determined by the Ito chain rule. For imaginary time evolution, we get

$$\begin{aligned}\frac{\mathrm{d}}{\mathrm{d}\tau} R_i^n(\tau) I_i^m(\tau) =& n R_i^{n-1} I_i^m (A_R + B_R\phi) + m R_i^n I_i^{m-1} (A_I + B_I\phi) \\ &+ \frac{1}{2}\Big(n(n-1) R_i^{n-2} I_i^m B_R B_R^T + m(m-1) R_i^n I_i^{m-2} B_I B_I^T \\ &+ nm R_i^{n-1} I_i^{m-1} (B_R B_I^T + B_I B_R^T)\Big).\end{aligned} \tag{B.69}$$

Using the property $O_I O_R^T = O_R O_I^T = 0$ for the O_{ij} matrix (Appendix B.2), we can simplify

$$B_R B_R^T = R^2 O_R O_R^T + I^2 O_I O_I^T, \tag{B.70a}$$
$$B_R B_I^T = B_I B_R^T = -RI(O_I O_I^T + O_R O_R^T), \tag{B.70b}$$
$$B_R B_R^T = I^2 O_R O_R^T + R^2 O_I O_I^T. \tag{B.70c}$$

We can apply the notation we have introduced to compactly write the time evolution of an expectation value $|n,m\rangle$. Recalling the property $\langle f(t)\phi(t)\rangle = 0$ for Ito calculus, we obtain

$$\begin{aligned}\frac{\mathrm{d}}{\mathrm{d}\tau}|n,m\rangle =& \Big\{ \frac{\Gamma}{2}\left(1 - a_R^\dagger a_R^\dagger + a_I^\dagger a_I^\dagger\right) a_R - \Gamma a_R^\dagger a_I^\dagger a_I \\ &+ \frac{1}{2}[(O_R O_R^T a_R^\dagger a_R^\dagger + O_I O_I^T a_I^\dagger a_I^\dagger) a_R a_R \\ &+ (O_I O_I^T a_R^\dagger a_R^\dagger + O_R O_R^T a_I^\dagger a_I^\dagger) a_I a_I] \Big\} |n,m\rangle \end{aligned} \tag{B.71}$$
$$\equiv - H_I |n,m\rangle, \tag{B.72}$$

where we have used $(O_I O_I^T)_{ii} = (O_R O_R^T)_{ii}$ (Appendix B.2) and defined an *effective Hamiltonian* H_I. Eq. (B.69), describing the imaginary time evolution of a general expectation value $\langle R_i^n(\tau) I_i^m(\tau)\rangle$, was thus cast in a form reminding of a Schroedinger equation in imaginary-time. This is a formal analogy, as the standard rules of quantum mechanics do

not hold, e.g. there is no specific definition of an inner product between states. The same procedure can be followed for the real time evolution, yielding

$$\frac{\mathrm{d}}{\mathrm{d}t}|n,m\rangle = -H_R|n,m\rangle \tag{B.73}$$

with

$$\begin{aligned} H_R \equiv \Gamma a_R^\dagger a_I^\dagger a_R + \frac{\Gamma}{2}\left(1 - a_R^\dagger a_R^\dagger + a_I^\dagger a_I^\dagger\right) a_I \\ + \frac{1}{2}(O_I O_I^T + O_R O_R^T)(a_R^\dagger a_R^\dagger + a_I^\dagger a_I^\dagger)(a_R a_R + a_I a_I). \end{aligned} \tag{B.74}$$

The real time variable t plays the role of imaginary time in the pseudo-Schroedinger equation (B.73). The machinery we have introduced allows us to straightforwardly obtain an infinite number of identities for monomials in R_i, I_i. From the form of Eq. (B.71), it is clear that the Hamiltonian H_I does not contain any term that raises or lowers the index m of a state $|n,m\rangle$ by an odd number. Hence, states with odd and even m belong to separate even and odd subspaces $\mathcal{H}_{I,e}$ and $\mathcal{H}_{I,o}$. At $\tau = 0$ we have the initial conditions $|n,m\rangle = \delta_{n0}\delta_{m0}$. Since $|0,0\rangle \equiv \langle 1\rangle$ does not belong to the odd subspace $\mathcal{H}_{I,o}$, all states $|n,m\rangle \in \mathcal{H}_{I,o}$ vanish identically at all times. Analogously, Eq. (B.73) implies that for real time evolution states $|n,m\rangle$ with odd and even n are not coupled by the time evolution, and the space of states factorizes into two separate subspaces $\mathcal{H}_{R,e}$ and $\mathcal{H}_{R,o}$. In this case, it is all the states $|n,m\rangle \in \mathcal{H}_{R,o}$ with odd n that vanish identically at all times due to the initial conditions. These findings can be summarized as

$$\langle R_i^n(\tau) I_i^m(\tau)\rangle = 0 \quad \forall \quad m \text{ odd}, \tag{B.75a}$$

$$\langle R_i^n(t) I_i^m(t)\rangle = 0 \quad \forall \quad n \text{ odd}. \tag{B.75b}$$

The operator description of the stochastic evolution introduced in this Section allowed us to derive the vanishing expectation values in a transparent way. However, this formulation provides a rather general alternative viewpoint and could turn out be a useful tool for future developments.

B.7 Gaussian Approximation

The moments of $R_i \equiv \mathrm{Re}(\xi_i^+)$, $I_i \equiv \mathrm{Im}(\xi_i^+)$ can be computed in closed form under the assumption that ξ_i^+ is Gaussian distributed. We define time-dependent means m_X and covariances C_{XY} as

$$m_X \equiv \langle X \rangle, \tag{B.76a}$$
$$X = m_X + \delta X, \tag{B.76b}$$
$$C_{XY} \equiv \langle \delta X \delta Y \rangle, \tag{B.76c}$$

for $X, Y \in \{R, I\}$. Within the Gaussian approximation, all moments can be expressed in terms of these quantities, e.g.

$$\langle R^3 \rangle = \langle (m_R + \delta R)^3 \rangle \tag{B.77}$$
$$= m_R^3 + 3 m_R C_{RR}, \tag{B.78}$$

where we used $\langle \delta R^3 \rangle = \langle \delta R \rangle = 0$. All quantities vanish at $\tau = 0$. Using this approximation, we get the imaginary time Gaussian time-evolution equations

$$\dot{m}_R(\tau) = \frac{1}{2}\Gamma\left(C_{II} - C_{RR} - m_R^2 + m_I^2 + 1\right), \tag{B.79}$$
$$\dot{m}_I(\tau) = -\Gamma m_I m_R = 0, \tag{B.80}$$
$$\begin{aligned}\dot{C}_{RR}(\tau) =& \Gamma\left(C_{II} m_R + 2 m_I C_{IR} - 3 C_{RR} m_R - m_R^3 + m_I^2 m_R + m_R\right) + o_{II}\left(C_{II} + m_I^2\right) \\ & - \Gamma\left(m_R\left(C_{II} + m_I^2\right) - m_R\left(C_{RR} + m_R^2\right) + m_R\right) + o_{RR}\left(C_{RR} + m_R^2\right),\end{aligned} \tag{B.81}$$
$$\begin{aligned}\dot{C}_{IR}(\tau) =& \frac{1}{2}\Gamma\left(3 m_I C_{II} - 2 C_{IR} m_R - m_I C_{RR} - m_I m_R^2 + m_I^3 + m_I\right) \\ & - \frac{1}{2}\Gamma\left(m_I\left(C_{II} + m_I^2\right) - m_I\left(C_{RR} + m_R^2\right) + m_I\right) \\ & + \Gamma m_R\left(C_{IR} + m_I m_R\right) - \Gamma\left(2 C_{IR} m_R + m_I C_{RR} + m_I m_R^2\right) = 0,\end{aligned} \tag{B.82}$$
$$\begin{aligned}\dot{C}_{II}(\tau) =& -2\Gamma\left(C_{II} m_R + 2 m_I C_{IR} + m_I^2 m_R\right) + 2\Gamma m_I\left(C_{IR} + m_I m_R\right) \\ & + o_{II}\left(C_{RR} + m_R^2\right) + o_{RR}\left(C_{II} + m_I^2\right),\end{aligned} \tag{B.83}$$

where we defined $o_{XX} = (O_X O_X^T)_{ii}$ (these are all equal by translational invariance) and we set some of these quantities to zero using the results of Section B.6 (this can however be confirmed by direct solution of the full ODEs). For sufficiently large Γ, we find that the Gaussian approximation accurately captures the behaviour of $\xi_i^+(\tau)$, as shown in Fig. 3.4.

The same procedure can be repeated in real time, giving the Gaussian equations

$$\dot{m}_R(t) = \Gamma m_R m_I = 0, \tag{B.84}$$

$$\dot{m}_I(t) = \frac{1}{2}\Gamma\left(C_{II} - C_{RR} - m_R^2 + m_I^2 + 1\right), \tag{B.85}$$

$$\begin{aligned}\dot{C}_{RR}(t) =& \frac{1}{2}\left(o_{II} + o_{RR}\right)\left(C_{II} + C_{RR} + m_R^2 + m_i^2\right) - 2\Gamma m_R\left(C_{IR} + m_I m_R\right) \\ &+ 2\Gamma\left(2C_{IR}m_R + m_I C_{RR} + m_I m_R^2\right),\end{aligned} \tag{B.86}$$

$$\dot{C}_{IR}(t) = 0, \tag{B.87}$$

$$\begin{aligned}\dot{C}_{II}(t) =& \Gamma\left(3m_I C_{II} - 2C_{IR}m_R - m_I C_{RR} - m_I m_R^2 + m_I^3 + m_I\right) - \Gamma m_I\left(C_{II} - C_{RR} - m_R^2 + m_I^2 + 1\right) \\ &+ \frac{1}{2}\left(o_{II} + o_{RR}\right)\left(C_{II} + C_{RR} + m_R^2 + m_I^2\right).\end{aligned} \tag{B.88}$$

In contrast to the imaginary time case, we find that for real time evolution the Gaussian approximation breaks down at a particular time scale, where a strongly non-Gaussian behaviour emerges (Fig. 3.5).

Appendix C

Stochastic Differential Equations for the XYZ Model

The one-dimensional XYZ chain in a magnetic field is defined by the Hamiltonian

$$\hat{H}_H = -\sum_i \left(J_x \hat{S}_i^x \hat{S}_{i+1}^x + J_y \hat{S}_i^y \hat{S}_{i+1}^y + J_z \hat{S}_i^z \hat{S}_{i+1}^z \right) - h \sum_i \hat{S}_i^z. \tag{C.1}$$

This Hamiltonian contains many well-known models as special cases, including

- $J_z = h = 0$: XY model, solvable in terms of free fermions.
- $J_z = J_y = 0$: transverse-field Ising chain, solvable in terms of free fermions.
- $J_y = J_x$: XXZ model, solvable by Bethe ansatz.

In the stochastic approach, the model in Eq. (C.1) is described by the imaginary time SDEs

$$\dot{\xi}_i^+(\tau) = \frac{1}{2} \sum_j \left(O_{ij}^x \phi_j^x - i O_{ij}^y \phi_j^y \right) + \left(h + \sum_j O_{ij}^z \phi_j^z \right) \xi_i^+ - \frac{1}{2} \sum_j \left(O_{ij}^x \phi_j^x + i O_{ij}^y \phi_j^y \right) {\xi_i^+}^2, \tag{C.2a}$$

$$\dot{\xi}_i^z(\tau) = h + \sum_j O_{ij}^z \phi_j^z - \sum_j \left(O_{ij}^x \phi_j^x + i O_{ij}^y \phi_j^y \right) \xi_i^+, \tag{C.2b}$$

$$\dot{\xi}_i^-(\tau) = \frac{1}{2} \sum_j \left(O_{ij}^x \phi_j^x + i O_{ij}^y \phi_j^y \right) \exp \xi_i^z, \tag{C.2c}$$

where the matrices O_{ij}^a satisfy $\sum_k O_{ik}^a O_{jk}^a = J_a \left(\delta_{ij+1} + \delta_{ij-1} \right)$ with $a \in \{x, y, z\}$. The real time SDEs are obtained as per the general discussion in Chapter 2. By setting $J_z = J_y = 0$,

we obtain a stochastic description of the quantum Ising model where the drifts in the SDEs for $\xi_i^{\pm}$ are linear while the diffusion terms are non-linear. This is in contrast with the Ising SDEs we introduce in Chapter 3, which have non-linear drifts and linear diffusion coefficients, showing that the stochastic representation of a given model is not unique and different representations may be useful for different purposes.

Appendix D

Numerical Aspects

D.1 Simulation Schemes

In the stochastic formalism, observables are expressed as expectation values over the trajectories of a set of disentangling variables $\xi_i^a(t)$, which satisfy stochastic differential equations. For definiteness, let us consider the quantum Ising model, whose Hamiltonian is given by

$$\hat{H}_{\mathrm{I}} = -J\sum_{j=1}^{N}\hat{S}_j^z\hat{S}_{j+1}^z - \Gamma\sum_{j=1}^{N}\hat{S}_j^x + h\sum_{j=1}^{N}\hat{S}_j^z, \tag{D.1}$$

where N is the number of lattice sites. This model is discussed in Chapter 3. We consider ferromagnetic interactions $J > 0$ and impose periodic boundary conditions. In numerical simulations we set $J = 1$ and measure time in units of $1/J$. For this model, the explicit form of the SDEs is given by

$$-i\dot{\xi}_j^+ = \frac{\Gamma}{2}(1-\xi_j^{+2}) - h\xi_j^+ + \xi_j^+\sum_k O_{jk}\phi_k, \tag{D.2a}$$

$$-i\dot{\xi}_j^z = -h - \Gamma\xi_j^+ + \sum_k O_{jk}\phi_k, \tag{D.2b}$$

$$-i\dot{\xi}_j^- = \frac{\Gamma}{2}\exp\xi_j^z, \tag{D.2c}$$

where the fields $\phi_j(t)$ ares Gaussian white noises with an imaginary action (Appendix B.1) and the matrix O_{ij} diagonalises the noise action (Appendix B.2). To the best of our knowledge, these SDEs cannot be solved exactly. Furthermore, it can be shown that taking the expectation value of the SDE for an observable yields a system of ODEs whose solution amounts to diagonalising the Hamiltonian (Appendix B.4). Thus, in order to calculate

observables, we need to solve these stochastic equations numerically. All numerical solutions are based on discretising the disentangling variables: the discretised variables are defined at times t_n, and at each time-step they are updated by $\xi_i^a(t_{n+1}) = \xi_i^a(t_n) + \Delta\xi_i^a(t_n)$. In this Section, we outline different numerical schemes that can be used to solve the SDEs. The best scheme is likely to depend on the specific problem one is interested in, so having a range of techniques at hand is in itself a valuable resource. We conclude this Section by comparing the performances of different schemes in computing a physical observable.

D.1.1 Euler Scheme

The simplest discretisation scheme is the Euler-Maruyama (or simply Euler) scheme, which prescribes an update rule for the stochastic variables given by

$$\begin{aligned} -i\Delta\xi_j^+(t_n) = &\left\{\frac{\Gamma}{2}\left[1-\xi_j^+(t_n)^2\right] - h\xi_j^+(t_n)\right\}\Delta t \\ &+ \sqrt{i}\xi_j^+(t_n)\sum_k O_{jk}\Delta W_k, \end{aligned} \tag{D.3a}$$

$$-i\Delta\xi_j^z(t_n) = \Delta t\left[-h-\Gamma\xi_j^+(t_n)\right] + \sqrt{i}\sum_k O_{jk}\Delta W_k, \tag{D.3b}$$

$$-i\Delta\xi_j^-(t_n) = \frac{\Gamma}{2}\exp[\xi_j^z(t_n)]\Delta t. \tag{D.3c}$$

The quantities ΔW_j are increments of independent Wiener processes (Appendix A.3), and can be simulated as $\Delta W_j = \phi_j\sqrt{\Delta t}$ where ϕ_j are delta-correlated Gaussian-distributed variables with unit variance. This scheme achieves an order of strong convergence 0.5 and order of weak convergence 1.0 [143], as defined in Appendix A.5.

D.1.2 Milstein Scheme

The next-higher order discretisation method is the Milsten scheme, which attains the order of strong convergence 1.0 [143]. For a general multi-component SDE of the form

$$\dot{X}_i = a_i(X,t) + \sum_j B_{ij}(X,t)\phi_j. \tag{D.4}$$

the Milstein update rule is identical to the Euler one, plus the additional term

$$\Delta X_i^M(t_{n+1}) = \sum_{jlk} B_{kj}(X,t_n)\frac{\partial}{\partial X_k}B_{il}(X,t_n)I_{jl}, \tag{D.5}$$

where I_{jl} are Ito stochastic integrals $I_{jl} \equiv \int_{t_n}^{t_{n+1}} \int_{t_n}^{s_1} \mathrm{d}W_j(s_2)\mathrm{d}W_k(s_1)$. In general, stochastic integrals cannot be expressed in terms of the increments ΔW_j, and have to be approximated. A notable exception is the case of *commutative noise* [143], namely when the condition

$$\sum_k B_{kj}(n)\frac{\partial}{\partial X_k}B_{il} = \sum_k B_{kl}(n)\frac{\partial}{\partial X_k}B_{ij} \tag{D.6}$$

is satisfied. In this case, the Ito stochastic integrals can be written as $I_{jk} + I_{kj} = \Delta W_j \Delta W_k$. For the quantum Ising model, the diffusion matrix does satisfy this condition. This enables one to explicitly express the Milstein update rules in terms of Gaussian-distributed random variables, leading to:

$$\begin{aligned} -i\Delta\xi_j^+(t_n) = &\left\{-\frac{\Gamma}{2}\left[1-\xi_j^+(t_n)^2\right] - h\xi_j^+(t_n)\right\}\Delta t \\ &+ \frac{1}{2}\xi_j^+(t_n)\left(\sum_k O_{jk}\Delta W_k(t_n)\right)^2 \\ &+ \xi_j^+(t_n)\sum_k O_{jk}\Delta W_k, \end{aligned} \tag{D.7}$$

whereas the update rules for $\xi_i^z(t_n)$, $\xi_i^-(t_n)$ are the same as for the Euler prescription. Discretisation schemes with higher convergence orders involve high-order stochastic integrals, which cannot be expressed exactly in terms of Gaussian variables and need to be approximated. This introduces additional levels of computational cost and complexity to the problem, so higher order schemes were not considered here.

D.1.3 Change of Variables: Additive Noise

In numerically simulating the trajectories of ξ_i^+, which has a non-linear equation of motion and - as argued in Chapter 3 - is the most important disentangling variable, at each time-step we have to approximate both the increments due to the diffusion and the drift terms. This suggests that, to get more accurate sampling for a given Δt, we may try to perform a change of variables so that at least part of the equation can be solved exactly. This can be achieved by considering

$$\zeta_i \equiv \log(\xi_i^+).$$

The equation of motion for $\zeta_i(t)$ is given by

$$-i\dot{\zeta}_i = -\Gamma \sinh \zeta_i - h + \sum_j O_{ij}\phi_j, \tag{D.8}$$

where the extra term required by Ito calculus vanishes due to $\sum_k O_{ik}O_{ik} = 0$ (Appendix B.2). We notice that the initial condition $\xi_i^a(0) = 0$ implies that $\zeta_i(0)$ is not well-defined. Hence, we cannot use this parameterisation at the beginning of a given simulation, and we must switch to it at a later time, for example after a condition of choice is met. To leading order in Δt, the update rule for ζ_i can be found from linearisation:

$$-i\Delta\zeta_i(t_{n+1}) = (-\Gamma \sinh \zeta_i(t_n) - h)\Delta t + \sqrt{i}\sum_j O_{ij}W_j(\Delta t), \tag{D.9}$$

where $W_j(\Delta t)$ is a standard Wiener process starting from zero at $t = 0$. Hence, when simulating this equation numerically we are only approximating the drift part, whilst the integration of the diffusion part is exact through the full Δt.

D.1.4 Random Walk Between Deterministic Trajectories

Still in the spirit of obtaining at least part of the time evolution exactly, we can apply a different approach to the numerical simulation of ζ_i. Namely, we can simulate ζ_i as a random walk between deterministic trajectories. The key idea is that we can find the exact solution $\zeta_i^d(t)$ of the deterministic ODE

$$-i\dot{\zeta}_i^d(t) = -\Gamma \sinh \zeta_i^d(t) - h \tag{D.10}$$

subject to $\zeta_i^d(0) = \zeta_i^0$. Then, suppose we want to simulate ζ_i starting from time t_0. We initialise $\zeta_i(t_0) = \zeta_i^0 = \log \xi_i^+(t_0)$, and using the exact solution of Eq. (D.10) we calculate $\zeta_i^d(\Delta t)$. Finally, we consider the effect of the diffusion term by setting $\zeta_i(t_0 + \Delta t) = \zeta_i^d(\Delta t) + \sqrt{i}\sum_j O_{ij}W_i(\Delta t)$, where $W_j(\Delta t)$ is a standard Wiener process with $W_i(0) = 0$. The fact that the noise is simply additive means that we don't have to perform stochastic integrals involving ζ_i, which is a key simplification. This procedure is then iterated by

setting $\zeta_i^0 = \zeta_i(t_0 + \Delta t)$. Let us summarise how to generate a single realisation of the trajectory of ζ_i evolving from $t = t_0$ to t_f in algorithmic form:

Algorithm 1: Random walk simulation of ξ_i^+

1 Obtain an analytical expression for $\zeta_i^d(t)$ satisfying Eq. (D.10) subject to $\zeta_i^d(0) = \zeta_i^0$;
2 Select the initial time $t = t_0$;
3 Get the initial condition $\zeta_i(t) = \log \xi_i^+(t_0)$;
4 **while** $t < t_f$ **do**
5 Set $\zeta_i^0 = \zeta_i(t)$;
6 Obtain the exact form of $\zeta_i^d(\Delta t)$ for the current ζ_i^0;
7 Set $t = t + \Delta t$;
8 Set $\zeta_i(t) = \zeta_i^d(\Delta t) + \sqrt{i}\sum_j O_{ij} W_j(\Delta t)$;
9 **end**
10 Compute $\xi_i^+(t) = \exp \zeta_i(t)$.

Thus, in this approach the diffusion term is seen as inducing a random walk between the deterministic trajectories $\zeta^d(t)$, which can be calculated exactly. This scheme was found not to be affected by the issue of divergent trajectories.

D.1.5 Exact Integration of the Noise

For SDEs with linear multiplicative noise, it is possible to decouple the drift and diffusion parts of the equation via a sequence of transformations [161]. Consider the SDE

$$-i\dot{\xi}_i^+ = f_i(\xi_i^+, t) + \sqrt{i}\xi_i^+ \sum_j O_{ij}\phi_j, \tag{D.11}$$

where the Ising SDE for ξ_i^+ is given by the choice $f_i = \Gamma[1 - (\xi_i^+)^2]/2$. Let us define auxiliary variables

$$Y_i \equiv \frac{\xi_i^+}{Z_i}, \tag{D.12}$$

where $Z_i = \exp\left(\sqrt{i}\int_0^t \sum_j O_{ij}\phi_j \mathrm{d}t\right)$ is the solution of

$$Z_i = \sqrt{i} Z_i \sum_j O_{ij}\phi_j. \tag{D.13}$$

With these definitions, Y_i satisfies the ODE

$$-i\dot{Y}_i = \frac{f_i(Y_i, Z_i, t)}{Z_i}. \tag{D.14}$$

Using this sequence of transformations, the stochastic part of the problem is solved exactly (i.e. $Z_i(t)$ is exact) and one is left with solving an ODE in which the function $Z_i(t)$ is known at the relevant discrete times. Using this approach, the simulation of a trajectory of ξ_i^+ is performed as follows:

Algorithm 2: Simulation of $\xi_i^+(t)$ via exact integration of noise

1. Generate $Z_i(t)$ at all times - this is done exactly;
2. Numerically solve the ODE $\dot{Y}_i = f(Z_i, Y_i)/Z_i$ using a method of choice ;
3. Compute $\xi_i^+ = Y_i Z_i$.

D.1.6 Other Changes of Variables

The form of the SDE (D.2a) for ξ_i^+ suggests a number of other changes of variables. As usual, the equation of motion for the new variable $f(\xi)$ is given by the Ito chain rule:

$$\dot{f} = \sum_{ai} \frac{\partial f}{\partial \xi_i^a} \left(A_i^a + \sum_{jb} B_{ij}^{ab} \phi_j^b \right) + \frac{1}{2} \sum_{ab,ij} \frac{\partial^2 f}{\partial \xi_i^a \partial \xi_j^b} \sum_{ck} B_{ik}^{ac} B_{jk}^{bc}. \tag{D.15}$$

For the quantum Ising model and a variable $f(\xi_i^+)$, we have $B_{ij}^{+a} = \delta_{az} \xi_i^+ O_{ij}$ so that the last term in Eq. (D.15) is given by

$$\frac{1}{2} \sum_{ij} \frac{\partial^2 f}{\partial \xi_i^+ \partial \xi_j^+} \xi_i^+ \xi_j^+ \sum_k O_{ik} O_{jk},$$

which vanishes for the properties of the O_{ij} matrix (Appendix B). So, if $f \equiv f(\xi_i^+)$ is a function of a single ξ_i^+ variable, the Ito drift term vanishes. This is the case for all of the transformations introduced in this Section. Here, we consider a range of possible changes of variables, discussing their rationale and providing the corresponding equations of motion.

1. $\xi_i^+ = \cos\theta_i$:

$$-i\dot{\theta}_i = -\frac{\Gamma}{2} \sin\theta_i + h\cot\theta_i - \cot\theta_i \sum_j O_{ij} \phi_j. \tag{D.16}$$

This transformation is based on the fact that the $(1-\xi_i^2)$ term in Eq. (D.2a) suggests a trigonometric parameterisation. The real part of θ_i can be compactified because of the periodicity of the cosine function.

2. $\xi_i^+ = \tanh\lambda_i$:

$$-i\dot{\lambda}_i = \frac{\Gamma}{2} - h\sinh\lambda_i\cosh\lambda_i + \sinh\lambda_i\cosh\lambda_i\sum_j O_{ij}\phi_j. \tag{D.17}$$

This transformation is based on the fact that the $\xi_i^+ = \tan(\Gamma t/2)$ is the exact solution for a non-interacting spin in a transverse field, when $J=0$ and $h=0$, so that the drift in the equation for λ_i is constant in this limit.

3. $\xi_i^+ = (1-x_i)/x_i$:

$$-i\dot{x}_i = \frac{\Gamma}{2}(1-2x_i) - hx_i(x_i-1) + x_i(x_i-1)\sum_j O_{ij}\phi_j. \tag{D.18}$$

This change of variables makes the drift term linear for $h=0$, corresponding to the transverse field Ising chain, at the expense of making the diffusion term quadratic.

4. $\xi_i^+ = (1-2y_i)/(1+2y_i)$:

$$-i\dot{y}_i = -2\Gamma y_i - h(y_i^2-1/4) + (y_i^2-1/4)\sum_j O_{ij}\phi_j. \tag{D.19}$$

Similarly to the previous case, this transformation makes the drift term linear for $h=0$.

Of the above possibilities, the parameterisations 1, 3 and 4 share the property that, for the non-interacting transverse field Ising chain with $h=0$, $J=0$, they do not diverge at $t^* = \pi/\Gamma$, whereas $\xi^+(t^*) = \infty$. This suggests that change of variables 1, 3, 4 could be better suited for sampling in the presence of dynamical quantum phase transitions, which develop as J is increased from zero.

D.1.7 Variable Δt

It can be expected that, for any of the above algorithms, a smaller Δt will be required in order to attain a desired precision in regions of the parameter space where the drift and diffusion coefficients are varying rapidly. By the same token, a larger Δt can be expected to be sufficient in areas of the parameter space characterised by a smoother behaviour. This

suggests that, having acquired an intuition for the behaviour of the stochastic processes of interest, one can vary the value of Δt over the course of a given simulation. This would provide a straightforward way to decrease the computational cost of any algorithm. However, this idea is based on the assumption that one is able to correctly estimate the regions where different Δt can be used. In turn, this means that for a given Δt one should be able to assess whether the trajectories of the stochastic variables are being sampled adequately. Imprecise sampling at an earlier time, due to insufficiently small Δt, could propagate errors to a later time in spite of subsequently switching to a finer Δt.

D.1.8 Comparison of Numerical Methods

We will now compare the performance of a number of the schemes introduced in this Section by looking at the Loschmidt rate function for a quench across the quantum critical point. We consider a 1D quantum Ising chain of size $N = 10$ initialised in the state $|\Downarrow\rangle$ with all spins down, and perform a quench of the transverse field from $\Gamma = 0$ to $\Gamma = 16\Gamma_c$. We compare the result for fixed time step $\Delta t = 10^{-5}$ and number of runs $n = 10000$, estimating the fluctuations for the different numerical schemes by looking at the standard deviation over two batches of n simulations, shown as bars in the relative plots. The algorithms we compare are: the Euler and Milstein schemes (Sections D.1.1-D.1.2), the 'exact noise' and 'random walk' versions of the additive noise parameterisation (Sections D.1.3-D.1.4), the solution via mapping to an ordinary differential equation (Section D.1.5) using different methods to perform Step 2, and a variable-Δt implementation of the Euler scheme (Section D.1.7). All schemes have comparable runtimes, except for 'variable Δt' where the runtime depends on the chosen time steps and intervals. The results of the comparison are shown in Fig. D.1. The Euler and Milstein schemes (a-b) show very similar performance and a similar pattern of fluctuations, as it is visible from the standard deviation. The same applies for the Random Walk scheme (d), in which case however no trajectories were found to diverge. The Exact Noise scheme (c) is evidently affected by sudden large fluctuations and showed the worst performance out of all methods. The three different methods (e), (f) and (g) based on the ODE approach show very different behaviour. Scheme (e), where the ODE is solved by the Euler scheme, gets closer to the peak value but shows a substantial deviation from ED after the peak. The more sophisticated solution schemes (f-g) did not produce any diverging trajectories; however, the high-order Matlab numerical solver ODE45 (f) appears to underestimate fluctuations, whereas the stiff Matlab numerical solver ODE15s (g) shows large deviations from ED. These results suggest that the integration of

the ODE via high-order, variable-time-step numerical schemes may fail. This could be due to the fact that the function Z_i containing the exact solution of the noise part of the equation is non-differentiable, and hence higher-order schemes which approximate the dynamics assuming differentiability may not be appropriate. The variable Δt approach (f) for the chosen parameters ($\Delta t = 10^{-4}$ for $t < 0.25$, $\Delta t = 10^{-6}$ for $t > 0.25$) produced the best performance both at the peak and overall, but the calculation took ~ 4 times longer than the other schemes. The fraction of finite trajectories at the end of the simulation is shown in the following Table:

Euler	Milstein	Exact Noise	Random Walk
0.9959	0.9967	0.9991	1

ODE (Euler)	ODE (ODE45)	ODE (ODE15s)	Variable Δt
0.9949	1	1	0.9996

It can be seen that the Random Walk scheme and the ODE scheme solved with variable time-step integrators are not affected by the issue of divergent trajectories.

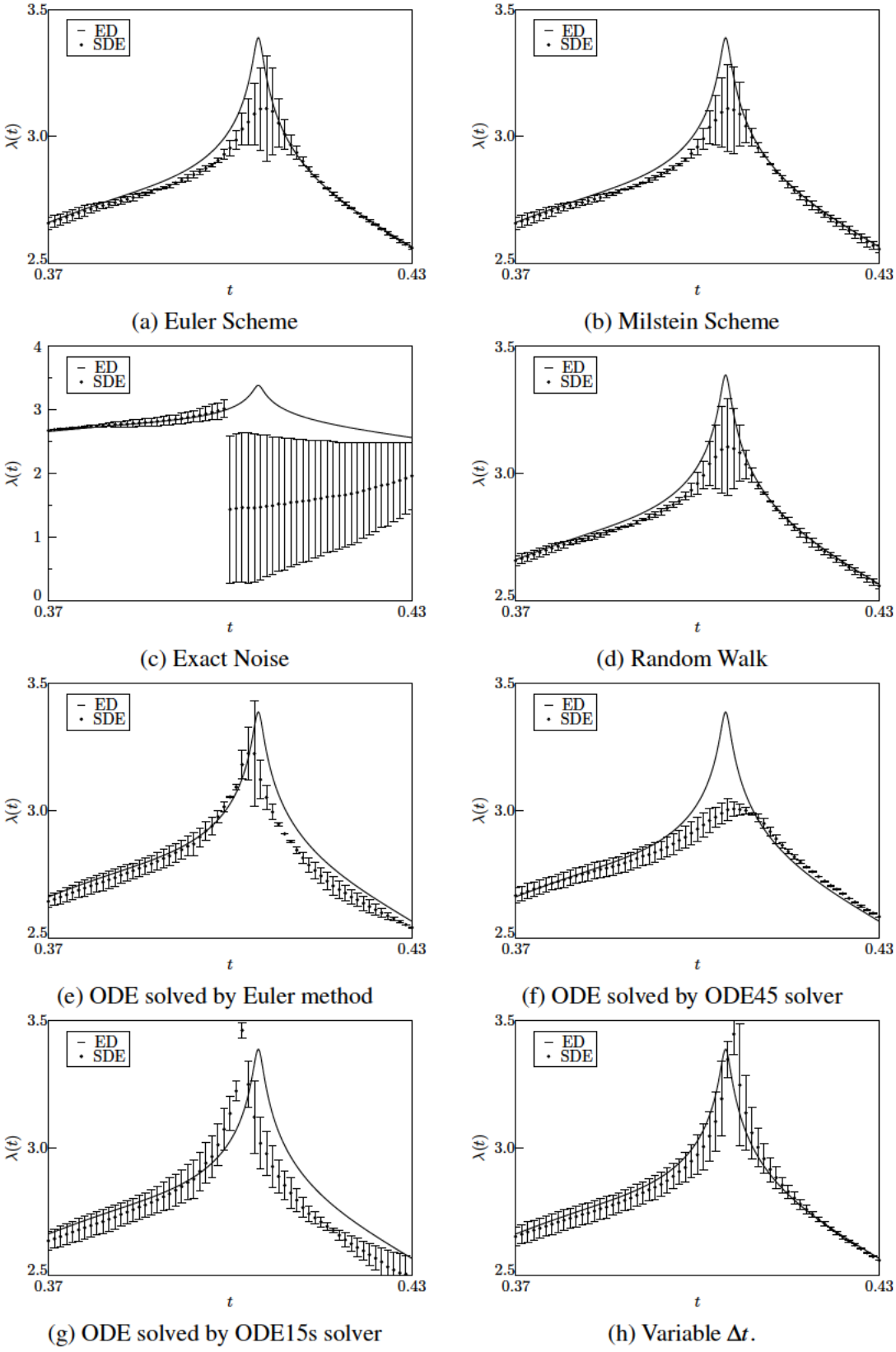

(a) Euler Scheme

(b) Milstein Scheme

(c) Exact Noise

(d) Random Walk

(e) ODE solved by Euler method

(f) ODE solved by ODE45 solver

(g) ODE solved by ODE15s solver

(h) Variable Δt.

Figure D.1: Detail of the first Loschmidt peak for a quantum Ising chain of size $N = 10$, following a quantum quench from the initial state $|\Downarrow\rangle$ with $\Gamma = 0$ to $\Gamma = 16\Gamma_c$. We show the Loschmidt rate function $\lambda(t)$ computed using different simulation schemes. The bars represent the standard deviation over the averages obtained by splitting the data set into 2 batches, similarly to Fig. 4.23. The results are compared in the main text.

D.2 Divergent Trajectories

In the stochastic formalism, the quantum expectation value of an observable $\hat{\mathcal{O}}$ is computed as the average of a corresponding classical quantity $\mathcal{O}_c(t)$ over stochastic processes $\phi(t)$:

$$\langle \hat{\mathcal{O}} \rangle = \langle \mathcal{O}_c(t) \rangle_\phi . \tag{D.20}$$

However, when the non-linear stochastic differential equations (SDEs) describing the stochastic evolution of $\mathcal{O}_c(t)$ are solved numerically using the Euler scheme, for any finite discretisation step Δt there is a certain probability that a trajectory diverges to infinity at some time t^*. A trajectory which has diverged cannot be used when performing the necessary averaging to calculate observables at a later time $t > t^*$. This is an important issue to address when applying the stochastic method numerically and it will be discussed in detail in this Section.

D.2.1 Numerical Condition for the Divergence of a Trajectory

The key equation to consider in order to understand the phenomenon of divergent trajectories is the equation of motion of ξ_i^+. For the quantum Ising model in the presence of a transverse field Γ and a longitudinal field h, this is given in real time by:

$$-i\dot{\xi}_i^+ = -\frac{\Gamma}{2}(1-\xi_i^+)^2 - h\xi_i^+ + \xi_i^+ \sum_j O_{ij}\phi. \tag{D.21}$$

When $\Gamma = 0$, corresponding to the classical case, Eq. (D.21) is linear, and no trajectories are seen to diverge in simulations even for non-zero initial conditions. However, for non-zero Γ Eq. (D.21) is a non-linear SDE; when equations of this kind are discretised and solved numerically, as we do using the Euler scheme, certain trajectories may diverge to infinity at $t < t_s$. We consider simulations with a finite discretisation step Δt, parameters Γ, h and stopping time t_s. In real time, the fraction of trajectories that diverge for fixed Δt, t_s is seen to increase with the physical parameters N or Γ. However, the number of diverging trajectories for fixed physical parameters decreases when reducing the discretisation step Δt. For a given set of parameters $N = 7, \Gamma = 4$, $h = 0$, $t_s = 1$, we observe that:

- For $\Delta t = 10^{-2}$, $\sim 55\%$ of trajectories diverge
- For $\Delta t = 10^{-3}$, $\sim 12\%$ of trajectories diverge
- For $\Delta t = 10^{-4}$, $\sim 2\%$ of trajectories diverge.

This effect highlights how the divergence of trajectories is closely related to the discretisation of time. Hence, it is sensible to seek a condition on the time-discretised variables that determines whether a given trajectory will diverge. For fixed time-step Δt, the discretised SDE for $\xi_i^+(t_n)$ reads:

$$\xi_i^+(t_{n+1}) - \xi_i^+(t_n) = i\Delta t[\frac{\Gamma}{2}(1-{\xi_i^+}^2(t_n))] - i\Delta t h\xi_i^+(t_n) - \sqrt{i\Delta t}\xi_i^+(t_n)\sum_j O_{ij}\tilde{\phi}_j(t_n), \tag{D.22}$$

where $\tilde{\phi}_j(t_n)$ are independent random variables drawn at each time t_n from a Gaussian distribution with zero mean and unit variance. The initial condition is $\xi_i^+ = 0$. So long as $|\xi_i^+| \lesssim 1$, the leading term in the increment of ξ_i^+, given by the RHS of Eq. (D.22), is linear in ξ_i^+. Linear SDEs are not affected by divergent trajectories [143]. Hence, we can seek conditions for divergence restricting our attention to times t such that $|\xi_i^+(t)| > 1$. At any such t, it is reasonable to expect that if the increment of $|\xi_i^+|$ is greater than $|\xi_i^+|$ itself, then $|\xi_i^+|$ can only increase. In other words, once this condition is satisfied, $|\xi_i^+(t)|$ will grow unboundedly. This reasoning can be summarised in the divergence condition

$$\left|\frac{\frac{\Gamma}{2}(1-{\xi_i^+}^2(t))}{\xi_i^+(t)}\Delta t\right| = \frac{\frac{\Gamma}{2}(|\xi_i^+(t)|^2-1)}{|\xi_i^+(t)|}\Delta t \gtrsim 1 \text{ for } |\xi_i^+(t)| > 1. \tag{D.23}$$

Since typically $\Gamma\Delta t \ll 1$, the above condition implies $|\xi_i^+(t)| \gg 1$. We can then simplify Eq. (D.23) and expect a trajectory to diverge whenever

$$|\xi_i^+(t)| \gtrsim \frac{2}{\Gamma\Delta t} \equiv \xi_*^+(\Gamma,\Delta t). \tag{D.24}$$

We checked whether this condition correctly captures the onset of divergences. Using data from numerical simulations, we numerically computed the probability $P_d(R)$ for a given trajectory to diverge if $|\xi_i^+(t)|/\xi_*^+ > R$ for any time t and plotted it as a function of R. This procedure was repeated for several choices of Γ, h and Δt, giving very similar results. The probability distribution $P_d(R)$ for a specific choice of parameters is shown in Fig. D.2. In all cases, it was found that $P_d(R) \sim 1$ for $R = 2$. Conversely, it was also found that all trajectories that diverge satisfy $|\xi_i^+(t)|/\xi_*^+ > 2$ for some t before they reach 'numerical infinity'. Hence, this condition correctly captures the origin of divergences and can be confidently used to diagnose which trajectories are going to become divergent. The condition is visualized in Fig. D.3: whenever a trajectory crosses the dashed line at $\xi_i^+ = \xi_*^+$, it is bound to rapidly diverge to infinity.

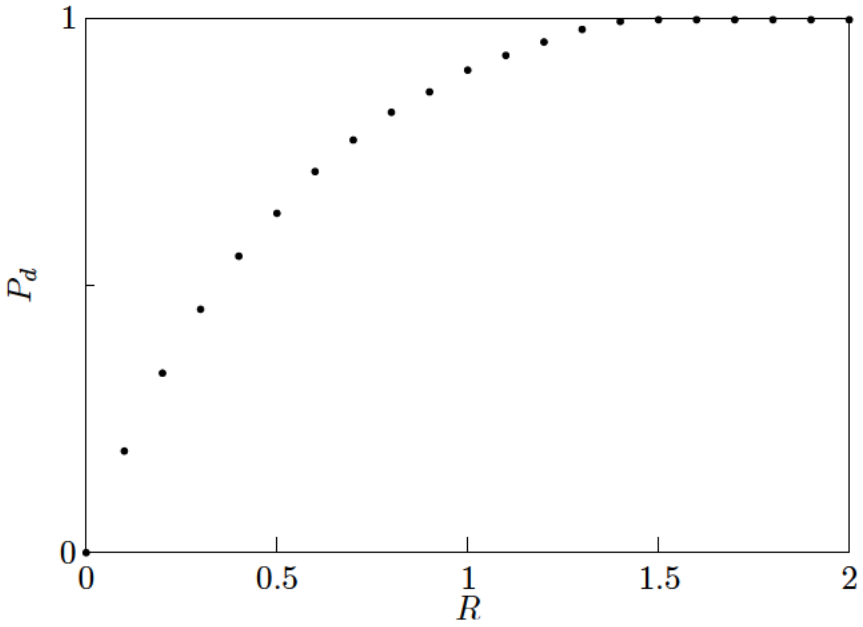

Figure D.2: Probability that a given trajectory diverges given that it satisfies $|\xi^+(t)|/\xi^+_* > R$ for some time t, where the threshold ξ^+_* is defined in Eq. (D.24). We show results obtained from 3000 realisations of the stochastic process with $\Gamma = 8$, $h = 0$, $N = 7$ and discretisation time-step $\Delta t = 10^{-3}$. It can be seen that $P_d \sim 1$ at $R = 2$. This finding is consistent across all parameters we considered.

D.2.2 Number of Time-Steps Until Divergence

Once the condition for divergence is met for a given trajectory, it is instructive to consider the number of time steps n_t required before the trajectory reaches 'numerical infinity'. Over this range of time-steps, the trajectory is still finite but it can already be regarded as pathological as it is bound to grow. By considering different simulations covering a range of Δt between 10^{-1} and 10^{-4}, it was found that the number of required time steps for a trajectory to diverge once the divergence condition is met is only weakly dependent on Δt, peaked at $n_t = 9$ and never greater than $n_t = 10$. This can be understood by a similar argument as the one given in the previous Section: if at time-step n we have the condition $|\xi^+_i(t_n)|/\xi^+_* \equiv R_n \gtrsim 1$, then $R_{n+1} \sim (R_n + R_n^2)$. Thus, from $t = t_n$ onwards we get superexponential growth:

$$R_{n+m} = R_n + (\cdots + (R_n + (R_n + R_n^2)^2)^2 \ldots)^2 \sim O(R_n^{2^m}) \tag{D.25}$$

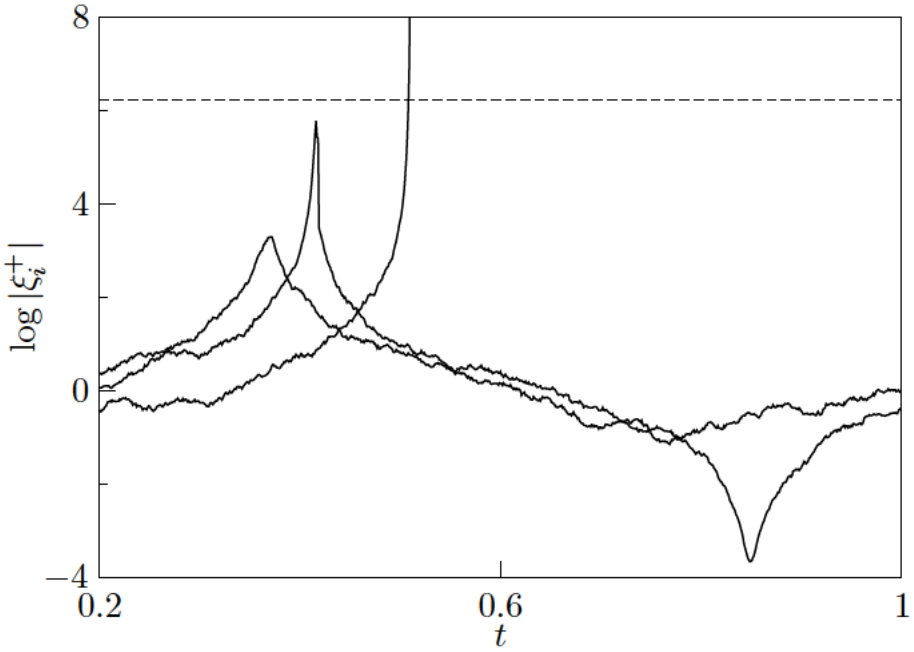

Figure D.3: Visualisation of the divergence condition. Whenever a trajectory satisfies $|\xi_i^+| > \xi_*^+$, represented by crossing the dashed line, it rapidly diverges. This figure shows 3 trajectories, one of which divergent, for a quench $\Gamma = 0$ to $\Gamma = 16\Gamma_c$ in a system of size $N = 7$.

so that $|\xi_i^+(t_{n+m})| \sim O\left(R_n^{2^m}/\Gamma\Delta t\right)$. Taking the numerical infinity to be $\infty_n \sim 2 \times 10^{308}$ (the maximum value handled by Matlab), the numerical solution of the recursive equation Eq. (D.25) correctly predicts the values of $n_t(\Gamma, \Delta t)$ observed in simulations.

D.2.3 Effect of Δt

The condition (D.24) is given as a function of Δt, so this parameter can be reduced to mitigate the phenomenon of diverging trajectories. However, reducing Δt linearly increases the computational cost of a given simulation. Based on the earlier arguments, one can expect that for a given set of physical parameters it is possible to find a value Δt^* such that for $\Delta t < \Delta t^*$ divergent trajectories become arbitrarily rare. However, for $\Delta t > \Delta t^*$, the divergence condition implies that each trajectory for which $\xi_i^+(t) \gtrsim \xi_*^+(\Gamma, \Delta t)$ will inevitably diverge. This condition systematically biases the numerical sampling of the underlying probability distribution of $\xi_i^+(t)$. The discarded trajectories are those with the largest absolute value, so they belong to the tails of the underlying probability distribution. Failure to take them into account when computing averages can be expected to significantly

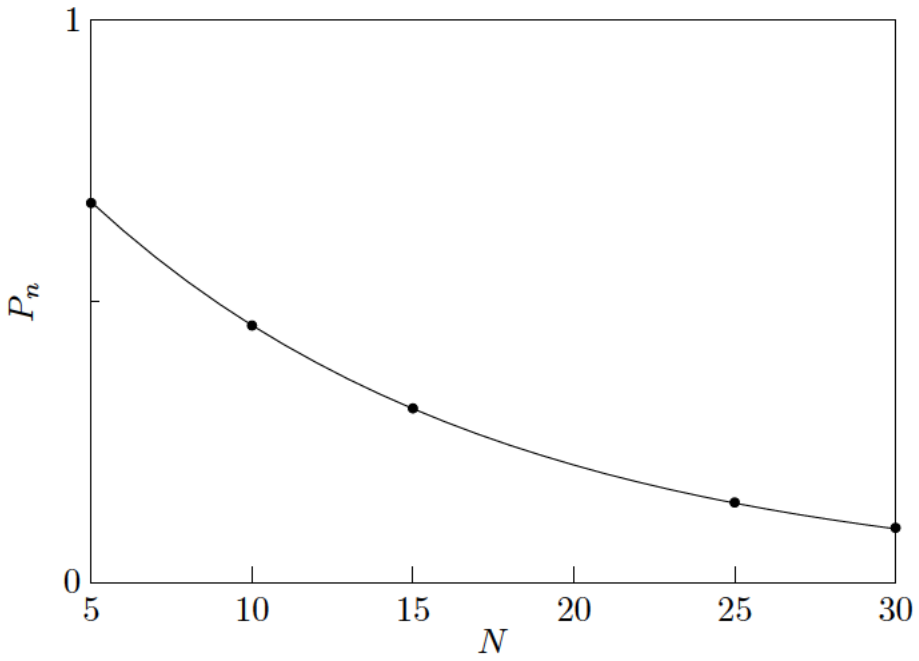

Figure D.4: Probability $P_n(N)$ of no trajectories diverging for a system of size N, following time evolution with $\Delta t = 10^{-2}$, $\Gamma = 4$, $t_s = 1$. The dots are obtained from numerical simulations for different system sizes, whereas the solid line shows the prediction obtained from the $N = 7$ result assuming that the trajectories ξ_i^+ for different i are independent of each other.

affect the sampling if the distribution is heavy-tailed. The choice of Δt could therefore be interconnected with how the probability distribution of the stochastic variables is sampled.

D.2.4 Effect of N

It was observed in simulations that, for a given choice of parameters, the number of diverging trajectories increases upon increasing the number of spins N. The simplest way of modelling this effect is assuming that each trajectory diverges independently of all others. Starting from this hypothesis, if P_d is the probability that a particular trajectory diverges for a set of given parameters and P_n is the probability of no trajectories diverging, for a system with N spins we expect:

$$P_n(N) = (1 - P_d)^N. \tag{D.26}$$

This assumption was tested by performing simulations for a number of different parameters. The probability P_d for a single trajectory to diverge was estimated based on Eq. (D.26) from

simulations for $N = 7$ (an arbitrarily chosen system size). Using this result, the expected $P_n(N)$ for different system sizes $N = 5, 10, 15, 25, 30$ was computed using Eq. (D.26) and compared to the values obtained from simulations. Figure D.4 shows $P(N)$ obtained from 10000 realisations of the stochastic processes with $\Delta t = 10^{-2}$, $\Gamma = 4$, $t_s = 1$. It can be seen that the prediction based on the assumption that the trajectories at different sites are independent (solid line) matches the observed values (points). A similar analysis for other quenches showed qualitatively similar results. These findings show that the effect of N on the number of divergent trajectories is indeed compatible with the hypothesis that each trajectory has a certain probability of diverging independently of all others.

D.2.5 Temporal Distribution of the Divergence of Trajectories

The trajectories ξ_i^+ don't diverge uniformly over time. In fact, most trajectories diverge in the vicinity of the Loschmidt peaks. This is clearly shown in Fig. D.5. Notably, since the equation for ξ_i^+ only depends on the quench parameters, this effect is independent of which observable one is interested in. So, in real time, the existence of the Loschmidt peaks when quenching across a quantum critical point affects the calculation of every observable. This provides further evidence that the behaviour of the disentangling variables is intimately related to the underlying Loschmidt dynamics.

D.2.6 Different Averaging Conventions

The issue of diverging trajectories poses a question as to how to perform the required averaging for a given stopping time t_s. A number of choices are possible, each coming with its own advantages and disadvantages. To investigate their relative merits, they were compared by considering the calculation of the Loschmidt rate function for the quantum Ising model, following a quantum quench of the transverse field from $\Gamma = 0$ to $\Gamma = 16\Gamma_c$. Three possible averaging prescriptions are:

(i) For all times t, average over all trajectories that have survived up to the final time t_s.

(ii) At any particular time $t \leq t_s$, average over all trajectories that are still finite at t.

(iii) At any particular time $t < t_s$, average over all trajectories are still finite at time $t + n\Delta t$, i.e. after n more time-steps, for a suitably chosen n. Based on the findings of Section D.2.2, the obvious choice is $n = 10$.

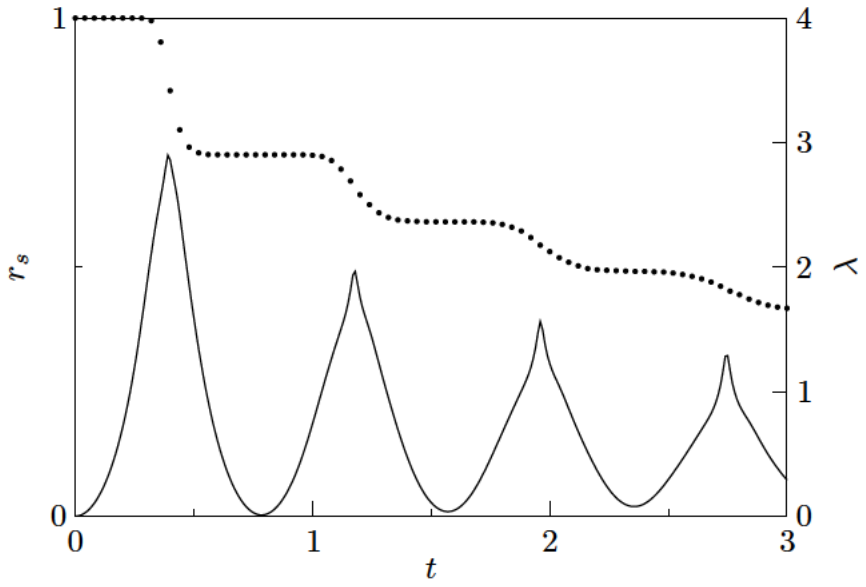

Figure D.5: Fraction r_s of finite trajectories as a function of time following a quantum quench $\Gamma = 0$ to $\Gamma = 16\Gamma_c$ in a transverse field Ising chain of size $N = 7$ initialised in the state $|\Downarrow\rangle$ with all spins down. The enhanced divergence rate of trajectories in the vicinity of the Loschmidt peaks in the rate function $\lambda(t)$ (obtained from exact diagonalisation) is clearly visible.

In prescription (i), the average of a given observable is computed using the same number of trajectories at all times $t \leq t_s$. While it may appear like a reasonable choice, this prescription actually introduces a non-Markovian behaviour in the calculation of observables, as the average at a given time t becomes dependent on the choice of stopping time $t_s > t$. This effect was indeed observed in simulations. Furthermore, in this prescription trajectories that are still valid at some $t < t_s$ are discarded provided that they eventually diverge, so an additional amount of statistics is lost.

Approach (ii) involves the least degree of arbitrariness, because averages at a given time t are independent of the endtime t_s and no further parameter choices are required. However, averages computed by prescription (ii) are affected by very large fluctuations, as shown in Fig. D.6(a). This is due to the fact that, as clarified in Sections D.2.1 and D.2.2, trajectories that are still finite at some t may be regarded as already pathological (i.e. 'on track to diverge') if they satisfy $|\xi_i^+| > \xi_*^+$.

Prescription (iii) is found to be the best choice. Using this prescription, trajectories are used for averages for as long as they can be regarded as non-pathological. The interval n_s is chosen in a way that is informed by a numerical understanding of the diverging of trajectories (Section D.2.2). In Fig. D.6, we plot the results obtained by using (a)

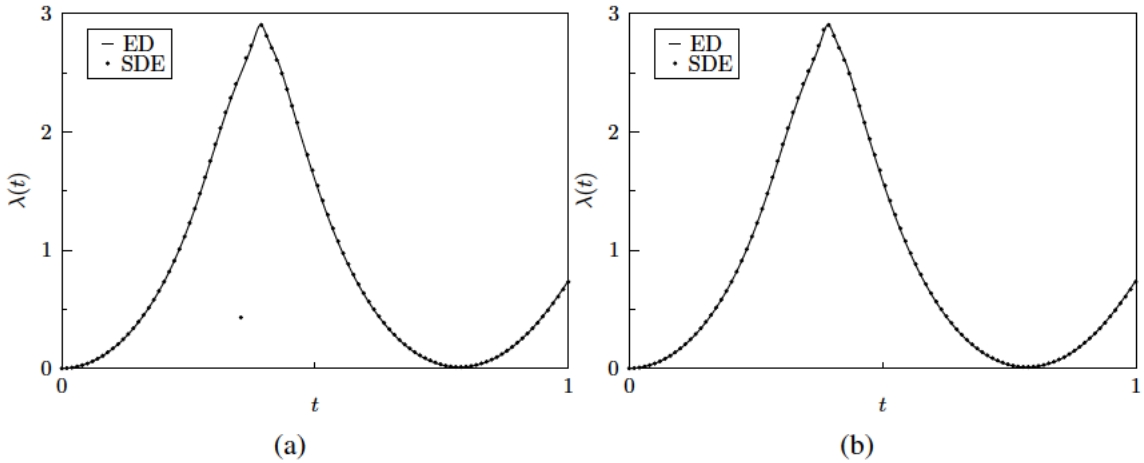

Figure D.6: Loschmidt rate function following a quantum quench from $\Gamma = 0$ to $\Gamma = 16\Gamma_c$ for a transverse field Ising chain of size $N = 7$ initialised in the state $|\Downarrow\rangle$ with all spins down. Panel (a) was obtained using prescription (ii), wheares panel (b) was obtained following prescription (iii) with $n_s = 10$. The two averages used the same data set, consisting of 10000 simulations with discretisation time-step $\Delta t = 10^{-4}$. It can be seen that the average in (a) is affected by large fluctuations: some points are very far from the expected curve, even outside the visible region. This is due to the inclusion in the average of trajectories that are still finite yet should be regarded as pathological according to Eq. (D.24). This effect is absent in (b).

Prescription (ii) and (b) Prescription (iii). It can be seen that the effect of pathological trajectories causes strong fluctuations in (a), which are absent in (b). For all plots presented in this Thesis, we computed the relevant averages following Prescription (iii).

D.3 Numerical Performance for Computing the Magnetisation

Similarly to the analysis carried out for the Loschmidt rate function, we begin by inspecting $m(t)$ obtained using the same computational parameters for different quench parameters. For simplicity, we focus on quenches where the system is initialised in the ferromagnetic ground state $|\psi_0\rangle = \otimes_i |\downarrow\rangle_i$. Figure D.8 shows the magnetisation $m(t)$ as a function of time for various quenches within the ferromagnetic phase up to criticality, $\Gamma_f \leq \Gamma_c$. We use the same physical and computational parameters as we previously did for the Loschmidt rate function. It can be seen that, relatively to the respective scales, fluctuations are much stronger for the magnetisation. The same can be seen for quenches across the

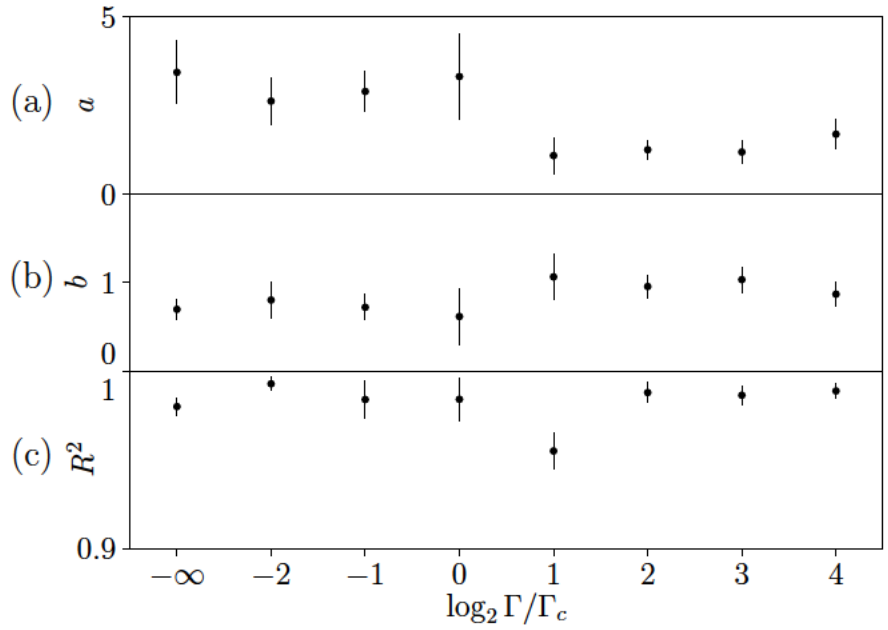

Figure D.7: Coefficients obtained by fitting the error on the magnetisation $m(t)$ to an exponential. We consider a TFIC with $N = 5$ spins initialised in the FM ground state with all spins down, following quantum quenches to different values of Γ. We find that the exponential parameterisation (D.27) is a good approximation to the time dependence of the error, as illustrated by the value of R^2 (panel (c)). Across the parameter range, we see that the growth is approximately exponential with $b \sim 1$. The overall prefactor a decreases for larger values of Γ. The bars show the standard deviation over the parameters obtained for 5 batches of 2×10^5 independent simulations each.

quantum critical point, shown in Fig. D.9. The extent of the fluctuations makes it difficult to provide a quantitative estimate of the performance of the method in computing the magnetisation; the results we observe are however compatible with exponential growth in time parameterised as

$$\Delta m(t) \sim e^{a+bt}. \tag{D.27}$$

In Fig. D.7 we show the parameters a, b obtained from fitting the numerical data to Eq. (D.27). The growth of error is well approximated by the suggested exponential parameterisation with $b \sim 1$ across all the parameter range. Comparable results were obtained for larger system sizes. Because of the large fluctuations, we were not able to identify a clear pattern concerning the effect of N on the error.

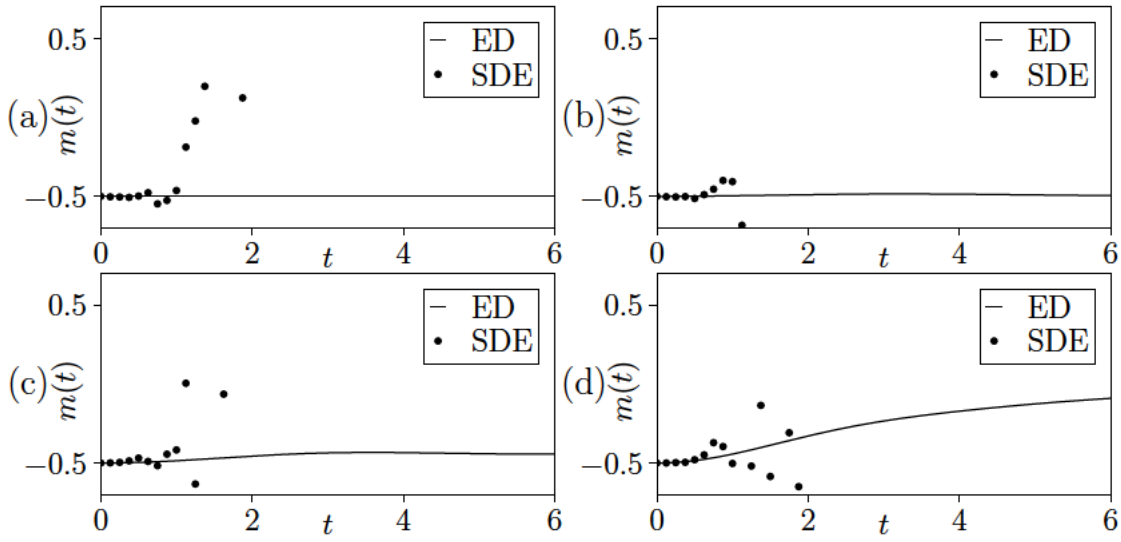

Figure D.8: Magnetisation $m(t)$ for a TFIC of size $N = 10$. We consider quantum quenches from the all-down state to different final transverse fields (a) $\Gamma = 0$, (b) $\Gamma = \Gamma_c/4$, (c) $\Gamma = \Gamma_c/2$, (d) $\Gamma = \Gamma_c$. The SDEs results were obtained from 10^5 simulations. Compared to the Loschmidt rate function, we find that large fluctuations arise at earlier times and have a more pronounced effect.

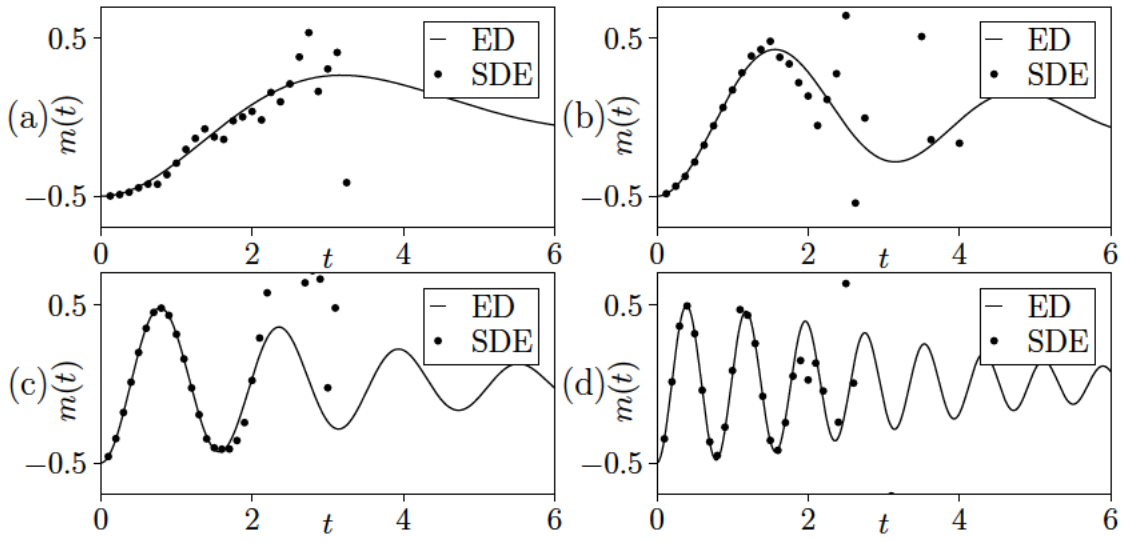

Figure D.9: Magnetisation $m(t)$ for a TFIC of size $N = 10$ initialised in the ferromagnetic ground state, for final transverse field (a) $\Gamma = 2\Gamma_c$, (b) $\Gamma = 4\Gamma_c$, (c) $\Gamma = 8\Gamma_c$, (d) $\Gamma = 16\Gamma_c$. The SDEs results were obtained from 10^5 simulations. Again we find that the SDE result is affected by strong fluctuations, although they are slightly mitigated compared to quenches within the critical point.

Appendix E

Multimode Dicke Model via Equations of Motion Method

The stochastic formalism discussed in this Thesis is not limited to spin chains, and can also be applied to effective spin models describing the dynamics of more complex interacting systems. An example of this is provided in Ref. [4] in the case of a single spin of magnitude j in a photonic waveguide. For this problem, an effective description involving only the spin operators is obtained by integrating out the photonic degrees of freedom. By translating the problem into the stochastic formalism and explicitly averaging the SDEs, the authors of Ref. [4] obtain a system of ordinary differential equations which they solve recursively, computing scattering and decay amplitudes.

Here we revisit this problem from a different point of view, showing that the necessary system of equations can be obtained directly by considering the equations of motion of certain amplitudes rather than using the stochastic approach, exploiting the relation between the system of ODEs obtained from averaging the SDEs and the more conventional language of quantum mechanics discussed in Appendix B.4. Using this method, we compute scattering and decay amplitudes, finding a discrepancy with the results obtained in Ref. [4] for which we provide a rationale. We conclude this Appendix by showing that the same approach can also be used to compute time-dependent quantities, considering the Loschmidt echo as an example.

E.1 Multimode Dicke Model

We begin our discussion by briefly outlining the model studied in Ref. [4] and the derivation of the effective single-spin Hamiltonian. Let us consider a single spin-j situated in a 1D photonic waveguide. The spin can be regarded as describing a collection of $2j$ spin-$1/2$ atoms confined to a region that is small compared to the wavelength of light. This system can be described by the Hamiltonian of the multimode Dicke model [162, 4]:

$$\hat{H} = \sum_k k\hat{a}_k^\dagger \hat{a}_k + \Delta(t)\hat{S}^z + g(t)\sum_k (\hat{S}^+\hat{a}_k + \hat{S}^-\hat{a}_k^\dagger). \tag{E.1}$$

The time-evolution operator, including time-dependent sources $J_k^{(*)}(t)$, is given by

$$\hat{U}(t_f,t_0) = \mathrm{Texp}\left[-i\int_{t_0}^{t_f} \mathrm{d}t \left(\hat{H}(t) + \sum_k [J_k^*(t)\hat{a}_k + J_k(t)\hat{a}_k^\dagger]\right)\right]. \tag{E.2}$$

Consider two states $|in\rangle$, $|out\rangle$, each of which is the direct product of the vacuum of the photon subspace and a given spin state, i.e.

$$|in\rangle = |\Omega_p\rangle \otimes |in\rangle_S. \tag{E.3}$$

The matrix element of $\hat{U}$ with respect to these states is given by

$$U_{oi}(t_f,t_0) \equiv \langle out|\hat{U}(t_f,t_0)|in\rangle. \tag{E.4}$$

We are interested in computing physical observables such as decay or scattering amplitudes. As pointed out in Ref. [4], all these observables can be ultimately obtained from the matrix element $U_{oi}(t_f,t_0)[J,J^*]$, where the photonic sources $J_j^{(*)}$ are usually set to zero at the end of a given calculation. For example, scattering amplitudes can be computed using the LSZ reduction formula [163]:

$$iT_{\boldsymbol{p},\boldsymbol{k}} = \frac{(2\pi)^n G_{\boldsymbol{p},k}(\omega_k,\omega_p)}{\prod_{j=1}^n [G_0(\omega_{p_j},p_j)G_0(\omega_{k_j},k_j)]}\Big|_{\text{on shell}} \tag{E.5}$$

where $G_0(\omega_{k_j},k_j)$ is the propagator and $G_{p,k}(\boldsymbol{t}',\boldsymbol{t})$ is computed as

$$G_{p,\boldsymbol{k}}(\boldsymbol{t}',\boldsymbol{t}) = \frac{\delta^n \log Z[\boldsymbol{J},\boldsymbol{J}^*]}{\delta J_{p1}^*(t_1')\ldots\delta J_{p2}(t_1)\ldots}\Big|_{J,J^*=0} \tag{E.6}$$

from the generating functional

$$Z[\boldsymbol{J},\boldsymbol{J}^*] \equiv \lim_{T\to\infty(1-i\varepsilon)} \langle 0|\hat{U}_\Omega(T,-T)|0\rangle. \tag{E.7}$$

with $\hat{U}_\Omega = \langle \Omega_p|\hat{U}|\Omega_p\rangle$. In this Appendix, for later convenience, we label the spin states by the number of spins up rather than by the eigenvalue of $\hat{S}^z$, e.g. $\hat{S}^z|0\rangle = -j$, $\hat{S}^z|2j\rangle = j$.

We can also compute the decay amplitude for a given state. Considering an initial state $|0;2j\rangle$ where the spin is fully excited and there are no photons, the amplitude for this initial state decay into a state with $2j$ photons and a fully relaxed spin $|k_1,\ldots,k_2 j;0\rangle$ at $t=\infty$ is given by

$$T_k \equiv \langle k_1,\ \ldots,k_{2j};0|\hat{U}(\infty,0)|_{J=0}|0;2j\rangle \tag{E.8}$$

$$= \lim_{t\to\infty}\lim_{T\to\infty} \frac{\delta^{2j}}{\delta J^*_{k_1}(T)\ \ldots \delta J^*_{k_{2j}}(T)} \langle 0|\hat{U}_\Omega(t,0)|2j\rangle. \tag{E.9}$$

A more detailed discussion of these expressions is provided in Section E.5.

E.1.1 Effective Time Evolution Operator

Let us Trotter-slice the matrix element U_{oi} and insert resolutions of the identity in the photonic subspace, defined in terms of photonic coherent states [164]

$$|\psi\rangle = e^{\sum\limits_\alpha \psi_\alpha a^\dagger_\alpha}|\Omega_p\rangle. \tag{E.10}$$

We can express the bosonic part of the problem as a path integral, while objects in the spin subspace are not affected:

$$U_{oi} = \langle out|_S \int D[\psi,\psi^\dagger]\,\mathrm{Texp}\left(iS[\psi,\psi^\dagger]\right)|in\rangle_S \tag{E.11}$$

$$S[\psi,\psi^\dagger] \equiv \int \mathrm{d}t \left(\sum_k \psi^\dagger_k(i\partial_t - k)\psi_k + \sum_k[-g(\psi^\dagger_k\hat{S}^- + \psi_k\hat{S}^+) + J^*_k\psi_k + J_k\psi^\dagger_k] - \Delta S^z\right) \tag{E.12}$$

where an overall normalization factor has been absorbed in the integration measure. The bosonic degrees of freedom can now be integrated out (the details of this procedure are

given in Section E.6), yielding

$$U_{oi} = \langle out|_S \hat{U}_\Omega |in\rangle_S \tag{E.13}$$

$$= \langle out|_S U_0 \,\mathrm{Texp}\left[\int \mathrm{d}t \left(-\frac{1}{2}g^2\hat{\boldsymbol{S}}^2 + \frac{1}{2}g^2(\hat{S}^z)^2 - (i\Delta + \frac{g^2}{2})\hat{S}^z + Y^-\hat{S}^+ + Y^+\hat{S}^-\right)\right]|in\rangle_S, \tag{E.14}$$

where we have defined the integrated source fields [4]

$$Y^+(t') \equiv g(t')\sum_k \int_0^\infty e^{-ik\tau} J_k^*(t'+\tau)\mathrm{d}\tau, \tag{E.15}$$

$$Y^-(t) \equiv g(t)\sum_k \int_0^\infty e^{-ik\tau} J_k(t-\tau)\mathrm{d}\tau, \tag{E.16}$$

and U_0 represents the free evolution of the bosonic system.

E.1.2 Disentanglement Transformation

By inspecting the effective Hamiltonian in Eq. (E.14) we notice that the term $\sim \hat{\boldsymbol{S}}^2$ gives a constant: for spin j, we get $\hat{\boldsymbol{S}}^2 = j(j+1)$. The remaining quadratic term $\propto (\hat{S}^z)^2$ in the exponential can be decoupled by means of a Hubbard-Stratonovich transformation as per the general procedure outlined in Chapter 2:

$$\hat{U}_\Omega = U_0 \int D\phi \,\mathrm{Texp}\left[\int \mathrm{d}t \left(-\frac{1}{2}g^2\hat{\boldsymbol{S}}^2 - (i\Delta + \frac{g^2}{2} - g\phi)\hat{S}^z + Y^-\hat{S}^+ + Y^+\hat{S}^-\right)\right]. \tag{E.17}$$

We can thus read off Stratonovich SDEs describing the evolution of the stochastic variables:

$$\dot{\xi}_+ = Y^- - i\Delta\xi_+ - \frac{g^2}{2}\xi_+ - Y^+\xi_+^2 + g\xi_+\phi, \tag{E.18a}$$

$$\dot{\xi}_z = -i\Delta - g^2/2 - 2Y^+\xi_+ + g\phi, \tag{E.18b}$$

$$\dot{\xi}_- = Y^+ \exp\xi_z. \tag{E.18c}$$

Because of the term $(\hat{S}^z)^2$ in the effective Hamiltonian, i.e. an interaction term supported at a single site, the Stratonovich and Ito equation of motions for this model are different, providing an exception to the the general observation made in Chapter 2. In particular, the

equation for ξ_+ can be converted according to Eq. (2.25a) to yield the Ito SDEs

$$\dot{\xi}_+ = Y^- - i\Delta\xi_+ - Y^+\xi_+^2 + g\xi_+\phi, \tag{E.19a}$$

$$\dot{\xi}_z = -i\Delta - g^2/2 - 2Y^+\xi_+ + g\phi, \tag{E.19b}$$

$$\dot{\xi}_- = Y^+ \exp\xi_z. \tag{E.19c}$$

Following the same procedure as for the quantum Ising model, we could now derive stochastic expressions for the physical observables of interest. This is the strategy followed in Ref. [4]; the SDEs are then averaged to produce a system of ODEs that are then solved exactly. Here, we will follow a different approach, outlined in the next Section.

E.2 Derivation of the Equations of Motion

By integrating out the photons, we obtained an effective time-evolution operator Eq. (E.14). In this Section, we will explain how the systems of ordinary differential equations (ODEs) given in Ref. [4] can be derived directly from Eq. (E.14) by considering the equations of motion of a family of amplitudes.

E.2.1 Scattering Amplitudes

In order to obtain scattering amplitudes we need to calculate $\log(Z)$, where Z is defined in Eq. (E.7). For our problem, we are only going to need the $Y^{\pm}$-dependent terms, since all other terms do not contribute when computing functional derivatives. We thus get

$$\log Z[\boldsymbol{J},\boldsymbol{J}^*] = \log\left[\langle 0|\mathrm{Texp}\int\left(\frac{g^2}{2}(\hat{S}^z)^2 - [i\Delta + \frac{g^2}{2}]\hat{S}^z + Y^-\hat{S}^+ + Y^+\hat{S}^-\right)\mathrm{d}t|0\rangle\right] + \ldots, \tag{E.20}$$

where the dots denote terms that do not contribute. Thus, we only need to compute

$$F_0 \equiv \langle 0|\mathrm{Texp}[\int\left(\frac{g^2}{2}(\hat{S}^z)^2 - [i\Delta + \frac{g^2}{2}]\hat{S}^z + Y^-\hat{S}^+ + Y^+\hat{S}^-\right)\mathrm{d}t]|0\rangle \equiv \langle 0|\hat{U}_{\mathrm{eff}}|0\rangle, \tag{E.21}$$

where we have defined an effective time-evolution operator. The corresponding effective Hamiltonian is given by:

$$-iH_{\text{eff}} = \left(\frac{g^2}{2}(\hat{S}^z)^2 - [i\Delta + \frac{g^2}{2}]\hat{S}^z + Y^-\hat{S}^+ + Y^+\hat{S}^-\right). \tag{E.22}$$

Then, we can differentiate Eq. (E.21) to obtain the equation of motion for F_0:

$$\begin{aligned}
\frac{dF_0}{dt} &= \langle 0|\frac{d\hat{U}_{\text{eff}}}{dt}|0\rangle && \text{(E.23)}\\
&= \langle 0|(-i\hat{H}_{\text{eff}})\hat{U}_{\text{eff}}|0\rangle && \text{(E.24)}\\
&= \sum_n \langle 0|(-i\hat{H}_{\text{eff}})|n\rangle\langle n|\hat{U}_{\text{eff}}|0\rangle && \text{(E.25)}\\
&= \sum_n \langle 0|(-i\hat{H}_{\text{eff}})|n\rangle F_n, && \text{(E.26)}
\end{aligned}$$

where we have inserted a complete set of states labelled by the number n of spins up and we have defined objects F_n analogous to F_0. The matrix elements of the Hamiltonian can be computed directly:

$$\langle n|\hat{H}_{\text{eff}}|0\rangle = \begin{cases} i\Delta j + \frac{g^2}{2}j(j+1) & \text{for } n \text{ even},\\ 2jY^+ & \text{for } n \text{ odd}. \end{cases} \tag{E.27}$$

Similarly, we can find the equations of motion for the other functions F_n using the relations

$$\begin{aligned}
\hat{S^z}|n\rangle &= (n-j)|n\rangle, && \text{(E.28)}\\
\hat{S^+}|n\rangle &= (2j-n)|n+1\rangle, && \text{(E.29)}\\
\hat{S^-}|n\rangle &= n|n-1\rangle, && \text{(E.30)}
\end{aligned}$$

while all other matrix elements are zero. We find:

$$\frac{dF_n}{dt} = \left[-i\Delta(n-j) + \frac{g^2}{2}\left((n-j)(n-j) - (n-j)\right)\right]F_n + nY^-F_{n-1} + (2j-n)Y^+F_{n+1} \tag{E.31}$$

$$\equiv a_nF_n + nY^-F_{n-1} + (2j-n)Y^+F_{n+1}. \tag{E.32}$$

This is precisely the hierarchy of equations given in Ref [4], which contains all information about scattering; here, we derived it without using the stochastic approach.

E.2.2 Decay of a Fully Excited State

To calculate the decay amplitude for a fully excited state, we need to compute the amplitude

$$\lim_{t\to\infty}\lim_{T\to\infty}\frac{\delta^{2j}}{\delta J^*_{k_1}(T)\ \ldots\delta J^*_{k_{2j}}(T)}\langle 0|\hat{U}_\Omega|2j\rangle.$$

Let us define

$$R_{2j}\equiv\langle 0|\hat{U}_\Omega|2j\rangle. \tag{E.33}$$

We can find the equation of motion for this object by directly differentiating:

$$\begin{aligned}
\frac{dR_{2j}}{dt} &= \langle 0|\frac{d\hat{U}_\Omega}{dt}|2j\rangle && \text{(E.34)}\\
&= \langle 0|\frac{d}{dt}\left(e^{-\int\frac{g^2}{2}\hat{S}^2\mathrm{d}t}Te^{-i\int\hat{H}_{\text{eff}}\mathrm{d}t}\right)|2j\rangle && \text{(E.35)}\\
&= \langle 0|\left(-\frac{g^2}{2}\hat{S}^2-i\hat{H}_{\text{eff}}\right)\hat{U}_\Omega|2j\rangle && \text{(E.36)}\\
&= \sum_n\langle 0|\left(-\frac{g^2}{2}\hat{S}^2-i\hat{H}_{\text{eff}}\right)|2j-n\rangle\langle 2j-n|\hat{U}_\Omega|2j\rangle && \text{(E.37)}\\
&\equiv \sum_n\langle 0|\left(-\frac{g^2}{2}\hat{S}^2-i\hat{H}_{\text{eff}}\right)|2j-n\rangle R_n, && \text{(E.38)}
\end{aligned}$$

where we defined a family of amplitudes

$$R_n\equiv\langle 2j-n|\hat{U}_\Omega|2j\rangle \tag{E.39}$$

and an effective Hamiltonian

$$-iH'_{\text{eff}}=\left(\frac{g^2}{2}(\hat{S}^z)^2-[i\Delta+\frac{g^2}{2}]\hat{S}^z+Y^-\hat{S}^++Y^+\hat{S}^-\right), \tag{E.40}$$

which is different from the effective Hamiltonian (E.22) for decay amplitudes. The overlap in Eq. (E.38) can be readily computed and, by proceeding analogously, we can find the equations of motion for all the amplitudes R_n:

$$\begin{aligned}
\frac{dR_n}{dt} &= \left[-i\Delta(j-n)-\frac{g^2}{2}(2j-n)(n+1)\right]R_n+Y^+nR_{n-1} && \text{(E.41)}\\
&\equiv a_nR_n+Y^+nR_{n-1}. && \text{(E.42)}
\end{aligned}$$

We thus retrieve the hierarchy of equations given in Ref. [4], which describe the decay of an excited state.

E.3 Recursive Solution of the Equations of Motion

In the previous Section, we have derived two systems of coupled ODEs encoding all information about scattering and decay amplitudes respectively. In this Section, we will show how these can be solved recursively, following the approach explained in Ref. [4]. We will find that, while the result we obtain for the scattering amplitude matches the finding of Ref. [4] (up to a misprint), the results for the decay amplitude differ significantly. We will argue in favour of our result by providing a rationale as to the origin of this discrepancy.

E.3.1 Scattering of 2 Photons

To illustrate how to compute a scattering amplitude from Eq. (E.41), we will consider the simplest case of a $1 \to 1$ scattering process. We are interested in

$$G_{p,k} = \frac{\delta^2 \ln Z[J,J^*]}{\delta J_p^*(\omega_p)\delta J_k(\omega_k)}. \tag{E.43}$$

We can obtain this term from its Fourier transform

$$G_{p,k}(t_1,t_2) = \frac{\delta^2 \ln Z[\boldsymbol{J},\boldsymbol{J}^*]}{\delta J_p^*(t_2)\delta J_k(t_1)}\Big|_{\boldsymbol{J},\boldsymbol{J}^*=0}. \tag{E.44}$$

Using the fact that

$$\log Z[\boldsymbol{J},\boldsymbol{J}^*] = \log F_0[\boldsymbol{J},\boldsymbol{J}^*](t=\infty,t_0=-\infty) + C \tag{E.45}$$

where C is a constant independent of $J^{(*)}$, we can expand $\log Z[\boldsymbol{J},\boldsymbol{J}^*]$ in powers of $J_k,\ J_k^*$. Using $Z[J,J^*]/(Z[0]) = 1+\alpha_1+\alpha_2+\ldots$, where $\alpha_n = O((JJ^*)^n)$, we find that the α_1 term gives the $1 \to 1$ scattering amplitude.
So, we only need to compute

$$\alpha_1 = \frac{\delta^2 F_0(t=\infty,t_0=-\infty)}{\delta J_p^*(t_2)\delta J_k(t_1)}\Big|_{J,\boldsymbol{J}^*=0} \equiv F^{+-}_{0;p,k}(t=\infty,t_0=-\infty;t_2,t_1). \tag{E.46}$$

Every term in the expansion of F_0 is the solution of a finite system of equations which can be obtained from Equation (E.31). Let's focus on the equation for the term in Eq. (E.46):

$$\dot{F}^{+-}_{0;p,k}(t;t_2,t_1) = a_0 F^{+-}_{0;p,k}(t;t_2,t_1) + 2j\frac{\delta^2}{\delta J^*_p(t_2)\delta J_k(t_1)}\left(Y^+(t)F_1(t)\right)\Big|_0 \tag{E.47}$$

where

$$\frac{\delta Y^+(t)}{\delta J^*_p(t_2)} = g\, e^{-ip(t_2-t)}, \tag{E.48}$$

$$\frac{\delta Y^-(t)}{\delta J_k(t_1)} = g\, e^{-ik(t-t_1)}. \tag{E.49}$$

We can similarly find the equation of motion for

$$\frac{\delta F_1(t)}{\delta J_k(t_1)}\Big|_0 \equiv F^-_{1;k}(t;t_1), \tag{E.50}$$

given by

$$\dot{F}^-_{1;k}(t;t_1) = a_1 F^-_{1;k}(t;t_1) + \frac{\delta Y^-(t)}{\delta J_k(t_1)} F_0[0](t). \tag{E.51}$$

F_0 in turn satisfies

$$\dot{F}_0[0] = a_0 F_0[0](t). \tag{E.52}$$

The boundary conditions are $F_0[0](t=t_0)=1$ and $F_n[0](t=t_0)=0\ \forall\ n>0$. Crucially, the equation for $F_0[0](t=t_0)=1$ is decoupled from the other F_n, and in general the equation for each F_n only depends on F_m with $m \leq n$. Thus, we solve these equations working upwards from F_0:

$$F_0(t) = e^{a_0(t-t_0)}, \tag{E.53}$$

$$F^-_{1;k}(t;t_1) = g\,\frac{e^{a_0(t-t_0)-ik(t-t_1)} - e^{a_1(t-t_0)-ik(t_0-t_1)})}{a_0-a_1-ik_1}, \tag{E.54}$$

$$F^{+-}_{0;p,k}(t;t_2,t_1) = 2g^2 j\ (A+B+C), \tag{E.55}$$

with

$$A \equiv -\frac{e^{i[k(-t_0+t_1)+p(t_0-t_2)]}}{(p-k)(ijg^2+p-\Delta)}, \tag{E.56}$$

$$B \equiv \frac{e^{i(k(t_1-t)+p(t-t_2))}}{(p-k)\,(ijg^2+k-\Delta)}, \tag{E.57}$$

$$C \equiv -\frac{\exp\left[g^2 j(t_0-t)+i(-kt_0+kt_1+p(t-t_2)-\Delta t+\Delta t_0)\right]}{(\Delta-ijg^2-k)\,(\Delta-ijg^2-p)}. \tag{E.58}$$

Taking the infinite time limit, we find that $C \to 0$ and

$$\lim_{t\to\infty} A+B = 2\pi i\ \delta(x)\frac{1}{p-\Delta+ijg^2}e^{ip(t_1-t_2)}. \tag{E.59}$$

Fourier-transforming with respect to $t_1,\ t_2$:

$$\mathrm{FT}[A+B,t_1,t_2] = \frac{1}{2\pi}\frac{i\ \delta(p-k)}{p-\Delta+ijg^2}\left(\frac{\varepsilon^2}{((p-\omega_k)^2+\varepsilon^2)\,((p-\omega_p)^2+\varepsilon^2)}\right). \tag{E.60}$$

Then, applying the LSZ reduction formula, we find

$$iT_{\boldsymbol{p},\boldsymbol{k}} = -2jg^2\left(\frac{i\varepsilon^2\delta(p-k)}{(p-\Delta+ijg^2)\,((p-\omega_k)^2+\varepsilon^2)\,((p-\omega_p)^2+\varepsilon^2)}\right)\times\frac{\omega_k-\varepsilon_p+i\varepsilon}{i}\frac{\omega_p-\varepsilon_p+i\varepsilon}{i}\Big|_{\text{on sh}} \tag{E.61}$$

$$= -\frac{2ijg^2}{p-\Delta+ijg^2}\ \delta(p-k). \tag{E.62}$$

Up to a misprint $p-\Delta \to p$ in the denominator, this result matches the finding of Ref. [4].

E.3.2 Decay of a Fully Excited State

The hierarchy of equations describing the decay of a fully-excited state is given by:

$$\dot{R}_n = b_n R_n + nY^+ R_{n-1} \quad (0<n<2j). \tag{E.63}$$

As an example of an observable, we can compute the one-photon spectrum, given by

$$P_{2j}(q) = \int\prod \mathrm{d}p_m\left(\sum_m \delta(q-p_m)\right)|T_{p_1,\ \ldots,p_{2j}}|^2, \tag{E.64}$$

where $T_{p_1,\,\ldots,p_{2j}}$ is the amplitude for the decay of a fully excited state into $2j$ photons of momenta $p_1,\,\ldots,p_{2j}$, given by Eq. (E.8); this quantity can be written as:

$$T_{\mathbf{p}} \propto \lim_{T\to\infty} \frac{\delta^{2j}}{\delta J^*_{p_1}(T)\,\ldots\delta J^*_{p_{2j}}(T)} R_{2j}(t\to\infty, t_0=0)\Big|_{\mathbf{J}^*=0}. \tag{E.65}$$

Proportionality factors are not relevant here, as they can be fixed by requiring that the spectrum is appropriately normalised. In Ref. [4], the general result is given as

$$P_{2j}(q) = \sum_{m=0}^{2j-1} \frac{1}{2j\pi} \frac{g[j(j+1)-(j-m)^2]}{g^4[j(j+1)-(j-m)^2]^2+(q-\Delta)^2}. \tag{E.66}$$

Since the general form of a normalized Lorentz peak with width parameter Ξ and peaking at $x = x_0$ is given by

$$L(x) = \frac{1}{\pi}\frac{\Xi}{(x-x_0)^2+\Xi^2}, \tag{E.67}$$

Eq. (E.66) is seen to be a sum of $2j$ Lorentz peaks. Let us consider the case with $j = 1$, corresponding to the flipping of the spin from $+1$ to -1 with the emission of 2 photons. In this case, we have:

$$b_0 = -g^2 - i\Delta, \tag{E.68}$$

$$b_1 = -g^2, \tag{E.69}$$

$$b_2 = i\Delta. \tag{E.70}$$

To compute the decay amplitude, we only need three equations:

$$\frac{\delta^2 \dot{R}_2(t)}{\delta J^*_{p_1}(T)\delta J^*_{p_2}(T)} \equiv \dot{R}^{++}_{2;p_1,p_2} = b_2 R^{++}_{2;p_1,p_2} + \frac{\delta Y^+}{\delta J^*_{p_2}} R^+_{1;p_1} + \Big(p_1 \leftrightarrow p_2\Big), \tag{E.71a}$$

$$\dot{R}^+_{1;p_1} = b_1 R^+_{1;p_1} + \frac{\delta Y^+}{\delta J^*_{p_1}} R_0[0], \tag{E.71b}$$

$$R_0 = e^{b_0 t}. \tag{E.71c}$$

Again, working upwards from the equation for R_0, we find:

$$R^{+}_{1;p_1}(t) = \frac{g\left(-1+e^{t(ip_1-i\Delta)}\right)e^{-g^2t-ip_1T}}{ip_1-i\Delta}, \tag{E.72}$$

$$\begin{aligned} R^{++}_{2;p_1,p_2}(t) =& 2g^2 e^{i\Delta t - iT(p_1+p_2)}\Big[\frac{2g^2-i(-2\Delta+p_1+p_2)}{(g^2-i(p_1-\Delta))\,(g^2-i(p_2-\Delta))\,(g^2-i(-2\Delta+p_1+p_2))} \\ &- \frac{(-2\Delta+p_1+p_2)e^{t\left(-g^2+i(-2\Delta+p_1+p_2)\right)}}{(p_1-\Delta)(p_2-\Delta)\,(-2\Delta+ig^2+p_1+p_2)} + \frac{e^{-t\left(g^2-i(p_1-\Delta)\right)}}{(\Delta-p_2)\,(\Delta-ig^2-p_1)} \\ &+ \frac{e^{-t\left(g^2-i(p_2-\Delta)\right)}}{(\Delta-p_1)\,(\Delta-ig^2-p_2)}\Big], \end{aligned} \tag{E.73}$$

such that

$$\lim_{t\to\infty}|R^{++}_{2;p_1,p_2}|^2 = \frac{4g^4\left(4g^4+(p_1+p_2-2\Delta)^2\right)}{(g^4+(p_1-\Delta)^2)\,(g^4+(p_2-\Delta)^2)\,(g^4+(+p_1+p_2-2\Delta)^2)}. \tag{E.74}$$

Integrating over the momentum p_2, relabelling $p_1 \to q$ and normalising, we obtain

$$P(q) = \frac{3g^2}{2\pi\,(g^4+(q-\Delta)^2)} - \frac{g^2}{\pi\,(4g^4+(q-\Delta)^2)}, \tag{E.75}$$

whereas, for $j=1$, Eq. (E.66) from Ref. [4] gives

$$\tilde{P}(q) = \frac{g^2}{2\pi\,(g^4+(q-\Delta)^2)} + \frac{g^2}{\pi\,(4g^4+(q-\Delta)^2)}. \tag{E.76}$$

The origin of this discrepancy can be understood by noticing that $\tilde{P}$ is obtained if we omit the term in braces in the system of equations (E.71):

$$\frac{\delta^2\dot{R}_2(t)}{\delta J^*_{p_1}(T)\delta J^*_{p_2}(T)} \equiv \dot{R}^{++}_{2;p_1,p_2} = b_2 R^{++}_{2;p_1,p_2} + \frac{\delta Y^+}{\delta J^*_{p_2}} R^{+}_{1;p_1} + \cancel{\left\{p_1 \leftrightarrow p_2\right\}}, \tag{E.77a}$$

$$\dot{R}^{+}_{1;p_1} = b_1 R^{+}_{1;p_1} + \frac{\delta Y^+}{\delta J^*_{p_1}} R_0[0], \tag{E.77b}$$

$$R_0 = e^{b_0 t}. \tag{E.77c}$$

Solving this modified system, we find an amplitude that is asymmetric in p_1, p_2:

$$T_{p_1,p_2} = \lim_{t\to\infty}\lim_{T\to\infty}|R^{++}_{2;p_1,p_2}|^2 = \frac{4g^4}{(g^4+(p_2-\Delta)^2)\,(g^4+(-2\Delta+p_1+p_2)^2)}. \tag{E.78}$$

The corresponding one-photon spectrum,

$$\tilde{P}(q) = \frac{g^2}{2\pi\left(g^4 + (q-\Delta)^2\right)} + \frac{g^2}{\pi\left(4g^4 + (q-\Delta)^2\right)}, \tag{E.79}$$

matches Eq. (E.76). We thus attribute the mismatch between this result and Eq. (E.75) to the omission of the last term in Eq. (E.77a).

E.4 Loschmidt Echo for a Fully Excited State

We have shown how from an effective spin Hamiltonian we can directly compute scattering amplitudes and decay rates. This approach can be similarly used to analytically compute time-dependent quantities. As an example, we consider the Loschmidt echo, defined as

$$L(t) \equiv |\langle in|\hat{U}(t,0)|in\rangle|^2, \tag{E.80}$$

i.e. the probability of finding the system in the same state as it was initialised, after non-trivial time evolution. Initialising the system in a fully excited state, $|in\rangle = |\Omega\rangle_p \otimes |2j\rangle$, this quantity is given by R_0 as defined in Eq. (E.39). We consider the case where both the atomic detuning Δ and the coupling constant g are time-dependent. The result is

$$L(t) = \left|\exp\left[-j\int (g^2(t) + i\Delta(t))\mathrm{d}t\right]\right|^2. \tag{E.81}$$

It would be interesting to investigate if other matter-light models can be solved exactly by means of a similar recursive procedure.

E.5 Physical Observables

In this Section, we provide details on the formulae for the physical observables introduced in Section E.1.

E.5.1 Scattering Amplitudes

Scattering amplitudes can be computed using the LSZ formalism [163], since this is the appropriate language to compute T-matrix elements defined between n-particle eigenstates $|k1,\ k2,\ \ldots\rangle$ that are the eigenstates of the non-interacting theory. The LSZ machinery

tells us that we can extract these states from the eigenstates of the full, interacting theory by multiplying by a propagator per each external (incoming or outgoing) particle, and then imposing the on-shell condition. This effectively allows us to extract the correct asymptotic n-particle state from the interacting one, since the former is the residue of the latter at a pole corresponding to the on-shell condition. We also have to consider large times $-T$, T with $T \to \infty(1-i\varepsilon)$, in order for the vacuum of the interacting theory to evolve into the vacuum of the free theory. Equipped with these ingredients, we can write the LSZ formula (in momentum space) as:

$$iT_{\boldsymbol{p},k} = \frac{(2\pi)^n G_{p,k}(\omega_k, \omega_{\boldsymbol{p}})}{\prod_{j=1}^n [G_0(\omega_{p_j}, p_j) G_0(\omega_{k_j}, k_j)]}\Big|_{\text{on shell}}, \tag{E.82}$$

where

$$G_0(\omega_{k_j}, k_j) = \frac{i}{\omega_p - \varepsilon_p + i\varepsilon} \tag{E.83}$$

is the propagator (or non-interacting 2-particle Green's function), whereas $G_{p,\boldsymbol{k}}(\omega_{\boldsymbol{k}}, \omega_p)$ is the Fourier transform of the Green's function:

$$G_{\boldsymbol{p},k}(\omega_{\boldsymbol{k}}, \omega_p) = \int \prod_{j=1}^n \Big[\frac{\mathrm{d}t_j \mathrm{d}t'_j}{2\pi}\Big] G_{p,k}(\boldsymbol{t}', \boldsymbol{t}) \prod_{j=1}^n \big[-\exp\left[i(\omega_{p_j} t'_j - \omega_{k_j} t_j)\right]\big]. \tag{E.84}$$

We can compute the Green's function as

$$G_{p,\boldsymbol{k}}(\boldsymbol{t}', \boldsymbol{t}) = \frac{\delta^n \ln Z[\boldsymbol{J}, \boldsymbol{J}^*]}{\delta J^*_{p1}(t'_1) \ldots \delta J_{p2}(t_1) \ldots}\Big|_{J, \boldsymbol{J}^*=0}, \tag{E.85}$$

where the generating functional of Green's functions is defined as

$$Z[J, J^*] \equiv \lim_{T \to \infty(1-i\varepsilon)} \langle 0 | \hat{U}_\Omega(T, -T) | 0 \rangle \tag{E.86}$$

with $\hat{U}_\Omega = \langle \Omega_p | \hat{U} | \Omega_p \rangle$.

E.5.2 Decay of a Fully Excited State

The amplitude for the decay of a fully excited state is given by the overlap of a final state at $t = \infty$ having $2j$ photons with momenta $k_1, \ldots, k_{2j}$ and $\langle \hat{S}^z \rangle = -j$, and an initial state at $t_0 = 0$ with no field excitations and $\langle \hat{S}^z \rangle = j$ (fully excited spin), after the latter has been

evolved by $\hat{U}_0(\infty,0)$ (where the suffix 0 denotes the absence of sources):

$$T_{k_1\ldots k_{2j}} = \langle k_1,\ \ldots, k_{2j}; 0|U_0(\infty,0)|0; 2j\rangle. \tag{E.87}$$

In order to produce excitations, we need to act appropriately on the source fields J_k, J_k^*. In the effective action, these appear within the integrated source fields Y^+, Y^- defined in Eq. (E.15). The desired amplitude is given by

$$T_{\boldsymbol{k}} \equiv \langle k_1,\ \ldots, k_{2j}; 0|\hat{U}_0(\infty,0)|0; 2j\rangle \tag{E.88}$$

$$= \lim_{t\to\infty}\lim_{T\to\infty} \frac{\delta^{2j}}{\delta J^*_{k_1}(T)\ \ldots \delta J^*_{k_{2j}}(T)} \langle 0|\hat{U}_\Omega(t,0)|2j\rangle. \tag{E.89}$$

A little care is required with the above limits. If we want to inspect what particles are present at infinity, we must consider $t \geq T$ (i.e., the time when we observe the system must be greater than the time at which the particles are created).

E.6 Integration of the Bosonic Degrees of Freedom

In this Section, we provide the details of the integration of the bosonic degrees of freedom carried out in Section E.1.1. Consider the $\psi^{(\dagger)}$-dependent terms in the integrand of the action Eq. (E.12):

$$\hat{I}(\psi) = i\sum_k [\psi_k^\dagger (i\partial_t - k)\psi_k - g(\psi_k^\dagger \hat{S}^- + \psi_k \hat{S}^+) + J_k^*\psi_k + J_k\psi_k^\dagger]. \tag{E.90}$$

The right Green's function $G(t-t_0)$ is defined as the solution of

$$(i\partial_t - k)G(t-t_0) = \delta(t-t_0), \tag{E.91}$$

so that

$$\int \mathrm{d}t_0 (i\partial_t - k)G(t-t_0) = 1. \tag{E.92}$$

The Green's function can be computed in Fourier space:

$$G(t-t_0) = \int_{-\infty}^{\infty} \frac{e^{i\omega(t-t_0)}}{2\pi}\tilde{G}(\omega)\mathrm{d}\omega, \tag{E.93}$$

$$\delta(t-t_0) = \int_{-\infty}^{\infty} \frac{e^{i\omega(t-t_0)}}{2\pi}\mathrm{d}\omega. \tag{E.94}$$

From the defining equation we get

$$\tilde{G}(\omega) = -\frac{1}{k+\omega}, \tag{E.95}$$

$$G(t-t_0) = -\int_{-\infty}^{\infty} \frac{1}{2\pi} \frac{1}{k+\omega-i\varepsilon} e^{i\omega(t-t_0)} \mathrm{d}\omega, \tag{E.96}$$

where the $i\varepsilon$ shift (with $\varepsilon > 0$) was added to ensure causality, i.e. $G(t) = 0 \; \forall \; t < t_0$. The integral can be carried out using Cauchy's residue theorem. The pole of the integrand is at $\omega = -k + i\varepsilon$. For $t < t_0$ we have to close the contour in the lower half plane, and thus we get 0. For $t > t_0$ we have to close the contour in the upper half plane ($\omega \to -i\infty$) and, in the limit $\varepsilon \to 0$, we get $-e^{-ik(t-t_0)}$. Thus, we find:

$$G(t-t_0) = -ie^{-ik(t-t_0)}\theta(t-t_0). \tag{E.97}$$

Conjugating the defining equation for G, we find that

$$(-i\partial_t - k)G^*(t-t_0) = \delta(t-t_0) \tag{E.98}$$

$$G^*(t-t_0)(i\partial_t - k) = \delta(t-t_0) \tag{E.99}$$

where in the second step we have integrated by parts.
Equipped with these results, we can re-write Eq. (E.90) (temporarily suppressing the k suffices to avoid notational clutter)

$$\begin{aligned}\hat{I}(\psi) = i\Big\{ &\left(\psi_k + \int G(t-t')[J(t') - g\hat{S}^-]\mathrm{d}t'\right)^\dagger (i\partial_t - k)\left(\psi_k + \int G(t-t')[J(t') - g\hat{S}^-]\mathrm{d}t'\right) \\ &- \int G^*(t-t')[J^*(t') - g\hat{S}^+]\mathrm{d}t'(i\partial_t - k)\int G(t-t'')[J(t'') - g\hat{S}^-]\mathrm{d}t'' \Big\}.\end{aligned} \tag{E.100}$$

We can now perform the Gaussian integral over the ψ variables. Reintroducing the k subscripts and the t integral, we find an effective action:

$$\hat{I}_e = -i\sum_k \int \mathrm{d}t \int \mathrm{d}t' G(t-t')(J_k^*(t) - g\hat{S}^+)(J_k(t') - g\hat{S}^-) \tag{E.101}$$

$$= -\sum_k \int \mathrm{d}t \int \mathrm{d}t' e^{-ik(t-t')}\theta(t-t')(J_k^*(t) - g\hat{S}^+)(J_k(t') - g\hat{S}^-). \tag{E.102}$$

This expression comprises four terms. The first one,

$$-\sum_k \int \mathrm{d}t \int \mathrm{d}t' e^{-ik(t-t')}\theta(t-t')J_k^*(t)J_k(t'), \tag{E.103}$$

describes the free evolution of the bosonic system. There is then a term quadratic in spin operators:

$$-\sum_k \int \mathrm{d}t \int \mathrm{d}t' e^{-ik(t-t')}\theta(t-t')g^2\hat{S}^+\hat{S}^-. \tag{E.104}$$

We can perform the sum over k, which yields a Kronecker delta; however, using a regularisation $\varepsilon \to 0$, we find that the presence of the $\theta(t-t')$ implies that only $1/2$ of the weight of the delta contributes. The above term is thus equal to

$$-\frac{1}{2}\int \mathrm{d}t g^2 \hat{S}^+\hat{S}^- = -\frac{1}{2}\int \mathrm{d}t g^2(\hat{\boldsymbol{S}}^2 - \hat{S}^z\hat{S}^z - \hat{S}^z), \tag{E.105}$$

where in the second step we used the commutation relations of SU(2). Finally, we consider the remaining two terms, which represent the annihilation/creation of bosons from the source fields:

$$g\sum_k \int \mathrm{d}t \int \mathrm{d}t' e^{-ik(t-t')}\theta(t-t')J_k^*(t)\hat{S}^- + g\sum_k \int \mathrm{d}t \int \mathrm{d}t' e^{-ik(t-t')}\theta(t-t')\hat{S}^+J_k(t'). \tag{E.106}$$

By defining the integrated source fields $Y^\pm$ as in Eq. (E.15) and relabeling $t' \to t$ in the final expression for Y^+, the final two terms can be rewritten compactly as:

$$\int (Y^+(t)\hat{S}^- + Y^-(t)\hat{S}^+)\mathrm{d}t. \tag{E.107}$$

The final effective time evolution operator is thus given by

$$U_\Omega = U_{oi}^0 \,\mathrm{Texp}\left[\int \mathrm{d}t \left(-\frac{1}{2}g^2\hat{\boldsymbol{S}}^2 + \frac{1}{2}g^2(\hat{S}^z)^2 - (i\Delta + \frac{g^2}{2})\hat{S}^z + Y^-\hat{S}^+ + Y^+\hat{S}^-\right)\right]. \tag{E.108}$$